CONTACTLESS REAL-TIME MONITORING OF PAPER MECHANICAL BEHAVIOR DURING PAPERMAKING

PHASE I

Report submitted to

Office of Industrial Technologies
U.S. Department of Energy

RESEARCH TEAM

Institute of Paper Science and Technology (IPST)

Pierre H. Brodeur (Associate Professor of Physics, Principal Investigator)
Joseph P. Gerhardstein (Associate Engineer)
Charles C. Habeger, Jr. (Professor of Physics)
Jimmy Jae Ho Jong (Research Scientist – Mechanical Engineering)
Emmanuel F. Lafond (Research Scientist – Physics)
Brian Pufahl (Assistant Engineer)

Idaho National Engineering and Environment Laboratory (INEEL)

Vance A. Deason (Consulting Scientist)
Robert S. Schley (Scientist)
Kenneth L. Telschow (Consulting Scientist)
John B. Walter (Scientist)
Scott M. Watson (Scientist)

Georgia Institute of Technology (GIT)

Yves H. Berthelot (Professor of Mechanical Engineering)

Institute of Paper Science and Technology
500 10th St. N.W., Atlanta, GA 30318

October 13, 1998

CONTACTLESS REAL-TIME MONITORING OF PAPER MECHANICAL BEHAVIOR DURING PAPERMAKING

PHASE I

Report submitted to

Office of Industrial Technologies
U.S. Department of Energy

RESEARCH TEAM

Institute of Paper Science and Technology (IPST)

Pierre H. Brodeur (Associate Professor of Physics, Principal Investigator)
Joseph P. Gerhardstein (Associate Engineer)
Charles C. Habeger, Jr. (Professor of Physics)
Jimmy Jae Ho Jong (Research Scientist – Mechanical Engineering)
Emmanuel F. Lafond (Research Scientist – Physics)
Brian Pufahl (Assistant Engineer)

Idaho National Engineering and Environment Laboratory (INEEL)

Vance A. Deason (Consulting Scientist)
Robert S. Schley (Scientist)
Kenneth L. Telschow (Consulting Scientist)
John B. Walter (Scientist)
Scott M. Watson (Scientist)

Georgia Institute of Technology (GIT)

Yves H. Berthelot (Professor of Mechanical Engineering)

Institute of Paper Science and Technology
500 10th St. N.W., Atlanta, GA 30318

October 13, 1998

EXECUTIVE SUMMARY

This project is a three Phase project with the final goal of demonstrating a single-point, non-contact monitoring system which can be mounted to a scanning platform. Ultimately, this monitoring system will be used to control the papermaking process. Phase I of the project, which this report covers, was concerned with evaluating available technologies for the monitoring system, including stiffness and fiber orientation measurement methods. Phase II will demonstrate an integrated system in a laboratory setting. Phase II will also begin to look at the process control issues, in particular, what to do with the information available from the monitoring system. Phase III will take the integrated system from Phase II to several mills for field trials.

At the end of Phase I, we are proud to announce that all goals for the first year have been met or exceeded.

On the instrumentation side of the project, a pair of web simulators were constructed which can take strips of machine made papers and move them at speeds in excess of 40 m/s, plus apply a simulated "flutter". These instruments have allowed the evaluation of 5 different types of laser based ultrasound detection systems (for determination of stiffness properties) on moving paper in a laboratory setting. These detectors included:

- Fabry-Pérot
- Frequency domain photorefractive interferometers
- Time domain photorefractive interferometers
- Self-mixing vibrometer
- Photoinduced-EMF

All five detectors were capable of measuring ultrasound waves on stationary paper, and three (Fabry-Pérot, self-mixing vibrometer, and photoinduced-EMF) were able to make measurements on various grades of paper at production speeds (up to 25 m/s) completely non-contact.

Fiber orientation distribution (FOD) is another area of investigation during Phase I of the project. Two fiber-orientation measuring instruments were built and successfully tested. The first is based upon the measuring of dyed fibers in a sample, and is intended as a reference instrument. The second is based upon non-contact light transmission/scattering through the sample. Both were found to agree well with each other.

Also beginning earlier than originally planned, the equipment to evaluate the effect of moisture content and temperature on ultrasonic velocities has begun to be assembled.

Phase II of the project will involve the integration of these technologies into an instrument that will be used to probe the fundamentals of the papermaking process, with the intent to control the paper machine for optimal product properties.

TABLE OF CONTENTS

LIST OF FIGURES

LIST OF TABLES

1 INTRODUCTION

1.1 *Motivation for Present Work*

Baum stated in a landmark paper published in 1987 the following (Baum, 1987):

> "The elastic properties of paper form a basic set of parameters which are useful for monitoring the effects caused by changes in process variables, capable of predicting end use performance, and overall, help to provide a better understanding of the fibrous network we call paper. Elastic parameters also are important in product design and modeling, e.g., in the construction of tubes, boxes, food containers, etc. Eventually their use will help to control the paper machine automatically. Because most of the elastic parameters needed to describe paper can now be determined easily and non-destructively using wave propagation methods, the opportunity exists to move forward in each of these areas."

In the context of real-time control of the papermaking process, which is the long-term motivation behind the present project, Table 1.1.1 summarizes in a very simple way the effect of machine variables on different elastic stiffness properties (Baum, 1987; Ishisaki, 1997). It can be seen that the inverse problem of predicting the behavior of individual sub-processes from elastic stiffness measurements is complex because some of the processes can produce similar trends on stiffnesses (e.g., refining and wet pressing). This implies that additional information is needed such as the geometrical fiber orientation distribution (FOD) and the stiffness orientation distribution (SOD). Differences between FOD and SOD can be appreciated in Figures 1.1.1 and 1.1.2. In Figure 1.1.1, one can see that the FOD for laboratory machine-made paper samples manufactured under different wet straining and restrained conditions is unaffected by these processes. This is not the case for the SOD in Figure 1.1.2, which is sensitive to wet straining and/or restrained drying. Contrary to FOD, SOD depends upon built-in stresses.

Table 1.1.1 Effect of machine variables on elastic stiffness properties.

Elastic Stiffness Constants	Refining Level	Anisotropy Ratio	Wet Pressing Level	MD Wet Straining Level	Restrained Drying
	From Low to High	*From Low to High*	*From Low to High*	*From Low to High*	*From Full Restraints to CD Only*
MD: C_{11}	↑	↑	↑	↑	0
CD: C_{22}	↑	↓	↑	↓	↑
ZD: C_{33}	↑	0	↑	↓	0
MD-CD: C_{66}		↓	↑	0	
MD-ZD: C_{55}		↑	↑	↓	
CD-ZD: C_{44}		↓	↑	↓	

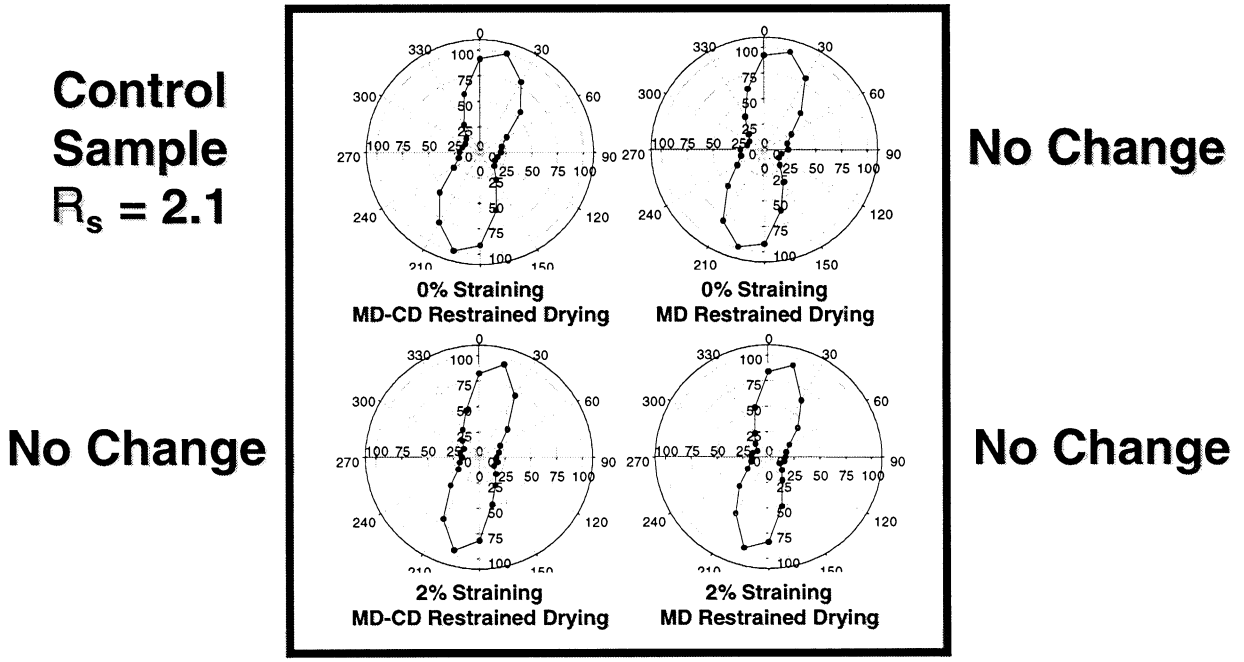

Figure 1.1.1 Geometrical Fiber Orientation Distribution (FOD) for different paper samples manufactured under different wet straining and restrained drying conditions. Control sample (MD/CD ratio = 2.8) is in upper left corner. Straining and restraint drying do no appreciably affect the FOD.

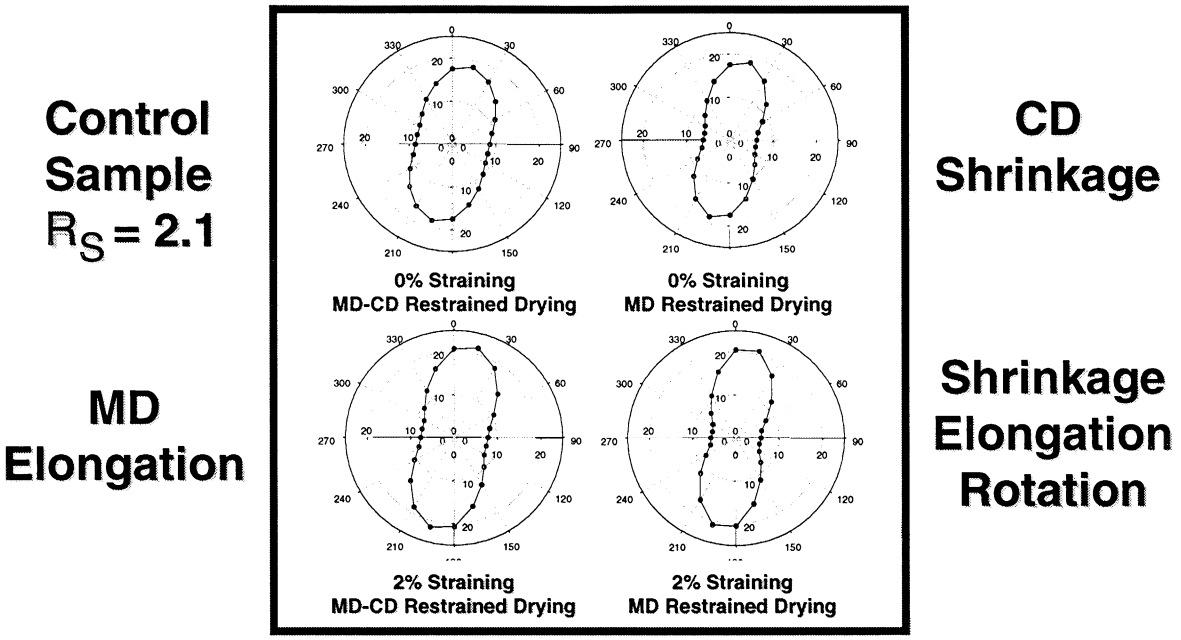

Figure 1.1.2 Stiffness Orientation Distribution (SOD) obtained for different paper samples manufactured under different wet straining and restrained drying conditions. Control sample is in the upper left corner. Restraint drying and wet straining affect SOD.

To this day, nobody has attempted to tackle the inverse problem presented by Baum, experimentally, numerically, or theoretically. Because it is so difficult, it is believed that an experimental approach must first be investigated to gather hard evidence. Also, it is postulated that existing information obtained on a paper machine (grammage, thickness, moisture content, web temperature) and currently unavailable information such as stiffness properties, FOD and SOD, can be used in a meaningful manner to provide a preliminary layout of a model to control the papermaking process.

1.2 *Introduction to the Project*

The task of achieving real-time control of the papermaking process is a long-term goal. First it is necessary to develop appropriate instrumentation to determine stiffness properties, FOD, and

SOD, and demonstrate the functioning of this instrumentation first in the laboratory, then in a mill environment. Since measurements would be of limited interest without an attempt to interpret them and predict the impact of machine variables on paper mechanical properties, it is important to begin as early as possible an investigation of the relationships between machine variables and mechanical properties. This is the essence of this project. Commercialization of technology, development of process control strategies, actuators, and development of a monitoring system considering full sheet inspection rather than a scanner-based approach are beyond the scope of the project.

The purpose of the project is two-fold:

1) To develop and demonstrate from the laboratory to the mill a new technology aimed at determining stiffness properties, FOD and SOD on a moving paper web;

2) To begin an investigation of the inverse problem of relating paper mechanical properties to paper machine variables.

There have been several research and development efforts associated with the development of test methods to monitor paper stiffness properties on a moving web. However, all of them have focused on the use of contact methods to probe paperboard. It is believed that the availability of a non-contact method is largely preferable for several reasons: no potential damage to the web, rich information content, extended grade monitoring. There are two possible approaches: air-coupled transduction and laser-based ultrasound. The use of air-coupled transducers is a priori attractive because it offers simplicity and is cost-effective. However, it suffers from one major problem: measurements are sensitive to air path parameters (temperature, humidity level, turbulence level). Also, the available information may be inadequate. The second approach, laser ultrasonics, is more complex, but can provide the desirable information (stiffness properties, FOD, and SOD). This approach was chosen for the following reasons:

- Extensive scientific support;
- Rich and reliable information content;
- Simultaneous detection of FOD and SOD;
- Unlikely to damage to the web;
- Test method suitable for fine papers and paperboards (universal method);
- Potential for 100% web inspection implementation.

As a first step aimed at demonstrating the concept of laser ultrasonics on non-moving paper, The Institute of Paper Science and Technology requested the assistance of the Georgia Institute of Technology (GIT) in 1994 to initiate research work on the use of lasers to excite and detect Lamb waves in paper. Exploratory internal funding for a one-year project was awarded by both institutions in September 1994. Results were obtained very early in the project (see Figure 1.2.1) and showed that the technique was very promising. Since then, results have been reported on different paper and paperboard grades (Brodeur et al., 1997).

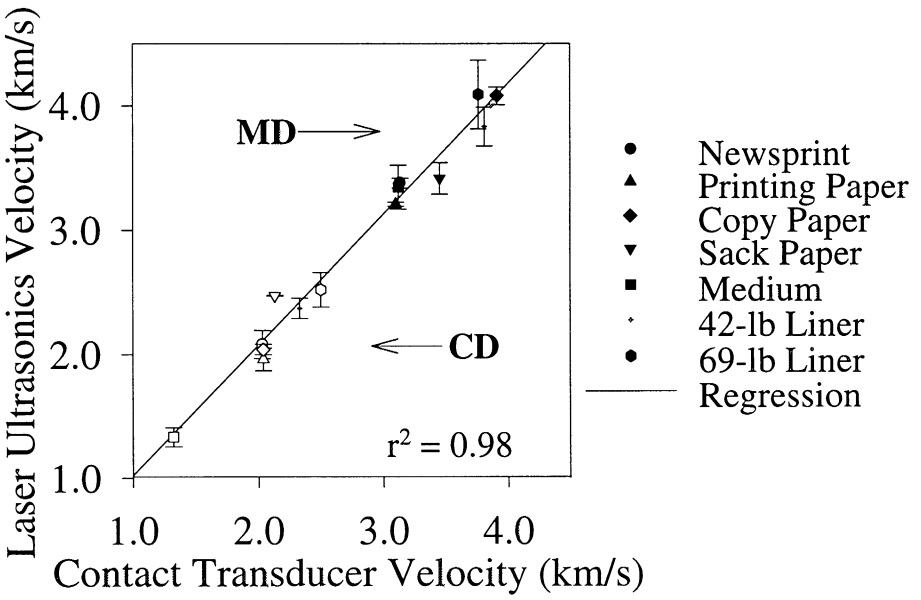

Figure 1.2.1 Laser ultrasonics validation results as obtained using different non-moving paper and paperboard samples. One can see that machine direction (MD) and cross-machine direction (CD) velocity results gathered using contact transducers and laser ultrasonics are in very good agreement (Brodeur et al., 1997).

The next step in this endeavor was to address the more challenging task of performing laser ultrasonics measurements on moving paper, first in the laboratory, then on a paper machine. A research proposal was submitted to the Department of Energy, Office of Industrial Technologies Agenda 2020 Program in 1996. The following organizations were invited to collaborate with IPST: Idaho National Engineering and Environmental Laboratory, Georgia Institute of Technology, and Honeywell-Measurex Corporation. The proposed work considered a three-phase project over a four-year period:

- Phase I (Year 1): Laboratory Demonstration on Moving Paper (Proof of Concept);
- Phase II (Years 2 and 3): Laboratory Demonstration of On-machine Prototype System;
- Phase III (Year 4): Field Demonstration of On-machine Prototype System.

The proposal was reviewed and recommended for funding by the Sensors and Controls Task Group of the American Forest and Paper Association. The Department of Energy awarded a three-year contract to IPST in September 1997 and funding was granted for the first two phases of the project. It was agreed that additional funding would be provided for Phase III on the basis of successful completion of Phase II. An updated version of the original proposal, which was submitted to DOE in June 1997 to reflect the initial funding of Phases I and II, is reproduced in Appendix A.

As soon as the project was authorized, the research team met for the first time at IPST. Following an intensive brainstorming session on the latest scientific and technical developments in the field of laser ultrasonics, a research plan for Phase I was devised. This plan was continuously reviewed and updated to optimize resources and fully meet or exceed project

objectives. Also, two extensive review meetings were held in March and May. The actual Statement of Work for Phase I can be seen in Appendix B. Also, anticipated Tasks for Phases II and III, and an updated Time Schedule for the full project are displayed in Appendix B.

Now, one year later, we are very pleased to report that we were able to fully meet or exceed project objectives for Phase I, especially the laboratory demonstration of laser ultrasonics on moving paper. The experimental methodology and the results are reported in the following sections.

1.3 *Deliverables*

Deliverables for the full project duration are:

Phase I (Year I):

- Laboratory demonstration of laser ultrasonic characterization of moving paper (Proof of Concept).
- Development of image analysis and light scattering methods for fiber orientation measurements.

Phase II (Years II and III):

- Laboratory demonstration of single-point on-machine prototype system to monitor the mechanical behavior of paper during papermaking (include integrated detection of fiber and stiffness orientation distributions).
- Development of a preliminary model relating mechanical properties of paper to papermaking processes.

Phase III (Year IV):

- Mill demonstrations (fine paper and linerboard paper machines) of single-point on-machine prototype system mounted on a scanning platform to monitor the mechanical behavior of paper during papermaking.
- Technical and economical assessment of technology.

2 EXPERIMENTAL METHODOLOGY

2.1 *Introduction*

One of the major unknown variables in the strategy to understand and control the papermaking process is the stiffness properties of the web. Ultrasonics has long been used to determine, non-destructively, the stiffness of materials. This section details the use of non-contact, laser-based ultrasound generation and detection on a moving web.

This section starts off with a review of laser ultrasound generation and detection. Five different laser ultrasound detectors are then described and evaluated. In order to determine how well they work on moving paper, a laboratory web simulator was constructed. Finally, an optical scanning technique is described which reduces surface noise, and the effect of laser wavelength on generation is investigated.

2.2 *Spectral Absorption of Paper (J. Gerhardstein, IPST)*

From an optics standpoint, paper is a diffuse reflecting material with widely varying spectral response. Some papers are designed to reflect most visible light to appear to have a high brightness, and others absorb much of the visible spectrum. From the standpoint of building a laser ultrasonic measurement system, it would be best to choose lasers with wavelengths that will provide consistent results across grades for their desired tasks. Hence a literature search was undertaken to try to determine what regions of the visible or non-visible spectrum would be best for detection and excitation.

The majority of work in the literature available on light absorption in paper is concerned with the visible region (400-700 nm), and for the most part is only concerned with a single value called "Brightness". TAPPI has several methods to measure optical properties in the visible region (T-442, T-452, T-480, T-519, T-524, T-525, T-527, T-534, T-646, T-653, T-1209) (TAPPI, 1998), and these heavily populate the available literature.

There are several good references in the literature as to spectrophotometric measurements of paper. Jordan and O'Neill (1988) performed a round-robin study on four samples to determine the accuracy and precision of colorimeters. These samples cover a wide range of products and pulp types. A graph of the percent reflectance for these samples in the visible region is shown in Figure 2.2.1. The manilla is the only unbleached sample of the four. It shows much lower reflectance from 400-500 nm than the bleached samples do. Reflectance generally increases from the blue (400 nm) to the red (700 nm).

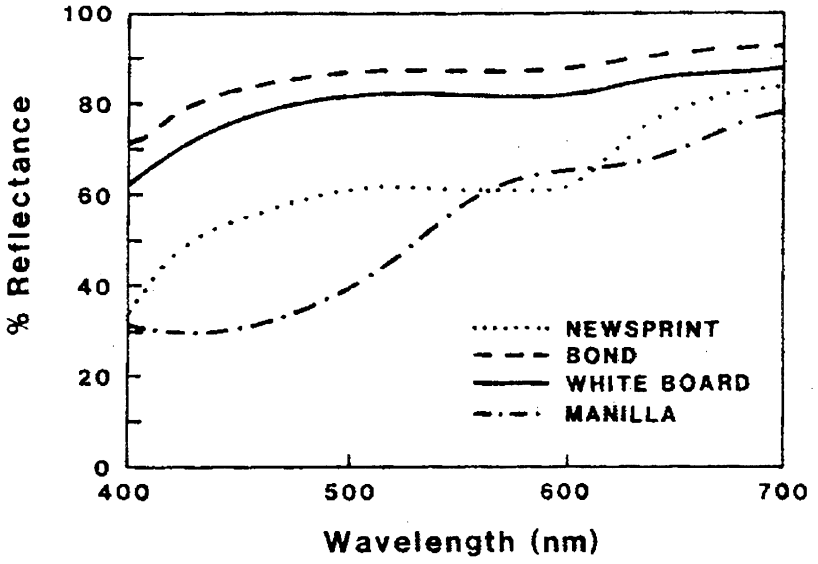

Figure 2.2.1 Reflectance curves for a series of samples used in a round-robin study for wavelengths from 400-700 nm, reproduced from Jordan and O'Neill (1988).

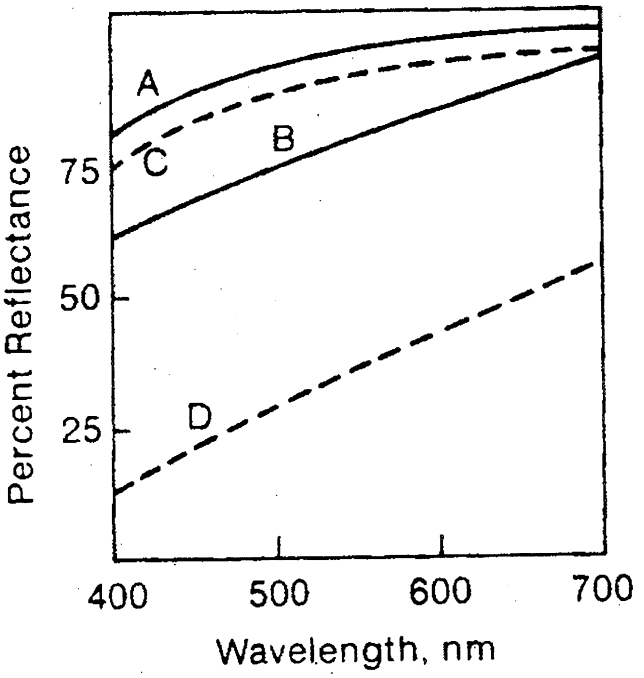

Figure 2.2.2 Spectral response of bleached and unbleached sulfite and kraft pulps from 400-700 nm. Samples are: A) bleached sulfite; B) unbleached sulfite; C) bleached kraft; D) unbleached kraft. Reproduced from Scott and Dearth (1992).

Figure 2.2.2, from Scott and Dearth (1992), shows reflectance for bleached sulfite (A), unbleached sulfite (B), bleached kraft (C) and unbleached kraft (D). All four pulps have a higher reflectance at higher wavelengths. As expected, bleached pulps (A & C) reflect more light across the entire visible region than their respective unbleached pulps (B & D).

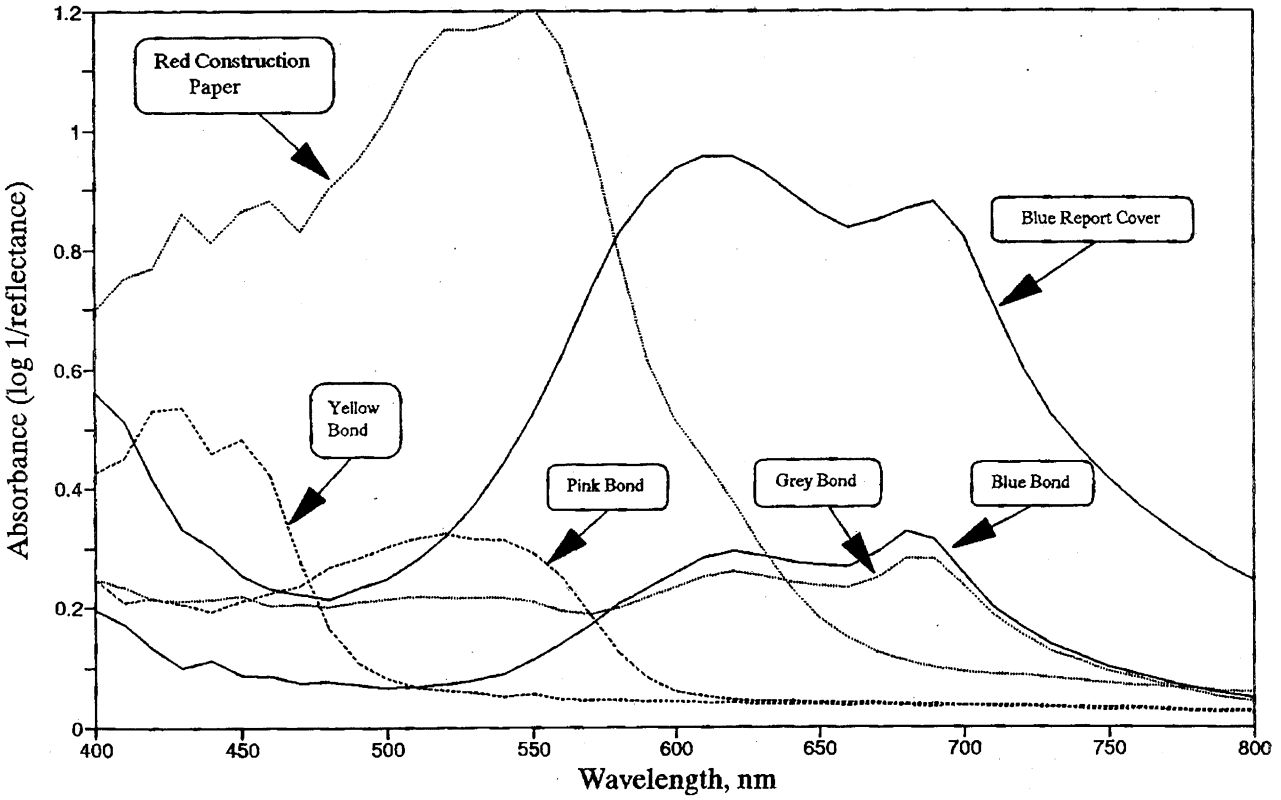

Figure 2.2.3 Spectral response for dyed papers. Reproduced from Biermann (1996).

In Figure 2.2.3, Biermann (1996) shows absorbance (=$\log_{10}$ 1/reflectance) for different colored papers. As expected, different colors absorb different wavelengths. This diversity of spectral responses makes the visible region a difficult area to try to find a universally high reflection or absorption band in.

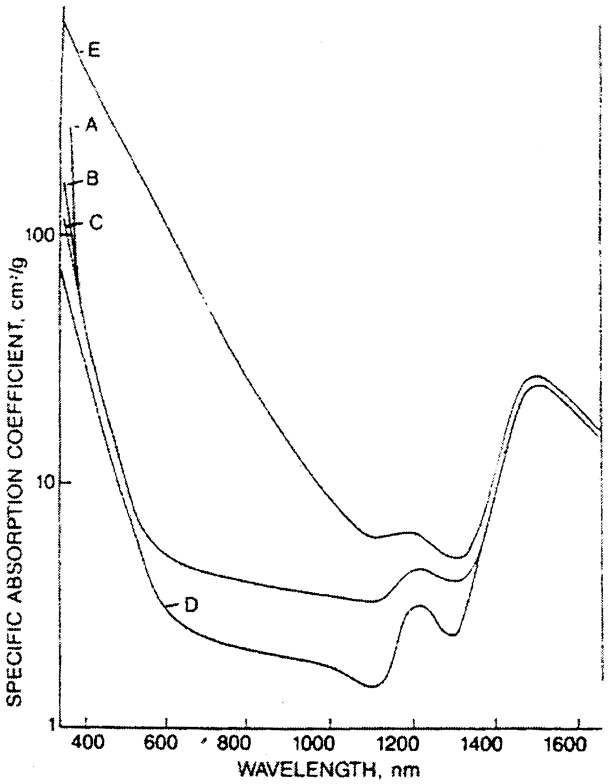

Figure 2.2.4 Specific Absorption Coefficient, pulps A-C are bleached hardwoods, D is a bleached softwood, and E is an unbleached softwood. Reproduced from Scott and Dearth (1992).

Figure 2.2.4, from Scott and Dearth (1992) shows the specific absorption coefficient from 350-1600 nm. Five pulps are shown; A through D are bleached and E is unbleached. There is a weak absorption peak in the infrared (IR) at 1250 nm and stronger one at 1500 nm, and a general trend of increasing absorption from 600 nm down into the ultraviolet (UV). Absorption reaches a minimum around 1100 nm for all samples except the unbleached one (E).

Fluorescent dyes are common in many high brightness papers. Figure 2.2.5 shows measurements from Scott and Dearth (1992) on the effect of fluorescence in paper. Addition of fluorescent dye increases emission in the blue (450 nm) region while increasing absorption in the UV (375-400 nm).

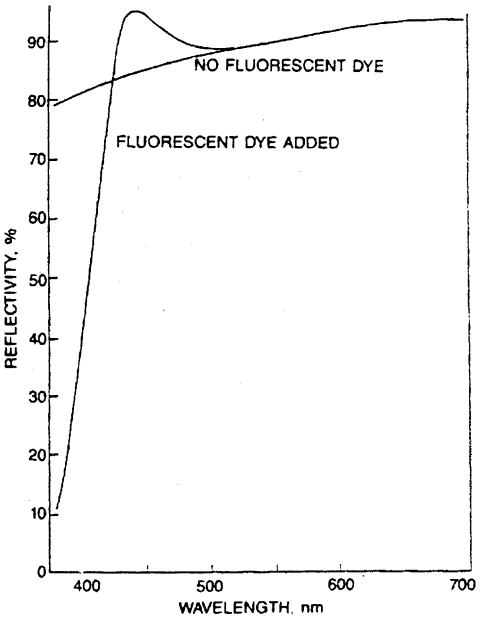

Figure 2.2.5 Effect of fluorescence in paper. Reproduced from Scott and Dearth (1992).

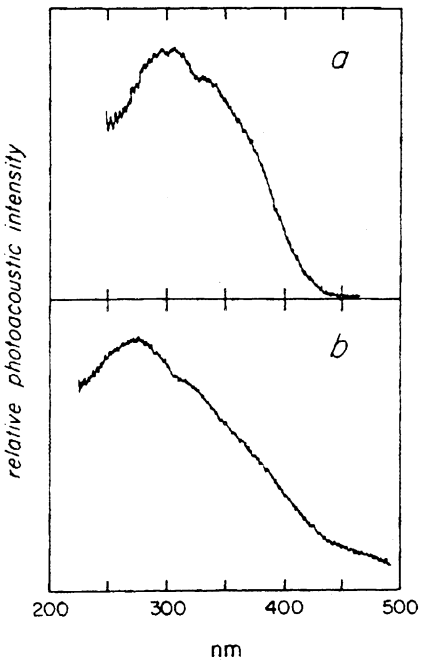

Figure 2.2.6 Absorption by lignin in the UV as measured by the photoacoustic technique. Graph *a* is data for pine wood lignin *in situ.* Graph *b* is data for milled wood lignin powder from spruce. The effect of cellulose absorption has been removed. Reproduced from Gould (1982).

Absorption in the UV is quite strong for most samples due to lignin. Figure 2.2.6 shows work by Gould (1982) in which a photoacoustic technique was used to measure absorption in lignin. The data shown is for pine and spruce lignin, where the effect of cellulose has been removed. Strong absorption is seen in both samples in the 250-300 nm region.

The IR is a particularly interesting region to look for absorbance in paper, as many lasers have fundamental frequencies in the 1-2 micron region due in part to the telecommunication industry's use of fiber optic communications. In Figure 2.2.7, results from Pope (1995) show absorbance spectrum from 1200 to 2400 nm. Absorbance peaks at 1500, 1920, 2100 and 2300 nm are present.

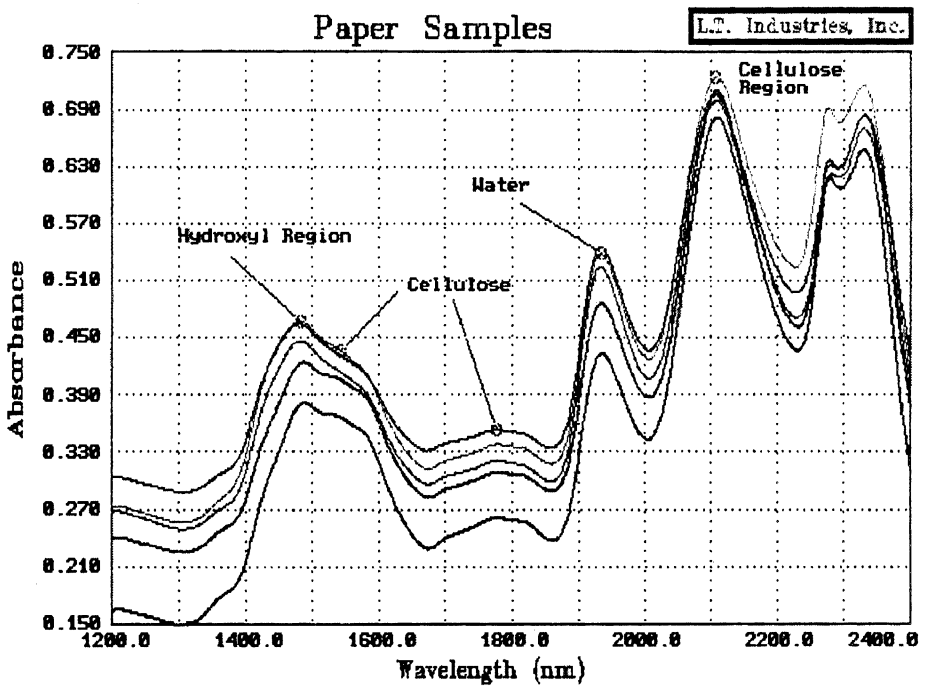

Figure 2.2.7 Absorbance spectrum of paper from 1200-2400 nm, showing absorbance regions attributed to cellulose and water. Reproduced from Pope (1995).

Two lasers are currently used in the laser ultrasound setup: one for detection and one for generation. In order to optimize the detection laser, a wavelength that provides good reflection

from the web is preferred. In order to optimize generation, a wavelength that provides good absorption would likely be best. Widely varying absorption spectrum of different papers in the visible (400-800 nm) region due to dyes, fluorescence, bleaching and pulping methods (see Figures 2.2.1 – 2.2.5) indicate that this region would not provide a universal solution for either generation or detection. However, relatively good absorption bands in the UV and near IR due to lignin and cellulose, respectively, exist. From the perspective of getting light to absorb into paper, running either a UV (200-350 nm, see Figures 2.2.4 and 2.2.6) or an IR (1400 or 2100 nm, see Figures 2.2.4 and 2.2.7) laser should be best. As lignin content in paper tends to vary significantly as a function of pulping processes and bleaching, using the IR absorption band due to cellulose should provide more repeatable generation.

Reflection generally increases with increasing wavelength in the visible region (see Figures 2.2.1, 2.2.2, and 2.2.4), to a minimum absorbance around 1100 nm (see Figure 2.2.4).

Several lasers exist in these suggested bands. For excitation, a laser such as Er:glass, which has a fundamental at 1540 nm and sufficient pulse energy and repetition rate would be a good choice. This region is also typically referred to as "eye safe", as the human eye is less sensitive to wavelengths in this region than other wavelengths around it. Safety is a serious concern with the generation laser due to the high optical powers typically needed to produce ultrasound. The laser of primary interest in the suggested detection region is the CW Nd:YAG, with a fundamental wavelength of 1064 nm. This laser is very common and typically quite inexpensive. Both the Nd:YAG and Er:glass lasers are also solid state which will reduce their maintenance requirements, size and electrical power consumption.

2.3 *Paper Samples (B. Pufahl, IPST)*

In order to investigate laser ultrasonics techniques over a broad range of conditions, several paper and paperboard samples were obtained from different manufacturers. Samples were chosen based on percentage of total paper production and those that would benefit most from on-line stiffness measurements. Moreover, they represented a wide range of grammages and different bleaching conditions. Newsprint, art paper, copy paper, and raw stock paper were chosen because of the impact of on-line stiffness measurements to the operation of the paper machine. A medium sample and three grades of linerboard were chosen due to market share and also because of the need for enhanced strength properties of the final product (corrugated containers). Bleachboard and sack grades were chosen because of the need for uniform strength in these products. A summary of the basic properties of the paper samples is presented in Table 2.3.1. Machine direction surface roughness measurements utilized an Emveco stylus contact system, which reports average differences between two successive samples.

Table 2.3.1 Basic Paper properties.

Paper Sample	Grammage (g/m^2)	Thickness (μm)	Felt Side Surface Roughness (μm)	Wire Side Surface Roughness (μm)
Newsprint	44	64	2.85	3.02
Art Paper	58	63	3.66	5.05
Copy Paper	80	91	2.66	2.83
Raw Stock Paper	87	106	3.20	4.66
Sack	87	109	5.36	5.96
26-lb Medium	125	195	8.53	9.80
33-lb Linerboard	163	203	7.98	6.73
42-lb Linerboard	205	276	9.81	7.62
Bleachboard	262	363	3.76	3.09
69-lb Linerboard	336	453	5.73	6.66

All samples of a particular grade were cut at the same cross-machine position from a single roll. To ensure uniformity of samples throughout the length of the paper, samples were cut alternating between static test and dynamic test samples. The static test samples were cut to dimensions of 18 cm machine direction by 18 cm cross machine direction while the dynamic test samples were cut to 100 cm machine direction by 20 cm cross machine direction.

The static samples were preconditioned at 23° C and 20% RH for 24 hours according to TAPPI test method T402 om-93 (TAPPI 1993). Following the preconditioning, the samples were conditioned at 23° C and 50% RH for another 24 hours. Every fifth sample of the twenty static samples was removed and measured under TAPPI standard conditions at 23° C and 50% RH. The static samples tested using the laser ultrasonic equipment at IPST were maintained at 23° C and 50% RH while the samples at INEEL were not kept under temperature and humidity constraints. However, temperature and humidity were monitored during experimentation at INEEL.

The following parameters were measured for the five samples: grammage (TAPPI T410 om-93), soft-platen thickness (TAPPI T551 pm-92), hard-platen thickness (TAPPI T411 om-89), surface roughness (see below), in-plane velocities (Van Zummeren et al, 1987), out-of-plane velocities (Habeger and Wink, 1986), and stiffness orientation angle (maximum stiffness angular offset with respect to machine direction). From these parameters, the following values were calculated: soft-platen apparent density, MD/CD velocity ratio, MD/CD stiffness ratio, MD-CD Poisson's ratio, CD-MD Poisson's ratio, and the stiffness constants C_{11}, C_{22}, C_{33}, C_{44}, C_{55}, C_{66}, and C_{12} (Mann et al, 1980). An 80 kHz wave was used for determination of in-plane ultrasonic velocities via contact transducers on all paper grades. A 1 MHz wave was used to determine out-

of-plane ultrasonic velocities for all grades except for the art paper, which was tested with a 5 MHz wave. Both out-of-plane waves were propagated through 20 mm neoprene-faced delay lines with a contact pressure of 50 kPa. Ultrasonic velocities obtained by contact methods were used as a basis for comparison with laser ultrasonic measurements. Table 2.3.2 contains the contact ultrasonic values recorded for the different paper grades.

Table 2.3.2 Contact Ultrasonic Stiffness Measurements.

	Newsprint	Art Paper	Copy Paper	Raw Stock Paper	Sack
Soft Platen Density (g/cm^3)	0.686	0.928	0.876	0.818	0.801
MD Longitudinal Velocity (km/s)			3.274	3.470	3.468
CD Longitudinal Velocity (km/s)			2.322	2.459	2.779
MD Shear Velocity (km/s)			1.651	1.757	1.893
CD Shear Velocity (km/s)			1.651	1.774	1.915
45° Shear Velocity (km/s)			1.634	1.744	1.882
MD/CD Longitudinal Velocity Ratio			1.410	1.411	1.248
MD/CD Longitudinal Stiffness Ratio			1.99	1.99	1.56
MD-CD Poisson's Ratio			0.19	0.18	0.20
CD-MD Poisson's Ratio			0.37	0.36	0.31
Stiffness Polar Angle (°)			-0.9	-1.8	-11.4
ZD Longitudinal Velocity (km/s)	0.217	0.631	0.415	0.411	0.444
ZD-MD Shear Velocity (km/s)			0.600	0.501	0.487
ZD-CD Shear Velocity (km/s)			0.540	0.485	0.440
C_{11} (GPa)			9.39	9.85	9.64
C_{22} (GPa)			4.72	4.95	6.19
C_{33} (GPa)	0.032	0.369	0.151	0.139	0.158
C_{44} (GPa)			0.251	0.195	0.145
C_{55} (GPa)			0.311	0.208	0.173
C_{66} (GPa)			2.39	2.53	2.87
C_{12} (GPa)			1.77	1.77	1.93

Table 2.3.2 Contact Ultrasonic Stiffness Measurements (Cont'd).

	Medium	33-lb Linerboard	42-lb Linerboard	Bleach-board	69-lb Linerboard
Soft Platen Density (g/cm^3)	0.640	0.800	0.742	0.720	0.741
MD Longitudinal Velocity (km/s)	3.317		3.728	3.360	3.484
CD Longitudinal Velocity (km/s)	2.076		2.234	2.488	2.176
MD Shear Velocity (km/s)	1.565		1.732	1.757	1.666
CD Shear Velocity (km/s)	1.577		1.730	1.755	1.679
45° Shear Velocity (km/s)	1.500		1.644	1.736	1.566
MD/CD Longitudinal Velocity Ratio	1.60		1.669	1.350	1.602
MD/CD Longitudinal Stiffness Ratio	2.56		2.79	1.82	2.57
MD-CD Poisson's Ratio	0.19		0.18	0.19	0.19
CD-MD Poisson's Ratio	0.47		0.49	0.34	0.49
Stiffness Polar Angle (°)	2.0		1.5	-1.1	-1.0
ZD Longitudinal Velocity (km/s)	0.403	0.316	0.368	0.274	0.227
ZD-MD Shear Velocity (km/s)	0.561		0.476	0.403	0.361
ZD-CD Shear Velocity (km/s)	0.456		0.437	0.376	0.322
C_{11} (GPa)	7.04		10.31	8.13	9.00
C_{22} (GPa)	2.76		3.70	4.46	3.51
C_{33} (GPa)	0.104	0.080	0.100	0.054	0.038
C_{44} (GPa)	0.126		0.136	0.107	0.077
C_{55} (GPa)	0.182		0.162	0.124	0.096
C_{66} (GPa)	1.57		2.23	2.22	2.06
C_{12} (GPa)	1.31		1.82	1.53	1.73

2.4 *Moving Web Simulator (B. Pufahl, IPST)*

A web simulator system was developed to provide a controlled environment for simulating the behavior of a paper web in an open draw. Factors considered during design of the system included: maintaining machine direction orientation of the paper sample, providing an unsupported area of paper for testing, variable speed capability, accurate positioning for flutter simulation, and an adjustable base for aligning the motion of the paper perpendicular to the laser. Two web simulators were built, one for use by IPST and another for INEEL. The INEEL system was installed in April. After some minor changes to the design of the drive system, the IPST system was installed in June.

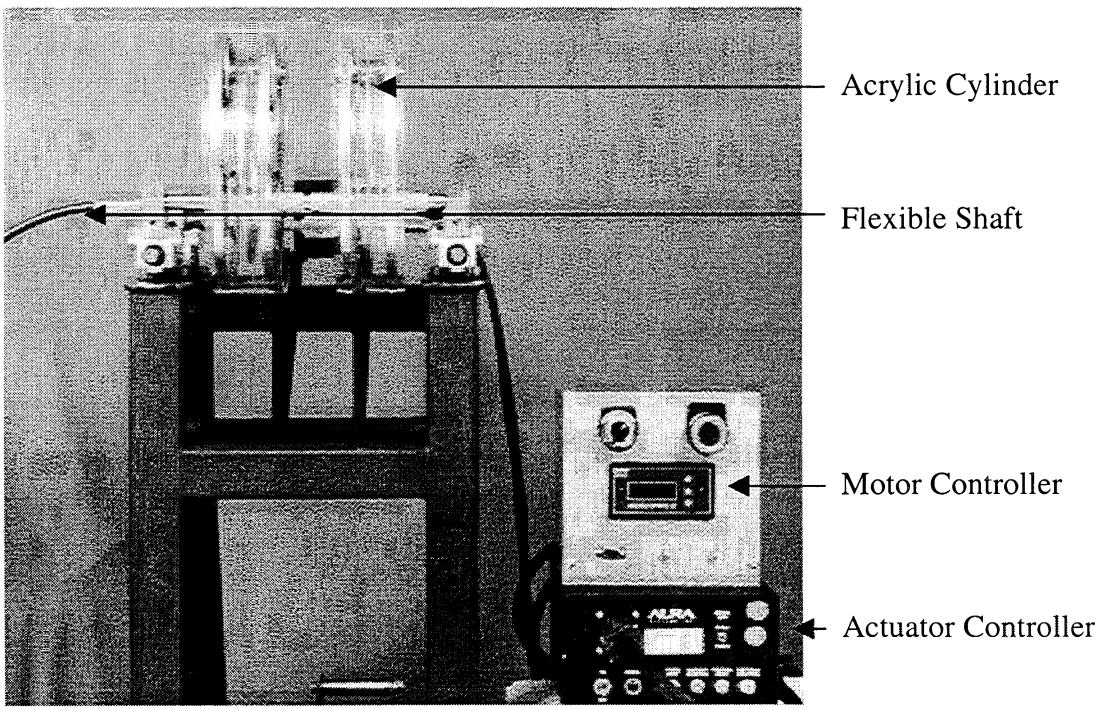

Figure 2.4.1 Web simulator cylinder detail.

Paper samples of the size 84 cm machine direction by 20 cm cross-machine direction are attached to two acrylic drums that are separated by 5 cm (see Figure 2.4.1). In addition to the separation gap, one configuration of the system utilizes drums that have 10.0 cm diameter access holes (see Figure 2.4.2). This configuration allows the transducers to be mounted behind the paper during sheet flutter simulation as well as during smooth operation (no flutter). Another configuration utilizes solid disks mounted to the drive shaft and the acrylic drums (see Figure 2.4.3). In this arrangement, the vibration of the surface of the drums is minimized while the maximum speed of the system is substantially increased.

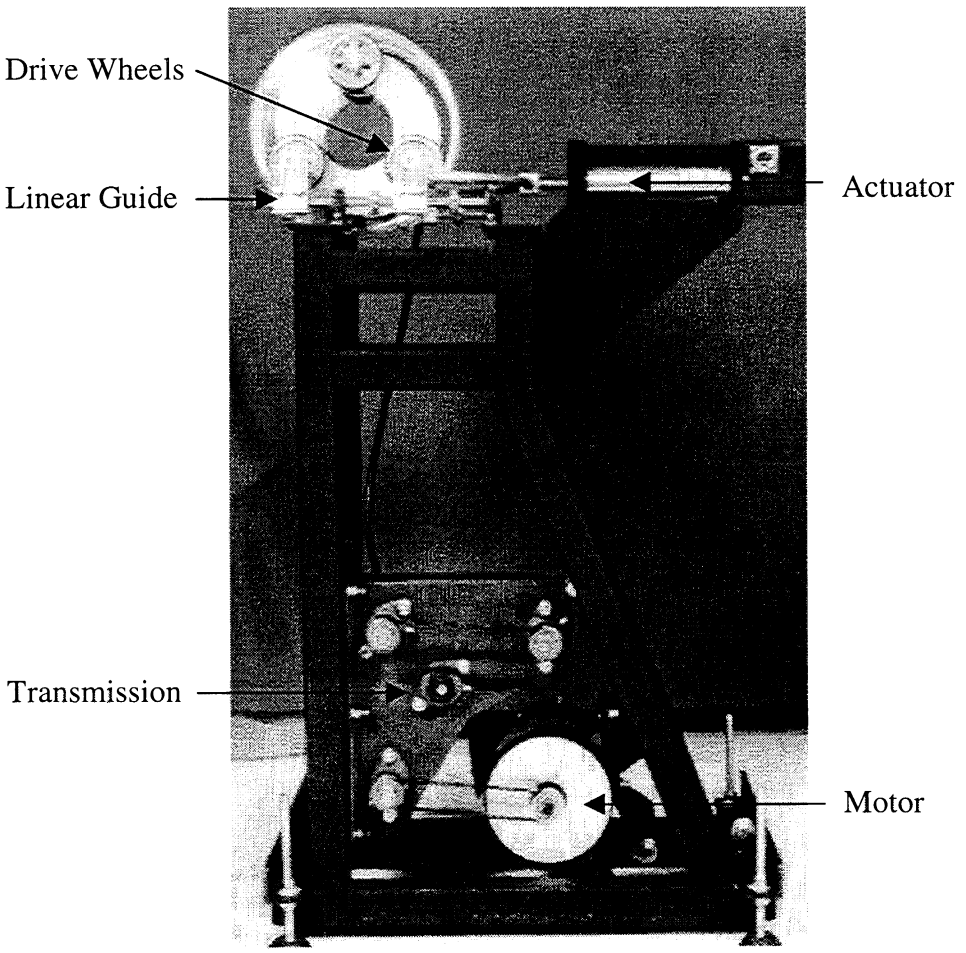

Figure 2.4.2 Wire side access configuration.

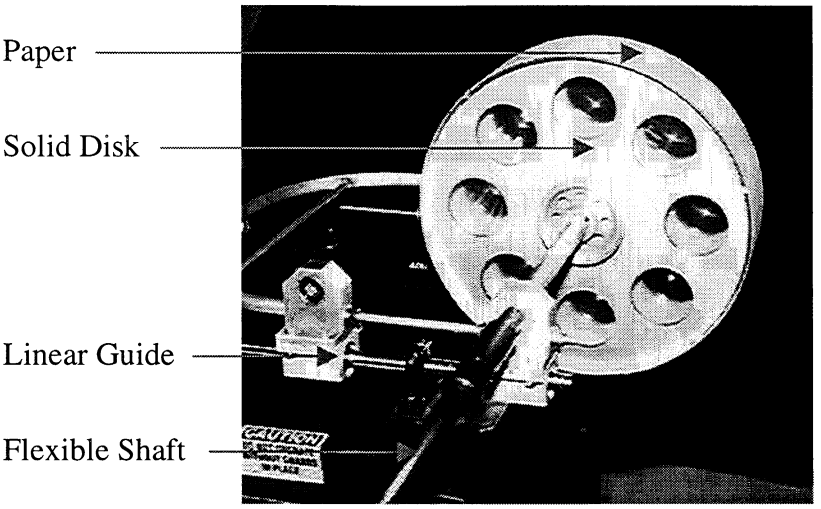

Figure 2.4.3 Solid Disk Configuration.

The system utilizes a variable speed DC drive that currently provides a speed range from 0.4 to 13.5 m/s (25 to 810 m/min or 82 to 2660 fpm) in the configuration with the access holes (configuration #1). In the configuration utilizing solid disks mounted to the drive shaft (configuration #2), the speed range is from 2 to 47.5 m/s (120 to 2850 m/min or 394 to 9350 fpm). A linear electromagnetic actuator with integral position feedback is utilized for simulation of sheet flutter. This arrangement provides 2 cm peak to peak displacement at frequencies up to 10 Hz with a reduction in displacement to 0.25 mm at 100 Hz. The actuator also has the capability of producing complex wave shapes in addition to basic sine waves. Accurate speed control of the cylinder during flutter trials is accomplished through the use of a flexible drive shaft. Surface speed is monitored by a fiber optic trigger that senses reflective tape attached to the cylinder.

All hardware is controlled by a custom LabVIEW program utilizing a National Instruments data acquisition card. The software allows the user to control surface speed via RS-232 cabling to the motor controller. Timing signals from the motor tachometer and cylinder

trigger are used to determine cylinder speed and rotation position at the time of lasing. Similarly, LVDT feedback from the linear actuator is used to determine distance from the paper sample to the optics, linear velocity, and direction of travel. The program also allows the user to control the frequency and amplitude of the linear displacement as well as step and hold to a given linear position.

Several safety features were added to the design to prevent operator injury or damage to the laser and optics in the event of a failure. These features include: a completely enclosed drive system; a detachable hood covering top, sides, and back of the acrylic cylinder; a fail-safe brake on the motor; an emergency switch to disable power to all system components; locking collars on the linear slides; and a cylinder design that includes aluminum backing rings for strength and prevents the cylinder from being thrown from the machine in the event of a failure. In addition, all rotating elements were specified to operate at approximately 75% of their recommended continuous speed.

At this time, the INEEL system has operated for over 100 hours at a maximum speed of 400 m/min. INEEL has also taken advantage of the linear actuator capabilities to determine the effects of depth of focus and sample movement on the laser detection system. The IPST system has operated for approximately 40 hours with a maximum speed of 1800 m/min. Both systems are currently using a single cylinder arrangement with a narrow paper sample attached to the cylinder.

2.5 *Laser Ultrasonics*

2.5.1 Introduction

The reception of ultrasonic signals propagating along moving paper webs is a challenging assignment. The webs travel at high speed in mechanically noisy environments. Progress has been made using piezoelectric techniques, nonetheless laser detection promises significant advantages. The ability to receive ultrasonic signals without contacting the web is the foremost attraction of the laser approach. Laser interferometry can recover a trace of the ultrasonic disturbance by mixing a reference beam with another coherent laser beam reflected from the surface. There is no need to struggle with direct piezoelectric connections to the paper. The papermakers' reservations about instrument damage to the product fall away. Also, laser interferometry is a more broadband detection method; pulse transmissions are not distorted and elongated as they are when using the more resonant piezoelectric techniques. Measurements can be made at higher frequencies allowing application to shorter ultrasonic paths. The laser detectors are much more sensitive to antisymmetric mode propagation than are piezoelectric instruments.

The experimental investigation of laser-based methods to generate and detect Lamb waves in paper constituted the bulk of the research work during Phase I. Since the main goal was to demonstrate that laser ultrasonics can indeed be successfully used to detect Lamb waves in moving paper, our first task was to analyze all existing approaches and determine which ones would most likely work on moving paper before proceeding to experimental work.

2.5.2 Principles of Laser Ultrasonics generation (E. Lafond, IPST)

On paper products, like many other materials, there are basically four ways to generate ultrasound with a laser beam. The means of generation depend on the power density of the spot (power/area of the spot) at the surface of the material (Scruby et al., 1990; Castagnede et al., 1992; Edwards et al., 1989).

At low power density, the generation occurs in the so-called thermoelastic regime. In this regime, the surface of the material is heated very quickly by the laser beam. The sudden thermal expansion and subsequent contraction caused by heating generate stresses inside the material in a very short time, which become ultrasonic waves. In this regime, the ultrasonic waves are generated in the plane of the material. In the case of paper, this regime is expected to generate mainly in-plane S_0 waves (see Figure 2.5.1).

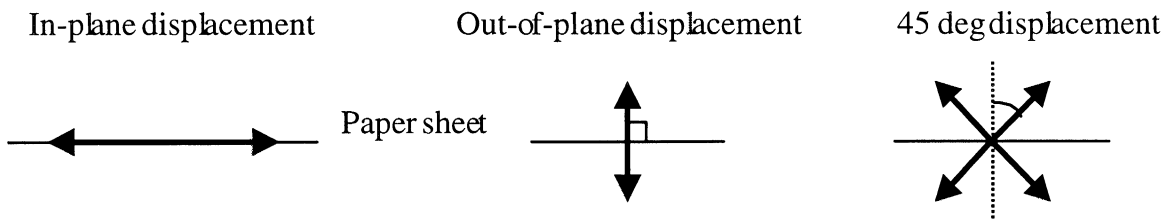

Figure 2.5.1 Definitions of displacement directions.

At higher power densities, the laser spot can be intense enough to vaporize the material surface to a depth of a few nanometers or micrometers. The sudden vaporization of the material creates a reaction over the surface that in turn generates stress mainly in the out-of plane direction. Waves generated using this ablation regime are essentially A_0 waves due to the out-of-plane stresses.

At an intensity in between those of the thermoelastic and ablation regimes occurs the so-called intermediate regime, which utilizes a combination of slight ablation and thermoelastic expansion. This regime generates both in-plane and out-of-plane waves and thus is appropriate when we need to generate both S_0 and A_0 waves.

The fourth way to generate ultrasonic waves is in the high energy plasma regime where vaporized and ionized particles from the material surface can start a laser-generated plasma at the laser spot. The plasma can also be ignited in the air by focusing the laser beam tight enough that the intensity exceeds the breakdown level of the air. This plasma creates a shock wave that propagates in the air and the incoming wavefront generates out-of plane stresses and displacements when it hits the material. The amount of energy required is much higher than for the other generation regimes and the spectrum of waves generated usually consists of lower frequencies. Therefore, this method of generating ultrasound was not investigated.

2.5.2.1 Generation of ultrasound

Table 2.5.1 FWHM and maximum pulse power for Continuum Surelite I-20 Nd:YAG pulse laser.

Wavelength:	1064 nm (infrared)	532 nm (green)	355 nm (ultraviolet)
Pulse FWHM	5-7 ns	4-6 ns	4-6 ns
Maximum energy per pulse	420mJ (theor.) 413mJ (meas.)	160mJ (theor.) 168mJ (meas.)	55mJ (theor.) 57mJ (meas.)
Repetition rate	20 Hz	20 Hz	20 Hz

The generation system used at IPST is a pulsed Nd:YAG laser capable of generating a 1064 nm fundamental wavelength (near infrared), plus harmonics at 532 nm (green) and 355 nm (ultraviolet) with the use of nonlinear optical crystals. The laser is a Continuum Surelite I-20

with doubling and tripling crystals, and wavelength separators. The FWHM (Full Width at Half Maximum) of the laser pulse and the maximum energy are displayed in Table 2.5.1.

The diameter of the beam at the output of the laser is 6 mm at $1/e^2$ intensity. This beam needs to be focused, typically into a spot of 1 mm or less on the paper so that it can generate high frequency acoustic waves.

INEEL also uses a pulsed Nd:YAG for laser generation of ultrasound. This laser operates at 1064 or 532 nm, with a pulse length of 15 ns and up to 400 mJ of energy per pulse.

The maximum energy available from the pulsed lasers is far too high for paper and would damage its surface when the spot is focused, so the beams are attenuated using an optical attenuator placed after the output of the laser beam.

Contact piezoelectric transducers specially designed for sending S_0 or A_0 waves into the paper can also be used for ultrasound generation.

The set up of the laser based ultrasound system used at IPST is a relatively standard one. The pulsed generation laser is the master of the system and triggers the data acquisition. The detection system detects displacements continuously since the laser used for the detection system is CW (Continuous Wave). The setup at INEEL is very similar.

2.5.2.2 Data acquisition system

Traditional time based signals are recorded in a straightforward manner. At the output of the interferometer, the signal may be sent directly to the data acquisition system, or an ultrasonic preamplifier may be used to boost the signal before recording. The preamplifier used at IPST

has a gain of 39.2 dB with a bandwidth of 16 kHz to 6 MHz at -3 dB. Figure 2.5.2 shows a picture of the data acquisition system used at IPST.

Figure 2.5.2 Data acquisition system, IPST setup. Computer with A/D is on the left, and digital oscilloscope is on the right. Panametrics preamplifier is the small blue box between the computer monitor and the oscilloscope.

The A/D board used with the IPST laser-based ultrasound setup allows a sampling rate of 130 MSamples/sec on one channel or 65 MSamples/sec on 2 channels. It is an 8 bit (256 levels) A/D board which allows collection of pre- and post-trigger data for recording times ranging from a few μs up to a few ms on 5 different voltage scales. The A/D board is driven with custom software written in LabVIEW and the data files are saved in an ASCII format.

An alternate method is to use a digital oscilloscope with storage capabilities. This was done at INEEL. Frequency based data storage techniques are more complicated and are described later in Section 2.6.4.

2.5.2.3 Ultrasonic detection systems used at INEEL

Two different ultrasonic detection systems were evaluated at INEEL during Phase I:

- Fabry-Pérot system already in place from other research.
- Time domain PRC method already in place from other research.

Both of these systems were optimized for use on paper. The two detectors were completely self-sufficient (they did not share parts) and were both able to be run through the entire year. In addition, INEEL provided valuable help in establishing the BSO time based interferometer at IPST.

2.5.2.4 Ultrasonic detection systems used at IPST

Three different detection systems have been investigated at IPST on paper products during the first year.

- An in-house built Photorefractive interferometer with a BSO crystal for measurements on static paper only.
- A photoinduced-EMF interferometer with a custom optical design for paper, on loan from Lasson Technologies, Inc., both on static and moving paper.
- A vibrometer using the self-mixing method, on loan from Metrolaser, Inc.

The first two systems used an Innova 308, 1.9 Watt single line argon:ion laser from Coherent. The vibrometer used a built in 5 mW diode laser at 780 nm.

In Phase II of the project, an in-house built Photorefractive interferometer with a GaAs or CdTe:V crystal for detection will be used on static and moving paper. This interferometer will use a Compass Nd:YVO_4 laser from Coherent with fundamental output of 600 mW at 1064 nm.

2.5.3 Comparative analysis of interferometric methods (E. Lafond, IPST)

This section is focused on the choice of a laser-based ultrasonic detection device. The comparative analysis of interferometric methods is valid for paper products only. For other products, the results of the analysis could be quite different.

Paper is a very interesting material to inspect in the sense that its properties make it more difficult to do non-contact ultrasound detection than most of the usual industrial materials. The problems that need to be addressed are the following:

- Detection on a moving surface.
- Surface moving with a very high speed.
- Paper surface is highly scattering (diffuse reflection of light).
- Optically absorbing surface in some cases (unbleached grades) or partially transparent (low basis weight grades), therefore only a small portion of the incident light is retro-reflected.
- Paper surface is easily damaged by too much power.

The objective is to detect ultrasonic displacements as low as 1 nm (S_0 wave) with a bandwidth of 50 kHz to 4 MHz over a duration of about 200 μs on a surface moving at a speed between 10 m/s and 25 m/s.

All available "interferometric" optical methods can be separated into different groups and subcategories:

- Non-interferometric method: knife-edge detection.
- Mach-Zehnder and Michelson interferometers.
- Fabry-Pérot interferometer.
- Self-mixing laser interferometer.
- Photorefractive adaptive interferometers:
    - Self pumped phase-conjugate mirror and Double phase conjugate mirror techniques.
    - Two wave mixing using BSO or infrared photorefractive crystals, time domain detection.
    - Two and four wave mixing for imaging techniques, frequency domain detection.
    - Photoinduced electromagnetic force interferometer.

The main criteria when dealing with these interferometers are their response time, their étendue, and their sensitivity to displacement. The speckle pattern of the paper changes extremely quickly and can prevent the interferometer from working and thus prevent the ultrasonic signal from being detected. The different techniques for ultrasound detection are reviewed in the following sections.

2.5.3.1 Knife-edge detection

In the case of the knife edge detection, this type of detector only works well with a specular reflection, and the sensitivity to displacement is significantly reduced on scattering surfaces. Also any fluttering of the paper will induce huge artificial signals totally unrelated to ultrasonic

displacements, thus masking the signals of interest. Figure 2.5.3 shows a schematic diagram of the knife-edge detection system.

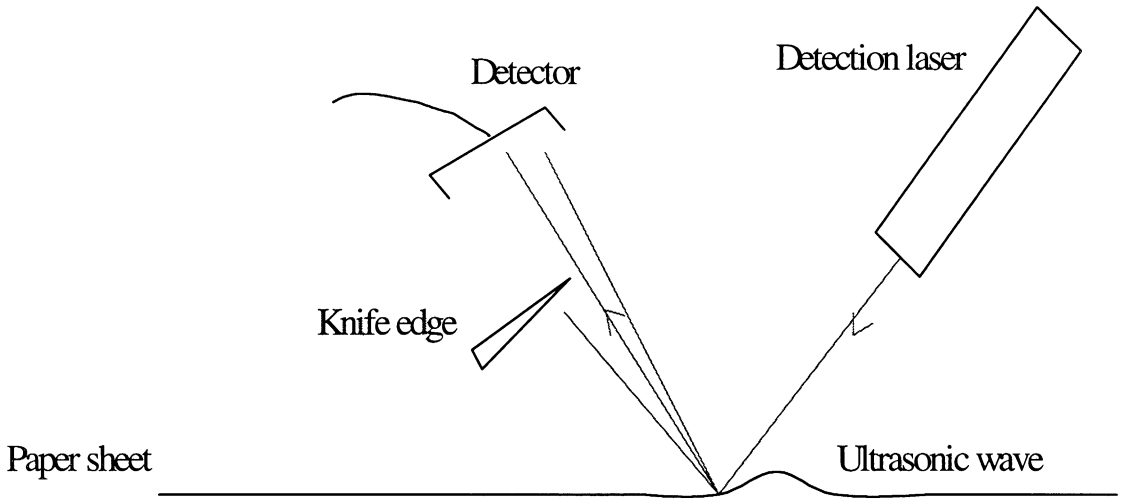

Figure 2.5.3Knife-edge detection system.

2.5.3.2 Mach-Zehnder and Michelson interferometers

In the case of the Mach-Zehnder and Michelson interferometers (see Figure 2.5.4), another problem occurs caused by the changing speckle pattern of the paper. The Mach-Zehnder and Michelson interferometers work correctly only when they detect a single speckle of light. In order to detect a single coherent speckle, the detection laser beam needs to be focused close to the diffraction limit onto the surface of the sample. This makes these detectors very sensitive to small displacements but also leads to the disadvantage of a very small étendue (product of the solid angle of scattered light collected by the detection optics and the area of illuminated surface). The étendue parameter characterizes the ability for an optical system to collect light efficiently. Hence, these two interferometers have to be aligned very accurately to pick up a good speckle pattern.

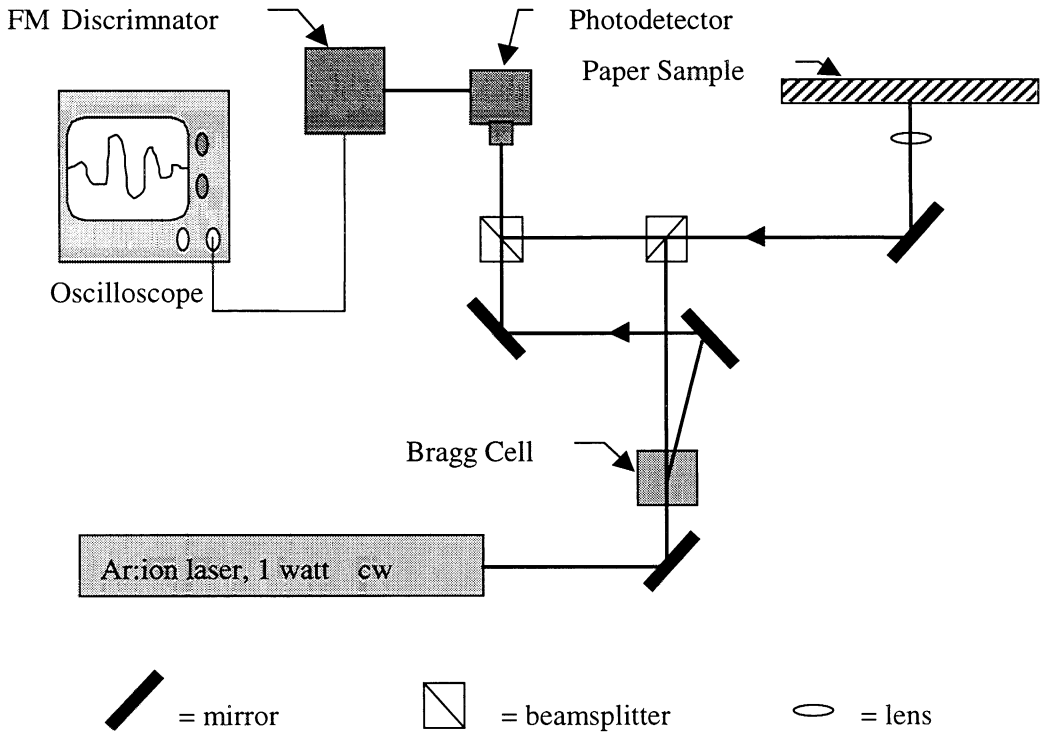

Figure 2.5.4 Mach-Zehnder heterodyne interferometer (from Johnson 1996).

Since the speckle pattern is dependent on the sample surface roughness, as soon as the surface changes under the beam, the speckle pattern changes and the interferometer is no longer properly aligned, resulting in the loss of the ultrasonic signal. For a moving surface, the signal appears and disappears randomly and the higher the speed the greater the amount of time spent without a signal. Sagnac and/or polarimatric interferometers (which are not described here) have the same problem as the Mach-Zehnder and the stabilized Michelson do: they only work with a single speckle.

2.5.3.3 Fabry-Pérot interferometer

The Fabry-Pérot interferometer, as schematically shown in Figure 2.5.5, is a much better alternative than the previously described interferometers for measurements on moving products

since the interferometry is done between the same optical wavefront delayed by a very short time. This eliminates the single speckle requirement, so it does not matter if the light coming back from the surface is speckled or not. Also, the Fabry-Pérot is the fastest of the interferometers able to work on rough surface (typical response time: 0.1μs). A confocal Fabry-Pérot has a very large étendue so it collects light very efficiently and provides a good signal to noise ratio.

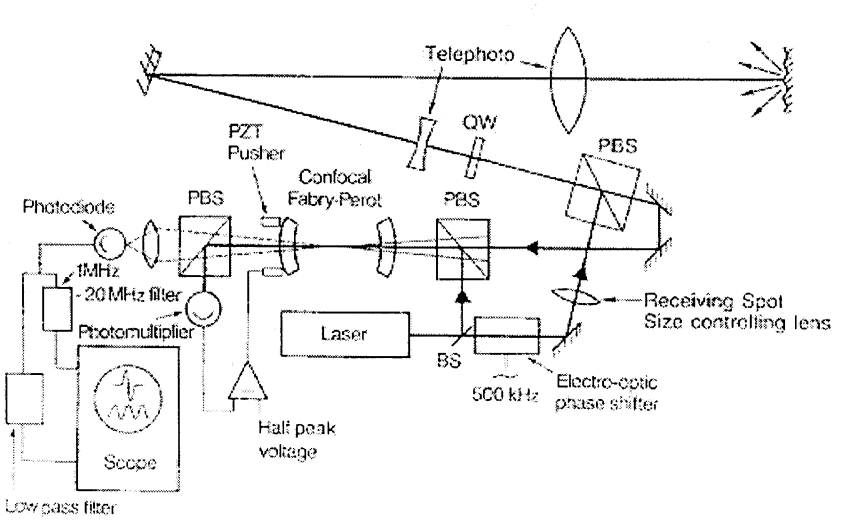

Figure 2.5.5 Fabry-Pérot interferometer (Monchalin and Héon 1986).

Up to now, the Fabry-Pérot is the only optical interferometer that has been successfully used in an industrial application for ultrasonic detection. J.P. Monchalin (1986) from Industrial Materials Institute in Canada has used the Fabry-Pérot for ultrasound detection on hot steel pipes moving over 4 m/s.

The two disadvantages of the Fabry-Pérot are as follows: first, the interferometer is quite large (typically 1 m long and 0.5 m wide), second, the frequency response of the device is not flat, and the sensitivity falls off rapidly outside its typical bandwidth of 1 to 100 MHz. The

second disadvantage makes this device not optimal for detection of Lamb waves in paper, which are mainly below 1 MHz. Bandwidth can be lowered into the region for paper by increasing the cavity length. However, this increases the size of the interferometer as well as making it more sensitive to alignment.

2.5.3.4 Self-mixing interferometer

For self-mixing interferometers, as shown in Figure 2.5.6, the weakness is the same as the one pointed out in the Mach-Zehnder interferometer; that is, it can only work with a single speckle. Nevertheless, an advantage exists in that it can work with much less light than the Mach-Zehnder interferometer.

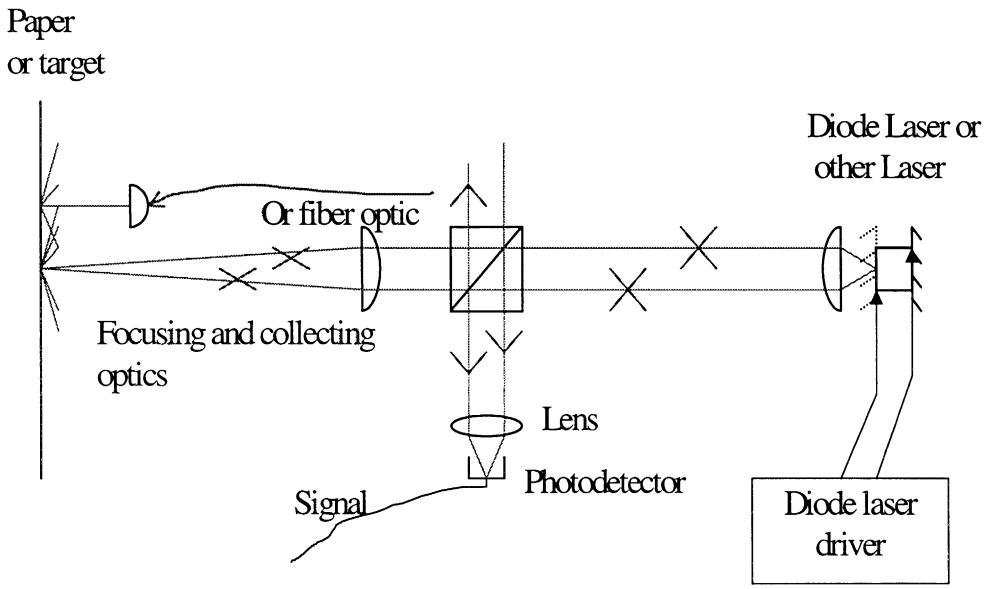

Figure 2.5.6 Self-mixing laser interferometer.

The self-mixing interferometer will likely have a decent signal to noise ratio (SNR) on both highly reflective and very absorbing surfaces (such as kraft linerboard) even with a low power laser. There is still the same problem of losing the signal with the change of speckle pattern caused by the moving paper. It is likely that the noise caused by the changing speckle pattern

caused by the moving paper. It is likely that the noise caused by the changing speckle pattern will be added to the signal coming from the ultrasonic displacements and will be of much higher amplitude than the signal (hence masking the signal).

2.5.3.5 Photorefractive adaptive interferometers

Photorefractive interferometers are the newest type of interferometer and have a high potential of further improvement as advances in material science (to produce quality optical crystals) are taking place very fast in this area. This type of interferometer uses photorefractive crystals to adapt a planar reference wavefront to a speckled signal wavefront (light back scattered from the paper). This can produce significantly more efficient interferometry than the Mach-Zehnder interferometers can on rough surfaces. Photorefractive interferometers can come in two beams designs like the Mach-Zehnder, as well as 4 beams designs. However, the theoretical sensitivity limit of such interferometers is smaller than that of a Mach-Zehnder heterodyne interferometer on mirror-like surfaces. Of course this theoretical sensitivity limit is irrelevant to paper products which have a very scattering surface. In this latter case, a higher sensitivity is achieved using the photorefractive interferometer even on static targets.

2.5.3.5.1 Self pumped phase-conjugate mirror and Double phase conjugate mirror techniques

These techniques, as shown in Figure 2.5.7, were not investigated experimentally because despite the fact that they can collect and use much more light than the Mach-Zehnder interferometer, they are extremely slow to achieve the effect they rely on (typically a few seconds).

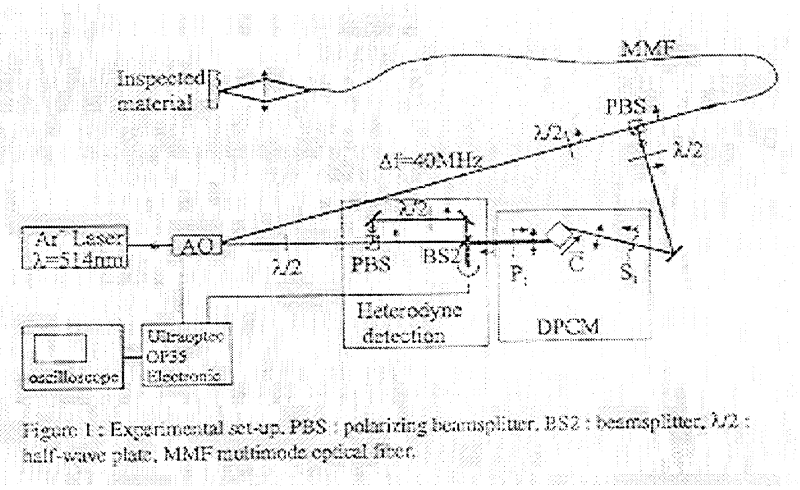

Figure 1 : Experimental set-up. PBS : polarizing beamsplitter, BS2 : beamsplitter, λ/2 : half-wave plate, MMF multimode optical fiber.

Figure 2.5.7 Double phase conjugate mirror (Delaye et al. 1996).

This slow response time makes them unsuitable for on-line detection in a mill and will prevent them from being used on moving paper.

2.5.3.5.2 Two-wave mixing using BSO or infrared photorefractive crystals, time domain detection

Two-wave mixing is the second fastest of the photorefractive techniques and has been used for ultrasound detection since 1991 (Ing et al., 1991). The response time of a two-wave mixing interferometer depends mainly on the type of photorefractive crystal employed. It can be used for detection in the frequency domain or in the time domain. The sensitivity to displacements (related to the gain of the crystal) and response time (related to laser power density) depends on many different factors such as the material constants, the wavelength used, and whether a DC or AC voltage is applied to the crystal.

There is a big difference both in sensitivity and response time between the two classes of photorefractive crystals: the Sillenite type, such as $Bi_{12}SiO_{20}$ (BSO), $Bi_{12}GeO_{20}$ (BGO),

$Bi_{12}TiO_{20}$(BTO), working in the visible range, and the semiconductor photorefractive crystals which work in the infrared range, such as undoped GaAs, InP:Fe and CdTe:V.

The Sillenite type crystals are very sensitive to displacements and have a slow response time (> 10 ms), whereas the semiconductor photorefractive crystals have the opposite properties. However, the sensitivity of semiconductors can be greatly increased by applying a DC or AC voltage to the sides of the crystal. By opposition, the response time cannot be dramatically reduced for crystals of the Sillenite type by any means.

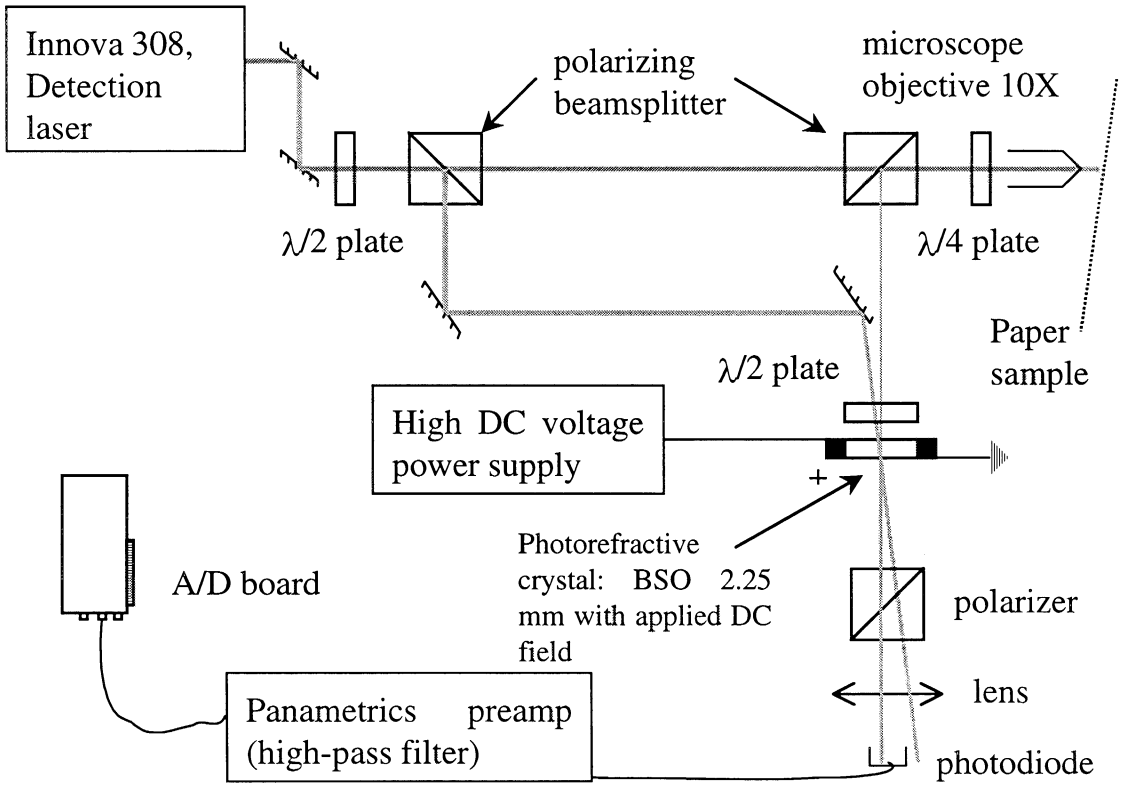

Figure 2.5.8 Two wave mixing photorefractive interferometer version 1.5, IPST setup.

IPST currently uses a BSO crystal in its photorefractive interferometer for measurements on static paper, as shown in Figure 2.5.8. It has been found that a crystal with a very fast

response (typically a semiconductor crystal) should be used with moving paper instead of the BSO because the speckle pattern changes so rapidly. A typical response time of a GaAs or CdTe:V crystal is between 1 and 10 μs, and this is probably the maximum acceptable for paper moving at high speeds.

A Canadian company, UltraOptec Inc. has recently been marketing a laser-ultrasonic receiver using an InP:Fe crystal, but it appears that the sensitivity of this detector decreases quickly with increasing speed. Its sensitivity goes down to 20% of its maximum value at speeds of 1-2 m/s. It is unlikely that this receiver would work without a device such as a scanning mirror (see Section 2.6.7.2) to reduce the differential speed between the detection beam and the web. However, an interferometer using a GaAs or CdTe:V crystal could be fast enough for paper and will be investigated in the future.

2.5.3.5.3 Four wave mixing and two wave mixing for imaging techniques (frequency domain detection)

This technique, as shown in Figure 2.5.9, uses four wave mixing or two wave mixing optical lock-in methods to display the ultrasonic displacement field of the paper's surface onto a CCD camera through the photorefractive crystal.

The crystals that can be used for this method are the same as the ones for two-wave mixing with the same advantages and drawbacks. The big advantage of this method on static paper is that it can obtain the complete information about wave velocity in all directions all at once, at one fixed frequency. The drawback is that instead of being focused, the beam of the detection laser is spread over a large surface and thus the quantity of light coming back onto the crystal (and hence on the detector) from any one speckle is very small. This method works well for

static paper samples. However, when it becomes necessary to detect waves on a moving web, it seems unlikely that both the signal to noise ratio and the response time will have adequate values.

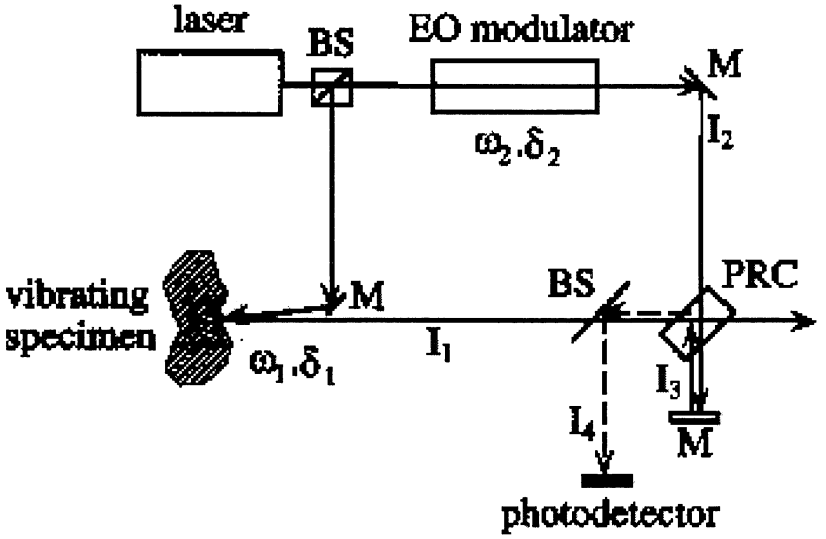

Figure 2.5.9 Four wave mixing imaging technique. PRC = photorefractive crystal; EOM = electro-optic modulator; BS = beam splitter; M = mirror; δ_1 and δ_2 = phase modulated signal and reference beams, respectively (reproduced from Hale and Telschow 1997).

Until there is a great improvement in the sensitivity of photorefractive crystals, the four wave mixing and two wave mixing imaging techniques in the frequency domain do not seem to be suitable for moving paper. But it is definitely a method that should be watched in the future when the sensitivity improves with better photorefractive materials (polymers for example) because of its capacity to do full field ultrasonic imaging.

2.5.3.5.4 Photoinduced electromagnetic force interferometer

This interferometer, as shown in Figure 2.5.10, relies on a phenomenon that makes it the fastest of all photorefractive interferometers because some of the usual steps required for a

photorefractive interferometer to work properly are skipped. Due to the photoconductivity property of a photorefractive crystal, a very small current is created on the surface of the crystal by the slight phase shift of the speckles caused by the ultrasonic motion of the paper surface. The current generated by photoconductivity is representative of the ultrasonic motion and can be measured between two electrodes on the sides of the crystal.

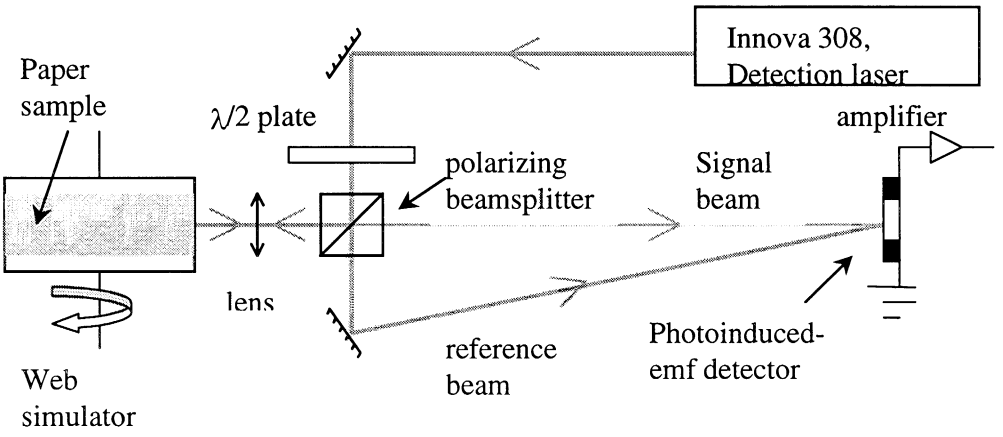

Figure 2.5.10 Photoinduced-EMF interferometer.

The detection spot can be either a point or a line, as with a two wave mixing-time domain interferometer. All photorefractive crystals create a photoinduced-EMF current, hence any crystals can be used. The device on loan from Lasson Technologies that was tested at IPST on the web simulator relies on a Chromium doped GaAs crystal (GaAs:Cr).

As in the case of two-wave mixing time domain interferometers, the frequency response of this interferometer is flat and very well adapted to the purpose of Lamb waves detection. It cuts off the low frequencies that are typically present in a mill (below 1 kHz) and the upper limit can be set at any value by the electronic bandwidth of the amplifier.

On 42-lb linerboard and bleachboard, the photoinduced-EMF detector was able to detect signals at speeds up to 14.5 m/s (maximum speed of the web simulator at that time).

2.5.3.6 Improvement of an interferometric method by using a scanner

Some of the interferometric methods cited above are likely to be improved when a scanning mirror is used. The scanning mirror should reduce the differential of speed between the laser detection beam and the web surface. Indeed, theoretical and experimental observations show that when the web speed increases, the signal to noise ratio drops sharply. This is caused by an increase of the noise with the speed and a decrease of the signal (not enough time for the speckle pattern to build up the diffracted beam).

The interferometric methods that can be improved using a scanning mirror are the Fabry-Pérot interferometer, the two-wave mixing using infrared crystals (not those of Sillenite type), and the photoinduced-EMF interferometer. Also, the interferometric methods that possibly could be improved are the two and four wave mixing for imaging techniques in the frequency domain, and the self-mixing method.

2.5.3.7 Preliminary conclusion on interferometric methods

The comparison among the interferometric techniques has identified several techniques that will not work for the detection of Lamb waves on moving paper at high speeds. These include the knife-edge detection, the Mach-Zehnder and the Michelson interferometers.

On moving paper, the most promising devices up to now are the Fabry-Pérot interferometer, the two-wave mixing using infrared crystals and the photoinduced-EMF interferometer. The Fabry-Pérot and the photoinduced-EMF interferometers have been successfully demonstrated on moving paper in a laboratory environment (Phase I).

2.6 *Laser Ultrasonics Measurements*

2.6.1 Analysis of Paper Using Orthotropic Plate Theory (J. Jong, IPST)

This section provides an overview of how to investigate stiffness properties of paper samples using a non-contact laser ultrasonic technique. Assuming that paper can be modeled as an orthotropic material, that is, a material that has three mutually orthogonal symmetry planes, then there exists an empirical relationship between the properties of paper stiffness and the elastic constants [Baum, 1987]. For a thin paper, two fundamental Lamb wave modes, the S_0 and A_0, are present (Figure 2.6.1). The S_0 mode is also called the fundamental dilatational mode and is used to predict longitudinal stiffness properties. The A_0 mode is the fundamental bending mode and is used to determine shear stiffness properties. As the signal propagates in the paper, the two modes are detected and analyzed in relation to the stiffness properties.

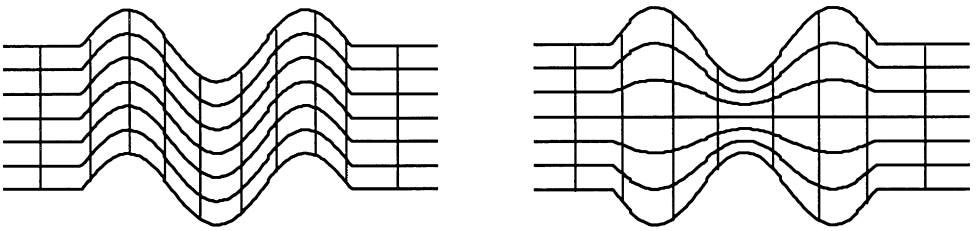

Figure 2.6.1 A_0 antisymmetric (left) and S_0 symmetric (right) mode shapes as viewed from the edge of a sheet of paper.

The symmetric S_0 mode is nondispersive in the low frequency limit, and a time-of-flight measurement can evaluate the longitudinal stiffness properties by measuring the velocity of ultrasound along MD and CD. On the other hand, the antisymmetric A_0 mode is dispersive and the asymptotic A_0 velocity in the high frequency region can be used to determine the shear stiffness properties in the out-of-plane directions. It is also possible to determine the stiffness

properties using the characteristics of the A_0 velocity in the low frequency region by way of non-linear curve fitting.

The velocity of the S_0 mode is analyzed for selected samples using a cross-correlation technique and compared with the one obtained using contact transducers by Brodeur et al. (1997). The analysis of the A_0 mode is an important tool because the A_0 mode is readily detectable in the signal due to its large amplitude.

Nevertheless, the interpretation of the A_0 mode is not straightforward because the phase velocity disperses as a function of frequency. A data analysis technique is developed to interpret the dispersive A_0 signal using a similar approach taken by Schumacher et al. (1993). The technique contains a method of extracting phase velocities from Fast Fourier Transformation and unwrapped phase angle spectrum. Furthermore, phase angle corrections are required to compensate for the phase shift in the low frequency region. The analysis technique is compared with the one described by Johnson (1996) on copy paper.

The theory of Lamb waves typically used in paper has been studied by Habeger et al. (1979), Cheng and Berthelot (1996) and Johnson (1996). They all have described an important relationship between frequency and wave velocity that must be satisfied for a Lamb wave to exist. It is known as the dispersion equation in the following form:

$$\frac{\tan(k_{z+} \cdot h)}{\tan(k_{z-} \cdot h)} = \left[\frac{H_- \cdot G_+}{H_+ \cdot G_-} \right]^{\pm 1} \qquad (1)$$

where h is the half thickness of paper, $k_{z\pm}$, $H_\pm$ and $G_\pm$ are functions of frequency f, wave velocity c and the elastic constants of paper. The wave motion of a particular mode can be predicted by choosing f and c that can satisfy the dispersion equation. The symmetric modes correspond to the

solutions of the dispersion equation with a positive exponent, while the antisymmetric modes correspond to those with a negative exponent.

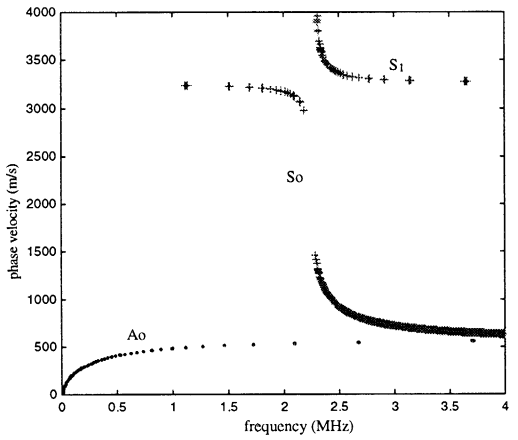

(a) Solutions for copy paper in MD

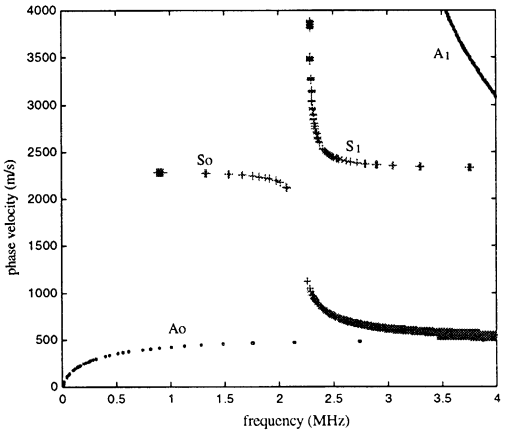

(b) Solutions for copy paper in CD

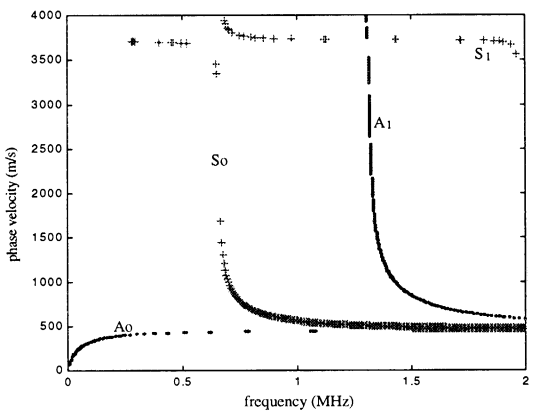

(c) Solutions for linerboard 42-lb in MD

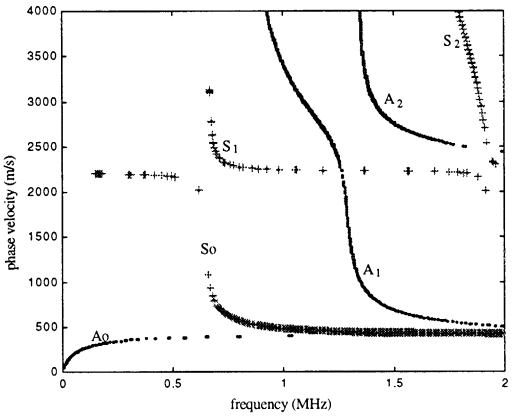

(d) Solutions for linerboard 42-lb in CD

Figure 2.6.2 Dispersion curves of copy paper and linerboard 42-lb : The grammages of copy paper and 42-lb linerboard are 80 g/m^2 and 205 g/m^2, respectively. Each wave mode is identified by a letter (S for symmetric and A for antisymmetric), followed by a number indicating the order of the mode. As the frequency increases, all modes are known to approach an asymptotic phase velocity, which is a Rayleigh surface wave.

A complete derivation of the dispersion equation is found in the study by Habeger et al. (1979), who also simplified the dispersion equation in the low frequency limit. For the two lowest modes, S_0 and A_0, the simplified relations are

$$c = \sqrt{\frac{C_{11}}{\rho}} \qquad \text{for the } S_0 \text{ mode} \qquad (2)$$

$$c = \left[2\pi \cdot f \cdot h \cdot \sqrt{\frac{C_{11}}{3\rho}} \right]^{1/2} \qquad \text{for the } A_0 \text{ mode.} \qquad (3)$$

where C_{11} is the elastic stiffness constant in MD (Pa), ρ is the apparent density of paper (kg/m^3), h is the half thickness of paper (m), f is the frequency (Hz) and c is the wave phase velocity (m/s). The error associated with using Equation 2 to approximate the value for C_{11} from the S_0 mode was found to be no more than 2% [Mann et al., 1980].

The dispersion equation was numerically solved for two paper grades: copy paper and 42-lb linerboard. The stiffness constants used to solve the equation were measured using the contact ultrasonic instruments at the Institute of Paper Science and Technology (see Section 2.3). The concept of this method is well described by Habeger et al. (1989). Figures 2.6.2 show dispersion curves for copy paper and 42-lb linerboard in MD and CD. Each wave mode is identified by a letter (S for symmetric and A for antisymmetric), followed by a number of the order. As the frequency increases, all modes are known to approach an asymptotic phase velocity [Viktorov, 1967, Mann, 1978]. This asymptotic velocity is known to be that of a Rayleigh wave, which exists on the surface of a half-space material.

Important characteristics of the dispersion curves are found by varying the values of the elastic constants. By raising or lowering the values of C_{11} or C_{22}, one can determine their effects

on the S_0 and A_0 modes. The major effect of C_{11} and C_{22} is on the low frequency limit of the S_0 mode, while only a minor change is observed in the initial slope of the A_0 mode. The primary effect of C_{33} is the location shift of the cut-off frequency for the S_0 and S_1 modes. C_{13} and C_{23} have only a minor effect on the S_0 mode. The effect of C_{44} and C_{55} is on the high frequency limit of the S_0 and A_0 modes [Johnson, 1996].

During the next phase of the project, dispersion curves will be studied to analyze the inverse problem of extracting stiffness properties from measured data; that is, the elastic constants will be predicted by fitting the measured A_0 and S_0 data with the dispersion curves using non-linear regression.

2.6.2 Fabry-Pérot Interferometer Measurements (J.B. Walter and K.L. Telschow, INEEL)

2.6.2.1 Fabry-Pérot Interferometer Methodology

Many optical techniques for measuring ultrasonic motion on surfaces have been developed for use in laser ultrasonic applications (Monchalin, 1986). Most of these methods have similar sensitivities and are based on time domain processing using homodyne, heterodyne, Fabry-Pérot, and, more recently, photorefractive interferometry (Wagner, 1990, Ing et al., 1991). Of the many optical techniques for ultrasound detection, only a few have proven capable of performing measurements in the presence of multiple speckle reflections from diffusely scattering surfaces like paper. One of these is the Confocal Fabry-Pérot self-referencing interferometry method (Monchalin and Héon, 1986) that was evaluated as a separate task on this program through the use of the facilities and expertise at the Idaho National Engineering and Environmental Laboratory (INEEL).

Multiple speckles are successfully demodulated due to the self-referencing nature of the Fabry-Pérot technique, i.e., the photodiode signal originates from the interference of light scattered from the paper surface and delayed portions of that light generated from multiple reflections within the Fabry-Pérot cavity. Since all of the optical wavefronts are nearly identical to that scattered from the paper surface, light from a relatively large surface area (1-4 mm^2) including many speckles is collected and interfered efficiently. This gives this detection technique the optical efficiency needed to provide sufficient sensitivity for detection on rough and/or optically diffuse material surfaces, as exist on most types of paper. Diffuse surfaces scatter radiation into a hemisphere, resulting in only a very small amount that returns directly to the interferometer detection system. For a normal standoff distance of a few centimeters, the optical collection efficiency is typically in the 0.1% – 1% range resulting in relatively little light collection. The detection system signal to noise ratio, in the shot noise limited regime, is controlled by the amount of light entering the interferometer. There is also a limitation on how much light can be focussed onto a particular paper sample without damage. These factors place severe requirements on the optical collection efficiency and greatly affect the overall system performance and cost. These considerations have led to the choice of the Fabry-Pérot system for most industrial applications of laser ultrasonics that are actually performed in the field today.

The Fabry-Pérot interferometer system employed at the INEEL utilized an argon ion laser capable of focusing up to 1.5 watts of light (514 nm) onto the paper surface (Telschow, et al., 1990). A pulsed Nd:YAG laser (1064 nm) with a pulse width of about 15 ns and pulse energy up to 400 mJ was used to excite elastic waves in the paper by the thermoelastic and ablation mechanisms. Paper samples were placed at the focus of the two laser beams, similarly to that shown in Figure 2.6.3. For the moving paper measurements, the IPST web simulator was placed

at the left end of the table allowing access for the laser beams to the paper surface on the revolving wheel.

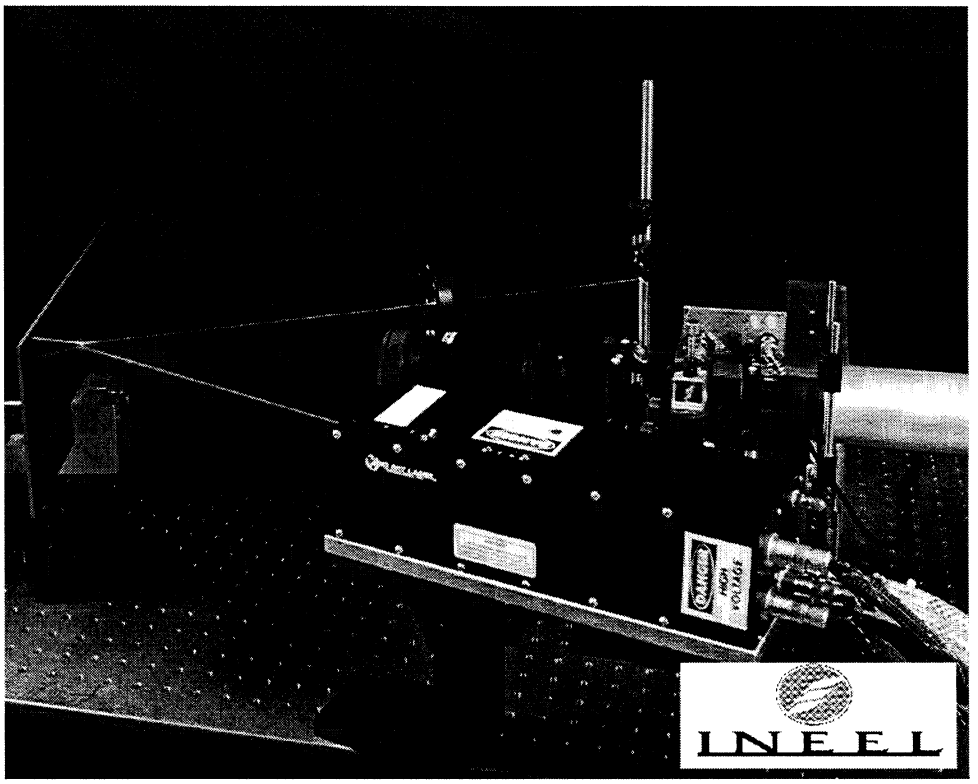

Figure 2.6.3 Picture of the INEEL laser ultrasonic point measurement system employing a confocal Fabry-Pérot interferometer (tube to the right), a pulsed Nd:YAG laser for excitation (black box in the foreground) and the generation and detection beams impinging onto a sample at the left.

2.6.2.2 Lamb Wave Measurements In Stationary Paper

Fabry-Pérot measurements were first conducted on stationary paper. Figures 2.6.4a,b show a comparison between the lowest order symmetric (S_0) and antisymmetric (A_0) waveforms recorded on a stationary 0.1mm thick stainless steel sheet, Figure 2.6.4a, and a piece of 0.1mm thick copy paper, Figure 2.6.4b. The laser generation was from a line source and produced clearly distinguished symmetric and anti-symmetric waves, as seen especially from the stainless

steel data in Figure 2.6.4a. It is also apparent from Figure 2.6.4a that a uniform line source produces little or no signals in the interval between the S_0 and A_0 waveforms (2.5 and 3.5 μs in the picture). Figure 2.6.4b shows results under similar conditions for Lamb waves recorded from copy paper. Taking note of the longer time scales for the paper waveforms, it can be seen that the general frequency content of these waves is lower in paper than for the stainless steel. This is due to the larger attenuation that both wave modes experience in paper. In addition, complexity due to the heterogeneity of the material at the fiber level resulted in non-uniform ultrasonic generation along the line producing multiple signals arriving between the first S_0 and the A_0 wave modes. It was also observed that the paper waveforms showed considerable changes in shape with position on the paper, especially for the S_0 mode. An attempt was made to eliminate this problem by using an excitation line width of about 1mm to average over many fibers. However, it was always found that the recorded waveforms showed some dependence on location on the paper.

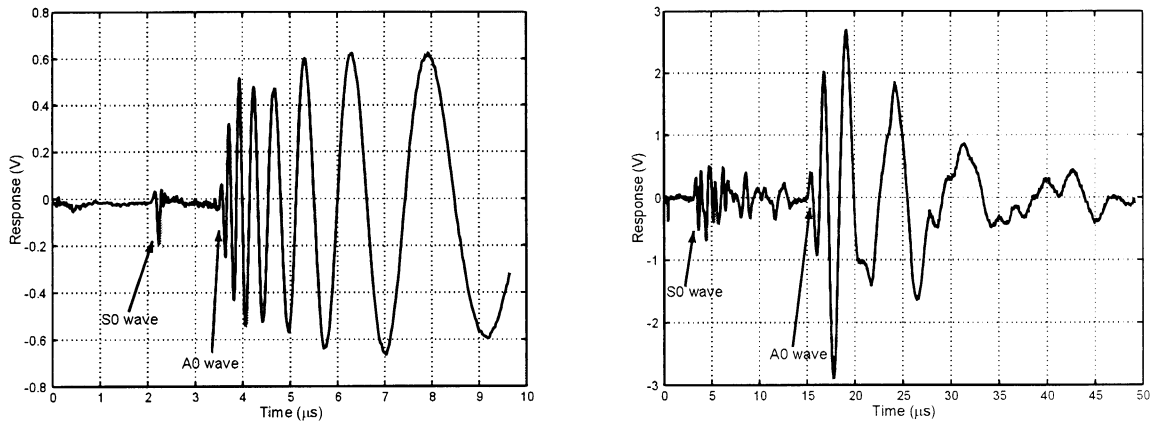

(a) (b)

Figure 2.6.4 (a) Lamb waves on thin sheets of stainless steel measured with the INEEL Fabry-Pérot interferometer system; (b) Lamb waves on thin sheets of copy paper measured with the INEEL Fabry-Pérot interferometer system.

2.6.2.2.1 Thermoelastic vs. Ablation Generation

Damage to the paper was easily accomplished at even moderate pulsed laser excitation energies. Figure 2.6.5 shows the results comparing the recorded signals both below and above the ablation threshold for 1064 nm source wavelength. The general ablation level for the papers appears to be around 20-80 MW/cm^2 for a pulse width of about 15 ns. Tests were performed to check the ablation level of copy paper using both the 1064 nm and the 532 nm radiation lines of the Nd:YAG source laser. Generally, it was observed that the first few pulses ablate something from the paper and produce a large A_0 wave. The top trace of Figure 2.6.5 shows an average of the first 16 pulses impinging on a virgin paper location. Subsequent pulses appeared to produce little or no ablation as the A_0 wave diminished. The bottom trace, taken from a different location, shows an average of 16 pulses taken after the A_0 wave diminished in amplitude. Similar results were obtained for the signals seen at 532 nm.

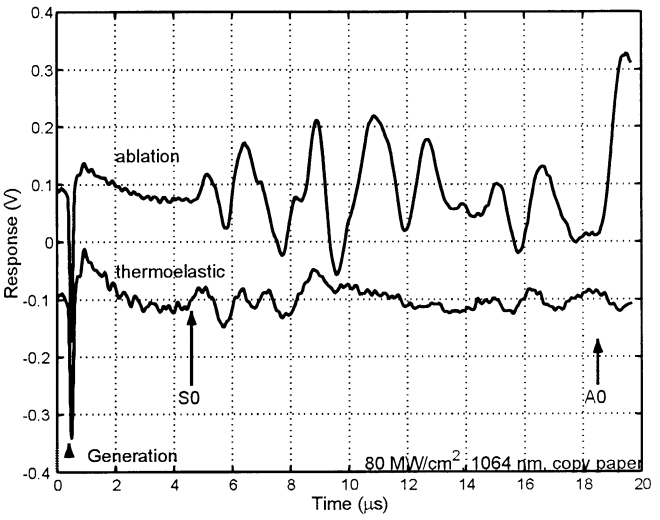

Figure 2.6.5 Thermoelastic vs. Ablation generation on copy paper.

Figure 2.6.6 compares recorded signals both below and above the ablation threshold for 532 nm source wavelength. The top of the figure shows an average of 1000 pulses at one location (40 μW detection light) at a pulse level that produced no ablation, as measured by subsequently observing no change in the paper fibers under microscopic examination. The bottom of Figure 2.6.6 shows an average of 1000 pulses at a different location (28 μW detection light) with slight ablation occurring about 30% of the time as seen from the appearance of the A_0 mode waveform on the recording oscilloscope. The ablation thresholds for copy paper were found to be approximately 80 MW/cm^2 @ 1064 nm and about 20 MW/cm^2 @ 532 nm. The difference is probably due to the lower absorption of light in this paper at the longer wavelength.

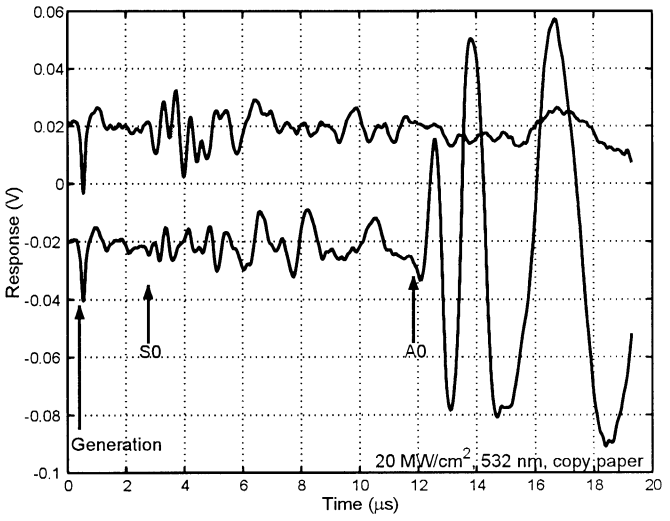

Figure 2.6.6 Comparison below and above the ablation threshold for copy paper at 532 nm showing the A_0 mode waveform when ablation is present.

2.6.2.2.2 Directional S_0 & A_0 Response for paper RSK59

Measurements are shown in Figure 2.6.7 of the ultrasonic S_0 and A_0 mode wave velocities taken as a function of propagation direction on the RSK59 paper. The S_0 wave velocity in the machine direction (MD) was 3.75 (mm/μs) as determined by measurements taken over multiple distances for a signal with a bandwidth of about 1 MHz. The source to detector distance was about 6 mm and the paper was rotated keeping the source and detector geometry fixed.

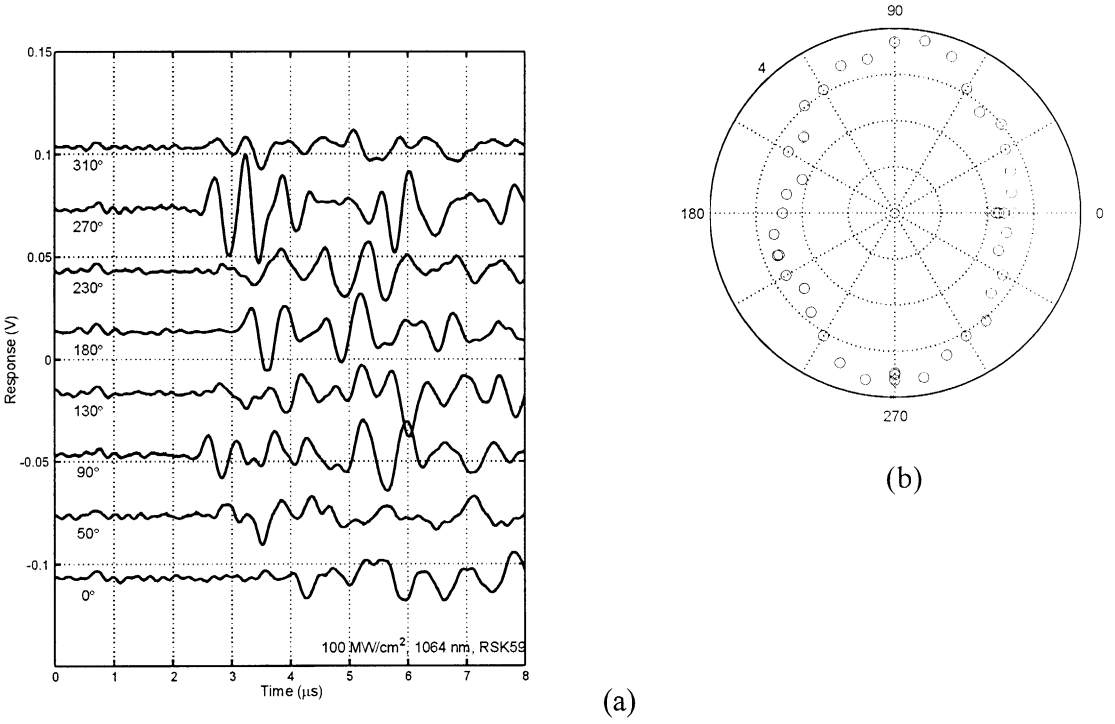

Figure 2.6.7 (a) S_0 waveforms for the RSK59 paper sample taken at varying angles with respect to the CD direction (0°); (b) S_0 wavefront velocity for the RSK59 paper sample taken at varying angles with respect to the CD direction (0°), maximum value shown in 4 mm/μs.

Significant variations in the S_0 waveforms as a function of angle were found as shown in Figure 2.6.7a, all single shot waveforms taken with slight ablation occurring on the paper. The S_0 wave speed was determined from the earliest signal arrival time. The recorded velocity ratio between the MD and the CD was CS(MD)/CS(CD) = 1.48 +/- .11 at 1 MHz which agrees well with contact measurement results for this paper. Figure 2.6.7b shows the measured velocity values taken at varying angles with respect to the CD direction. Any single measurement yields both the S_0 and A_0 waveform. The ablation mechanism yielded the larger signals and was used whenever possible as long as no significant paper damage resulted. This mechanism was particularly efficient at generating flexural motion of the paper, so the A_0 waveforms were always much larger

than the S_0 waveforms. Therefore, one would prefer to measure the A_0 modes to obtain the elastic data about paper, if possible, due to this advantage.

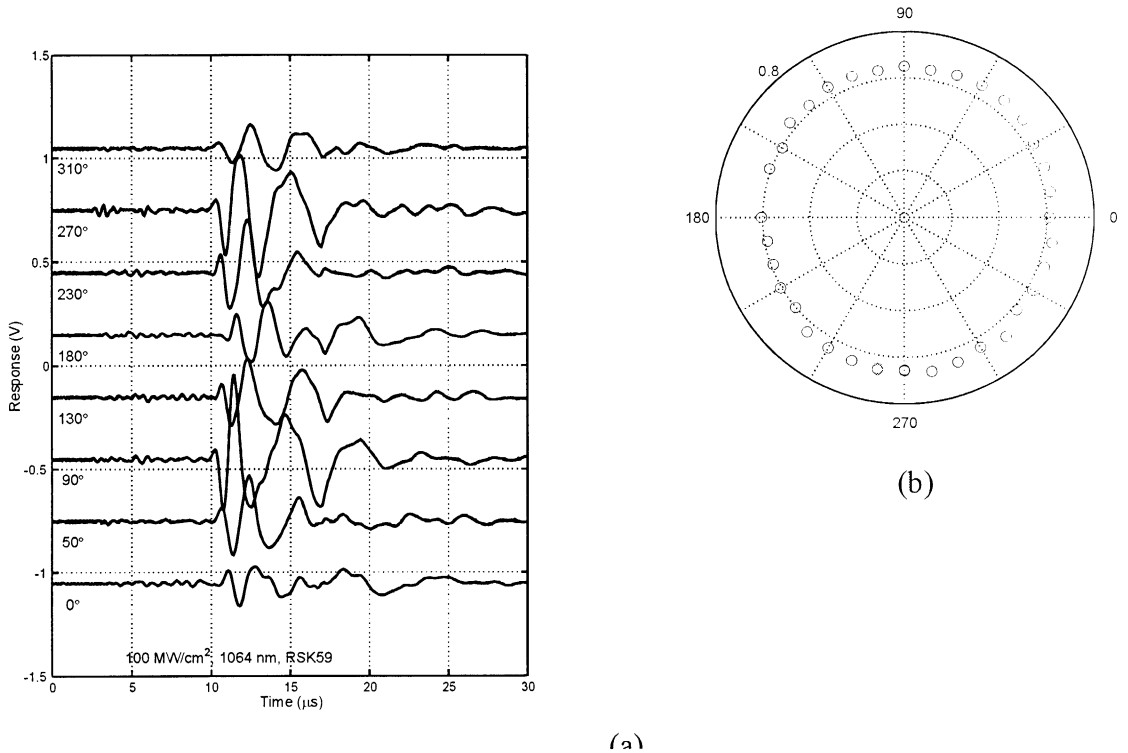

Figure 2.6.8 (a) A_0 waveforms for the RSK59 paper sample taken at varying angles with respect to the CD direction (0°); (b) A_0 wavefront velocity for the RSK59 paper sample taken at varying angles with respect to the CD direction (0°).

Figure 2.6.8a shows the complete waveforms recorded from the RSK59 paper including the region shown in Figure 2.6.7a. Here the time scale has been lengthened to show both the fast S_0 mode and the slower A_0 mode. Clearly the A_0 mode waveforms were the largest, but they were also dispersive. The phase velocity varied with frequency, such that it was difficult to get a unique phase velocity value from which to determine the elastic constants. However, at low frequencies, there is a well know relationship between the A_0 phase velocity and the frequency that suggests that the MD/CD ratio for the A_0 mode should be approximately the square root of that for the S_0

mode. Figure 2.6.8b shows the measured A_0 velocity values taken at varying angles with respect to the CD direction for a frequency around 1 MHz. The recorded A_0 velocity ratio between the two perpendicular directions was CA(MD)/CA(CD) = 1.07 +/- .05. Figure 2.6.9 illustrates the generally good agreement found between experimental Fabry-Pérot measurements (and photorefractive, described in Section 2.6.4) and that predicted by numerical calculation. The calculation was based on anisotropic plate wave propagation (Habeger, et al. 1979) using the elastic constants for the RSK59 paper independently determined by other means at the IPST. Some difference between experimental measurement and the theoretical calculation can be seen in the data of Figure 2.6.9 that is thought to be due to the dispersion effects present in both the S_0 and A_0 wave modes at the frequencies employed.

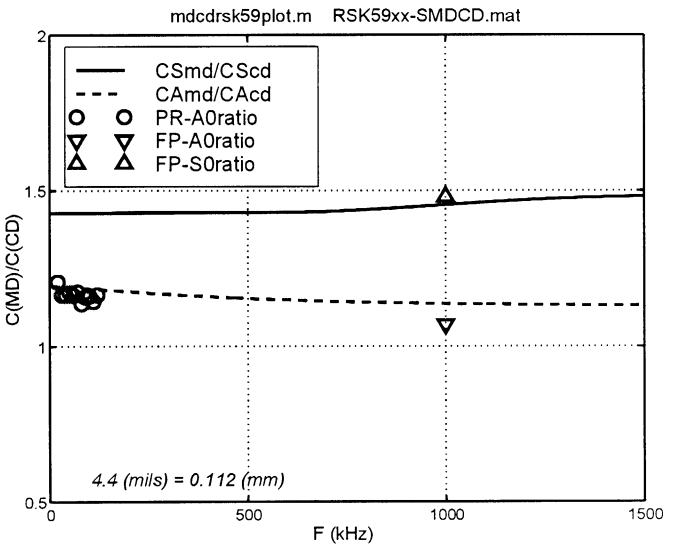

Figure 2.6.9 Comparison between the experimentally measured S_0 & A_0 MD/CD velocity ratios using the Fabry-Pérot and Photorefractive active methods with expectations calculated from elastic constants for this paper provided by independent IPST measurements.

2.6.2.2.3 Fabry-Pérot Laser Ultrasonic Static Paper Measurements (Summary)

The Fabry-Pérot interferometer has proven itself to be a useful device for laser ultrasonic detection on paper. It can effectively accommodate the diffusely reflecting surface of paper, readily be scanned over the paper surface to make measurements at different locations, automatically eliminates low frequency interfering signals due to vibration and laser phase noise, and has a fast response time that allows it to operate at high frequencies. This high frequency response can be detrimental. The Fabry-Pérot system at the INEEL is designed and optimized for operation above 1 MHz. Attenuation in the paper limited the primary wave components to occur at frequencies below 1 MHz. Dispersion in the S_0 mode occurred above 1 MHz. Both of these facts complicate the recorded waveform. Lower frequency operation would be better for recording the S_0 mode in its low frequency non-dispersive region providing simpler signal interpretation. However, the A_0 mode was always found to be the larger and its dispersion effects are well known. This opens the possibility that use of the A_0 mode would be more beneficial for determining elastic properties in paper. Additional signal processing would be required to account for the dispersion, but this is readily accomplished and performed routinely in other laser ultrasonic measurement applications.

2.6.2.2.4 Lamb Wave Measurements In Moving Paper

A machine was provided by IPST for simulation of the moving web of paper. This web simulator before modification was capable of moving the paper surface around a revolving wheel at speeds up to 400 meters/minute. Physically, the revolving paper surface allowed for contact free optical access to the moving surface that was placed approximately 1-10 cm from the optical input to the interferometer.

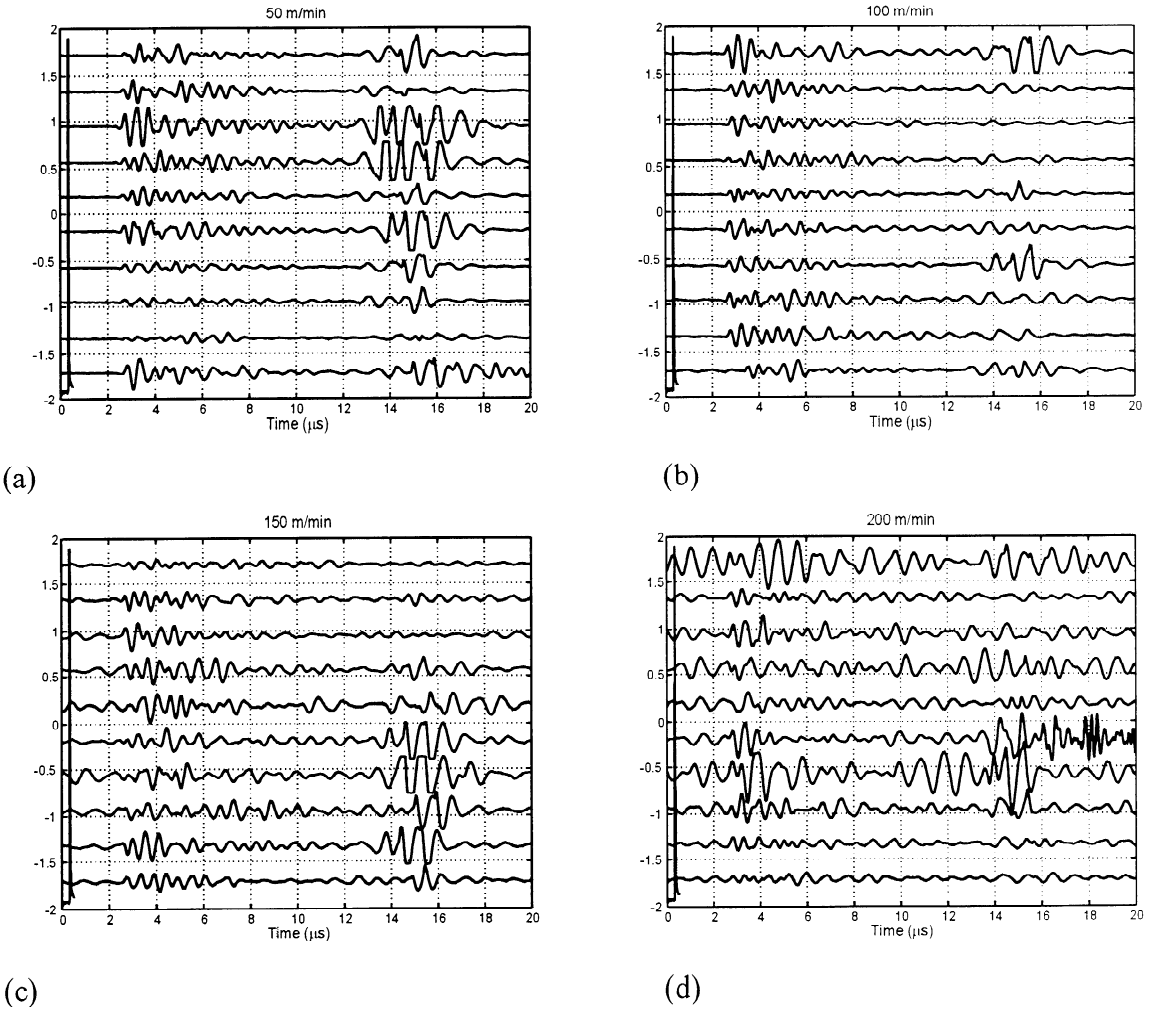

Figure 2.6.10 Repetitive single shot measurements on moving RSK59 paper showing the increase in noise due to the ambient vibration, laser, and changing speckle pattern phase noise at web speeds of (a) 50 m/min; (b) 100 m/min; (c) 150 m/min; (d) 200 m/min.

Figures 2.6.10a-d show a collection of single shot waveforms recorded successively, 1 second apart, from the moving paper surface. The first observation was that the moving paper surface added a significant source of additional noise to the detection process. This noise occurred from phase fluctuations and appeared to be due to several sources. Each waveform is from a single laser shot on a different location of the paper surface. These signals have been filtered with a 1 MHz high pass filter to remove some

of the larger low frequency phase noise. Filtering was performed to optimize the S_0 mode detection and alters the waveforms leaving only the high frequency components in each waveform. The figures show that there is some variation from shot-to-shot, due to local paper properties and the generation mechanism, and also shows significant additional noise at the higher web speeds. This is particularly apparent if one concentrates on the region before the first S_0 wave arrival with reference to the laser timing mark (bottom trace on Figures 2.6.10a-d).

Noise spectra taken at various web speeds for RSK59 are shown in Figure 2.6.11a for a detection spot size of 0.04 mm on the paper surface, Figure 2.6.12a for a 0.26 mm spot size and Figure 2.6.13a for a nearly specular plastic surface. Several observations can be made from these figures: (1) a large noise component appears at low frequencies even for stationary paper; (2) the low frequency component grows in amplitude as the web speed is increased; and (3) a plateau noise component appears that increases in frequency bandwidth but not amplitude as the web speed is increased. The overall general increase in noise with web speed is shown by the integrated noise amplitude shown in Figure 2.6.11b. These measurements were repeated for a larger detection spot size of 0.26 mm and the results are shown in Figures 2.6.12a and b. Clearly, similar behavior was seen as with the smaller spot size, but the larger spot averages over more of the paper roughness and reduces the bandwidth dependence on web speed as seen in Figure 2.6.11a. Some of the noise signals come from the moving speckle pattern recorded by the photodetector aperture. An attempt to eliminate this effect was performed by measuring the noise signals again but from a relatively smooth surface (the plastic wheel itself) that presents essentially a single speckle at the detector. The recorded noise spectrum for the plastic

wheel is shown in Figure 2.6.13a and the integrated noise signal in Figure 2.6.13b. A significant reduction in the higher frequency plateau noise signal was observed.

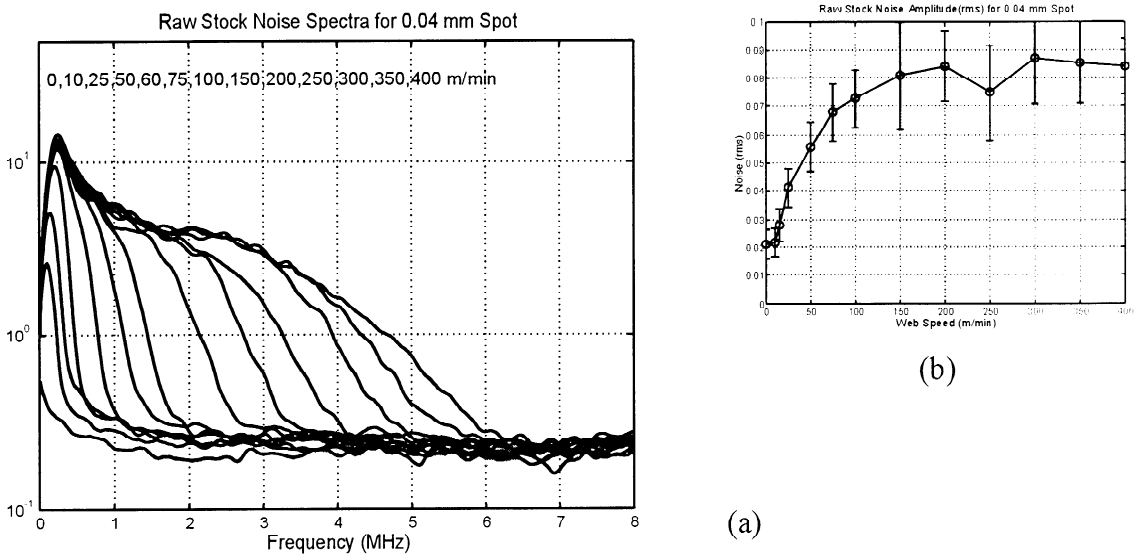

(a) (b)

Figure 2.6.11 (a) Web simulator noise measurements from RSK59 paper for a 0.04 mm diameter detection beam spot size at various web speeds; (b) integrated noise rms amplitude measurements from RSK59 paper for a 0.04 mm diameter detection beam spot size.

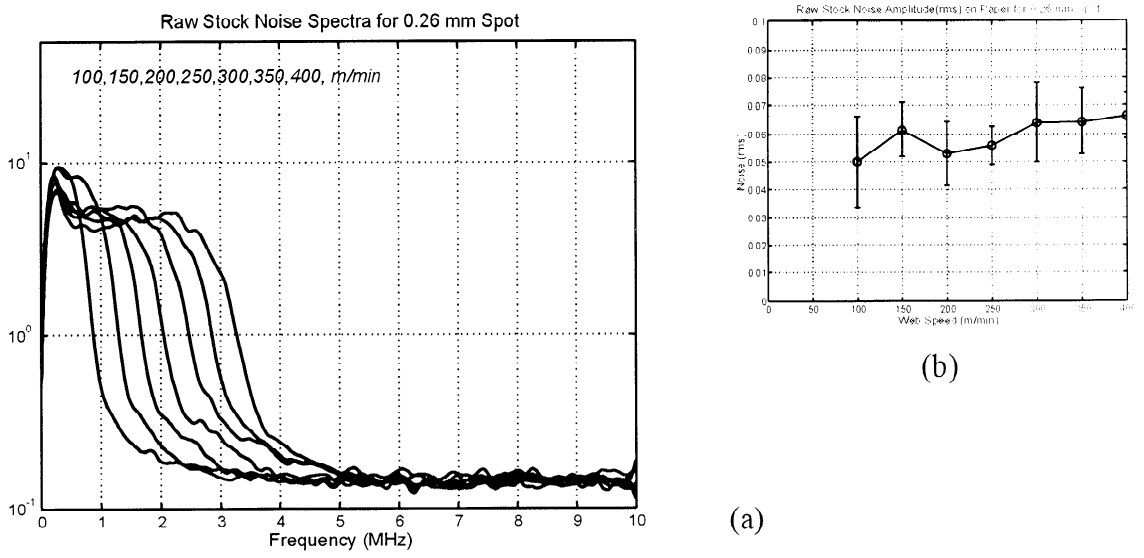

(a) (b)

Figure 2.6.12 (a) Web simulator noise measurements from RSK59 paper for a 0.26 mm diameter detection beam spot size at various web speeds; (b) integrated noise rms amplitude measurements from RSK59 paper for a 0.26 mm diameter detection beam spot size.

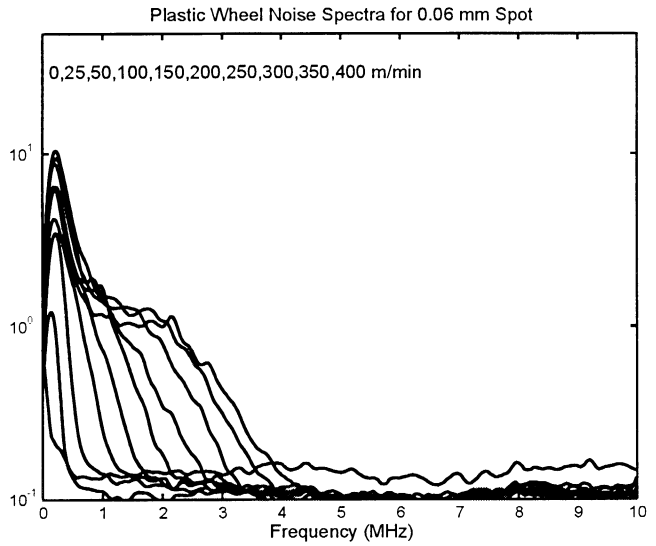

(a)

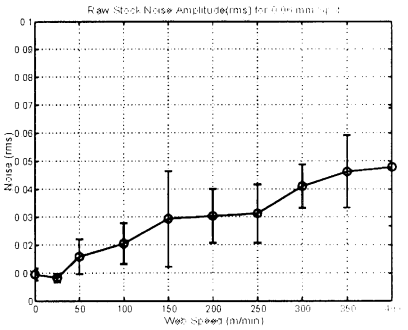

(b)

Figure 2.6.13 (a) Web simulator noise measurements from plastic wheel for a 0.08 mm diameter detection beam spot size at various web speeds; (b) integrated noise rms amplitude measurements from the plastic wheel for a 0.08 mm diameter detection beam spot.

The observed noise signal dependence on web speed can be explained by the contributions from several noise sources including

- INTRINSIC noise: inherent noise component even for stationary paper due to the phase noise from:
  - *Laboratory Vibrations* causing fluctuations in the optical path lengths between the detector and the sample surface
  - *Laser Phase Noise* in the detection laser (here an argon:ion laser)
  - *Electronic Interferometer Control Fluctuations*
  - *Electronic Signal Amplification Noise*
  - *Shot Noise* due to the detection process.

These noise components determine the maximum detectability of the Fabry-Pérot system used and are present in all the waveforms shown throughout this section. Additional noise sources due to the moving paper surface are

- FLUTTER noise: there is additional flutter and misalignment in the moving paper simulator that increases the phase noise seen as the web speed is increased. This noise source accounted for the noise component that appears to be limited to the low frequency region of the spectrum, but whose amplitude increases with web speed.
- SPECKLE noise: the moving rough paper surface produced a moving speckle pattern of light that crossed the photodetector aperture. This produced a noise component that had a fixed maximum amplitude (since the optical phase shift was limited to modulo(2π)). However, the frequency at which these speckle components move across the detector aperture increases with the web speed extending the noise bandwidth observed.

Speckle noise is seen in the spectra of Figures 2.6.11a and 2.6.12a. The plastic wheel data showed much less of this noise component, consistent with the speckle noise hypothesis.

These various noise sources combine to limit the detectability of the whole system. Figure 2.6.14 shows a comparison of the integrated noise levels described. One can conclude from these results that averaging over many speckles by using a larger detection spot size helps in that it moves the speckle noise to lower frequencies. Figure 2.6.15 shows the effect of increasing the detection spot size brought about by defocusing the instrument and normalizing for constant optical detection power. As wider spot sizes are

used, the spatial resolution and frequency response of the system decreases. Other schemes are under investigation to further reduce the noise levels.

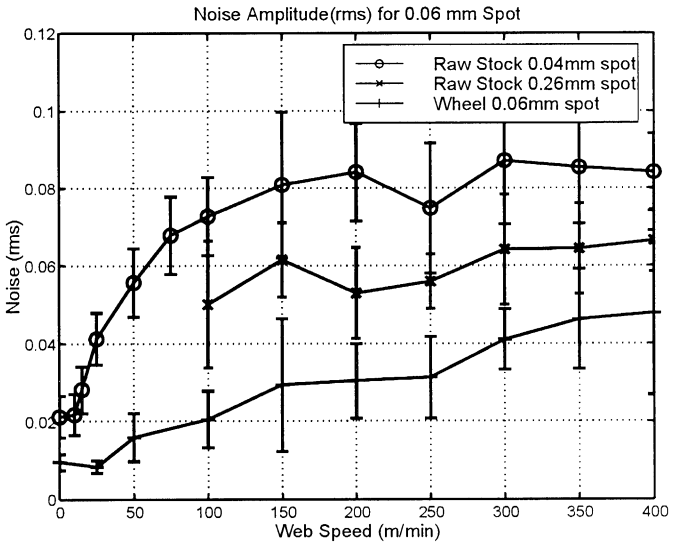

Figure 2.6.14 Comparison of the integrated noise signal amplitudes for the moving RSK59 paper with two spot sizes and for the moving plastic wheel.

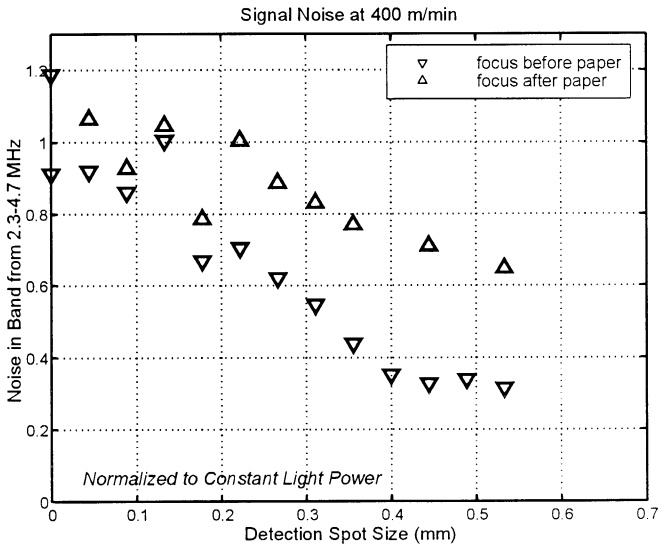

Figure 2.6.15 Integrated noise amplitude as a function of the detection spot size showing the decrease in noise level as more spatial averaging is performed on RSK59 paper.

2.6.2.2.5 Fabry-Pérot Interferometer Measurements (Summary)

To date, laser ultrasonic measurements of the S_0 and A_0 wave mode velocities in the MD & CD directions have been recorded with acceptable signal to noise ratios at web speeds up to 200 m/min using single shot detection with the INEEL Fabry-Pérot interferometer system. Higher speeds can be reached by using additional signal acquisition and processing techniques. Figures 2.6.16a and b show S_0 and A_0 waveforms for both the MD and CD directions on LNR42 and MED26 paper respectively. At relatively low speeds high signal to noise ratios were obtained for all the papers tested. Clearly the anisotropy between the MD and CD directions in wave speed is readily measured from either wave mode. At higher web speeds acceptable signal to noise ratios can be achieved by high pass filtering the data to eliminate the low frequency intrinsic and flutter noise. Figure 2.6.17 shows the S_0 and A_0 waveforms recorded with filtering for the RSK59 paper. Again the MD and CD anisotropy in the wave speeds is readily detectable. In order to reach an acceptable signal to noise ratio at the higher web speeds, up to 400 m/min, signals were averaged.

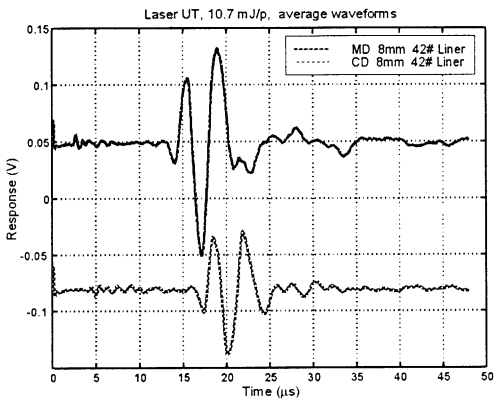

(a)

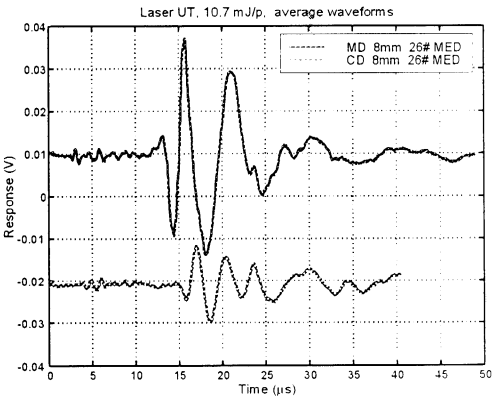

(b)

Figure 2.6.16 MD/CD Fabry-Pérot laser ultrasonic signals at low web speeds for (a) LRN42; (b) MED-26.

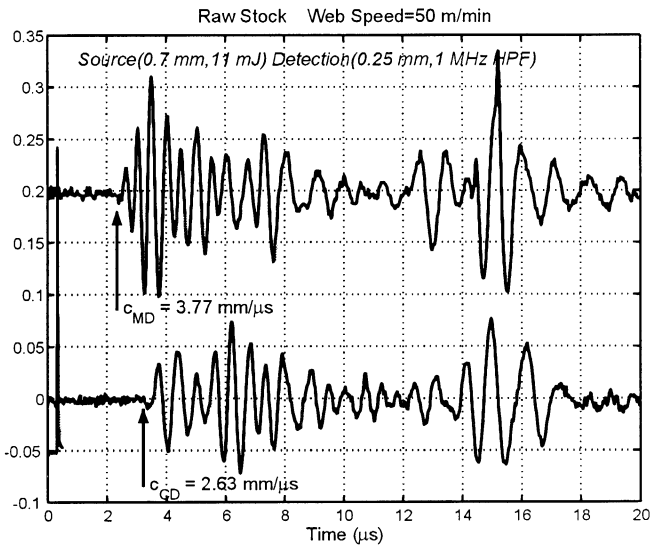

Figure 2.6.17 MD/CD Fabry-Pérot Web Simulator Laser Ultrasonic Signals – RSK59 paper at 50 m/min, 1 MHz high pass filter processed.

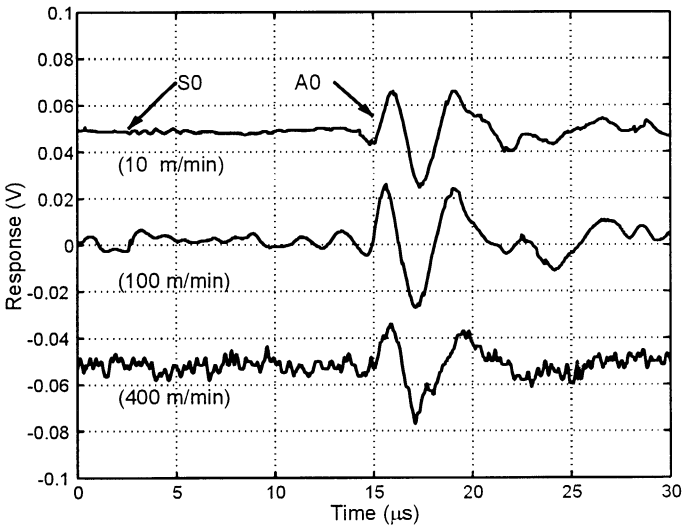

Figure 2.6.18 Comparison of the Fabry-Pérot interferometer detection signals on LNR42 paper (averaged 128 times) at three different web speeds.

Figure 2.6.18 shows the waveforms recorded from LNR42 paper at speeds of 10, 100 and 400 m/min averaging 128 times. Here the S_0 wave was not discernable at higher speeds because

the noise levels were too large for even averaging to filter out. However, the A_0 waveform is readily detected at all web speeds up to 400 m/min with averaging. Other mechanisms to reduce the noise level and enhance the signal detectability are under investigation. These include one described later in this report involving a reduction in the effective web speed by performing the measurements with a scanning laser detection beam as well as specialized signal processing routines for isolating signal properties from noise.

This work has shown that the Fabry-Pérot interferometer technology is a viable alternative for laser ultrasonic measurement of elastic waves in paper even under moving web conditions. All the work conducted so far has involved equipment designed for high frequency measurements not necessarily suitable for the paper measurement. Optimization of this approach would lead to improved performance over that presented here and presents a promising potential for future field implementation.

2.6.3 Time Domain Photorefractive Measurements (E. Lafond, IPST)

2.6.3.1 Introduction (the problem of speckled light)

Of the various laser-ultrasonic methods, two wave mixing in a photorefractive crystal (PRC) offers particular appeal. First of all, the detected mechanical signal has a natural, low frequency cut-off. The large-amplitude, mechanical vibrations of the moving web will not contribute to instrument noise since the dynamic grating in the PRC progresses fast enough to eliminate low frequency motion from the mixed signal. Laser interferometry works best on a specular reflecting surface; it is not normally good at utilizing diffuse light from a rough surface. The PRC method, however, is a holographic imaging technique. A large portion of the wave front participates in the mixing and in the ultrasonic detection. The PRC approach has a

reasonable chance of successfully finding tiny ultrasonic signals on rough surfaces traveling at high speed.

Because of the surface roughness of paper (many fibers) and that of fibers themselves, the light reflected from the surface is scattered almost isotropically in a half space (Lambertian source). From this arise two conclusions: 1) the power collected by a lens centered in the direction of the incoming beam will stay small, as long as the solid angle of collected light stays small; 2) the speckled nature of the reflection will make it very difficult to detect ultrasound with any interferometer which works with only one speckle, even on static surfaces.

On the other hand, the isotropic nature of light scattering on paper gives us an advantage: there is still enough power at relatively high incidence angles (40° off the normal or higher) for the detection of displacements. This allows the measurements of both out-of-plane (A_0) and in-plane (S_0) displacements at the same time and thus avoids the need for two different setups.

2.6.3.2 Choice of a photorefractive interferometer

The criteria that define a photorefractive interferometer are:

- Wavelength of the detection laser
- Type of the photorefractive crystal
- Optical head of the interferometer
- Application of a high voltage to the crystal.

These criteria are described in further detail in the following sections.

2.6.3.2.1 Wavelength

The wavelength of the detection laser used with the interferometer is very important since the detection laser is usually the most expensive device in an interferometer and its wavelength cannot be changed easily. It also determines the type of photorefractive crystal to be used with the interferometer, as each crystal has a certain optimal bandwidth. The reflection coefficient of paper at this specific wavelength defines the amount of light reflected back at this wavelength. This directly affects the signal strength from the interferometer.

The wavelengths selected at IPST are 514.5 nm (Ar:ion laser) and 1064 nm (Nd:YAG laser). Some alternative choices for wavelengths could be 532 nm (doubled Nd:YVO_4 laser), or 780 nm and 852 nm (diode lasers). The selection of 514.5 nm and 1064 nm comes from the fact that relatively low cost lasers with high output powers at these wavelength are available.

Pulsed lasers (a few hundreds of μs with instantaneous powers of a few kW) can be used as the detection laser instead of a continuous one. However, the cost and complexity of such lasers did not make them suitable for the experiments during Phase I.

2.6.3.2.2 Type of photorefractive crystal

As described in section 2.5.3.5, crystals useful in our application are either the Sillenite type or the Semiconductor type. The Sillenite type crystals which work in the visible range (need to be photorefractive and transparent) are $Bi_{12}SiO_{20}$ (BSO), $Bi_{12}GeO_{20}$ (BGO), $Bi_{12}TiO_{20}$ (BTO), and are well suited for Ar:ion lasers (514.5nm) or lasers at 532 nm. The Semiconductor type crystals need to be used at infrared wavelengths because their transmission band ranges

from 915nm to 1500nm. These semiconductor crystals are undoped GaAs, InP:Fe and CdTe:V. All of these can be potentially used for ultrasound detection on paper products.

In the very specific case of the photoinduced-EMF interferometer, the opposite effect is desired: total optical absorption of the beam by the crystal. For Cr:GaAs, a crystal very efficient for photoinduced-EMF detectors, the appropriate wavelength is thus in the visible (514.5 or 532nm) or in the near infrared (852 nm or lower).

For measurements on static paper, the Sillenite type crystals are appropriate since they have a high gain. Thus, the signal to noise ratio of the ultrasonic displacement is high, even with little light collected. Unfortunately, these crystals do not have a response time short enough to adapt to the constantly changing speckle pattern created by the displacement of the paper web under the beam.

Thus, for measurements on moving paper, the first choice is to use Semiconductor photorefractive crystals which have a very short response time (1 to 10 μs) but a small gain. These will, however, have smaller signal to noise ratio than Sillenite type crystals.

2.6.3.2.3 Optical head of the interferometer

The optical head of an interferometer can either use the same objective for the focusing of the detection laser beam and the collection of light scattered back by the paper sheet, or use two separate objectives.

For example, with two separate lenses, it is possible to have a small diameter lens to focus the beam on the paper surface, and a large diameter lens (at least 2.54 cm) for the collection of

the scattered light. When the incident beam and the collected beam are separated, they can have any polarization. This setup is known as a "V" type optical head, as shown in Figure 2.6.19.

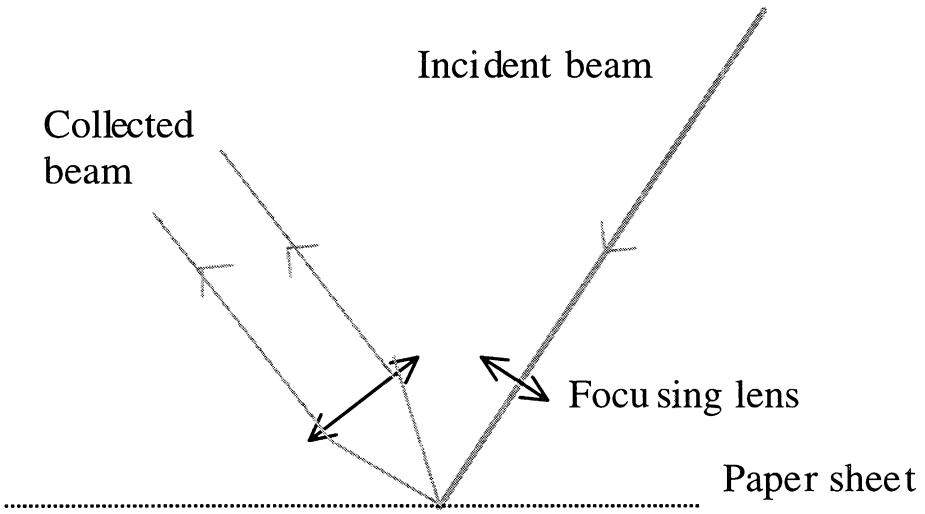

Figure 2.6.19 "V" type optical head.

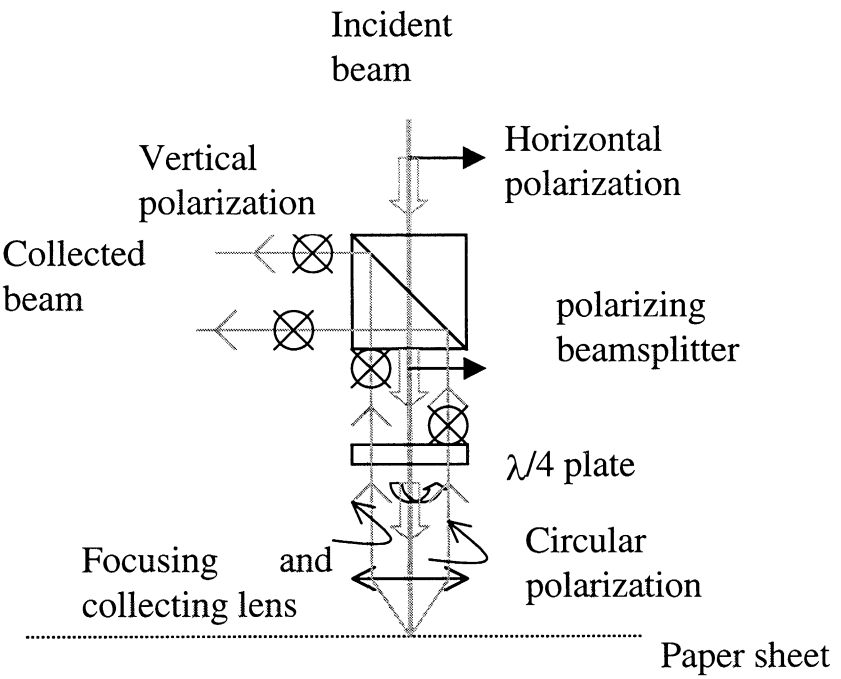

Figure 2.6.20 "T" type optical head.

Another configuration for the optical head, which uses the same objective for the incoming and backscattered beam, is the "T" type optical head, as shown in Figure 2.6.20. In this setup, the incoming beam is horizontally polarized, then passes through a quarter wave plate just before the focusing objective that makes the beam circularly polarized. The collected light (still circularly polarized) comes back through the focusing objective, then the quarter wave plate rotates the polarization 90 degrees to vertical. This allows a polarizing beam splitter to be used to separate the incoming beam (horizontally polarized) from the backscattered beam (vertically polarized).

When the diameter of the collecting lens is very large, a third possibility is to use a lens plus a mirror at 45 degrees or a Cassegrain type objective and a mirror at 45 degrees. This allows collection of light over a large solid angle (see Figure 2.6.21).

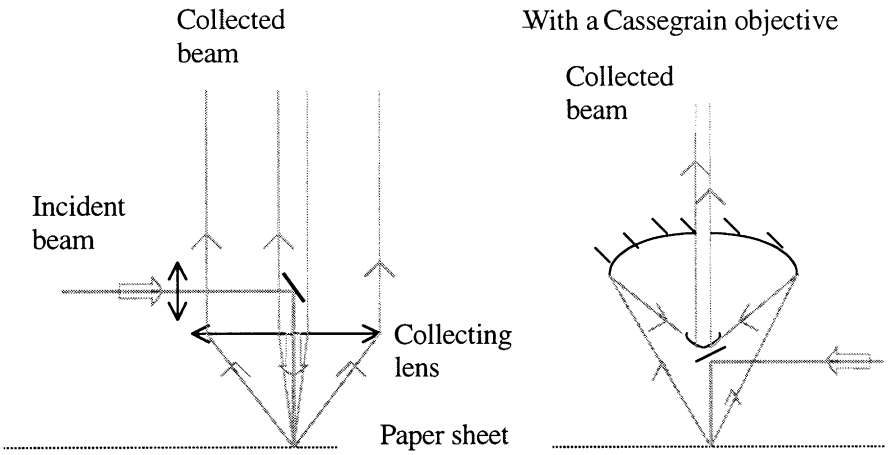

Figure 2.6.21 Large lens or Cassegrain objective for the optical head.

2.6.3.2.4 Application of high voltage to the crystal

The application of a high voltage, DC or AC, pulsed (at the moment when the ultrasonic waves need to be detected) or continuous, to a photorefractive crystal is necessary when the

photorefractive gain of the crystal is small, typically in the case of semiconductor photorefractive crystals. It can also enhance the gain of Sillenite type crystals.

The high voltage across the crystal has two effects: it moves more electrons from the bright fringes to the dark fringes and thus creates a stronger electric field grating, and it shifts the phase of the electric field closer to quadrature from the interference grating.

The drawback, however, is that the application of an electric field slows down the adaptation of the crystal to the changing speckle pattern (slower response time), which is a problem in the case of Semiconductor crystals.

2.6.3.3 Numerical Modeling of Two Wave Mixing and Ultrasonic Signal Detection in Cubic Photorefractive Crystals (C. Habeger, IPST)

2.6.3.3.1 Symbol Look-up Table for Section 2.6.3.3

E_a	amplitude of incoming plane wave 1
E_b	amplitude of incoming plane wave 2
k_a	wave vector of incoming plane wave 1
k_b	wave vector of incoming plane wave 2
k	magnitude of wave vector in PRC
2θ	angle between plane wave 1 and 2
$K = k_a - k_b$	grating wave vector
$I_0 = E_aE_a^* + E_bE_b^*$	average total intensity
$I_1 = E_bE_a^* + E_aE_b^*$	amplitude of intensity variation
N_D	donor sites in PRC per unit volume
N_A	acceptor sites in PRC per unit volume
k_T	Boltzman's constant times absolute temperature
E	space-charge field

E_0	applied DC electric field
E_1	amplitude of electric field
ε	low frequency permittivity of PRC
μ_o	permeability of free space
ε_o	permittivity of free space
n	index of refraction of PRC
j	current density
q	electronic charge
μ	mobility of electrons in conduction band
$k_D = \frac{q^2 N_A}{\varepsilon k_T}$	Debye wave number
γ_P	electron to ionized donor recombination rate constant
s	ratio of electron generation rate to intensity times density of unionized donors
ESs	the s polarization component of the electric field of the signal beam
ESp	the p polarization component of the electric field of the signal beam
EPs	the s polarization component of the electric field of the pump beam
ESs	the p polarization component of the electric field of the pump beam
ϕ	the phase of space charge field of Equation 1
α	PRC intensity attenuation coefficient
ρ	angular rotation of polarization of PRC per unit length
$r_{4,1}$	cubic linear electro-optic coefficient
t	PRC thickness

2.6.3.3.2 Introduction:

The purpose of the numerical work described below is to model two wave mixing and ultrasonic signal detection in PRC interferometers. This is to allow us to predict the influence of PRC parameters and instrument design on the ultrasonic signal-to-noise ratio. Guided by these results, we will be better able to specify crystals and arrange the detection scheme.

2.6.3.3.3 Two Wave Mixing Theory

Dynamic mixing of coherent light beams can be accomplished through interference in a PRC. Photorefractive crystals are often semiconductors with donor and acceptor impurities. When the beams interfere in the bulk of the crystal, regular patterns of variation in light intensity are established through the bulk of the crystal. The donor sites are optically sensitive: light energy is absorbed by the donor sites and electrons are excited into the conduction band. The conduction band electrons diffuse away from the regions of high light intensity and are trapped in the low light intensity regions. This trapping is achieved thanks to a small number of acceptor impurity atoms. The Fermi level lies between the acceptor and donor levels. Under no-light conditions, the acceptor states are filled by electrons from the donors; hence there are ionized donor sites in the absence of photo-ionization. The conduction band electrons which diffuse away from the intensity loops can be trapped in dimmer regions in the available donor sites. This charge migration destroys local charge neutrality and sets up an electric field pattern through the crystal. Mixing of the light beams now occurs since PRC's are subject to the Pockels effect: their index of refraction is altered by an electric field. In the two wave mixing case, interference of coherent light beams in a PRC results in a grating in the index of refraction whose form is determined by the interference pattern. The grating, in turn, diffracts the light beams.

Since this dynamic grating is a result of interference between the two beams, the first order diffraction process is an exchange energy between the two beams. The two waves are said to be "mixed" in the PRC.

The first step in modeling two wave mixing is to express the static space-charge field (the electric field pattern resulting from interference and electron excitation) as a function of PRC characteristics and of the established light pattern. To do this, the analysis presented in the third chapter of Yeh (1993) on photorefraction is used. Below, the results of the development are reviewed stressing the approximations imposed to reach tractable results.

First it is assumed that two coherent plane waves with wave vectors of magnitude k are established in the PRC. Their directions of propagation are at an angle 2θ apart. The resulting interference pattern has a wave vector $K = 2k \cdot \sin \theta$. The index of modulation (the ratio of the amplitude of the intensity variation to the average intensity) is I_1/I_0.

The four unknowns in the analysis (the number density of electrons in the conduction band, N, the number density of ionized donor sites, N_D^i, the current density j, and the electric field, E) are assumed to have an average value dictated by the overall intensity plus a sinusoidal variation with a wave number of K resulting from the interference. The variation in electron and ionized donor number are assumed to be small compared to the average values. Higher order sinusoidal variations are ignored. This postulates a small value for the index of modulation. The first order sinusoidal variations are found by imposing charge conservation, a linear constitutive equation for the drift and the diffusion current, Poisson's equation for the electric field, and that electron creation is proportional to light intensity times the number of unionized donors, whereas

recombination is proportional to the number of electrons times the number of ionized donors. The light intensity is assumed to be large enough that thermal generation of conduction band electrons can be ignored. The electric field variation, with phase relative to the interference pattern is

$$E_1 = \left(\frac{I_1}{I_0}\right)\frac{\left(\frac{i \cdot K \cdot k_T}{q} - E_0\right)}{\left(1 + \frac{K^2}{k_D^2} + \frac{i \cdot q \cdot K \cdot E_0}{k_t \cdot k_d^2}\right)} \quad . \tag{1}$$

To get to this point, it was also assumed that $\gamma_R N_A >> s\, I_0$ and $N_D s\, I_0 << \gamma_R N_A^2$.

Notice that, according to this simplified picture, the amplitude of the field variation is proportional to the modulation index; it does not depend on the overall light intensity. Of course, for the analysis to be valid, I_0 must be large enough for photo-ionization to dominate thermal ionization and small enough for the inequalities of the above paragraph to apply. Finally, to get the form of k_D reported in the symbol table, it was assumed that $N_D >> N_A$. When there is no external field applied, the field is ninety degrees out-of-phase with the intensity modulation. If k_D is small compared to K, E_1 is proportional to k_D. Adding the external DC field increases the magnitude of E_1 and moves the phase away from 90 degrees.

The next chapter in the two wave mixing story relates the conversion of the regular electric pattern into an index of refraction grating. In photorefractive crystals, electric fields induce a change in dielectric constant. The linear part of this interaction is expressed in terms of

the electro-optic coefficients, r_{ij}. For crystals of cubic symmetry (the subject of this exercise) there is one significant, non-zero component ($r_{4,1}$). Referenced to the principal coordinates of the PRC, the relation between the change in the permittivity tensor and the electric field can be written as (Yeh 1993)

$$\Delta\varepsilon = -\varepsilon_0 n^4 \begin{vmatrix} 0 & r_{41}E_z & r_{41}E_y \\ r_{41}E_z & 0 & r_{41}E_x \\ r_{41}E_y & r_{41}E_x & 0 \end{vmatrix}. \qquad (2)$$

So, the sinusoidally varying electric field produced by an interference of coherent light beams (and influenced by the applied electric field) as in Equation 1 causes a sinusoidally varying grating in permittivity to be established in the cubic PRC as expressed in Equation 2. A regular permittivity grating will diffract light. In first order diffraction theory, the wave vector of the diffracted light must equal the wave vector of the incoming light plus the wave vector of the grating. Since the grating is the result of the interference between the two incoming beams, the grating wave vector is the difference in the wave vectors of the incoming beams. Therefore, the PRC grating will diffract light between the two incoming beams. It mixes the signals. As two mixing waves progress through the PRC a rather complex, self-diffraction interaction ensues. Through diffraction, energy is exchanged between the two paths; the resulting adjustment in intensities affects the diffraction grating through the index of modulation term in Equation 1, and the diffraction interaction is altered.

Consider two plane waves propagating in a PRC at an equal (but opposite) angle (θ) to a face of the PRC as in Figure 2.6.22. Let ESs and ESp represent the amplitude components s of

one of the beams (the signal beam) polarized perpendicular to the plane of incidence and in the plane of incidence respectively. The two pump beam components are denoted by EPs and EPp. The differential equations (Yeh 1993) for the change in field amplitudes due to two wave mixing can be written as

$$\frac{dESs}{dx} = \left(\frac{i}{2k\cos(\theta)}\right) e^{i\phi} \left(\Lambda ss \cdot EPs + \Lambda spp \cdot EPp\right) \frac{I_1}{I_0},$$

$$\frac{dESp}{dx} = \left(\frac{i}{2k\cos(\theta)}\right) e^{i\phi} \left(\Lambda pss \cdot EPs + \Lambda pspp \cdot EPp\right) \frac{I_1}{I_0},$$

$$\frac{dEPs}{dx} = \left(\frac{i}{2k\cos(\theta)}\right) e^{-i\phi} \left(\Lambda ss \cdot ESs + \Lambda sps \cdot ESp\right) \frac{I_1^*}{I_0},$$

$$\frac{dEPp}{dx} = \left(\frac{i}{2k\cos(\theta)}\right) e^{-i\phi} \left(\Lambda pps \cdot ESs + \Lambda ppps \cdot ESp\right) \frac{I_1^*}{I_0}. \qquad (3)$$

The Λ tensor is defined as $-\omega^2 \mu \varepsilon_0 |\Delta\varepsilon|$. Each Λ coefficient in Equation 3 represents the operation of the Λ tensor on a unit vector in the direction of the polarization of the component by which it is multiplied and a unit vector of the polarization of the component on the left hand side of the equation. For example, Λpss is Λ operating of a unit vector with s polarization direction and a unit vector with direction of p polarization of the signal beam. Given the initial values of the internal incoming polarizations of the pump and signal beams, Equation 3 can used to integrate the two wave mixing process through the PRC.

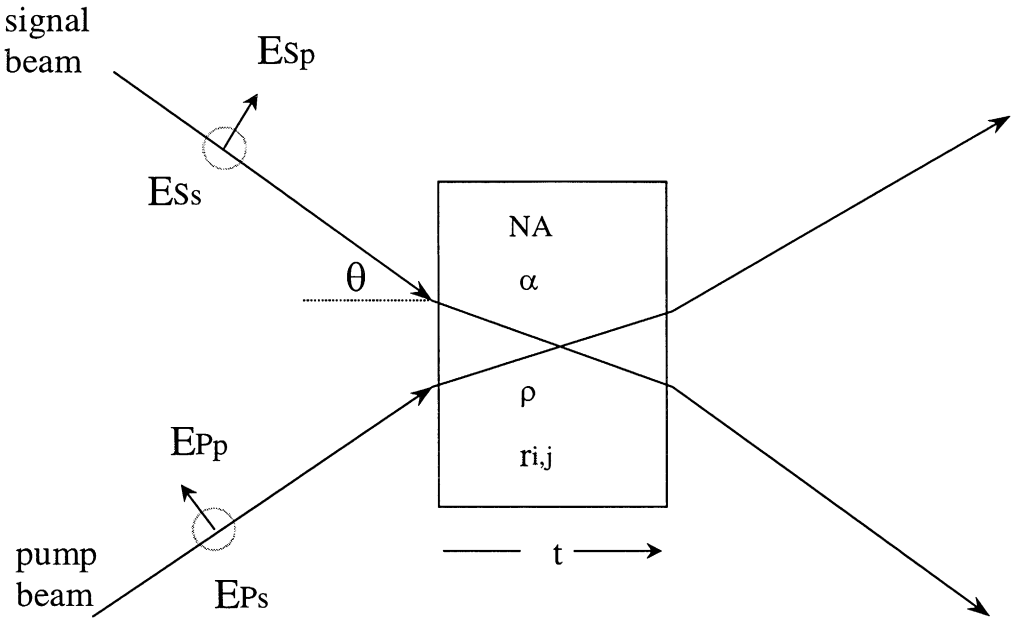

Figure 2.6.22 Two wave mixing in photorefractive crystals.

In addition to two wave mixing, propagation across the cubic PRC is influenced by attenuation and by rotation of the polarization. Attenuation is accounted for in the differential equations by subtracting a term on the right hand side of Equation 3 proportional to the amplitude of the component. The common cubic PRC's are optically active. There is a uniform rotation of polarization with propagation through the PRC (Yeh 1993). This is accounted for by adding an increment of the opposite polarization to each polarization component as it progresses. The full set of equations including mixing, attenuation and rotation are:

$$\frac{dESs}{dx} = \left(\frac{1}{2k\cos(\theta)}\right)\left[i \cdot e^{i\phi}\left(\Lambda ss \cdot EPs + \Lambda spp \cdot EPp\right)\frac{I_1}{I_0} - \alpha \cdot k \cdot ESs - 2k \cdot \rho \cdot ESp\right],$$

$$\frac{dESp}{dx} = \left(\frac{1}{2k\cos(\theta)}\right)\left[i \cdot e^{i\phi}\left(\Lambda pss \cdot EPs + \Lambda pspp \cdot EPp\right)\frac{I_1}{I_0} - \alpha \cdot k \cdot ESp + 2k \cdot \rho \cdot ESs\right],$$

$$\frac{dEPs}{dx} = \left(\frac{1}{2k\cos(\theta)}\right)\left[i \cdot e^{-i\phi}\left(\Lambda ss \cdot ESs + \Lambda sps \cdot ESp\right)\frac{I_1^*}{I_0} - \alpha \cdot k \cdot EPs - 2k \cdot \rho \cdot EPp\right],$$

$$\frac{dEPp}{dx} = \left(\frac{1}{2k\cos(\theta)}\right)\left[i \cdot e^{-i\phi}\left(\Lambda pps \cdot ESs + \Lambda ppps \cdot ESp\right)\frac{I_1^*}{I_0} - \alpha \cdot k \cdot EPp + 2k \cdot \rho \cdot EPs\right]. \quad (4)$$

Equations 4 are the basic two wave mixing non-linear coupled differential equations (with attenuation and rotation). They are numerically integrated using MathCad software on a PC. The non-linearity comes from the dependence of the index of modulation (I_1/I_0) on the field amplitudes. As, mathematically, light progresses through the PRC, I_1/I_0 must be updated in the numerical integration routine.

To perform an integration run, the initial values of the polarization components, the PRC coefficients, and the parameters of the experimental set up are input to the computer. The integration proceeds and results are reported as a function of the integration length (thickness of the PRC). For each thickness, the intensity of the signal and pump beams are calculated so that the relative response of the photo-detectors on the backside of the PRC can be determined. Sometimes, the output amplitudes are projected to the direction of a polarizer then added before the intensities are calculated. This demonstrates the considerable influence of output polarizers in two wave mixing (and later on in ultrasonic signal detection).

2.6.3.3.4 Validation of Two Wave Mixing Model

There are published experimental data on two wave mixing in cubic BSO crystals (Webb et al. 1994). The model described above will be justified by reference to these results. In

addition to experimental results, the same authors present analytical solutions of the two wave mixing equations in cubic crystals. Ignoring attenuation, but including rotation, they use a perturbation expansion to linearize the differential equations and integrate, ignoring the higher order terms included in my numerical model. Their correspondence of theory to experiment is evidence that the simplified theory of two wave mixing, with its many approximations, is useful in standard BSO crystals.

The crystal and experimental parameters necessary to make an integration are: n, ε, α, ρ, ω, θ, N_A, E_o, $r_{4,1}$, t, the incoming field amplitudes and polarizations, and the orientations of the crystal axes. With one exception, all these are known or readily measured. The effective number of acceptor sites per unit volume (N_A) is not easily established. Thus, the verification process allows the fitting of theory to experiment by adjusting N_A. If a single N_A can force correspondence for a large number of experimental set-ups, the theory is considered appropriate for the PRC under examination for that "effective N_A".

The degree of two wave mixing is often quantified through a two wave mixing gain determination. This gain is defined as the difference between the intensities at the output with and without two wave mixing divided by the intensity with no mixing. Intensities without mixing are experimentally obtained by noting the intensity of one output path when the other is temporarily blocked from entering the crystal. Theoretically, the no-mixing intensity is found by integrating Equation 4 separately with the Λ terms set to zero. Webb et al. (1994) determined the gain as a function of input polarization, then compared experiment and theory. They did this for both "longitudinal" and "transverse" mixing. With proper alignment of the crystal axes to experimental coordinates, some of the Λ terms in Equation 4 become zero. When

Λspp, Λpss, Λsps, and Λpps are zero, the mixing is said to be longitudinal. It is transverse when Λss, Λpspp, and Λppps are eliminated. These are rather fundamentally different types of mixing because in one case, like polarizations of the pump and signal beams mix, whereas in the other, normal polarizations mix. The alignment of theory and experiment over the range of input polarization for both longitudinal and transverse mixing is a good demonstration of a model.

A printout of the two wave mixing MathCad program used to simulate Webb et al. (Webb et al. 1994) type experiments is included as Section 2.6.3.3.10. It is well documented, and one can easily associate steps in the above theoretical discussion with the corresponding program commands. Figure 3 from Webb et al. (1994) corresponds to Figure 2.6.23 in this work; this presents their longitudinal two wave mixing experimental and theoretical results with N_A optimized at $3.5 \times 10^{21}/m^3$. Results from this work follow as Figure 2.6.24 (N_A was maintained at the same value). Notice that the correspondence is pretty good. Apparently, the neglect by Webb et al. (1994) of second order terms and any mistake made here are not significant in this case. Webb et al. (1994) do not consider the influence of light attenuation on the gain. Separate runs (not shown) made with non-zero a's verify, as expected, that attenuation has little effect on the two wave mixing gain. The transverse runs from Webb et al. (1994) and from the new program are documented as Figures 2.6.25 and 2.6.26, respectively. The agreement is also good this time. The reason for the minor differences is that the new program accounts for the change of index of modulation through the PRC, whereas Webb et al. (1994) keep it at its front-side value. In the 2 mm travel of the beam across the PRC, the new calculations generate variations in index of modulation of around 5%. Better matches with experimental data could have been achieved by adjusting N_A, but it's probably not worth the

effort. All and all, the demonstration appears satisfactory and ready to proceed to ultrasonic signal calculations.

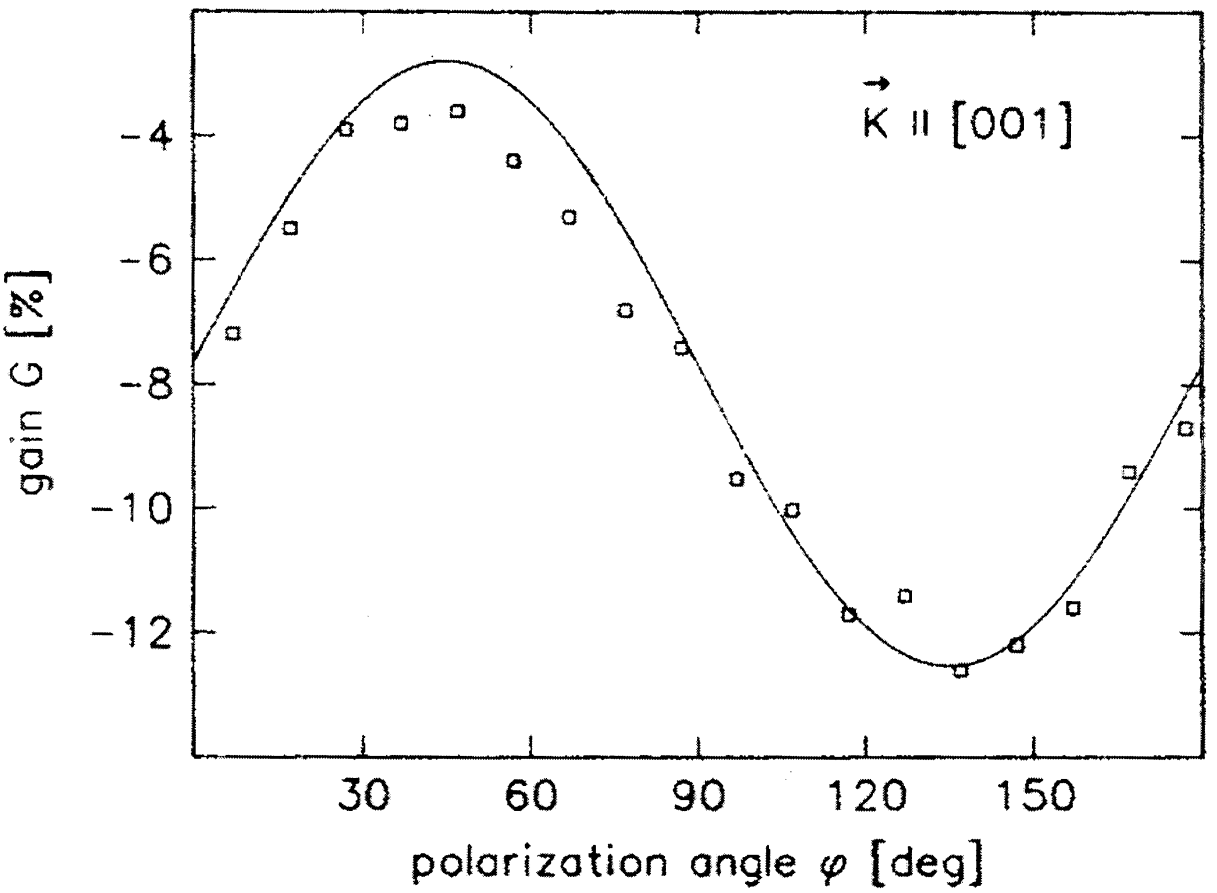

Figure 2.6.23 Gain as a function of polarization angle (φ) for θ=23°, I = 1.6 mW/cm^2, I_1/I_2 = 50 and N_t = 3.5 x 10^{21} m^{-3}. Reproduced from Webb et al. (1994).

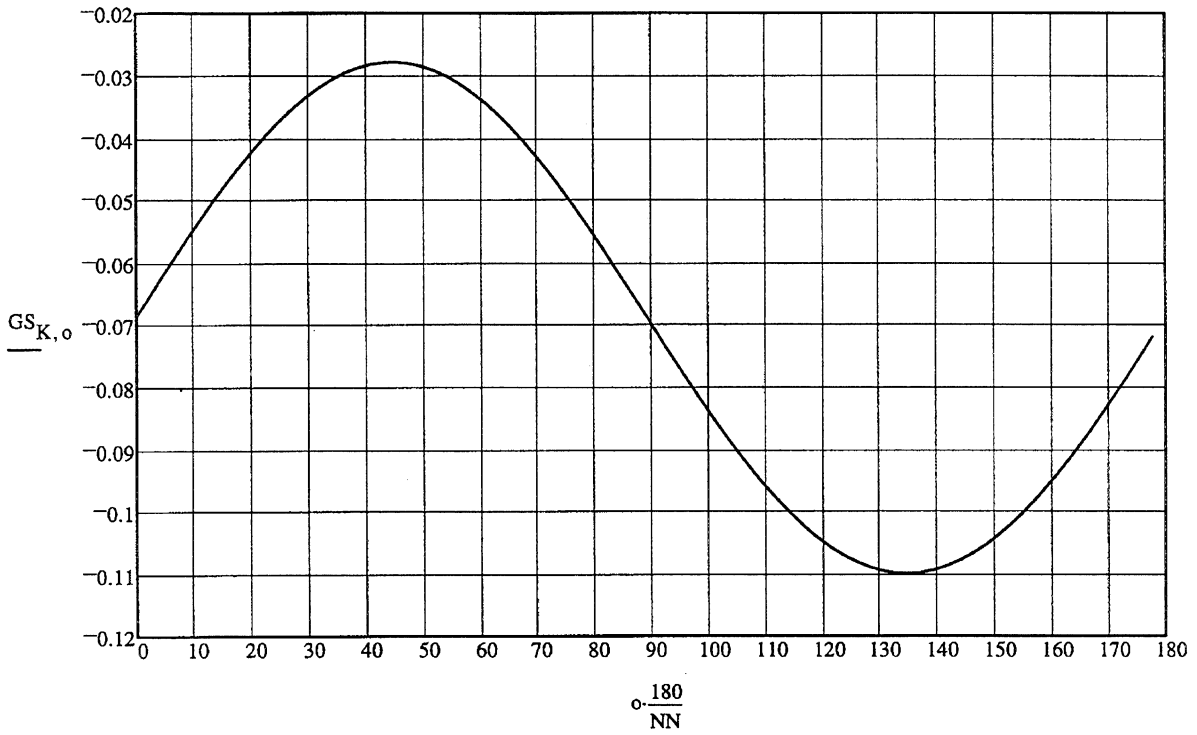

Plot of two wave mixing gain vs. polarization of incoming pump and signal beams relative to s polarization

$NA = 3.5 \times 10^{21}$	number of acceptor sites per m^3	$r_{4,1} = 4.5 \times 10^{-12}$	electro-optical coefficient
$n = 2.54$	PRC index of refraction	$\alpha = 0$	optical attenuation coefficient in 1/m
$\varepsilon = 56$	PRC dielectric constant	$tt = 2 \times 10^{-3}$	plotted PRC thickness in m
$\lambda_o = 0.514$	laser free space wavelength in microns	$t = 0.01$	maximum thickness calculated
$\rho_o = 45$	optical active param in degree/mm	$\theta_o = 23$	angle of incoming radiation to PRC normal in degrees
$IS = 1$	Input intensity of signal beam	$N = 200$	number of integration steps
$IP = 50$	Input intensity of pump beam		

$$R_{xo} = \begin{pmatrix} -1 \\ 1 \\ 0 \end{pmatrix} \qquad R_{yo} = \begin{pmatrix} 0 \\ 0 \\ 1 \end{pmatrix} \qquad R_{zo} = \begin{pmatrix} 1 \\ 1 \\ 0 \end{pmatrix}$$

Orientation of the PRC crystal axes

$\Lambda ss = 2.236 \times 10^9$	$\Lambda pss = 0$	$\Lambda ss = 2.236 \times 10^9$	$\Lambda pps = 0$
$\Lambda spp = 0$	$\Lambda pspp = 5.292 \times 10^7$	$\Lambda sps = 0$	$\Lambda ppps = 5.292 \times 10^7$

Figure 2.6.24 MathCad run meant to be compared with Webb et al. (1994) in Figure 2.6.23.

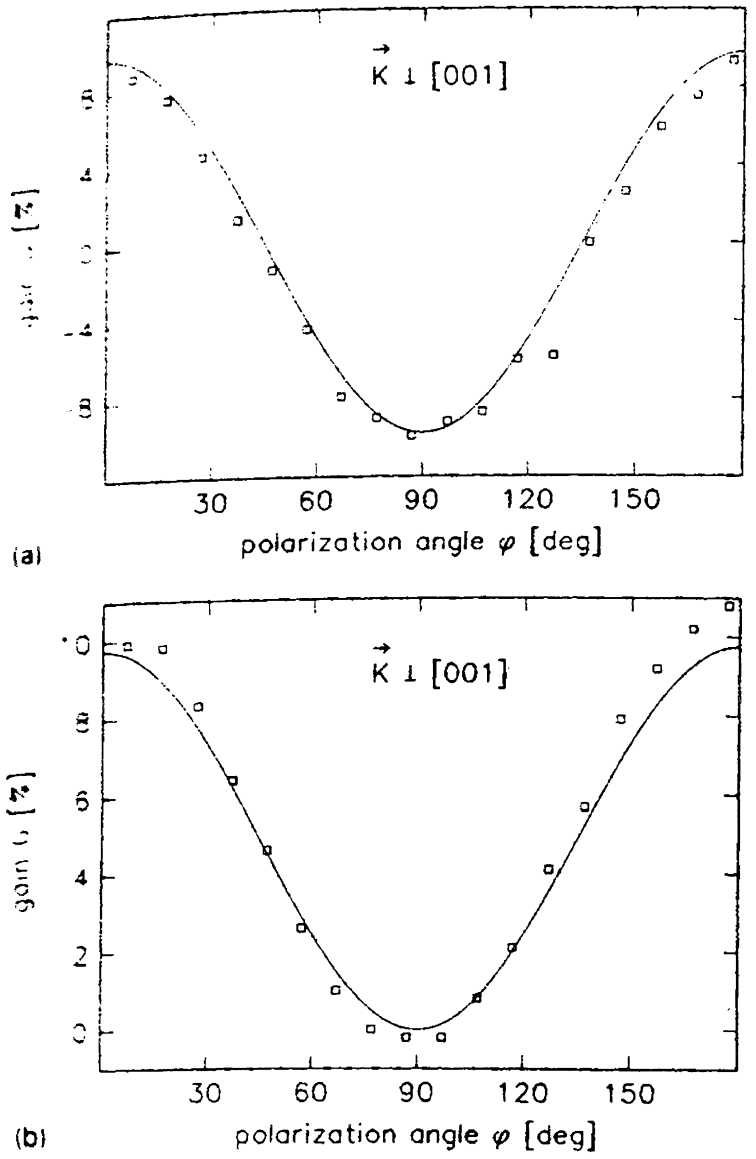

Figure 2.6.25 Gain [%] as a function of polarization angle (φ) for θ=23°, I_1/I_2=50; (a) $\varphi_1=\varphi_2=\varphi$, (b) $\varphi_1=0$, $\varphi_2=\varphi$. Reproduced from Webb et al. (1994).

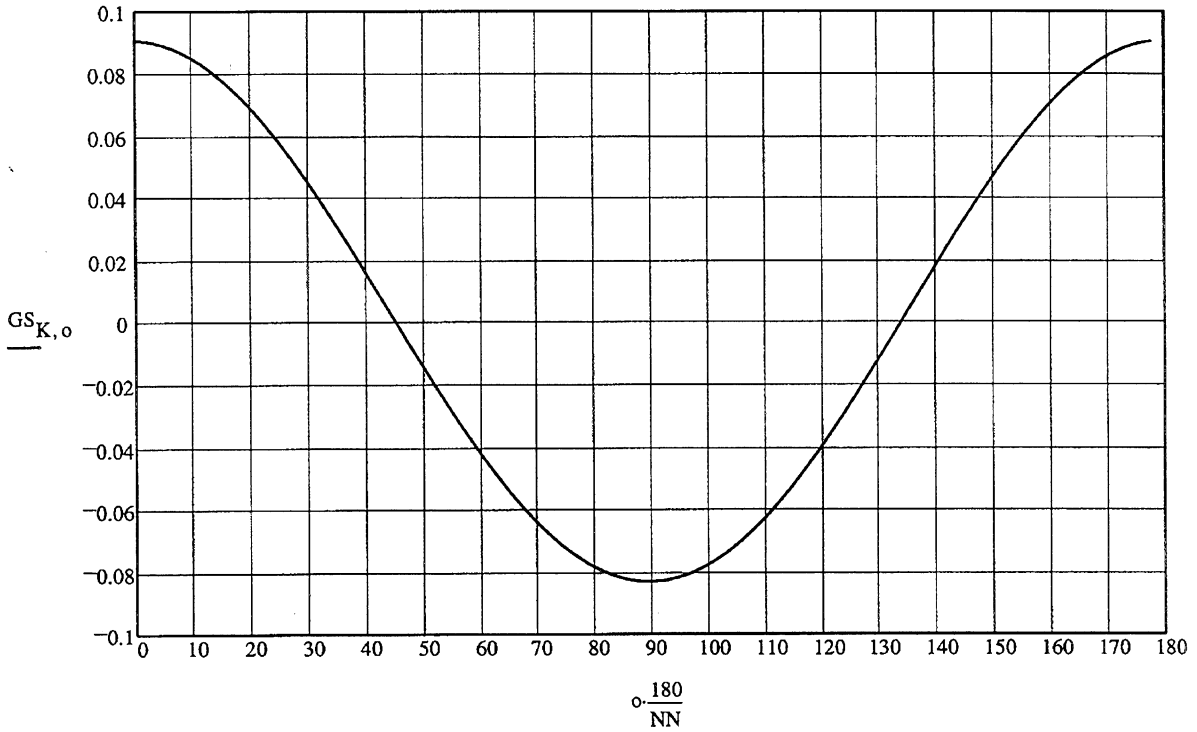

Plot of two wave mixing gain vs. polarization of incoming pump and signal beams relative to s polarization

$NA = 3.5 \times 10^{21}$	number of acceptor sites per m^3	$r_{4,1} = 4.5 \times 10^{-12}$	electro-optical coefficient
$n = 2.54$	PRC index of refraction	$\alpha = 0$	optical attenuation coefficient in 1/m
$\varepsilon = 56$	PRC dielectric constant	$tt = 2 \times 10^{-3}$	plotted PRC thickness in m
$\lambda_o = 0.514$	laser free space wavelength in microns	$t = 0.01$	maximum thickness calculated
$\rho_o = 45$	optical active param in degree/mm	$\theta_o = 23$	angle of incoming radiation to PRC normal in degrees
$IS = 1$	Input intensity of signal beam	$N = 200$	number of integration steps
$IP = 50$	Input intensity of pump beam		

$$R_{xo} = \begin{pmatrix} 1 \\ -1 \\ 0 \end{pmatrix} \qquad R_{yo} = \begin{pmatrix} 1 \\ 1 \\ 0 \end{pmatrix} \qquad R_{zo} = \begin{pmatrix} 0 \\ 0 \\ 1 \end{pmatrix}$$

Orientation of the PRC crystal axes

$\Lambda ss = 0$	$\Lambda pss = 2.21 \times 10^9$	$\Lambda ss = 0$	$\Lambda pps = 2.21 \times 10^9$
$\Lambda spp = 2.21 \times 10^9$	$\Lambda pspp = 0$	$\Lambda sps = 2.21 \times 10^9$	$\Lambda ppps = 0$

Figure 2.6.26 MathCad run to be compared with Webb et al. (1994) as in Figure 2.6.25.

2.6.3.3.5 Modeling of Ultrasonic Signal Generation in a Two Wave Mixing PRC

Except for a minor addition of second-order, non-linear terms to the two wave mixing integration, nothing new is presented here. Extension of the analysis to the determination of ultrasonic signals in PRC is the intended contribution of this work. The approach used will be presented in some detail for critique.

Ultrasonic signals are detected in two wave mixing experiments by reflecting one of the beams off surface of the disturbed sample. This causes a transient phase shift in the "signal" beam which changes the output of a photodetector on the backside of the PRC. The time constant (τ) for the formation of the index of refraction gratings is on the order of a millisecond in standard PRC's. The grating can adapt to input phase movements that last a long time relative to τ. These just move the grating a little, and there is no change in output intensities. On the other hand, when the signal phase movement is rapid, as it is when modulated by ultrasonic signals, the grating cannot keep up. Roughly speaking, the output of the signal beam is an interference between a straight-through signal and a signal diffracted from the pump beam. The ultrasonic signal affects the phase of the straight-through part only. This changes the interference between the two signal components and alters the intensity at the face of the photodetector. Therefore, it seems that ultrasonic signal detection should be handled mathematically in the following steps. First, as above, calculate the intensity at the photo-diode from two wave mixing. Compute a phase shift corresponding to twice the amplitude of the ultrasonic displacement. Then, add this phase shift to the signal beam at the input. Integrate the field amplitudes of the pump and signal beams across the PRC, again. The ultrasonic phase occurred too quickly for the grating to adjust, so, this time, do not recalculate the index of

modulation at each position. In the second integration, simply use the index of modulation as a function of distance that was determined in the first integration. At the detector, this will give a new intensity and a new output. The ultrasonic signal is the intensity calculated in the second integration minus the intensity of the first integration.

One example of a MathCad program that implements the above scheme is presented as Section 2.6.3.3.11. As before, the program is fairly well documented, and one should be able to identify the intended task of each command. In this case, the program was written to calculate the ultrasonic signals resulting from transverse two wave mixing as a function of PRC thickness for a range of applied DC fields. There is no polarizer before the photodiode. For PRC depths at which an appreciable signal is possible, notice (Section 2.6.3.3.11) that the applied field gives a dramatic boost to the ultrasonic signal. For the parameters entered, the effect peaks out at about 6,000 V/cm. Without a backside polarizer, the PRC performance depends greatly on the PRC thickness. The influence of polarizers will be documented later, but first how the PRC coefficients were determined experimentally is explained.

2.6.3.3.6 Determination of BSO PRC coefficients

One of the objectives of this exercise is to model the performance of the two BSO crystals on-hand at IPST (a 2.25 mm thick crystal and a 5.0 mm thick crystal). There are a large number of PRC setup adjustments in the detection of ultrasonic signals. These include: pump and signal beam input polarizations; Bragg angle; applied field; orientation of the PRC crystal axes; and output polarizer orientation. Before one can recommend specific procedures, one needs to know the PRC parameters. The dielectric constant, the index of refraction, and the

electro-optic coefficient have established values. No attempt to measure these was made; values were simply copied from reference book values: $\varepsilon = 56$, $n = 2.54$, and $r_{4,1} = 5 \times 10^{-12}$ m/V. Three other parameters (the rotation coefficient, ρ, the attenuation coefficient, α, and the effective number density of donor sites, N_A) vary with PRC manufacture and are subject to determination experimentally.

Redundant determinations of α were made by measuring single-beam reflection and transmission coefficients at different incident angles to the normal of the PRC. The procedure was different for the two crystals since one (5.0 mm) had an anti-reflective coating, whereas the other (2.25 mm) was not coated. For the 2.25 mm PRC, Fresnel's equations were used to calculate the plane reflection coefficients. The intensities of the multiple reflections across the PRC were added to find the total transmission and reflection as a function of α. Experiments were performed at 0, 10, and 25 degrees, giving five (no R determination at 0 degrees was feasible) separate measures. The result was $\alpha = 3.3$ (+- 0.1) cm^{-1}. The other PRC was over double the thickness and had an anti-reflection coating. The contributions from multiple reflections were easily shown to be negligible. α was calculated as the logarithm of the transmitted intensity divided by the incident intensity less the reflected intensity all divided through by the PRC propagation distance. It was found that $\alpha = 2.5$ cm^{-1}.

Optically active rotation coefficients were calculated from measurement of rotation of polarization through the PRC at different Bragg angles. For the 2.25 mm, the influence of multiple reflections was included; for the 5 mm PRC it was not. The results are: 2.25 mm PRC, $\rho = 40.0$ (+-1) degree/mm; 5.0 mm PRC, $\rho = 39.4$ (+-1) degree/mm.

The N_A determinations were somewhat ambiguous. Values were estimated by aligning measured two wave mixing gains with those generated by the two wave mixing program. There were a number of problems. To start with, the experimental orientation of the PRC axes was not well known. The gain measurements were not of sufficient accuracy to make precise determinations. In fact, often simple conservation arguments could demonstrate that there had to be large errors in the experimental gains. In the end, we were able to proscribe the N_A's to within a factor of two. We roughly determined that both PRC's had donor densities of 6×10^{21} donors/m^3. Since the two wave mixing parameters depend on the square root of N_A and since we are interested in rating competing experimental arrangements, we feel that this is sufficiently precise to give us valuable information in future modeling. More measurement details of the three parameters is available upon request.

2.6.3.3.7 The Influence of the Applied Electric Field

As a demonstration of utility, some application examples are presented. In the description of the ultrasonic signal program, you were teased with a graph showing that the influence of an applied field has a very strong, cyclic dependence on PRC thickness. There, the PRC parameters measured for the 2.25 mm crystal were used and demonstrated that the 2.25 mm was a very bad thickness choice. This was without a polarizer in front of the signal photodetector. The reason that PRCs of some thicknesses are insensitive is that the signal responses at different polarization are canceling out. By insertion of a polarizer, counteracting terms can be eliminated providing field-enhanced ultrasonic signals at all thicknesses. Take a look at Figures 2.6.27 and 2.6.28. There, a constant applied field level (1,000 V/cm) was chosen, and displayed is the ultrasonic signal strength as a function of the orientation of the output

polarizer to the s polarization direction and PRC thickness. Figure 2.6.27 is compiled with a pump and signal beam in s-polarization, whereas the common polarization is at 45 degrees in Figure 2.6.28. In both cases, it is assumed that the PRC was aligned for longitudinal two wave mixing. Now, by adjusting the output polarization one can get fairly strong ultrasonic signals at all thicknesses. Note, however, that in both cases it would have been better if the PRC were not grown as thick as 2.25 mm. Figure 2.6.29 and 2.6.30 are identical to Figures 2.6.27 and 2.6.28 respectively, except that the PRC orientation was changed from longitudinal to transverse. This time, the maximum signals are about 50% of the longitudinal values, and again 2.25 mm is not an optimum PRC thickness. Finally, a set of runs (Figures 2.6.31 and 2.6.32) was made with the PRC oriented half way between pure longitudinal and pure transverse. Comparatively, 2.25 mm looks better here, and the best polarizer orientation gives superior signal. Parenthetically, you are warned to beware when comparing experiment and theory for very thin PRC's. When the PRC is thin and attenuation across the crystal is not appreciable, multiple reflection back-and-forth across the PRC can contribute to the signal. The theory ignores multiple reflections, and (assuming α's of the order measured for the BSO PRC's) should be used with care for PRC's less than about 1.5 mm thick.

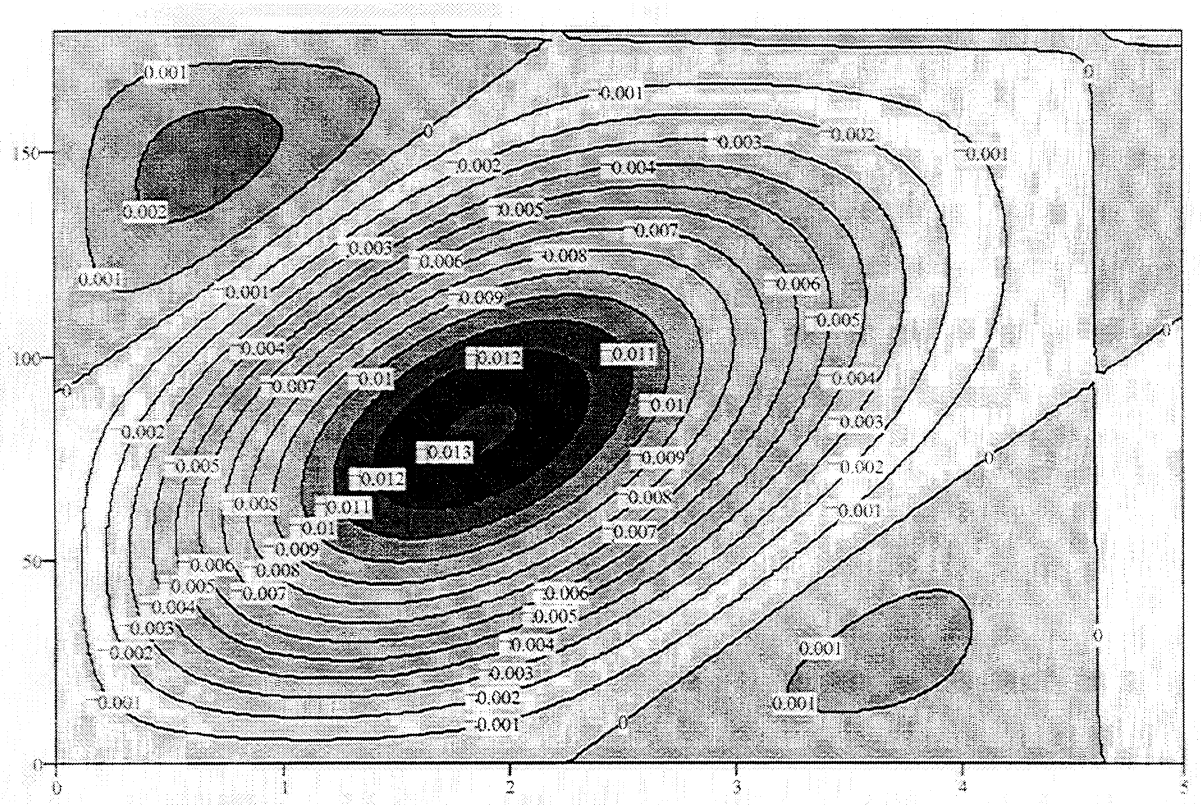

PIS

Intensity of the ultrasonic signal as a function of PRC thickness in mm and angle of exit polarizer to s direction in degrees

$ESs_{0,0} = 1$ $EPs_{0,0} = 3.162$ Input signal (S) and pump (P) field amplitudes for s (s) and p (p) polarizations $\Lambda ss = 3.659 \times 10^{9}$ $\Lambda pss = 0$ $ESp_{0,0} = 0$ $EPp_{0,0} = 0$ $\Lambda spp = 0$ $\Lambda pspp = 1.71 \times 10^{7}$

Orientation of the crystal axes with respect to propagation direction (x), diffraction grating direction (y), and normal to incidence plane (z)

$$R_{xo} = \begin{pmatrix} -1 \\ 1 \\ 0 \end{pmatrix} \quad R_{yo} = \begin{pmatrix} 0 \\ 0 \\ 1 \end{pmatrix} \quad R_{zo} = \begin{pmatrix} 1 \\ 1 \\ 0 \end{pmatrix}$$

$\theta_o = 10$ angle of incoming pump and signal beams to the PRC normal $\varepsilon = 56$ dielectric constant

$NA = 6 \times 10^{21}$ acceptor sites per m^3 $n = 2.54$ index of refraction

$r_{4,1} = 5 \times 10^{-12}$ electro-optical coeff $a = 10$ ultrasonic amplitude in nanometers $N = 100$

$E_o = 1 \times 10^{5}$ electric field in V/m $\alpha = 330$ attenuation coefficient in 1/m $NN = 80$

$t = 5 \times 10^{-3}$ max thickness in m $\rho_o = 40$ rotation coefficient in degrees/mm

Figure 2.6.27 MathCad run. Ultrasonic signal strength as a function of the orientation of the output polarizer to the s polarization direction and PRC thickness with a constant applied field level of 1,000 V/cm. Pump and signal beam in s-polarization with PRC aligned for longitudinal two wave mixing.

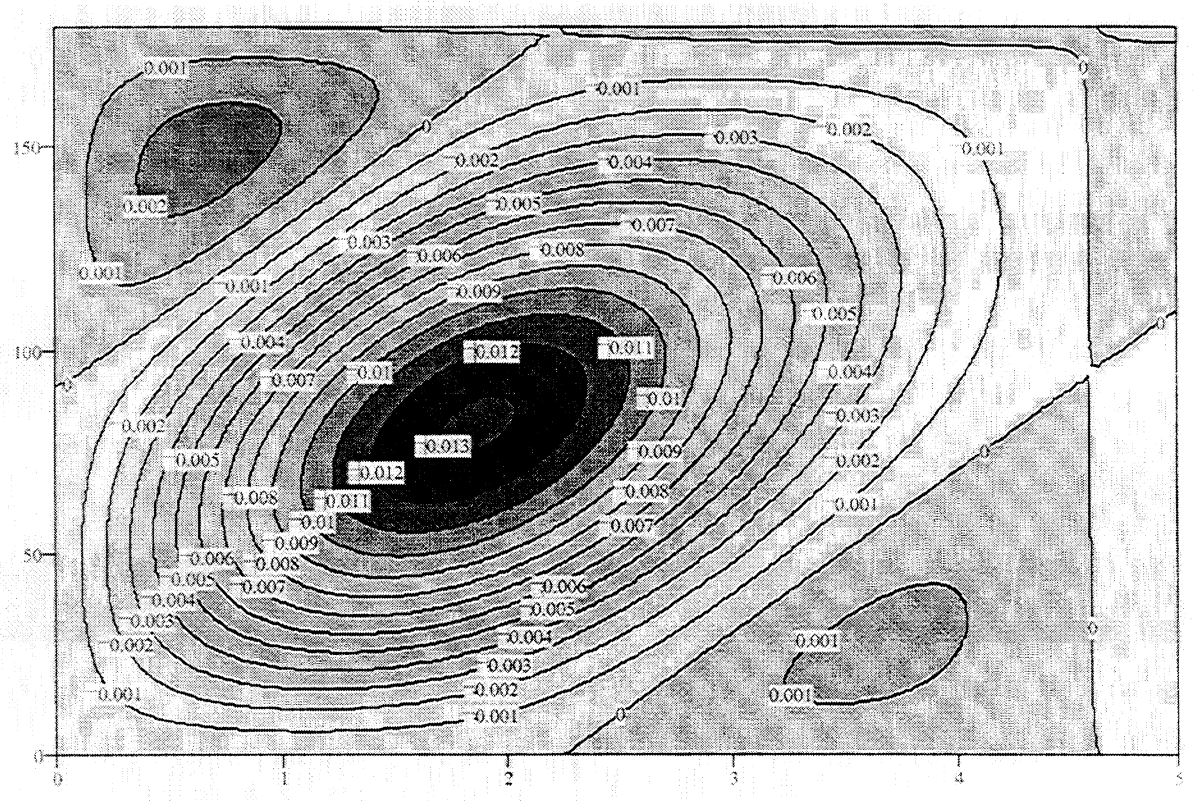

PIS
Intensity of the ultrasonic signal as a function of PRC thickness in mm and angle of exit polarizer to s direction in degrees

$ESs_{0,0} = 1$	$EPs_{0,0} = 3.162$	Input signal (S) and pump (P) field amplitudes for s (s) and p (p)	$\Lambda ss = 0$	$\Lambda pss = 3.65 \times 10^{9}$
$ESp_{0,0} = 0$	$EPp_{0,0} = 0$	polarizations	$\Lambda spp = 3.65 \times 10^{9}$	$\Lambda pspp = 0$

Orientation of the crystal axes with respect to propagation direction (x), diffraction grating direction (y), and normal to incidence plane (z)

$$R_{xo} = \begin{pmatrix} 1 \\ -1 \\ 0 \end{pmatrix} \qquad R_{yo} = \begin{pmatrix} 1 \\ 1 \\ 0 \end{pmatrix} \qquad R_{zo} = \begin{pmatrix} 0 \\ 0 \\ 1 \end{pmatrix}$$

$\theta_o = 10$	angle of incoming pump and signal beams to the PRC normal	$\varepsilon = 56$	dielectric constant		
$NA = 6 \times 10^{21}$	acceptor sites per m^3			$n = 2.54$	index of refraction
$r_{4,1} = 5 \times 10^{-12}$	electro-optical coeff	$a = 10$	ultrasonic amplitude in nanometers		$N = 100$
$E_o = 1 \times 10^{5}$	electric field in V/m	$\alpha = 330$	attenuation coefficient in 1/m		$NN = 80$
$t = 5 \times 10^{-3}$	max thickness in m	$\rho_o = 40$	rotation coefficient in degrees/mm		

Figure 2.6.28 MathCad run. Ultrasonic signal strength as a function of the orientation of the output polarizer to the s polarization direction and PRC thickness with a constant applied field level of 1,000 V/cm. Pump and signal beam at 45 degree polarization with PRC aligned for longitudinal two wave mixing.

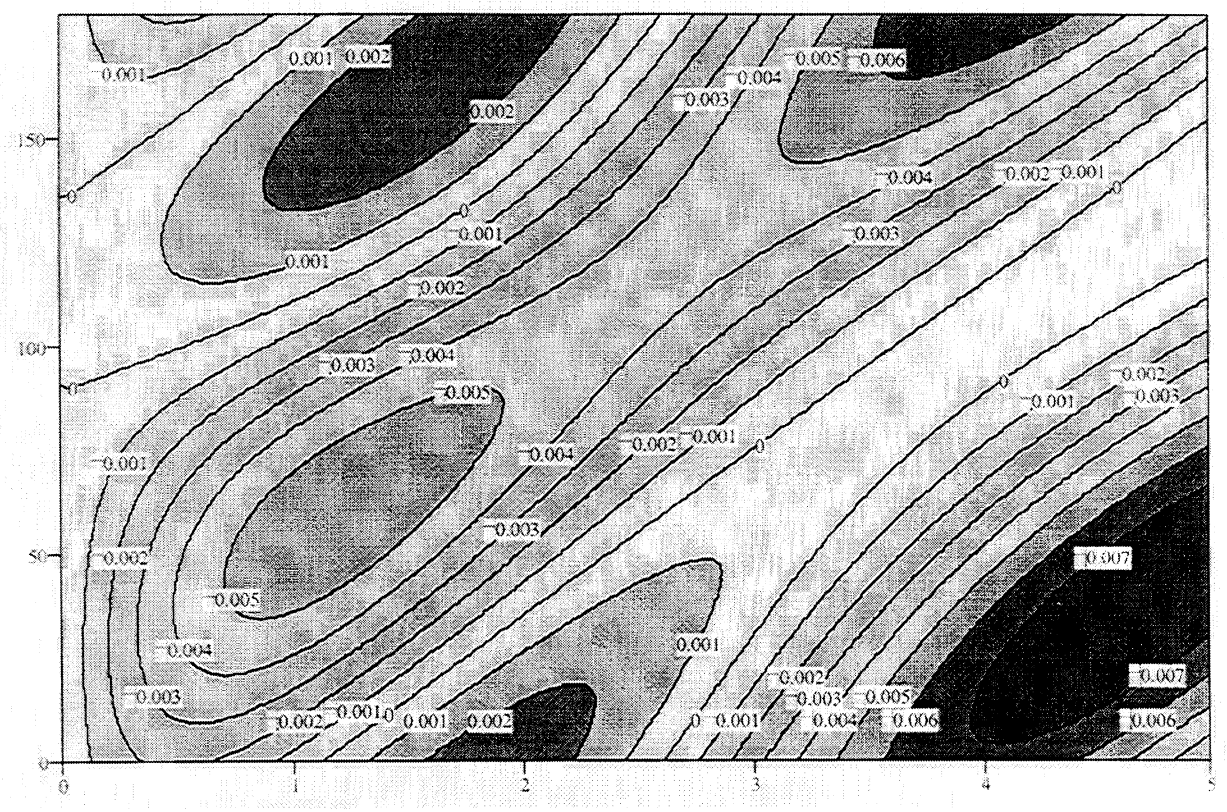

PIS
Intensity of the ultrasonic signal as a function of PRC thickness in mm and angle of exit polarizer to s direction in degrees

$ESs_{0,0} = 0.707$	$EPs_{0,0} = 2.236$	Input signal (S) and pump (P) field amplitudes for s (s) and p (p)	$\Lambda ss = 3.659 \times 10^{9}$	$\Lambda pss = 0$
$ESp_{0,0} = 0.707$	$EPp_{0,0} = 0.707$	polarizations	$\Lambda spp = 0$	$\Lambda pspp = 1.81 \times 10^{7}$

Orientation of the crystal axes with respect to propagation direction (x), diffraction grating direction (y), and normal to incidence plane (z)

$$R_{xo} = \begin{pmatrix} -1 \\ 1 \\ 0 \end{pmatrix} \quad R_{yo} = \begin{pmatrix} 0 \\ 0 \\ 1 \end{pmatrix} \quad R_{zo} = \begin{pmatrix} 1 \\ 1 \\ 0 \end{pmatrix}$$

$\theta_o = 10$	angle of incoming pump and signal beams to the PRC normal		$\varepsilon = 56$	dielectric constant	
$NA = 6 \times 10^{21}$	acceptor sites per m^3		$n = 2.54$	index of refraction	
$r_{4,1} = 5 \times 10^{-12}$	electro-optical coeff	$a = 10$	ultrasonic amplitude in nanometers		$N = 100$
$E_o = 1 \times 10$	electric field in V/m	$\alpha = 330$	attenuation coefficient in 1/m		$NN = 80$
$t = 5 \times 10^{-3}$	max thickness in m	$\rho_o = 40$	rotation coefficient in degrees/mm		

Figure 2.6.29 MathCad run. Ultrasonic signal strength as a function of the orientation of the output polarizer to the s polarization direction and PRC thickness with a constant applied field level of 1,000 V/cm. Pump and signal beam in s-polarization with PRC aligned for transverse two wave mixing.

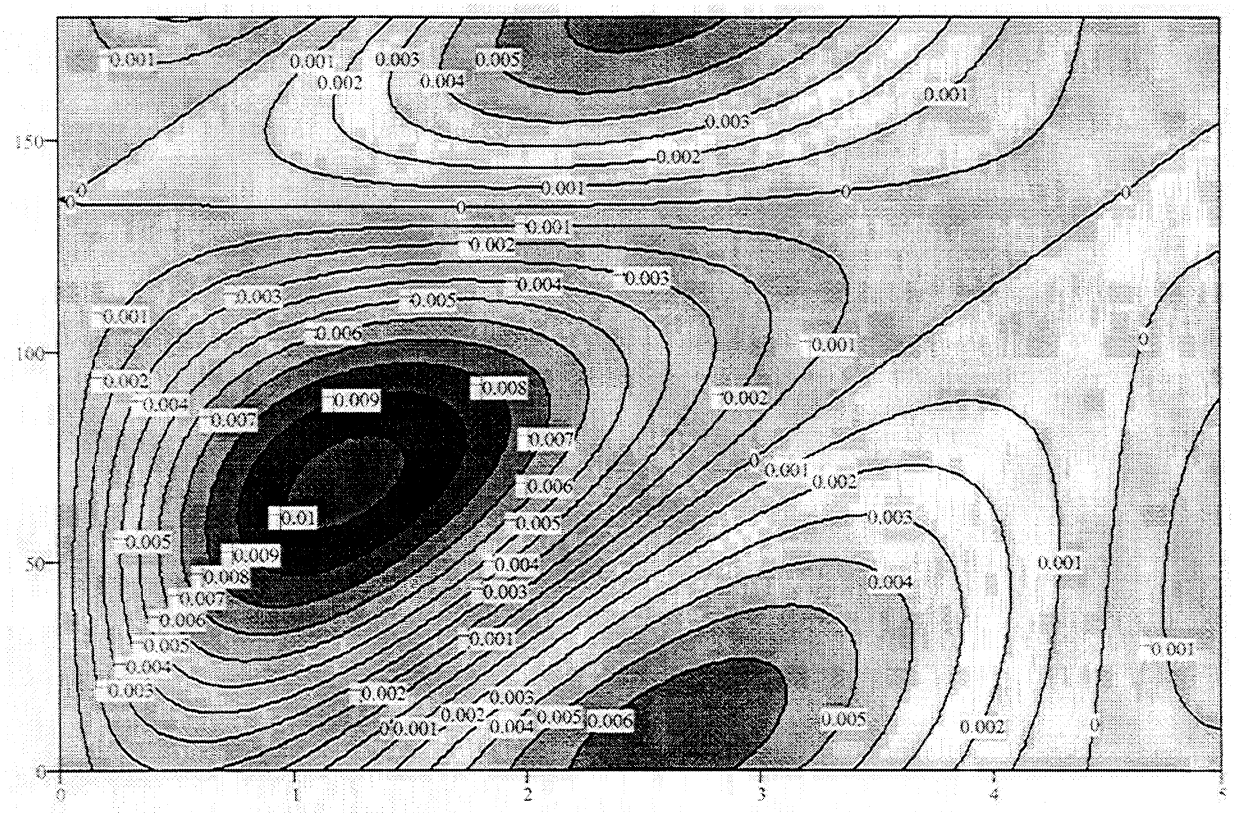

PIS

Intensity of the ultrasonic signal as a function of PRC thickness in mm and angle of exit polarizer to s direction in degrees

$ESs_{0,0} = 0.707$	$EPs_{0,0} = 2.236$	Input signal (S) and pump (P) field amplitudes for s (s) and p (p)	$\Lambda ss = 0$	$\Lambda pss = 3.65 \times 10^{9}$
$ESp_{0,0} = 0.707$	$EPp_{0,0} = 2.236$	polarizations	$\Lambda spp = 3.65 \times 10^{9}$	$\Lambda pspp = 0$

Orientation of the crystal axes with respect to propagation direction (x), diffraction grating direction (y), and normal to incidence plane (z)

$$R_{xo} = \begin{pmatrix} 1 \\ -1 \\ 0 \end{pmatrix} \quad R_{yo} = \begin{pmatrix} 1 \\ 1 \\ 0 \end{pmatrix} \quad R_{zo} = \begin{pmatrix} 0 \\ 0 \\ 1 \end{pmatrix}$$

$\theta_o = 10$	angle of incoming pump and signal beams to the PRC normal			$\varepsilon = 56$	dielectric constant
$NA = 6 \times 10^{21}$	acceptor sites per m^3			$n = 2.54$	index of refraction
$r_{4,1} = 5 \times 10^{-12}$	electro-optical coeff	$a = 10$	ultrasonic amplitude in nanometers		$N = 100$
$E_o = 1 \times 10^{5}$	electric field in V/m	$\alpha = 330$	attenuation coefficient in 1/m		$NN = 80$
$t = 5 \times 10^{-3}$	max thickness in m	$\rho_o = 40$	rotation coefficient in degrees/mm		

Figure 2.6.30 MathCad run. Ultrasonic signal strength as a function of the orientation of the output polarizer to the s polarization direction and PRC thickness with a constant applied field level of 1,000 V/cm. Pump and signal beam at 45 degree polarization with PRC aligned for transverse two wave mixing.

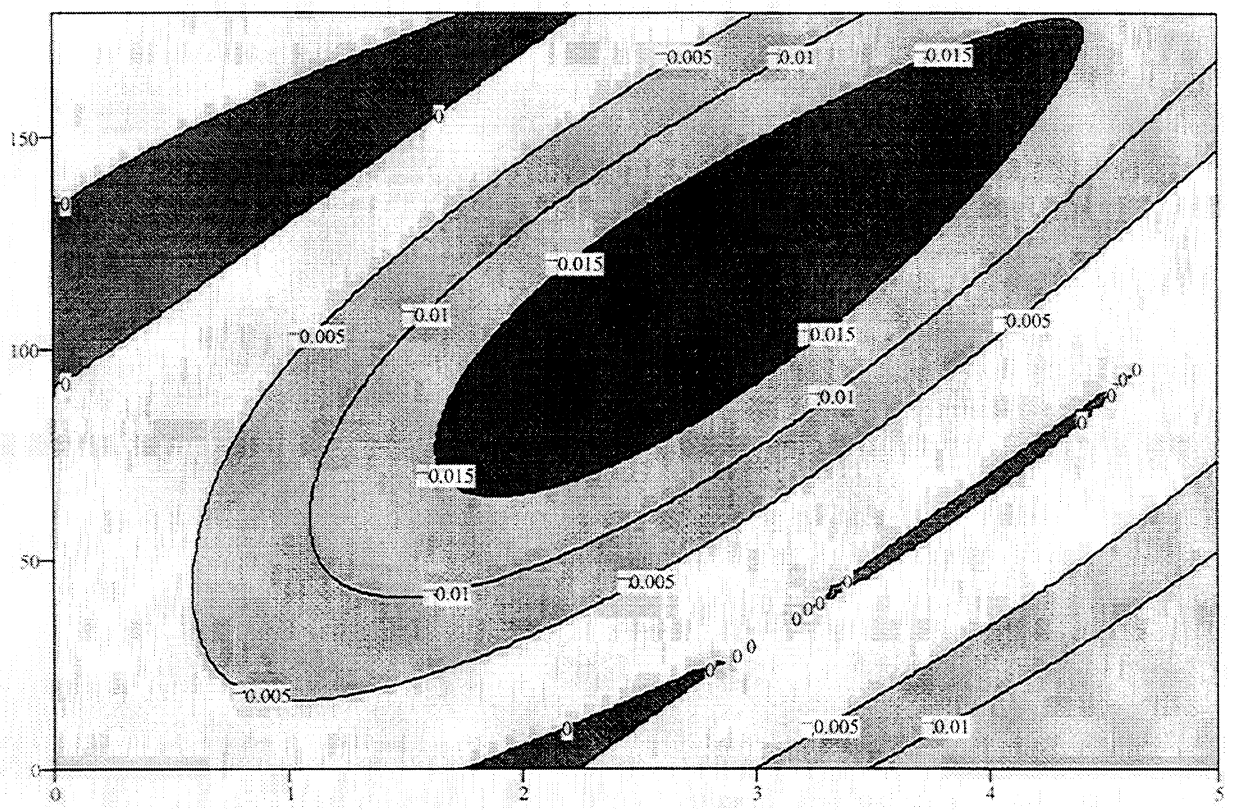

PIS

Intensity of the ultrasonic signal as a function of PRC thickness in mm and angle of exit polarizer to s direction in degrees

$ESs_{0,0} = 1$	$EPs_{0,0} = 3.162$	Input signal (S) and pump (P) field amplitudes for s (s) and p (p)	$\Lambda ss = 1.294 \times 10^{9}$	$\Lambda pss = 1.291 \times 10^{9}$
$ESp_{0,0} = 0$	$EPp_{0,0} = 0$	polarizations	$\Lambda spp = 1.291 \times 10^{9}$	$\Lambda pspp = 3.875 \times 10^{9}$

Orientation of the crystal axes with respect to propagation direction (x), diffraction grating direction (y), and normal to incidence plane (z)

$$R_{xo} = \begin{pmatrix} -1 \\ 1 \\ 0 \end{pmatrix} \quad R_{yo} = \begin{pmatrix} 1 \\ 1 \\ 1.414 \end{pmatrix} \quad R_{zo} = \begin{pmatrix} -1 \\ -1 \\ 1.414 \end{pmatrix}$$

$\theta_o = 10$	angle of incoming pump and signal beams to the PRC normal			$\varepsilon = 56$	dielectric constant
$NA = 6 \times 10^{21}$	acceptor sites per m^3			$n = 2.54$	index of refraction
$r_{4,1} = 5 \times 10^{-12}$	electro-optical coeff	$a = 10$	ultrasonic amplitude in nanometers		$N = 100$
$E_o = 1 \times 10^{5}$	electric field in V/m	$\alpha = 330$	attenuation coefficient in 1/m		$NN = 80$
$t = 5 \times 10^{-3}$	max thickness in m	$\rho_o = 40$	rotation coefficient in degrees/mm		

Figure 2.6.31 MathCad run. Ultrasonic signal strength as a function of the orientation of the output polarizer to the s polarization direction and PRC thickness with a constant applied field level of 1,000 V/cm. Pump and signal beam in s-polarization with PRC aligned half way between longitudinal and transverse two wave mixing.

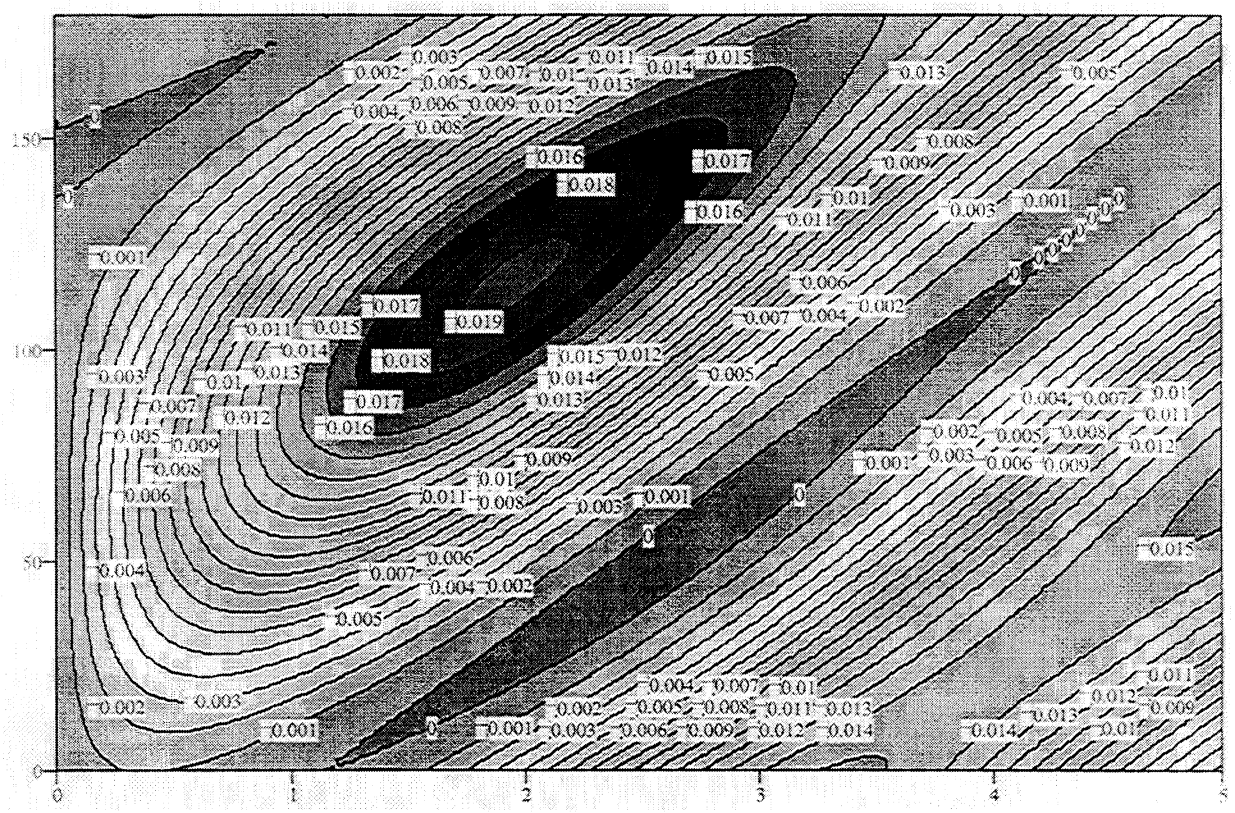

PIS
Intensity of the ultrasonic signal as a function of PRC thickness in mm and angle of exit polarizer to s direction in degrees

$ESs_{0,0} = 0.707$	$EPs_{0,0} = 2.236$	Input signal (S) and pump (P) field amplitudes for s (s) and p (p)	$\Lambda ss = 1.294 \times 10^{9}$	$\Lambda pss = 1.291 \times 10^{9}$
$ESp_{0,0} = 0.707$	$EPp_{0,0} = 2.236$	polarizations	$\Lambda spp = 1.291 \times 10^{9}$	$\Lambda pspp = 3.875 \times 10^{9}$

Orientation of the crystal axes with respect to propagation direction (x), diffraction grating direction (y), and normal to incidence plane (z)

$$R_{xo} = \begin{pmatrix} -1 \\ 1 \\ 0 \end{pmatrix} \quad R_{yo} = \begin{pmatrix} 1 \\ 1 \\ 1.414 \end{pmatrix} \quad R_{zo} = \begin{pmatrix} -1 \\ -1 \\ 1.414 \end{pmatrix}$$

$\theta_o = 10$	angle of incoming pump and signal beams to the PRC normal			$\varepsilon = 56$	dielectric constant
$NA = 6 \times 10^{21}$	acceptor sites per m^3			$n = 2.54$	index of refraction
$r_{4,1} = 5 \times 10^{-12}$	electro-optical coeff	$a = 10$	ultrasonic amplitude in nanometers		$N = 100$
$E_o = 1 \times 10^{5}$	electric field in V/m	$\alpha = 330$	attenuation coefficient in 1/m		$NN = 80$
$t = 5 \times 10^{-3}$	max thickness in m	$\rho_o = 40$	rotation coefficient in degrees/mm		

Figure 2.6.32 MathCad run. Ultrasonic signal strength as a function of the orientation of the output polarizer to the s polarization direction and PRC thickness with a constant applied field level of 1,000 V/cm. Pump and signal beam at 45 degree polarization with PRC aligned half way between longitudinal and transverse two wave mixing.

It is constructive to explain why an applied voltage augments the ultrasonic signal. Two wave mixing leads to ultrasonic signals because the output of the signal beam is really an interference between a diffracted pump beam and a straight-through signal beam. Changing the phase of the signal beam alters the interference and results in a change in the intensity at the photodiode. Look back at Equation 3. Without an applied field ϕ is 90 degrees (Equation 3). This makes the coefficient in front of the two wave term real. The diffracted wave is in-phase with the propagating wave, and two wave mixing is optimal. With $\phi = 0$, we are at a maximum in two wave mixing. To first order, an ultrasonic change in the phase of the signal beam does alter the magnitude of the signal beam diffracted; it makes changes at the photodiode only from the influence of the phase change on the interference with the diffracted beam. When an extra field is applied, ϕ deviates from 90 degrees (Equation 1). Notice that the effect increases as the magnitude of the grating wave vector (K) decreases at lower Bragg angles (θ). Now, to first order, the ultrasonic phase change does alter the magnitude of the diffracted signal beam. Phase and magnitude of the straight-through signal beam are both affected, and there is opportunity for greater ultrasonic signal.

2.6.3.3.8 The Influence of the Bragg Angle

Let's see what the Bragg angle does to the ultrasonic signal. For illustration, the program is set up for longitudinal two wave mixing on a PRC with the properties of our 2.25 mm BSO crystal. A 45 degree polarization was used for both signal and pump beams and the output looked at the ultrasonic signal with no polarizer. In Figure 2.6.33, the results with no applied electric field are shown. This time, the normalized ultrasonic signal intensity along with the

straight signal are plotted. If the noise on the RF signal is proportional to the DC signal level, the normalized signal gives a better estimate of expected signal-to-noise ratio. Please notice that the Bragg angle has very minor influence. Especially for the normalized calculation, very few contour lines are crossed in moving vertically on the plot. Figure 2.6.34 demonstrates the same process with an applied field of 2,000 V/cm. This time, E_o plays a major role. Incidence angles near the normal to the PRC surface clearly give stronger RF signals. This is because the shift in ϕ due to added E_o depends on the ratio of E_o to K, and K is smaller at smaller θ.

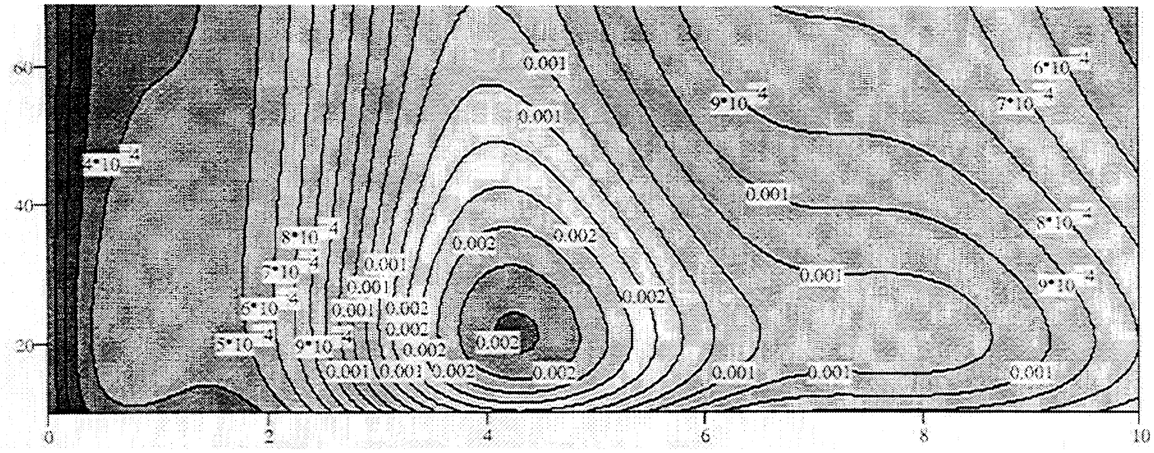

US

RF signal intensity as a result of the ultrasonic phase shift as function of PRC thickness in mm and Bragg angle in degrees (no output polarization)

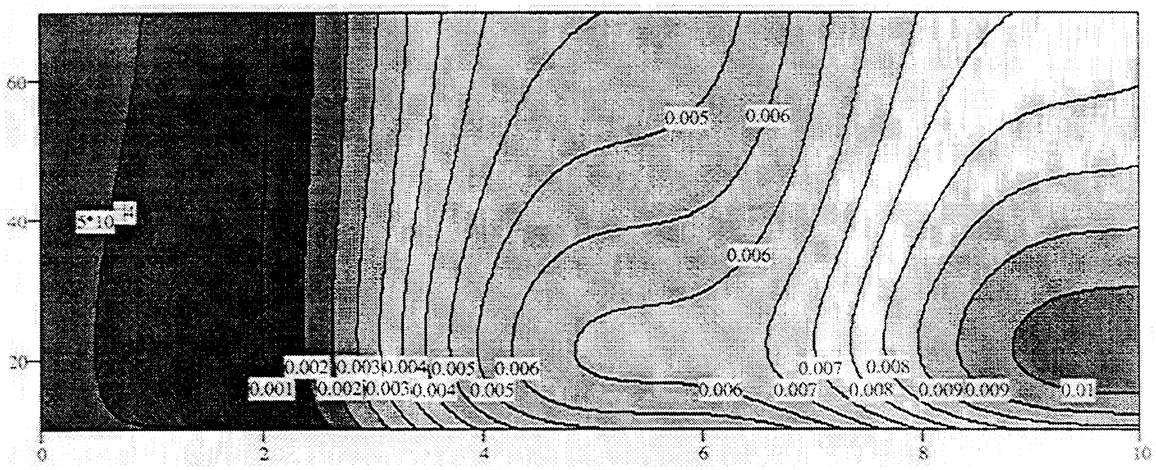

USN

RF signal intensity, normalized to no phase shift signal, as a result of the ultrasonic phase shift as function of PRC thickness in mm and Bragg angle in degrees (no output polarization)

NA = 6 x 10^{21}	number of acceptor sites per m^3	$r_{4,1}$ = 5 x 10^{-12}	electro-optical coefficient
n = 2.54	PRC index of refraction	α = 320	optical attenuation coefficient in1/m
ε = 56	PRC dielectric constant	t = 0.01	PRC thickness in m
E_o = 0	applied electric field V/m	ρ_o = 40	optical active param in degree/mm
$ESs_{0,0}$ = 0.707	$ESp_{0,0}$ = 0.707	Λss_0= 2.746 x 10^9	Λpss_0 = 0
$EPs_{0,0}$ = 2.236	$EPp_{0,0}$ = 2.236	Λspp_0 = 0	$\Lambda pspp_0$ = 1.238 x 10^7

Figure 2.6.33 Effect of the Bragg angle. The program is set up for longitudinal two wave mixing on a PRC with the properties of our 2.25 mm BSO crystal. A 45 degree polarization was used for both signal and pump beams and the output looked at the ultrasonic signal with no polarizer with no applied electric field.

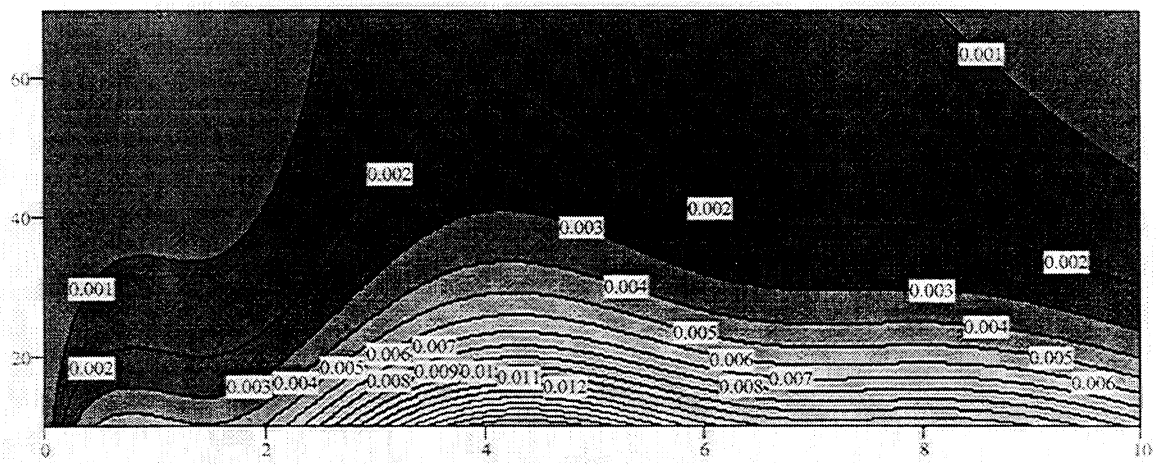

US

RF signal intensity as a result of the ultrasonic phase shift as function of PRC thickness in mm and Bragg angle in degrees (no output polarization)

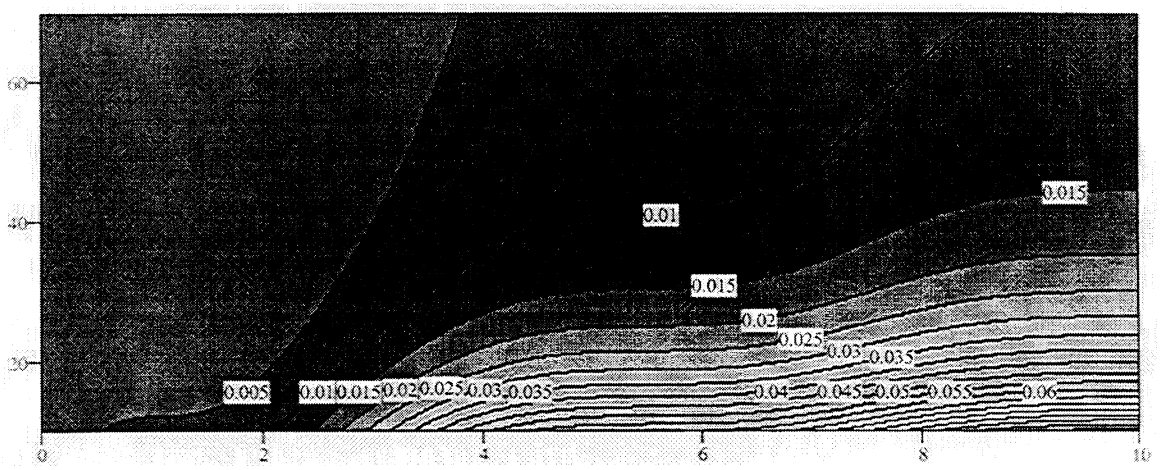

USN

RF signal intensity, normalized to no phase shift signal, as a result of the ultrasonic phase shift as function of PRC thickness in mm and Bragg angle in degrees (no output polarization)

$NA = 6 \times 10^{21}$ number of acceptor sites per m^3		$r_{4,1} = 5 \times 10^{-12}$	electro-optical coefficient
$n = 2.54$	PRC index of refraction	$\alpha = 320$	optical attenuation coefficient in1/m
$\varepsilon = 56$	PRC dielectric constant	$t = 0.01$	PRC thickness in m
$E_o = 2 \times 10^5$applied electric field V/m		$\rho_o = 40$	optical active param in degree/mm
$ESs_{0,0} = 0.707$	$ESp_{0,0} = 0.707$	$\Lambda ss_0 = 5.384 \times 10^9$	$\Lambda pss_0 = 0$
$EPs_{0,0} = 2.236$	$EPp_{0,0} = 2.236$	$\Lambda spp_0 = 0$	$\Lambda pspp_0 = 2.517 \times 10^7$

Figure 2.6.34 Effect of the Bragg angle. The program is set up for longitudinal two wave mixing on a PRC with the properties of our 2.25 mm BSO crystal. A 45 degree polarization was used for both signal and pump beams and the output looked at the ultrasonic signal with no polarizer with an applied electric field of 2000 V/cm.

2.6.3.3.9 Circular Polarization

Since the BSO crystal is optically active (linearly polarized radiation is rotated through propagation), the circular polarized plane waves are the normal modes of propagation. Circular polarized waves have this special distinction for the BSO crystal; therefore, ultrasonic detection with circular polarized radiation is of interest. Figures 2.6.35, 2.6.36, and 2.6.37 portray the ultrasonic signal as a function of PRC thickness and output polarizer angle for both input beams circularly polarized, the signal beam circularly polarized, and the pump beam circularly polarized, respectively. The other experimental parameters are the same as in Figure 2.6.27 and 2.6.29. Figure 2.6.27 gives the action for s polarized inputs, whereas Figure 2.6.29 reflects 45 degree polarization. When both inputs are circularly polarized, results are better than with 45 degree linear polarization and about as well as s polarization. Circular polarization on just one of the inputs (Figures 2.6.36 and 2.6.37) is not advised. All and all, the circular polarization arrangement seems to be satisfactory, but from this limited study it appears to be no great boon.

The three studies just discussed are intended to give the reader a feel for the utility of the program. Of course, many other investigations are possible.

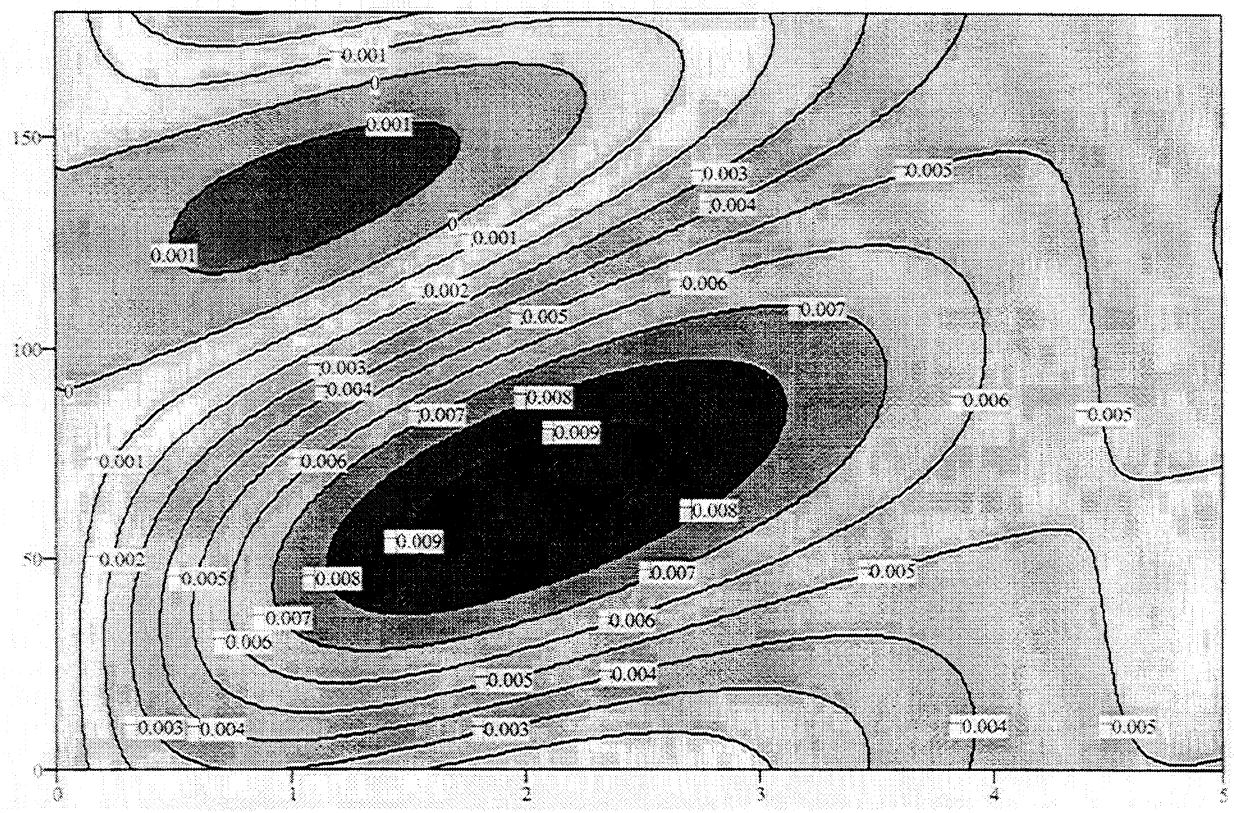

PIS

Intensity of the ultrasonic signal as a function of PRC thickness in mm and angle of exit polarizer to s direction in degrees

$ESs_{0,0} = 0.707$	$EPs_{0,0} = 2.236$	Input signal (S) and pump (P) field amplitudes for s (s) and p (p)	$\Lambda ss = 3.659 \times 10^{9}$	$\Lambda pss = 0$
$ESp_{0,0} = 0.707i$	$EPp_{0,0} = 2.236i$	polarizations	$\Lambda spp = 0$	$\Lambda pspp = 1.71 \times 10^{7}$

Orientation of the crystal axes with respect to propagation direction (x), diffraction grating direction (y), and normal to incidence plane (z)

$$R_{xo} = \begin{pmatrix} -1 \\ 1 \\ 0 \end{pmatrix} \quad R_{yo} = \begin{pmatrix} 0 \\ 0 \\ 1 \end{pmatrix} \quad R_{zo} = \begin{pmatrix} 1 \\ 1 \\ 0 \end{pmatrix}$$

$\theta_o = 10$	angle of incoming pump and signal beams to the PRC normal			$\varepsilon = 56$	dielectric constant
$NA = 6 \times 10^{21}$	acceptor sites per m^3			$n = 2.54$	index of refraction
$r_{4,1} = 5 \times 10^{-12}$	electro-optical coeff	$a = 10$	ultrasonic amplitude in nanometers		$N = 100$
$E_o = 1 \times 10^{5}$	electric field in V/m	$\alpha = 330$	attenuation coefficient in 1/m		$NN = 80$
$t = 5 \times 10^{-3}$	max thickness in m	$\rho_o = 40$	rotation coefficient in degrees/mm		

Figure 2.6.35 MathCad run. Ultrasonic signal as a function of PRC thickness and output polarizer angle for both input beams circularly polarized. The other experimental parameters are the same as in Figure 2.6.27 and 2.6.29.

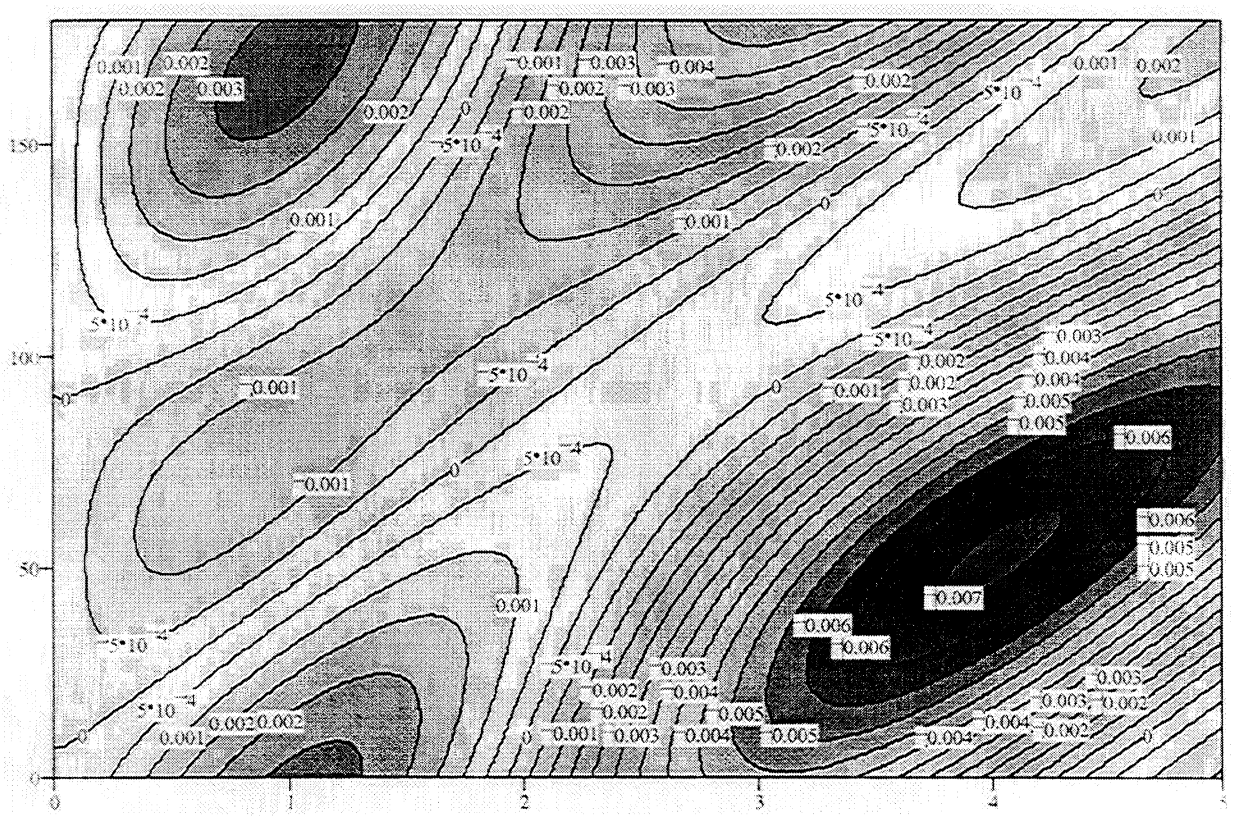

PIS

Intensity of the ultrasonic signal as a function of PRC thickness in mm and angle of exit polarizer to s direction in degrees

$ESs_{0,0} = 0.707$	$EPs_{0,0} = 2.236$	Input signal (S) and pump (P) field amplitudes for s (s) and p (p)	$\Lambda ss = 3.659 \times 10^{9}$	$\Lambda pss = 0$
$ESp_{0,0} = 0.707i$	$EPp_{0,0} = 2.236$	polarizations	$\Lambda spp = 0$	$\Lambda pspp = 1.71 \times 10^{7}$

Orientation of the crystal axes with respect to propagation direction (x), diffraction grating direction (y), and normal to incidence plane (z)

$$R_{xo} = \begin{pmatrix} -1 \\ 1 \\ 0 \end{pmatrix} \quad R_{yo} = \begin{pmatrix} 0 \\ 0 \\ 1 \end{pmatrix} \quad R_{zo} = \begin{pmatrix} 1 \\ 1 \\ 0 \end{pmatrix}$$

$\theta_o = 10$	angle of incoming pump and signal beams to the PRC normal			$\varepsilon = 56$	dielectric constant
$NA = 6 \times 10^{21}$	acceptor sites per m^3			$n = 2.54$	index of refraction
$r_{4,1} = 5 \times 10^{-12}$	electro-optical coeff	$a = 10$	ultrasonic amplitude in nanometers		$N = 100$
$E_o = 1 \times 10^{5}$	electric field in V/m	$\alpha = 330$	attenuation coefficient in 1/m		$NN = 80$
$t = 5 \times 10^{-3}$	max thickness in m	$\rho_o = 40$	rotation coefficient in degrees/mm		

Figure 2.6.36 MathCad run. Ultrasonic signal as a function of PRC thickness and output polarizer angle for the signal beam circularly polarized. The other experimental parameters are the same as in Figure 2.6.27 and 2.6.29.

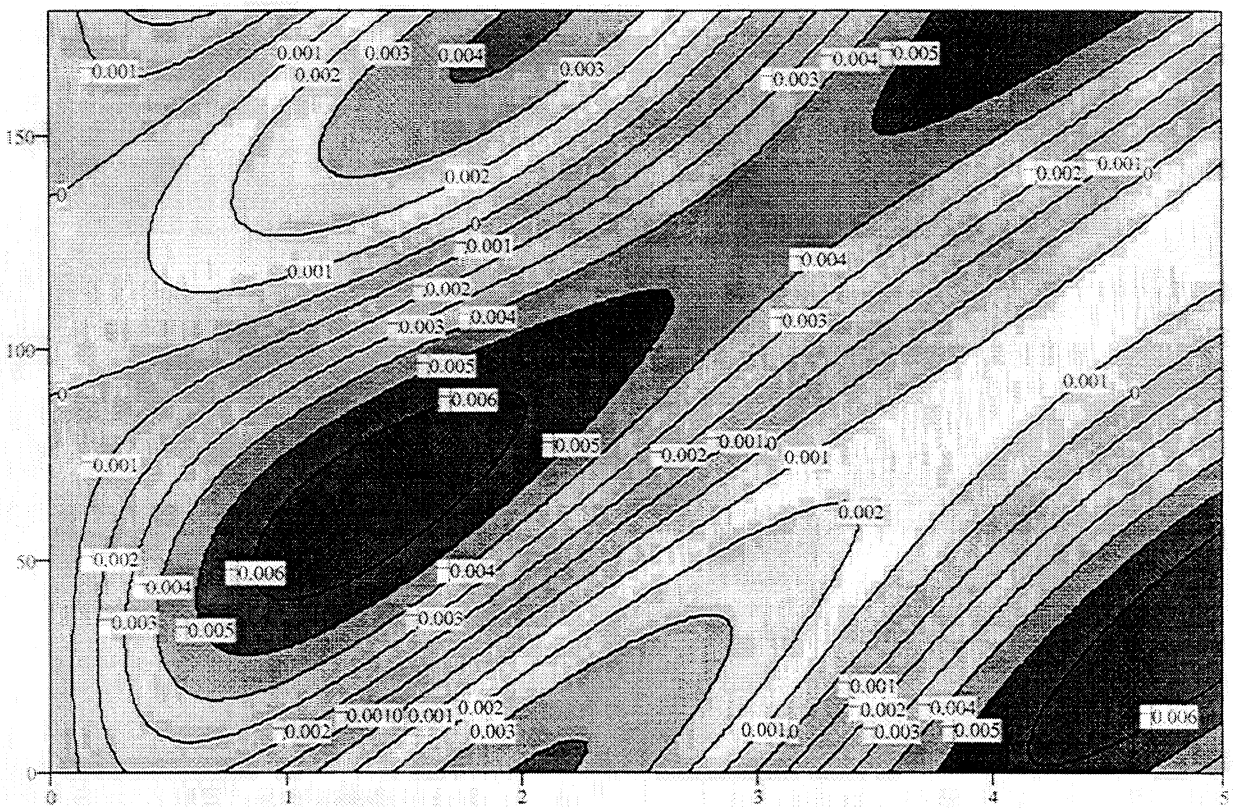

PIS

Intensity of the ultrasonic signal as a function of PRC thickness in mm and angle of exit polarizer to s direction in degrees

$ESs_{0,0} = 0.707$	$EPs_{0,0} = 2.236$	Input signal (S) and pump (P) field amplitudes for s (s) and p (p)	$\Lambda ss = 3.659 \times 10^{9}$	$\Lambda pss = 0$
$ESp_{0,0} = 0.707$	$EPp_{0,0} = 2.236i$	polarizations	$\Lambda spp = 0$	$\Lambda pspp = 1.71 \times 10^{7}$

Orientation of the crystal axes with respect to propagation direction (x), diffraction grating direction (y), and normal to incidence plane (z)

$$R_{xo} = \begin{pmatrix} -1 \\ 1 \\ 0 \end{pmatrix} \quad R_{yo} = \begin{pmatrix} 0 \\ 0 \\ 1 \end{pmatrix} \quad R_{zo} = \begin{pmatrix} 1 \\ 1 \\ 0 \end{pmatrix}$$

$\theta_o = 10$	angle of incoming pump and signal beams to the PRC normal			$\varepsilon = 56$	dielectric constant
$NA = 6 \times 10^{21}$	acceptor sites per m^3			$n = 2.54$	index of refraction
$r_{4,1} = 5 \times 10^{-12}$	electro-optical coeff	$a = 10$	ultrasonic amplitude in nanometers		$N = 100$
$E_o = 1 \times 10^{5}$	electric field in V/m	$\alpha = 330$	attenuation coefficient in 1/m		$NN = 80$
$t = 5 \times 10^{-3}$	max thickness in m	$\rho_o = 40$	rotation coefficient in degrees/mm		

Figure 2.6.37 MathCad run. Ultrasonic signal as a function of PRC thickness and output polarizer angle for the pump beam circularly polarized. The other experimental parameters are the same as in Figure 2.6.27 and 2.6.29.

2.6.3.3.10 MathCad program "PRCTWebb.mcd"

This program simulates two wave mixing in a cubic photo-refractive crystal. It is specifically written to check the PRC two wave mixing routine by comparing with published experimental data from Webb et al. (1994). The two wave mixing gain is the difference between intensity with and without two wave mixing divided by intensity without two wave mixing. The signal and pump gains are calculated as a function of incoming polarization (both pump and signal maintain the same polarization) and PRC thickness.

INTEGRATION PARAMETERS

N := 200	input the number of steps in the numerical integration
NN := 80	input the number of steps in the input polarizer rotation

PHYSCIAL CONSTANTS

i := i	make "i" the square root of minus 1
$\mu := 4\pi \cdot 10^{-7}$	permeability of free space in MKS units
$\varepsilon_0 := 8.854 \times 10^{-12}$	permittivity of free space in MKS units
$c_0 := \frac{1}{\sqrt{\mu\varepsilon_0}}$	velocity of light in free space
$k_B := 1.381 \times 10^{-23}$	Boltzman Constant in MKS units
$q := 1.602 \times 10^{-19}$	electronic charge in Coulombs

CRYSTAL PARAMETERS

n := 2.54	input PRC index of refraction at laser frequency (BSO = 2.54)
ε := 56	input PRC dielectric constant at RF frequencies (BSO = 56)
α := 0	input the exponential light absorption coefficient in unit of 1/cm
t := 10	input crystal thickness in mm
$NA := 3.5 \times 10^{15}$	input the number of acceptor sites per cubic centimeter of the PRC
$\rho_0 := 45$	input the optically active rotation coefficient in degrees per

mm

$\alpha := 100\,\alpha$ convert α to MKS units

$NA := NA \cdot 100^3$ convert NA to MKS

$t := \frac{t}{1000}$ convert t to MKS

$\rho := \rho_0\left(\frac{\pi}{180}\right)1000$ convert ρ to radians per m

EXPERIMENTAL PARAMETERS

$\theta_o := 10$ input angle of incidence in degrees of the incoming signal beam and pump beam to the normal of the crystal face

$\theta := \theta_o \frac{\pi}{180}$ convert θ to radians

$\theta := \sin^{-1}\left(\frac{\sin(\theta)}{n}\right)$ Use Snell's law to find convert to the angle inside the crystal

$\lambda_o := 0.5145$ input laser free-space wavelength in microns

$\lambda := \frac{\lambda_0 \cdot 10^6}{n}$ convert λ to wavelength inside the crystal in meters

$T := 300$ input absolute temperature in K

Set up iteration parameters for the applied fields, E_0

$P := 50$ input the number of applied field levels to be plotted

$E_{0max} := 10^6$ input the maximum applied electric field in V/m in the grating direction

$o := 0..(P-1)$ do the thickness integration for P applied fields

$E_{0_o} := E_{0max} \frac{o}{P-1}$ iterate E_0 from 0 to E_{max} in P steps

$ESs_{0,o} := \sqrt{0.5}$ Input the electric field amplitudes at the front face of the crystal. ESs is the initial component of the signal beam field polarized perpendicular to the plane of incidence; ESp is the signal field in the plane of incidence; EPs is the amplitude of the pump beam field perpendicular to the plane of

$ESp_{0,o} := \sqrt{0.5}$

$EPs_{0,o} := \sqrt{0.5}$

$EPp_{0,o} := \sqrt{0.5}$ incidence; and EPp is the initial pump field in the plane of incidence.

$$I_{0,o} := \frac{EPs_{0,o} \cdot \overline{ESs_{0,o}} + EPp_{0,o} \cdot \overline{ESp_{0,o}} \cdot \cos(2\theta)}{ESs_{0,o} \cdot \overline{ESs_{0,o}} + ESp_{0,o} \cdot \overline{ESp_{0,o}} + EPs_{0,o} \cdot \overline{EPs_{0,o}} + EPp_{0,o} \cdot \overline{EPp_{0,o}}}$$ calculate the initial modulation index

$k := 2\frac{\pi}{\lambda}$ calculate laser wave number

$\omega := \frac{2\pi c_o}{\lambda_0 \cdot 10^{-6}}$ calculate laser angular frequency in Hz

K := 2 k sin(θ) calculate the magnitude of the grating wave number

$k_T := k_B \cdot T$ calculate k_T

ELECTRO-OPTICAL COEFFICIENTS ENTERED BELOW

$r_{4,1} := 4.5 \times 10^{-12}$ please, input here the non-zero r coefficient in

$r_{5,2} := r_{4,1}$ MKS units (m/V) for the crystal of interest

$r_{6,3} := r_{4,1}$

DO THE CALCULATIONS

First specify the PRC crystal axis in terms of the natural experimental coordinates. For the experiment, the x-direction is normal to the illuminated face of the crystal; its positive direction is in the direction of propagation. The experimental y-direction is in the plane of incidence and normal to the x-axis. The experimental z-direction is perpendicular to the plane of incidence (in the s polarization direction); its orientation is determined by the right hand rule from the x and y axes. Input R_x, R_y, and R_z, where R_x is the crystal direction in the x-axis, R_y is the crystal axis along the y-axis, and R_z is the crystal axis along the z-axis.

please, input the Miller indices of the crystal axes in the experimental coordinates:

$$R_{xo} := \frac{R_{xo}}{|R_{xo}|} \qquad R_{yo} := \frac{R_{yo}}{|R_{yo}|} \qquad R_{zo} := \frac{R_{zo}}{|R_{zo}|}$$

normalize the crystal axes

$$R_{xo} := \begin{pmatrix} 1 \\ -1 \\ 0 \end{pmatrix} \quad R_{yo} := \begin{pmatrix} 1 \\ 1 \\ 0 \end{pmatrix} \quad R_{zo} := \begin{pmatrix} 0 \\ 0 \\ 1 \end{pmatrix}$$

creation of the orthogonal matrix that rotates the vectors from the experimental axes to the crystal axes

$$O := \begin{bmatrix} R_{x_0} & R_{y_0} & R_{z_0} \\ R_{x_1} & R_{y_1} & R_{z_1} \\ R_{x_2} & R_{y_2} & R_{z_2} \end{bmatrix}$$

Now, the electro-optical tensor is determined by user input of the standard two-dimensional electro-optical coefficients (Section 1.4 in Yeh book)

ESTABLISH THE INTEGRATION COEFFICIENTS

Convert the 2-D r matrix to a third order r tensor

$$r_3(u,v,w) := \delta(u,v)\cdot r_{u+1,w+1} + \delta(u+v,3)\cdot r_{4,w+1} + \left(\delta(|u-v|,2)\cdot r_{5,w+1} + \delta(u+v,1)\cdot r_{6,w+1}\right)$$

Calculate (Escmax) the proportionality constant between the space charge electric field and the ratio of grating intensity to total intensity

calculate the Debye wave number assuming ND >> NA, p89 Yeh

$$k_D := \sqrt{\frac{q^2 \cdot NA}{\varepsilon \cdot \varepsilon_0 \cdot k_T}} \qquad k_D = 6.613 \times 10^6$$

$$Escmax := \frac{\frac{i \cdot K \cdot k_T}{q} - E_0}{1 + \left(\frac{K}{k_D}\right)^2 + \frac{i \cdot q \cdot K \cdot E_0}{k_T \cdot k_D^2}} \qquad \phi := \arg(Escmax) \qquad Escmax = 8.006 \times 10^4 i$$

unit vector in the direction of the space charge field in experimental coordinate system

$$E := \begin{pmatrix} 0 \\ 1 \\ 0 \end{pmatrix}$$

unit vector perpendicular to the incidence place. This establishes the direction of the s-polarized wave component in experimental coordinates

$$s := \begin{pmatrix} 0 \\ 0 \\ 1 \end{pmatrix}$$

unit vector in the place of incidence and perpendicular to the direction of propagation of the pump beam. This establishes the direction of the p-polarized wave of the pump beam in experimental coordinates.

$$pp := \begin{bmatrix} -\sin(\theta) \\ \cos(\theta) \\ 0 \end{bmatrix}$$

along grating component of pump wave number

$$\beta p := k \cdot \cos(\theta)$$

unit vector in the plane of incidence and perpendicular to the direction of propagation of the signal beam. This establishes the direction of the p-polarized wave of the signal beam in experimental coordinates.

$$ps := \begin{bmatrix} \sin(\theta) \\ \cos(\theta) \\ 0 \end{bmatrix}$$

along grating component of signal wave number

$$\beta s := k \cdot \cos(\theta)$$

Express above unit vectors in the crystal coordinate system

ec := O·E sc := O·s ppc := O·pp psc := O·ps

CALCULATE THE DIFRACTION COUPLING COEFFICIENTS

mm := 0..2 nn := 0..2

$\Lambda_{mm,nn} := \omega^2 \cdot \mu \cdot \varepsilon_0 \cdot n^4 \cdot |Escmax| \cdot \sum_{k=0}^{2} r_3(mm, nn, k) \cdot ec_k$ Compute the Lambda tensor as in Yeh 4.4-7

$\Lambda ss := sc^T \cdot \Lambda \cdot sc$ $\Lambda pss := psc^T \cdot \Lambda \cdot sc$ $\Lambda ppps := ppc^T \cdot \Lambda \cdot psc$

$\Lambda sps := sc^T \cdot \Lambda \cdot psc$ $\Lambda spp := sc^T \cdot \Lambda \cdot ppc$ $\Lambda pspp := psc^T \cdot \Lambda \cdot ppc$ $\Lambda pps := ppc^T \cdot \Lambda \cdot sc$

j := 0..(N-1) set up iteration parameter

INTEGRATE NO TWO WAVE MIXING STATE

$$\begin{bmatrix} ESso_{j+1,o} \\ ESpo_{j+1,o} \\ EPso_{j+1,o} \\ EPpo_{j+1,o} \end{bmatrix} := \begin{bmatrix} ESso_{j,o} + \left(-\alpha \cdot ESso_{j,o} - 2\rho \cdot ESpo_{j,o}\right)\frac{1}{2\cos(\theta)} \cdot \frac{t}{N} \\ ESpo_{j,o} + \left(-\alpha \cdot ESpo_{j,o} + 2\rho \cdot ESso_{j,o}\right)\frac{1}{2\cos(\theta)} \cdot \frac{t}{N} \\ EPso_{j,o} + \left(-\alpha \cdot EPso_{j,o} - 2\rho \cdot EPpo_{j,o}\right)\frac{1}{2\cos(\theta)} \cdot \frac{t}{N} \\ EPpo_{j,o} + \left(-\alpha \cdot EPpo_{j,o} + 2\rho \cdot EPso_{j,o}\right)\frac{1}{2\cos(\theta)} \cdot \frac{t}{N} \end{bmatrix}$$

INTEGRATE TWO WAVE MIXING CASE

The first row in the expression below tracks the modulation index (I_1/I_0) through the PRC. The last four rows do the integration of field magnitudes for the signal and pump beam in the s and p polarizations. The first terms in the field increment expressions do the two-wave mixing the second accounts for PRC light attenuation, whereas the third does the optical active polarization rotation.

$$\begin{bmatrix} I_{j+1,o} \\ ESs_{j+1,o} \\ ESp_{j+1,o} \\ EPs_{j+1,0} \\ EPp_{j+1,o} \end{bmatrix} := \begin{bmatrix} \dfrac{EPs_{j,0}\cdot\overline{ESs_{j,o}} + EPp_{j,o}\cdot\overline{ESp_{j,o}}\cdot\cos(2\theta)}{ESs_{j,o}\cdot\overline{ESs_{j,o}} + ESp_{j,o}\cdot\overline{ESp_{j,o}} + EPs_{j,o}\cdot\overline{EPs_{j,o}} + EPp_{j,o}\cdot\overline{EPp_{j,o}}} \\ ESs_{j,o} + \left[\dfrac{i\cdot e^{-i\theta}}{k}\left(\Lambda ss\cdot EPs_{j,o} + \Lambda spp\cdot EPp_{j,o}\right)\overline{I_{j,o}} - \alpha\cdot ESs_{j,o} - 2\rho\cdot ESp_{j,o}\right]\dfrac{1}{2\cos(\theta)}\cdot\dfrac{t}{N} \\ ESp_{j,o} + \left[\dfrac{i\cdot e^{-i\theta}}{k}\left(\Lambda pss\cdot EPs_{j,o} + \Lambda pspp\cdot EPp_{j,o}\right)\overline{I_{j,o}} - \alpha\cdot ESp_{j,o} + 2\rho\cdot ESs_{j,o}\right]\dfrac{1}{2\cos(\theta)}\cdot\dfrac{t}{N} \\ EPs_{j,o} + \left[\dfrac{i\cdot e^{i\theta}}{k}\left(\Lambda ss\cdot ESs_{j,o} + \Lambda sps\cdot ESp_{j,o}\right)I_{j,o} - \alpha\cdot EPs_{j,o} - 2\rho\cdot EPp_{j,o}\right]\dfrac{1}{2\cos(\theta)}\cdot\dfrac{t}{N} \\ EPp_{j,o} + \left[\dfrac{i\cdot e^{i\theta}}{k}\left(\Lambda pps\cdot ESs_{j,o} + \Lambda ppps\cdot ESp_{j,o}\right)I_{j,o} - \alpha\cdot EPp_{j,o} + 2\rho\cdot EPs_{j,o}\right]\dfrac{1}{2\cos(\theta)}\cdot\dfrac{t}{N} \end{bmatrix}$$

$tt := 0.002$ input thickness for graphing in meters

$K := floor\left(\dfrac{tt}{t}N\right)$ calculate the value of j corresponding to thickness to be plotted

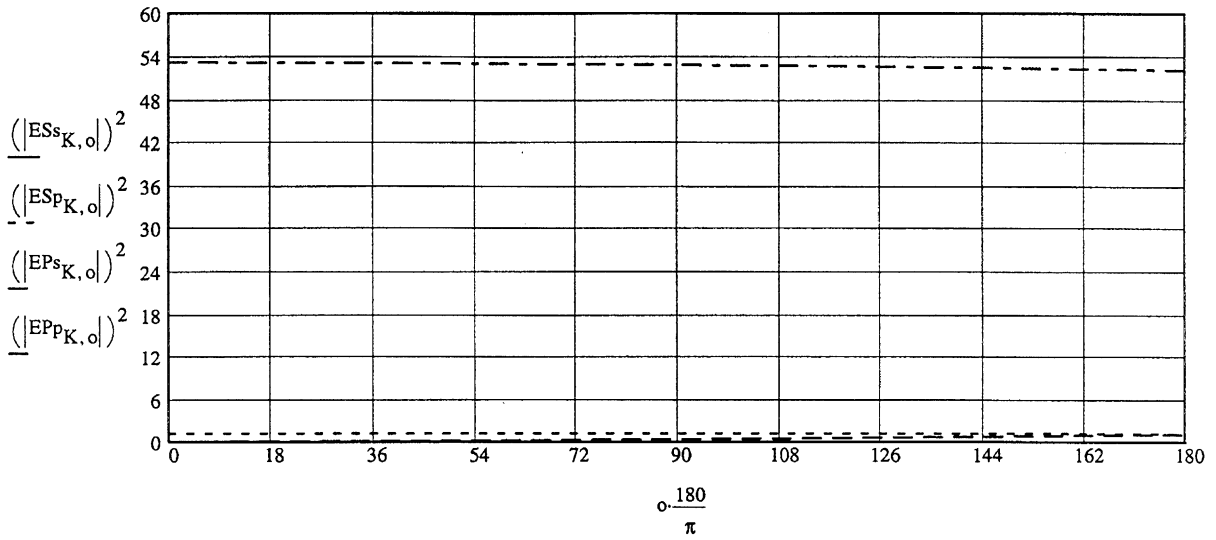

Intensities of s and p polarizations of the pump and signal beams with two wave mixing at thickness tt as a function of the mutual input polarization to the s direction

$NA = 3.5 \times 10^{21}$	number of acceptor sites per m^3	$r_{4,1} = 4.5 \times 10^{-12}$	electro-optical coefficient
$n = 2.54$	PRC index of refraction	$\alpha = 0$	optical attenuation coefficient in 1/m
$\varepsilon = 56$	PRC dielectric constant	$t = 0.01$	PRC thickness in m
$\lambda_o = 0.514$	laser free space wavelength in microns	$\theta_o = 23$	angle of incoming radiation to PRC normal in degrees
$\rho_o = 45$	optical active param in degree/mm	$N = 200$	number of integration steps
$IS = 1$	input intensity of signal beam	$IP = 50$	input intensity of pump beam

$$R_{xo} = \begin{pmatrix} 1 \\ -1 \\ 0 \end{pmatrix} \quad R_{yo} = \begin{pmatrix} 1 \\ 1 \\ 0 \end{pmatrix} \quad R_{zo} = \begin{pmatrix} 0 \\ 0 \\ 1 \end{pmatrix}$$ Orientation of the PRC crystal axes

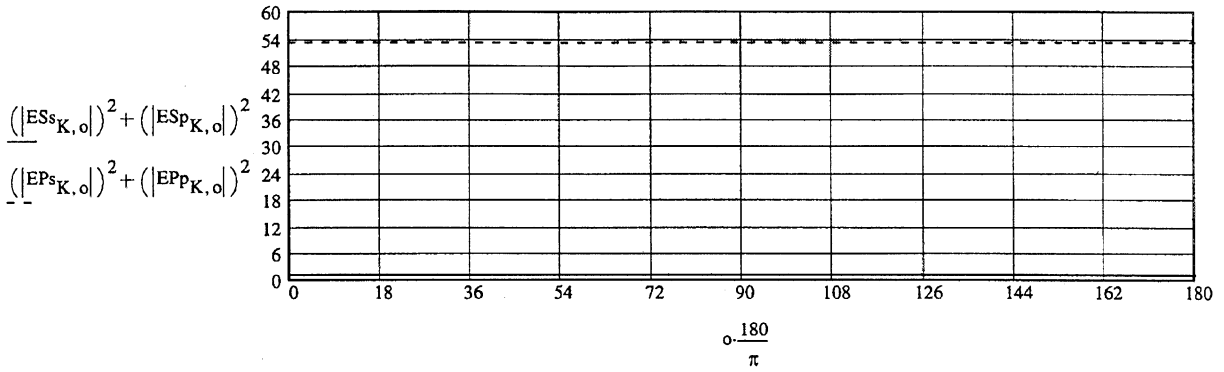

Total intensities of the pump and signal beams at tt as a function of Θ

Calculate the two wave mixing gains with no polarizer on output

signal beam gain:

$$GS_{j,o} := \frac{\left(ESs_{j,o}\cdot\overline{ESs_{j,o}}+ESp_{j,o}\cdot\overline{ESp_{j,o}}\right)-\left(ESso_{j,o}\cdot\overline{ESso_{j,o}}+ESpo_{j,o}\cdot\overline{ESpo_{j,o}}\right)}{\left(ESso_{j,o}\cdot\overline{ESso_{j,o}}+ESpo_{j,o}\cdot\overline{ESpo_{j,o}}\right)}$$

pump beam gain:

$$GS_{j,o} := \frac{\left(EPs_{j,o}\cdot\overline{EPs_{j,o}}+EPp_{j,o}\cdot\overline{EPp_{j,o}}\right)-\left(EPso_{j,o}\cdot\overline{EPso_{j,o}}+EPpo_{j,o}\cdot\overline{EPpo_{j,o}}\right)}{\left(EPso_{j,o}\cdot\overline{EPso_{j,o}}+EPpo_{j,o}\cdot\overline{EPpo_{j,o}}\right)}$$

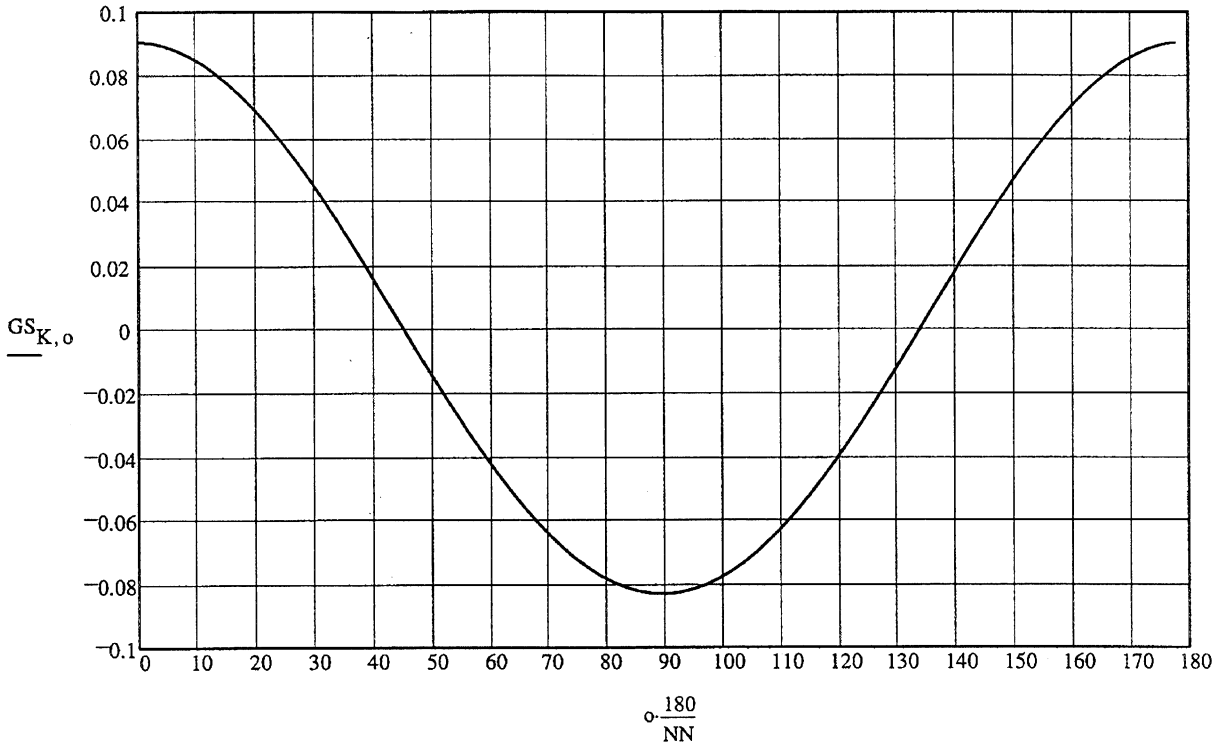

Pl

ot of two wave mixing gain vs. polarization of incoming pump and signal beams relative to s polarization

$NA = 3.5 \times 10^{21}$	number of acceptor sites per m^3	$r_{4,1} = 4.5 \times 10^{-12}$	electro-optical coefficient
$n = 2.54$	PRC index of refraction	$\alpha = 0$	optical attenuation coefficient in 1/m
$\varepsilon = 56$	PRC dielectric constant	$tt = 2 \times 10^{-3}$	plotted PRC thickness in m
$\lambda_o = 0.514$	laser free space wavelength in microns	$t = 0.01$	PRC thickness in m
$\rho_o = 45$	optical active param in degree/mm	$\theta_o = 23$	angle of incoming radiation to PRC normal in degree
$IS = 1$	input intensity of signal beam	$N = 200$	number of integration steps
$IP = 50$	input intensity of pump beam		

$$R_{xo} = \begin{pmatrix} 1 \\ -1 \\ 0 \end{pmatrix} \quad R_{yo} = \begin{pmatrix} 1 \\ 1 \\ 0 \end{pmatrix} \quad R_{zo} = \begin{pmatrix} 0 \\ 0 \\ 1 \end{pmatrix}$$

Orientation of the PRC crystal axes

$\Lambda ss = 0$	$\Lambda pss = 2.21 \times 10^9$	$\Lambda ss = 0$	$\Lambda pps = 2.21 \times 10^9$
$\Lambda spp = 2.21 \times 10^9$	$\Lambda pspp = 0$	$\Lambda sps = 2.21 \times 10^9$	$\Lambda ppps = 0$

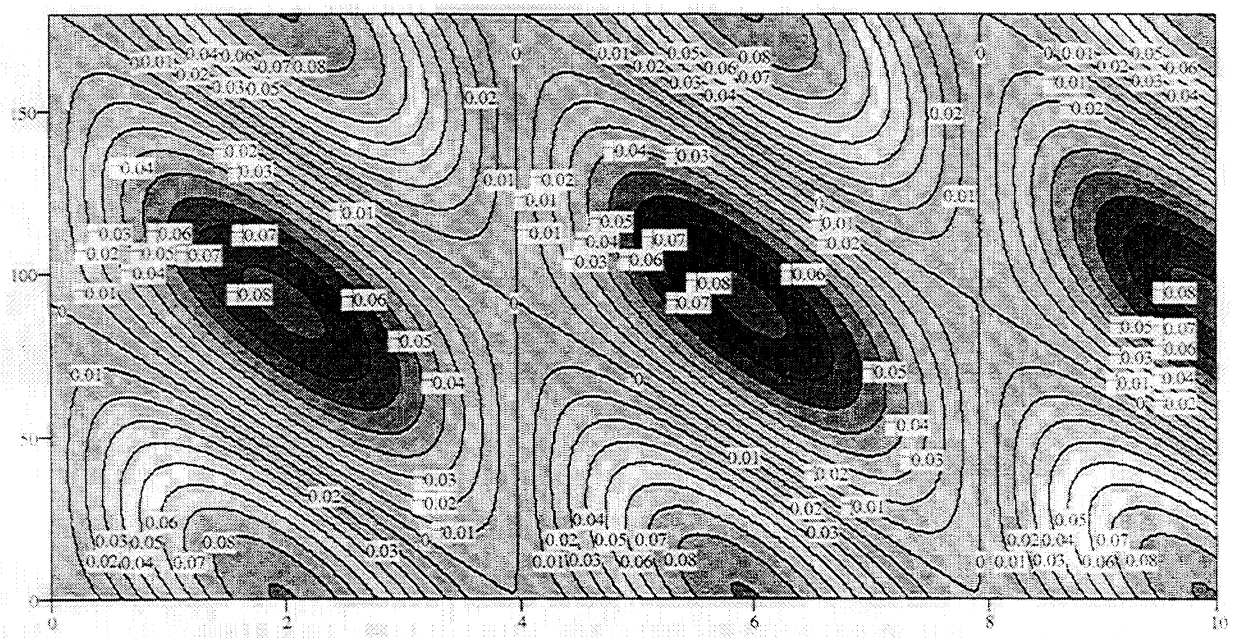

GS

Two wave mixing gain of signal beam as a function of input polarization and PRC thickness

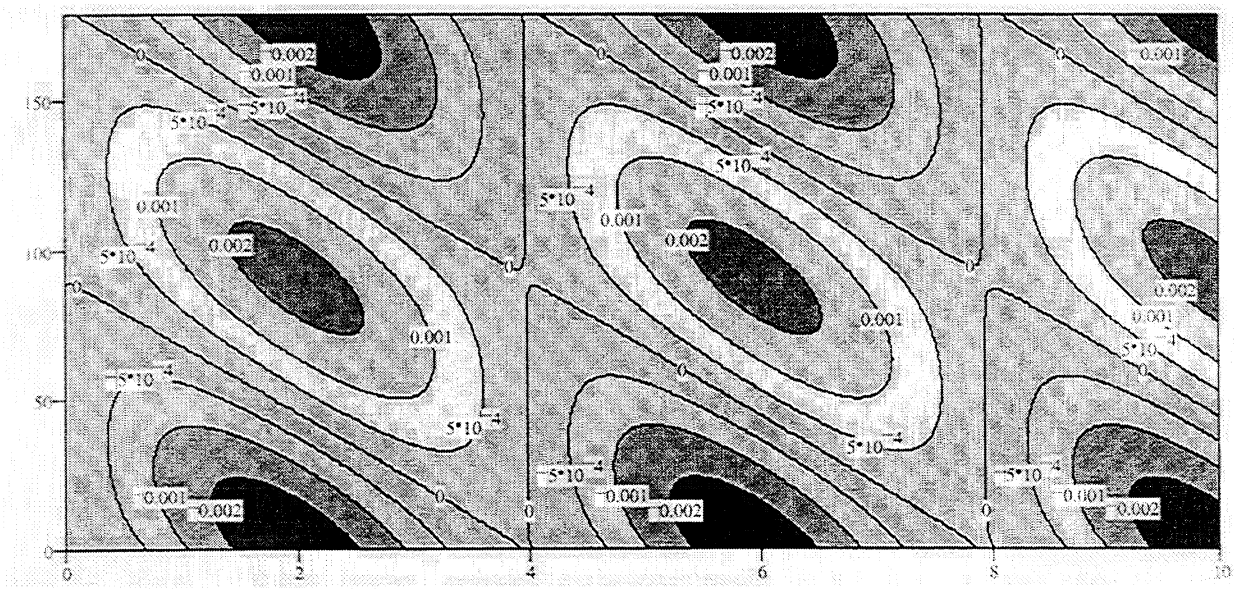

GP

Two wave mixing gain of pump beam as a function of input polarization and PRC thickness

2.6.3.3.11 MathCad program "PRCEo.mcd"

This program simulates two wave mixing in a cubic photo-refractive crystal using repeated integrations as presented in "PRC1.mcd". 2-D graphs of ultrasonic output as a function of applied voltage and PRC thickness are produced.

INTEGRATION PARAMETERS

$N := 200$ input the number of steps in the full length integration

PHYSCIAL CONSTANTS

$i := i$ make "i" the square root of minus 1

$\mu := 4\pi \cdot 10^{-7}$ permeability of free space in MKS units

$\varepsilon_o := 8.854 \times 10^{-12}$ permittivity of free space in MKS units

$c_0 := \frac{1}{\sqrt{\mu\varepsilon_0}}$ velocity of light in free space

$k_B := 1.381 \times 10^{-23}$ Boltzman Constant in MKS units

$q := 1.602 \times 10^{-19}$ electronic charge in Coulombs

CRYSTAL PARAMETERS

$n := 2.54$ input PRC index of refraction at laser frequency (BSO = 2.54)

$\varepsilon := 56$ input PRC dielectric constant at RF frequencies (BSO = 56)

$\alpha := 3.3$ input the exponential light absorption coefficient in unit of 1/cm

$t := 5$ input crystal thickness in mm

$NA := 6 \times 10^{15}$ input the number of acceptor sites per cubic centimeter of the PRC

$\rho_0 := 40$ input the optically active rotation coefficient in degrees per mm

$\alpha := 100 \cdot \alpha$ convert α to MKS units

$NA := NA \cdot 100^3$ convert NA to MKS

$t := \frac{t}{1000}$ convert t to MKS

$\rho := \rho_0\left(\frac{\pi}{180}\right)1000$ convert ρ to radians per m

EXPERIMENTAL PARAMETERS

$\theta_o := 23$ input angle of incidence in degrees of the incoming signal beam and pump beam to the normal of the crystal face

$\theta := \theta_o \frac{\pi}{180}$ convert θ to radians

$\theta := \sin^{-1}\left(\frac{\sin(\theta)}{n}\right)$ Use Snell's law to convert to the angle inside the crystal

$\lambda_o := 0.5145$ input laser free-space wavelength in microns

$\lambda := \frac{\lambda_0 \cdot 10^6}{n}$ convert λ to wavelength inside the crystal in meters

$T := 300$ input absolute temperature in K

$E_o := 0$ input the applied electric field in V/m in the grating direction

Iterate the input polarization of the S and P beams for 0 to 180 degrees with respect to s polarization. The S and P beams rotate together; they maintain the same polarization

$o := 0..(NN-1)$

$\Theta_o := \frac{\pi \cdot o}{NN}$ iterate input polarization from 0 to 180

$IS := 1$ input incoming intensity of signal beam

$IP := 50$ input incoming intensity of pump beam

$ESs_{0,o} := \sqrt{IS} \cdot \cos(\Theta_o)$ $ESp_{0,o} := \sqrt{IS} \cdot \sin(\Theta_o)$

$EPs_{0,o} := \sqrt{IP} \cdot \cos(\Theta_o)$ $EPp_{0,o} := \sqrt{IP} \cdot \sin(\Theta_o)$

Calculate initial input components for each polarization state.

$ESso_{0,o} := ESs_{0,o}$ $ESpo_{0,o} := ESp_{0,o}$

$EPso_{0,o} := EPs_{0,o}$ $EPpo_{0,o} := EPp_{0,o}$

give no two mixing calculation the same initial conditions

$$I_{0,o} := \frac{EPs_{0,o} \cdot \overline{ESs_{0,o}} + EPp_{0,o} \cdot \overline{ESp_{0,o}} \cdot \cos(2\theta)}{ESs_{0,o} \cdot \overline{ESs_{0,o}} + ESp_{0,o} \cdot \overline{ESp_{0,o}} + EPs_{0,o} \cdot \overline{EPs_{0,o}} + EPp_{0,o} \cdot \overline{EPp_{0,o}}}$$ calculate the initial modulation index

$K := \frac{2\pi}{\lambda}$ calculate laser wave number

$\omega := \frac{2\pi c_o}{\lambda_o \cdot 10^{-6}}$ calculate laser angular frequency in Hz

K := 2k · sin(θ) calculate the magnitude of the grating wave number

$k_T := k_B T$ calculate k_T

ELECTRO-OPTICAL COEFFICIENTS ENTERED BELOW

please, input here the non-zero r coefficient in MKS units (m/V) for the crystal of interest

$r_{4,1} := 5 \times 10^{-12}$

$r_{5,2} := r_{4,1}$

$r_{6,3} := r_{4,1}$

INPUT ULTRASONIC AMPLITUDE

a := 10 input ultrasonic amplitude in nanometers

$\psi := 2\frac{a}{\lambda_o} \cdot 2\pi \cdot 10^{-3}$ convert amplitude to a phase shift in the signal beam

DO THE CALCULATIONS

First specify the PRC crystal axis in terms of the natural experimental coordinates. For the experiment, the x-direction is normal to the illuminated face of the crystal; its positive direction is in the direction of propagation. The experimental y-direction is in the plane of incidence and normal to the x-axis. The experimental z-direction is perpendicular to the plane of incidence (in the s polarization direction); its orientation is determined by the right hand rule from the x and y axes. Input R_x, R_y, and R_z, where R_x is the crystal direction in the x-axis, R_y is the crystal axis along the y-axis, and R_z is the crystal axis along the z-axis.

please, input the Miller indices of the crystal axes in the experimental coordinates

$$R_{xo} := \begin{pmatrix} -1 \\ 1 \\ 0 \end{pmatrix} \quad R_{yo} := \begin{pmatrix} 1 \\ 1 \\ 0 \end{pmatrix} \quad R_{zo} := \begin{pmatrix} 0 \\ 0 \\ 1 \end{pmatrix}$$

normalize the crystal axes

$$R_{xo} := \frac{R_{xo}}{|R_{xo}|} \quad R_{yo} := \frac{R_{yo}}{|R_{yo}|} \quad R_{zo} := \frac{R_{zo}}{|R_{zo}|}$$

creation of the orthogonal matrix that rotates the vectors from the experimental axes to the crystal axes

$$O := \begin{bmatrix} R_{x_0} & R_{y_0} & R_{z_0} \\ R_{x_1} & R_{y_1} & R_{z_1} \\ R_{x_2} & R_{y_2} & R_{z_2} \end{bmatrix}$$

Now, the electro-optical tensor is determined by user input of the standard two-dimensional electro-optical coefficients (Section 1.4 in Yeh book)

ESTABLISH THE INTEGRATION COEFFICIENTS

Convert the 2-D r matrix to a third order r tensor

$$r_3(u,v,w) := \delta(u,v)\cdot r_{u+1,w+1} + \delta(u+v,3)\cdot r_{4,w+1} + \left(\delta(|u-v|,2)\cdot r_{5,w+1} + \delta(u+v,1)\cdot r_{6,w+1}\right)$$

Calculate (Escmax) the proportionality constant between the space charge electric field and the ratio of grating intensity to total intensity

$$k_D := \sqrt{\frac{q^2 \cdot NA}{\varepsilon \cdot \varepsilon_0 \cdot k_T}}$$

calculate the Debye wave number assuming ND >> NA, p89 Yeh

$$Escmax_o := \frac{\frac{i \cdot K \cdot k_T}{q} - E_{o_o}}{1 + \left(\frac{K}{k_D}\right)^2 + \frac{i \cdot q \cdot K \cdot E_{o_o}}{k_T \cdot k_D^2}} \qquad \phi_o := \arg(Escmax_o)$$

$E := \begin{pmatrix} 0 \\ 1 \\ 0 \end{pmatrix}$ unit vector in the direction of the space charge field in experimental coordinate system

$s := \begin{pmatrix} 0 \\ 0 \\ 1 \end{pmatrix}$ unit vector perpendicular to the incidence plane. This establishes the direction of the s-polarized wave component in experimental coordinates

$pp := \begin{bmatrix} -\sin(\theta) \\ \cos(\theta) \\ 0 \end{bmatrix}$ unit vector in the place of incidence and perpendicular to the direction of propagation of the pump beam. This establishes the direction of the p-polarized wave of the pump beam in experimental coordinates.

$\beta p := k \cdot \cos(\theta)$ along grating component of pump wave number

$ps := \begin{bmatrix} \sin(\theta) \\ \cos(\theta) \\ 0 \end{bmatrix}$ unit vector in the plane of incidence and perpendicular to the direction of propagation of the signal beam. This establishes the direction of the p-polarized wave of the signal beam in experimental coordinates.

$\beta s := -k \cdot \cos(\theta)$ along grating component of signal wave number

Express above unit vectors in the crystal coordinate system

ec := O·E sc := O·s ppc := O·pp psc := O·ps

CALCULATE THE DIFRACTION COUPLING COEFFICIENTS

mm := 0..2 nn := 0..2

$\Lambda_{mm,nn} := \omega^2 \cdot \mu \cdot \varepsilon_o \cdot n^4 \cdot \sum_{k=0}^{2} r_3(mm, nn, k) \cdot ec_k$ Compute the Lambda tensor as in Yeh 4.4-7

$\Lambda ss_o := sc^T \cdot \Lambda \cdot sc \cdot |Escmax_o|$ $\Lambda pss_o := psc^T \cdot \Lambda \cdot sc \cdot |Escmax_o|$

$\Lambda sps_o := sc^T \cdot \Lambda \cdot psc \cdot |Escmax_o|$ $\Lambda spp_o := sc^T \cdot \Lambda \cdot ppc \cdot |Escmax_o|$

$\Lambda pspp_o := psc^T \cdot \Lambda \cdot ppc \cdot |Escmax_o|$ $\Lambda pps_o := ppc^T \cdot \Lambda \cdot sc \cdot |Escmax_o|$

$\Lambda ppps_o := ppc^T \cdot \Lambda \cdot psc \cdot |Escmax_o|$

j := 0..(N-1) set up iteration parameter

INTEGRATE NO SIGNAL STATE

The first row in the expression below tracks the modulation index (I_1/I_0) through the PRC. The last four rows do the integration of field magnitudes for the signal and pump beam in the s and p polarizations. The first terms in the field increment expressions do the two-wave mixing, the second accounts for PRC light attenuation, whereas the third does the optical active polarization rotation.

$$\begin{bmatrix} I_{j+1,o} \\ ESs_{j+1,o} \\ ESp_{j+1,o} \\ EPs_{j+1,o} \\ EPp_{j+1,o} \end{bmatrix} := \begin{bmatrix} \dfrac{EPs_{j,o}\cdot\overline{ESs_{j,o}} + EPp_{j,o}\cdot\overline{ESp_{j,o}}\cdot\cos(2\theta)}{ESs_{j,o}\cdot\overline{ESs_{j,o}} + ESp_{j,o}\cdot\overline{ESp_{j,o}} + EPs_{j,o}\cdot\overline{EPs_{j,o}} + EPp_{j,o}\cdot\overline{EPp_{j,o}}} \\ ESs_{j,0} + \left[\dfrac{i\cdot e^{-i\phi_o}}{k}\left(\Lambda ss_o\cdot EPs_{j,o} + \Lambda spp_o\cdot EPp_{j,o}\right)\overline{I_{j,o}} - \alpha\cdot ESs_{j,o} - 2\rho\cdot ESp_{j,o}\right]\dfrac{1}{2\cos(\theta)}\cdot\dfrac{t}{N} \\ ESp_{j,0} + \left[\dfrac{i\cdot e^{-i\phi_o}}{k}\left(\Lambda pss_o\cdot EPs_{j,o} + \Lambda pspp_o\cdot EPp_{j,o}\right)\overline{I_{j,o}} - \alpha\cdot ESp_{j,o} + 2\rho\cdot ESs_{j,o}\right]\dfrac{1}{2\cos(\theta)}\cdot\dfrac{t}{N} \\ EPs_{j,0} + \left[\dfrac{i\cdot e^{i\phi_o}}{k}\left(\Lambda ss_o\cdot ESs_{j,o} + \Lambda sps_o\cdot ESp_{j,o}\right)I_{j,o} - \alpha\cdot EPs_{j,o} - 2\rho\cdot EPp_{j,o}\right]\dfrac{1}{2\cos(\theta)}\cdot\dfrac{t}{N} \\ EPp_{j,0} + \left[\dfrac{i\cdot e^{i\phi_o}}{k}\left(\Lambda pps_o\cdot ESs_{j,o} + \Lambda ppps_o\cdot ESp_{j,o}\right)I_{j,o} - \alpha\cdot EPp_{j,o} + 2\rho\cdot EPs_{j,o}\right]\dfrac{1}{2\cos(\theta)}\cdot\dfrac{t}{N} \end{bmatrix}$$

$\gamma_o := \dfrac{\Lambda pps_o}{2k\cos(\theta)}$ calculate the lambda parameter in 1/m

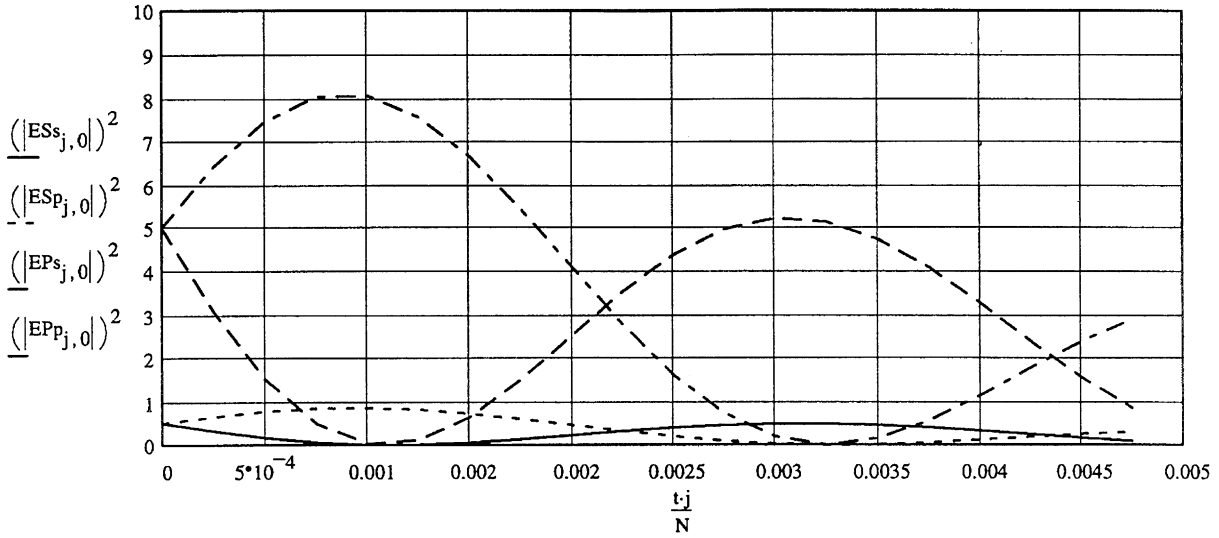

Signal and pump beam intensities with s and p polarizations as a function of PRC thickness in m

$NA = 6 \times 10^{21}$	number of acceptor sites per m^3	$r_{4,1} = 5 \times 10^{-12}$	electro-optical coefficient
$n = 2.54$	PRC index of refraction	$\alpha = 330$	optical attenuation coefficient
$\varepsilon = 56$	PRC dielectric constant	$t = 5 \times 10^{-3}$	PRC thickness in m
$\lambda_o = 0.514$	laser free space wavelength in microns	$\theta_o = 10$	angle of incoming radiation to PRC normal in degrees
$Escmax_o = 8.846 \times 10^4$ I	space charge field maximum V/m	$N = 20$	number of integration steps
$\rho_o = 40$	optical active param in deg/mm		

$ESs_{0,0} = 0.707$	free space input amplitude of signal beam with normal polarization
$ESp_{0,0} = 0.707$	free space input amplitude of signal beam with incident plane polarization
$EPs_{0,0} = 2.236$	free space input amplitude of pump beam with normal polarization
$EPp_{0,0} = 2.236$	free space input amplitude of pump beam with incident plane polarization

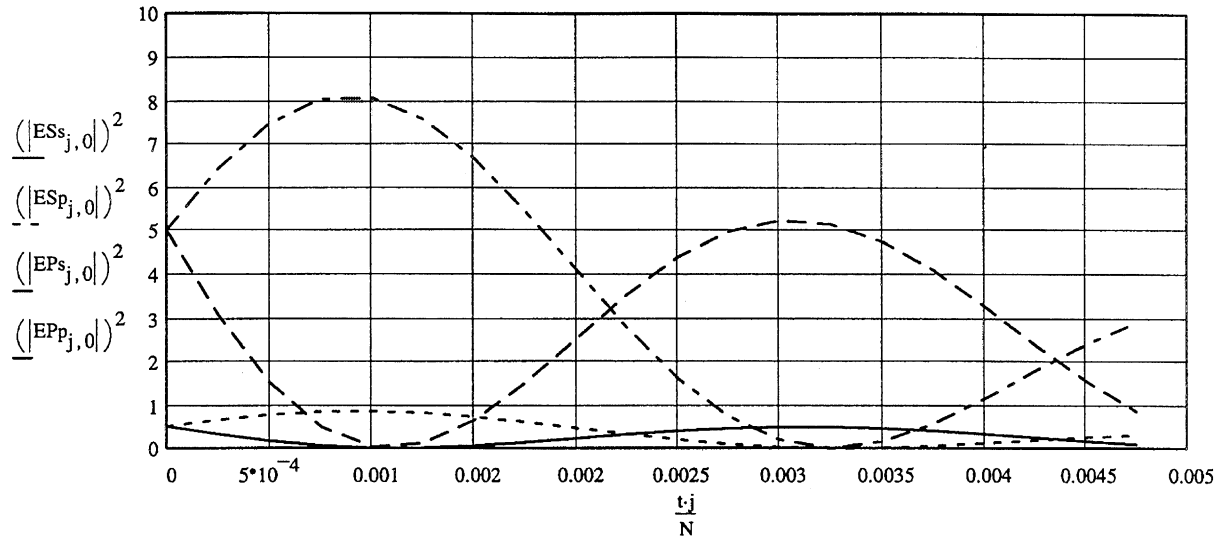

$ESsu_{0,o} := ESs_{0,o} \cdot e^{i\psi}$ $EPsu_{0,o} := EPs_{0,o}$

$ESpu_{0,o} := ESp_{0,o} \cdot e^{i\psi}$ $EPpu_{0,o} := EPp_{0,o}$

Apply an ultrasonic phase shift amplitude to both polarizations of the signal beam

INTEGRATE

Integrate through the PRC again but this time let the space charge remain as calculated with the no ultrasonic signal exercise above

$$\begin{bmatrix} ESsu_{j+1,o} \\ ESpu_{j+1,o} \\ EPsu_{j+1,o} \\ EPpu_{j+1,o} \end{bmatrix} := \begin{bmatrix} ESsu_{j,o} + \left[\frac{i\cdot e^{-i\phi_o}}{k}\left(\Lambda ss_o \cdot EPsu_{j,o} + \Lambda spp_o \cdot EPpu_{j,o}\right)\overline{I_{j,o}} - \alpha \cdot ESsu_{j,o} - 2\rho \cdot ESpu_{j,o}\right]\frac{1}{2\cos(\theta)}\cdot\frac{t}{N} \\ ESpu_{j,o} + \left[\frac{i\cdot e^{-i\phi_o}}{k}\left(\Lambda pss_o \cdot EPsu_{j,o} + \Lambda pspp_o \cdot EPpu_{j,o}\right)\overline{I_{j,o}} - \alpha \cdot ESpu_{j,o} + 2\rho \cdot ESsu_{j,o}\right]\frac{1}{2\cos(\theta)}\cdot\frac{t}{N} \\ EPsu_{j,o} + \left[\frac{i\cdot e^{i\phi_o}}{k}\left(\Lambda ss_o \cdot ESsu_{j,o} + \Lambda sps_o \cdot ESpu_{j,o}\right)I_{j,o} - \alpha \cdot EPsu_{j,o} - 2\rho \cdot EPpu_{j,o}\right]\frac{1}{2\cos(\theta)}\cdot\frac{t}{N} \\ ESpu_{j,o} + \left[\frac{i\cdot e^{i\phi_o}}{k}\left(\Lambda pps_o \cdot ESsu_{j,o} + \Lambda ppps_o \cdot EPpu_{j,o}\right)I_{j,o} - \alpha \cdot EPpu_{j,o} + 2\rho \cdot EPsu_{j,o}\right]\frac{1}{2\cos(\theta)}\cdot\frac{t}{N} \end{bmatrix}$$

Calculate the RF signal intensity at the photodiode imposed by the ultrasonic signal with no polarizer in-place

$$IS_{j,o} := \left|\left(|ESsu_{j,o}|\right)^2 - \left(|ESs_{j,o}|\right)^2 + \left(|ESpu_{j,o}|\right)^2 - \left(|ESp_{j,o}|\right)^2\right|$$

Calculate the RF signal intensity relative to the no signal amplitude at the photodiode imposed by the ultrasonic signal

$$ISn_{j,o} := \frac{IS_{j,o}}{\left(\left|ESp_{j,o}\right|\right)^2 + \left(\left|ESs_{j,o}\right|\right)^2} \qquad MS_{j,o} := \left(\left|ESs_{j,o}\right|\right)^2 + \left(\left|ESp_{j,o}\right|\right)^2$$

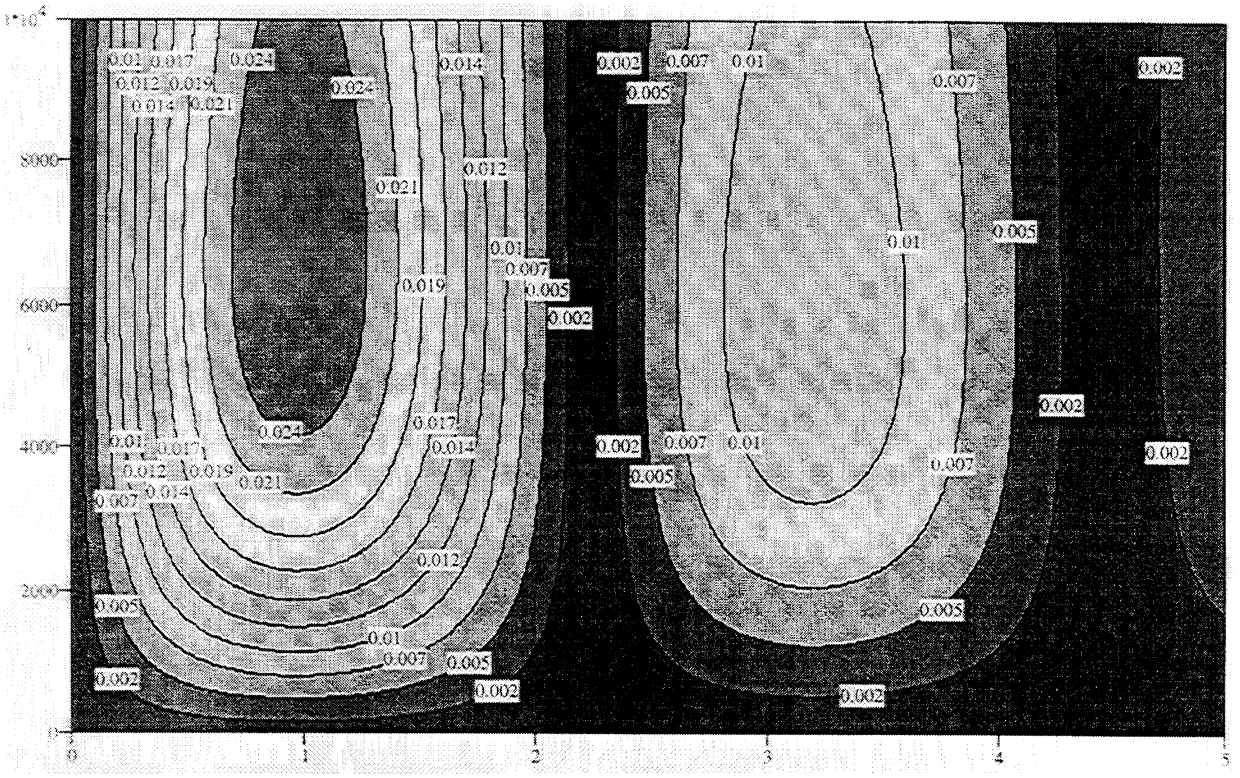

IS

Intensity of the ultrasonic signal as a function of PRC thickness in mm and applied field in V/m with no polarizer at output of signal beam

$ESs_{0,0} = 0.707$ $EPs_{0,0} = 2.236$ Input signal (S) and pump (P) field $\Lambda ss_{\frac{p}{2}} = 0$ $\Lambda pss_{\frac{p}{2}} = 9.686 \times 10^{9}$

amplitudes for s (s) and p (p)

$ESp_{0,0} = 0.707$ $EPp_{0,0} = 2.236$ polarizations $\Lambda spp_{\frac{p}{2}} = 9.686 \times 10^{9}$ $\Lambda pspp_{\frac{p}{2}} = 0$

Orientation of the crystal axes with respect to propagation direction (x), diffraction grating direction (y), and normal to incidence plane (z)

$$R_{xo} = \begin{pmatrix} -1 \\ 1 \\ 0 \end{pmatrix} \quad R_{yo} = \begin{pmatrix} 1 \\ 1 \\ 0 \end{pmatrix} \quad R_{zo} = \begin{pmatrix} 0 \\ 0 \\ 1 \end{pmatrix}$$

$\theta_o = 10$	angle of incoming pump and signal beams to the PRC normal			$\varepsilon = 56$	dielectric constant
$NA = 6 \times 10^{21}$	acceptor sites per m^3			$n = 2.54$	index of refraction
$r_{4,1} = 5 \times 10^{-12}$	electro-optical coeff	$a = 10$	ultrasonic amplitude in nanometers		$N = 200$
$E_{o\,max} = 1 \times 10^{6}$	max electric field in V/m	$\alpha = 330$	attenuation coefficient in 1/m		$P = 50$
$t = 5 \times 10^{-3}$	max thickness in m	$\rho_o = 40$	rotation coefficient in degrees/mm		

2.6.3.4 BSO Photorefractive Setup

2.6.3.4.1 Experimental Setup (evolution of the BSO PRC interferometer)

The first BSO photorefractive interferometers built at IPST used a mirror with a piezoelectric transducer attached to the back as a target sample. The mirror undergoes a sinusoidal displacement at 1 MHz (the resonant frequency of the transducer). Sine waves at 1 MHz were chosen at the beginning because this frequency was theoretically in the middle of the bandwidth of ultrasound generated by lasers on paper. The use of a mirror as a target sample provided a high intensity planar wavefront for the signal beam which maximized the photorefractive effect. This interferometer was labeled Version 0.1, and used an "X" shape setup for interference between the two beams. The BSO crystal thickness was 5 mm.

PRI Version 0.2 still used a mirror and a 1 MHz piezoelectric transducer, but with a "V" shape setup, crystal thickness was 5 mm.

PRI Version 0.3 continued to use the same mirror, but the optical head of the interferometer employed was a cube beam splitter plus a quarter wave plate for the first time. PRI Version 0.3 used 2.25 mm and 5 mm crystals. PRI Version 0.4 was very similar to Version 0.1 except that it used the 2.25 mm crystal which gave better results for ultrasound detection than the 5 mm one. The orientation of polarization of the incident beams and the crystal were also different.

PRI Version 0.5 was the first one to detect ultrasound on a rough surface, thus with a speckled wavefront for the signal beam. The signal beam was focused with a 20x microscope objective on an aluminum plate with the piezoelectric transducer attached on the back of the

plate. The optical head used a beam splitter and a quarter wave plate in addition to the microscope objective.

PRI Version 1.0 was the first one to make measurements on paper, using a "T" (beam splitter + quarter wave) setup, as shown in Figure 2.6.38. The angle between the reference beam on the left side and the signal beam on the right side was 50°, a value theoretically and experimentally optimum for the photorefractive effect without any applied electric field.

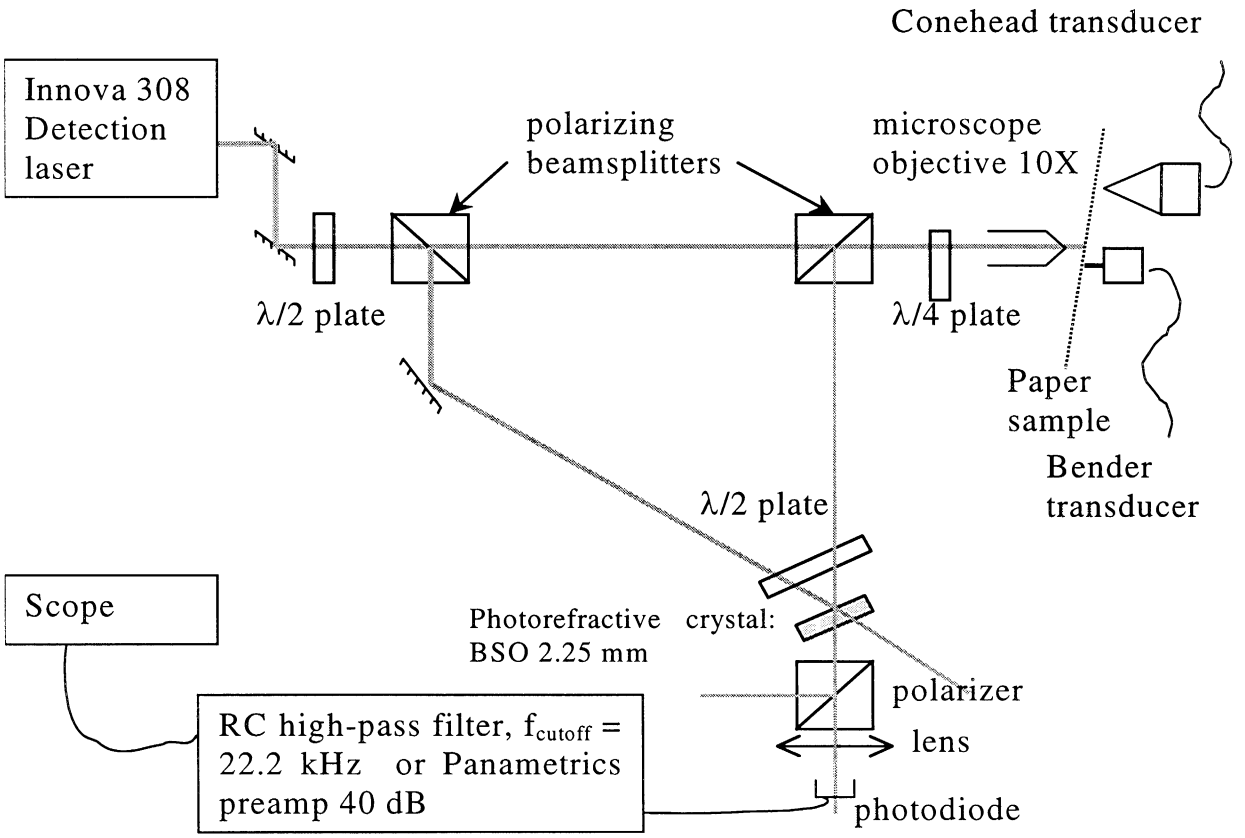

Figure 2.6.38 Schematic of Photorefractive Interferometer Version 1.0

For generating ultrasound on paper, two different contact transducers were used: a bender transducer generating mainly S_0 waves was excited at its resonance frequency of 57.8 kHz, and a

"conehead" transducer generating at 57.2 kHz. The conehead transducer was in contact with paper by the tip of the cone, which had a diameter of about 1.5 mm.

Figure 2.6.39 shows a picture of the Photorefractive Interferometer Version 1.0 using the bender transducer. Figure 2.6.40 displays the close view of the optical head in the interferometer. Figure 2.6.41 shows a combination of generation and detection signals captured in the oscilloscope. Also, Figure 2.6.42 shows the setup of the Photorefractive Interferometer Version 1.0 detecting ultrasound with the conehead transducer.

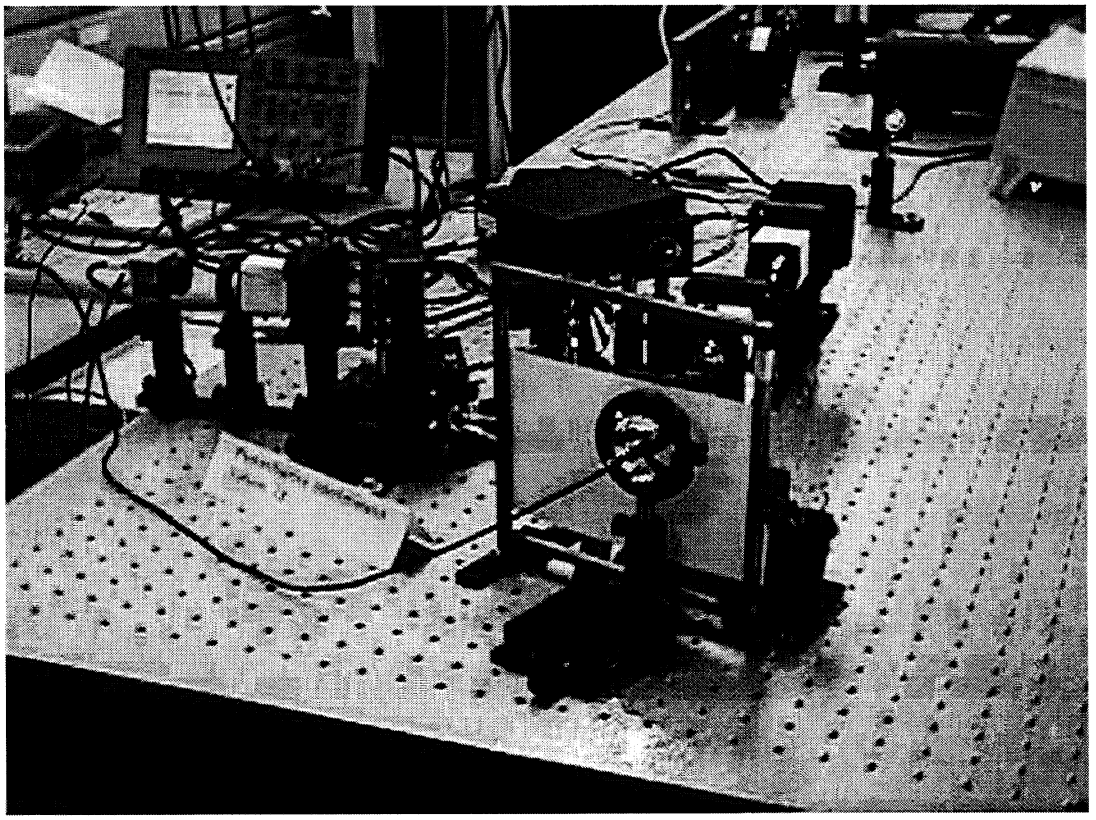

Figure 2.6.39 Photorefractive Interferometer version 1.0 detecting ultrasound on copy paper with generation made with the bender transducer.

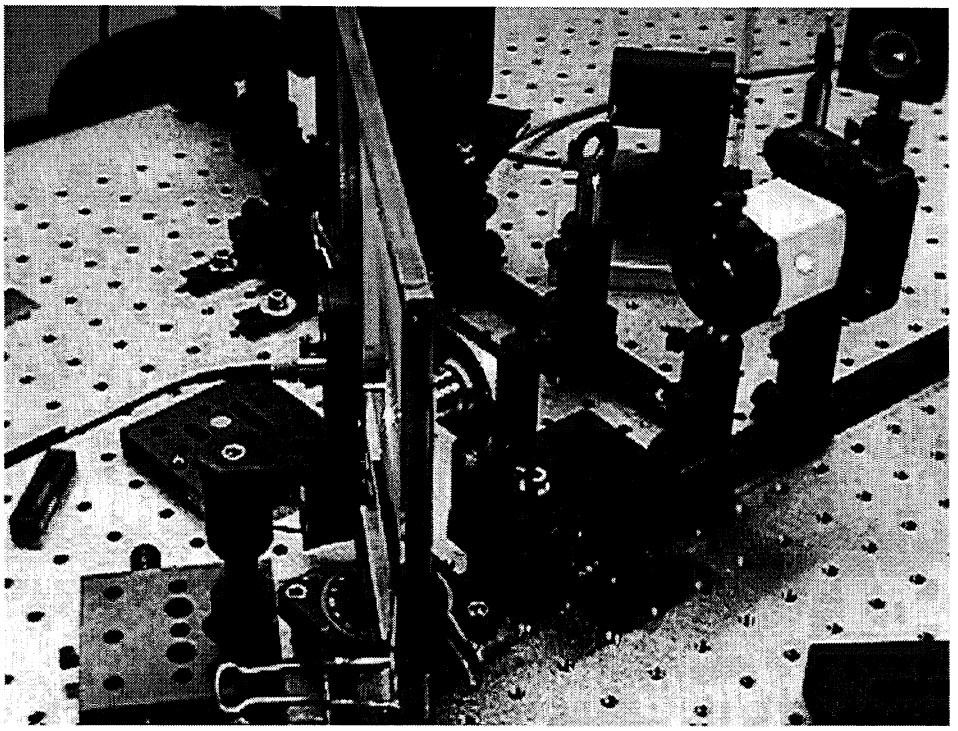

Figure 2.6.40 PRI Version 1.0, view of the optical head.

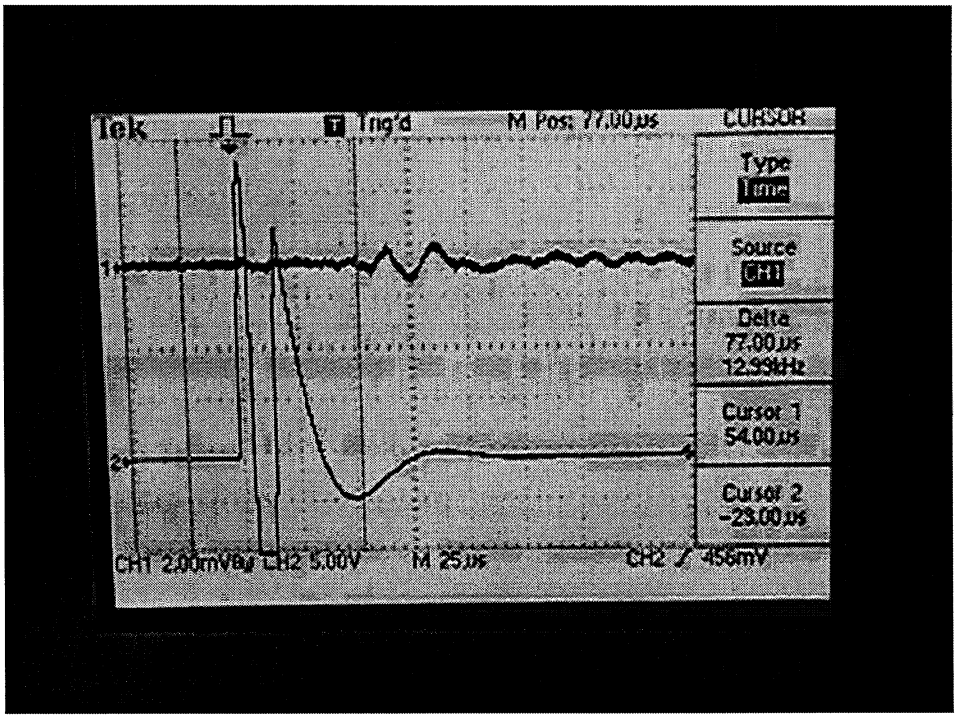

Figure 2.6.41 Voltage sent to the piezoelectric element (trace 2) and signal transmitted to the paper and detected by the interferometer (trace 1).

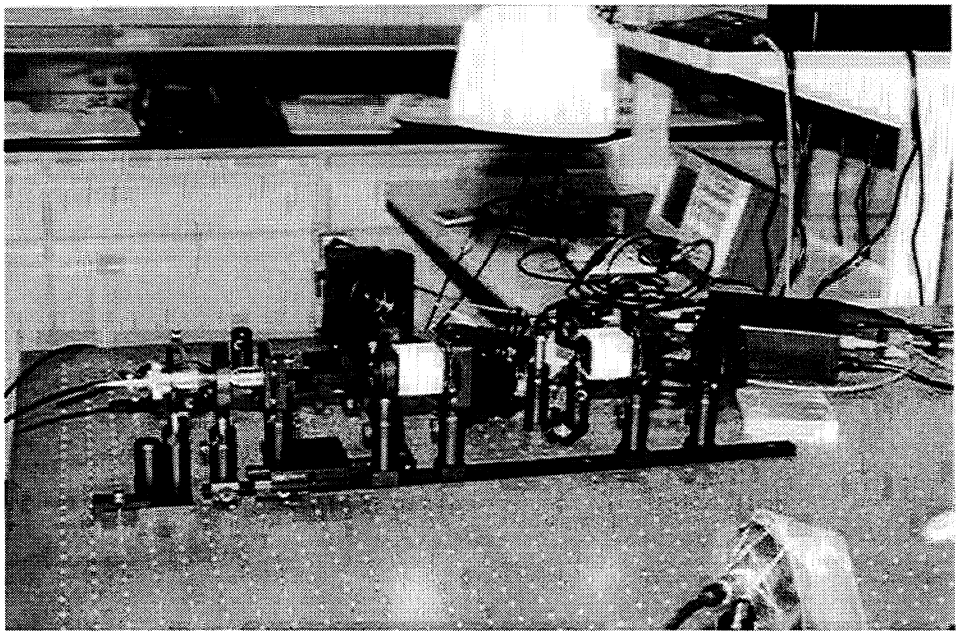

Figure 2.6.42 Photorefractive Interferometer Version 1.0 detecting ultrasound on copy paper (attached on a lens holder) with generation made with the "Conehead" transducer.

PRI Version 1.0 was used to detect ultrasonic waves on copy paper, with a 10x microscope objective instead of the 20x. Ultrasound was generated using the pulse Nd:YAG laser at 1064 nm with a 100 mm focal length spherical lens (point generation). Generation and detection of ultrasound were performed on the same side of the sheet, and the generation laser was steered to the sample using a mirror placed at 45 degrees. This setup made it easy to vary the distance between the generation and detection spots in order to check the time-of-flight of ultrasonic waves at different distances. The power of the detection laser was 140 mW.

Figure 2.6.43 shows the 1064 nm lens and the mirror used in the Version 1.0. Figure 2.6.44 displays the microscope objective for the detection beam. Also shown in Figure 2.6.45 are the signals obtained via the oscilloscope.

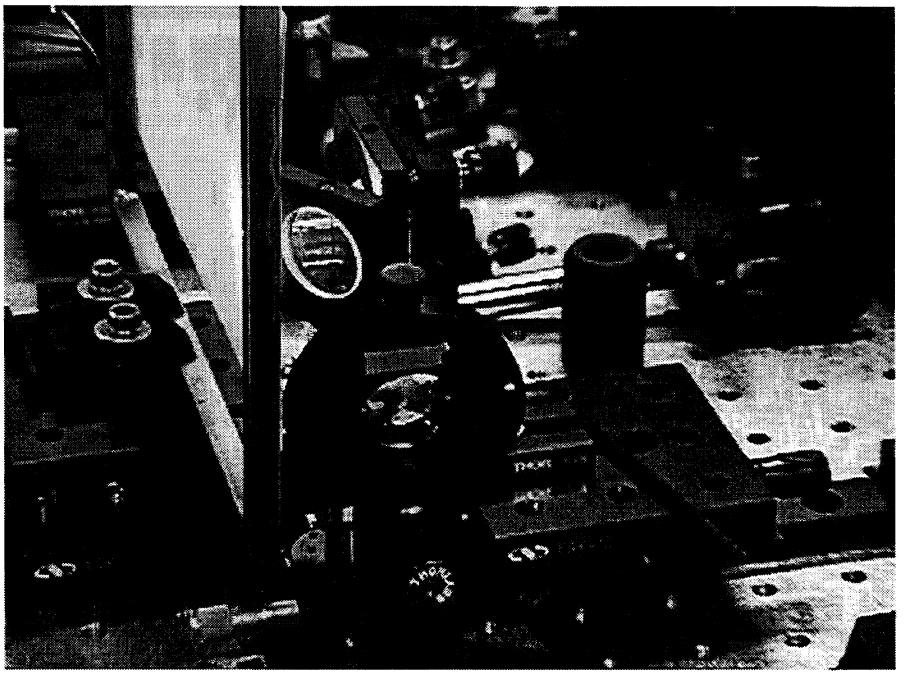

Figure 2.6.43 Photorefractive Interferometer Version 1.0 detecting laser generated ultrasound on copy paper (attached to a metallic frame), view of the 1064 nm lens (bottom) and mirror (center).

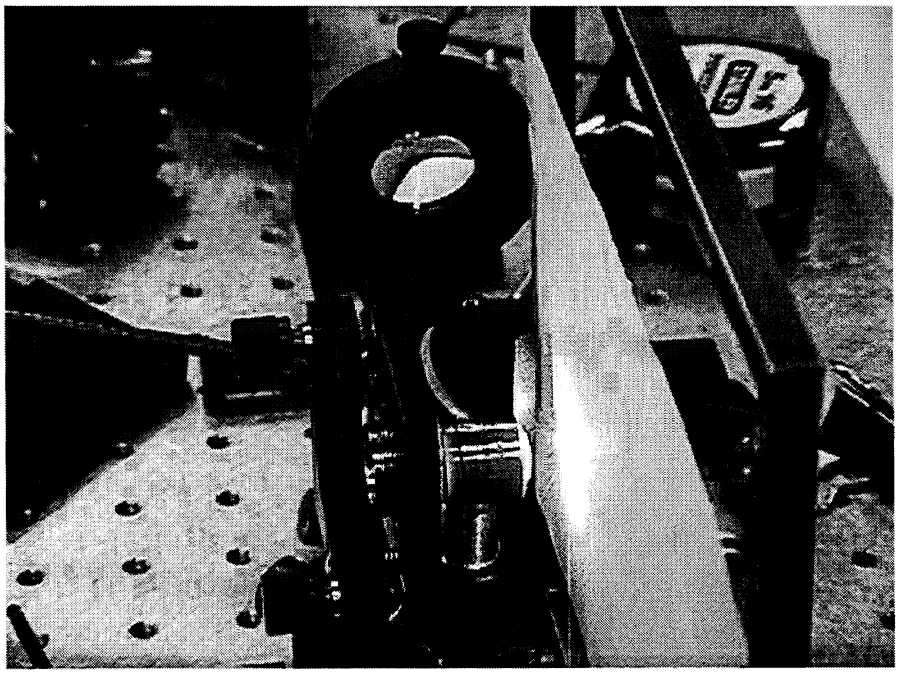

Figure 2.6.44 Copy paper, view of the microscope objective (center bottom) for the detection beam.

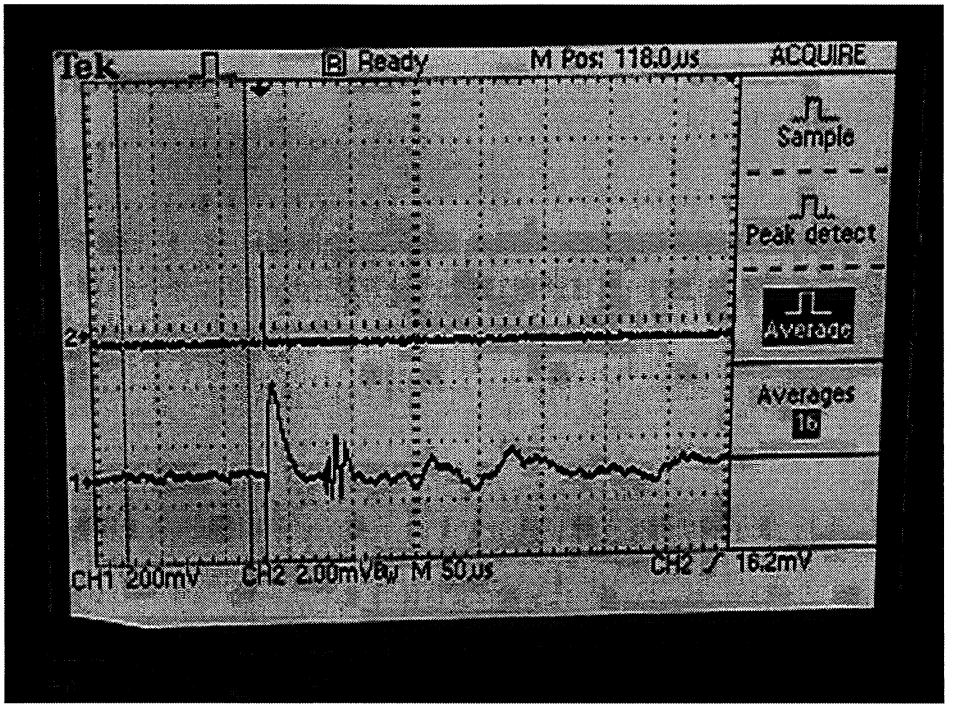

Figure 2.6.45 Trigger signal (upper trace) and laser generated ultrasonic signal (lower trace) on copy paper. Ultrasound signal starts at ~3.5 divisions from the left side of the screen. Signal is high pass filtered and averaged 16 times.

The signals in Figure 2.6.45 show a poor signal to noise ratio. This signal was obtained with an RC high pass filter without amplification, and was averaged 16 times. In order to improve the signal to noise ratio, a voltage was applied across the 2.25 mm BSO crystal and a new detection setup (PRI Version 1.5) was assembled as shown in Figure 2.6.46.

For this interferometer (version 1.5) the angle between the signal beam and the pump beam was decreased from 50° to 2-5°, which is ideal when a voltage is applied to the BSO crystal. A converging lens was placed in the path of the reference beam and had a focal length of 38 mm and the focal point was just before the 45° incidence mirror.

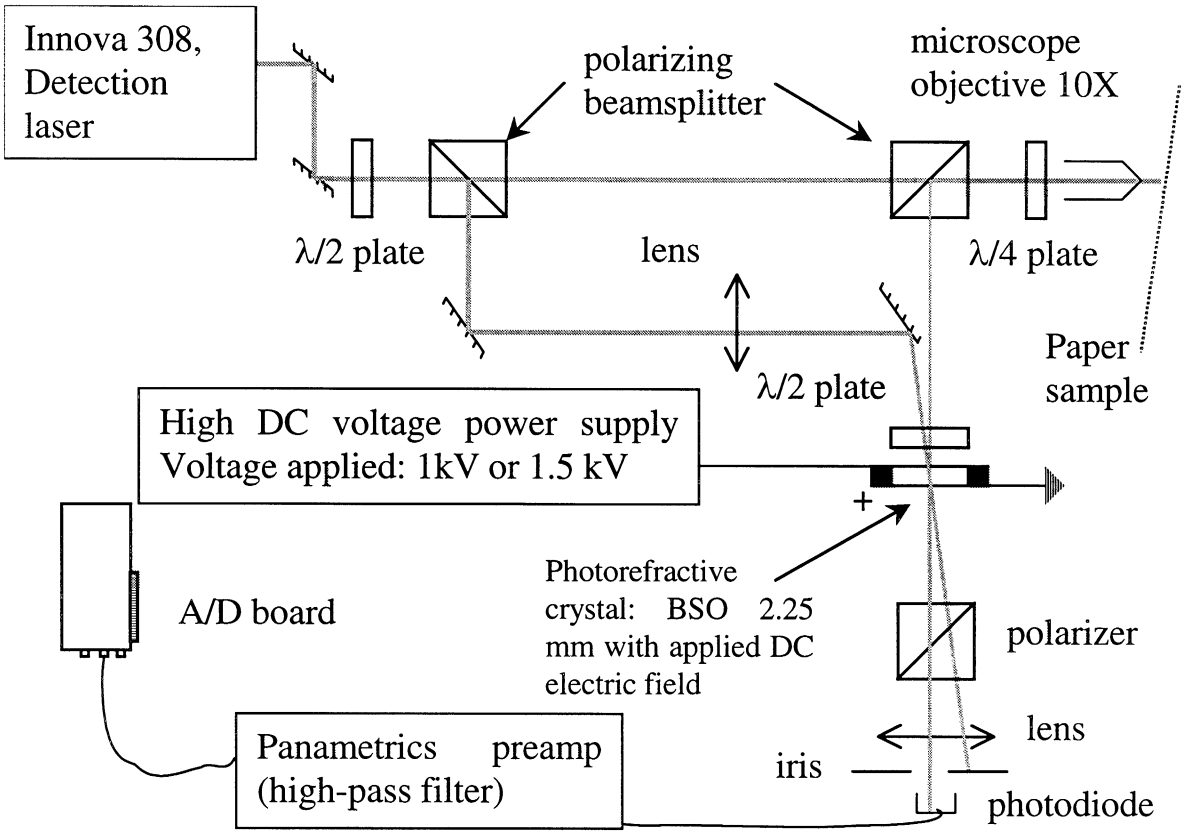

Figure 2.6.46 Schematic of Photorefractive Interferometer Version 1.5 using a BSO crystal with a DC applied voltage.

The reference beam diverges after the focal point and needs to impinge across the crystal from one electrode to another, in addition to overlapping the signal beam. This is necessary because if the electrons are not set free by this beam there will be no photoconductivity and the electric field will stay in the dark zone near the electrodes, eliminating its effect on the two-wave mixing. The iris just in front of the photodiode has been added to filter out the parasitic light of the generation pulse at 1064 nm directly scattered from the paper sample or collected by the interferometer optical head. Figures 2.4.47, 2.4.48 and 2.4.49 show several views of Version 1.5.

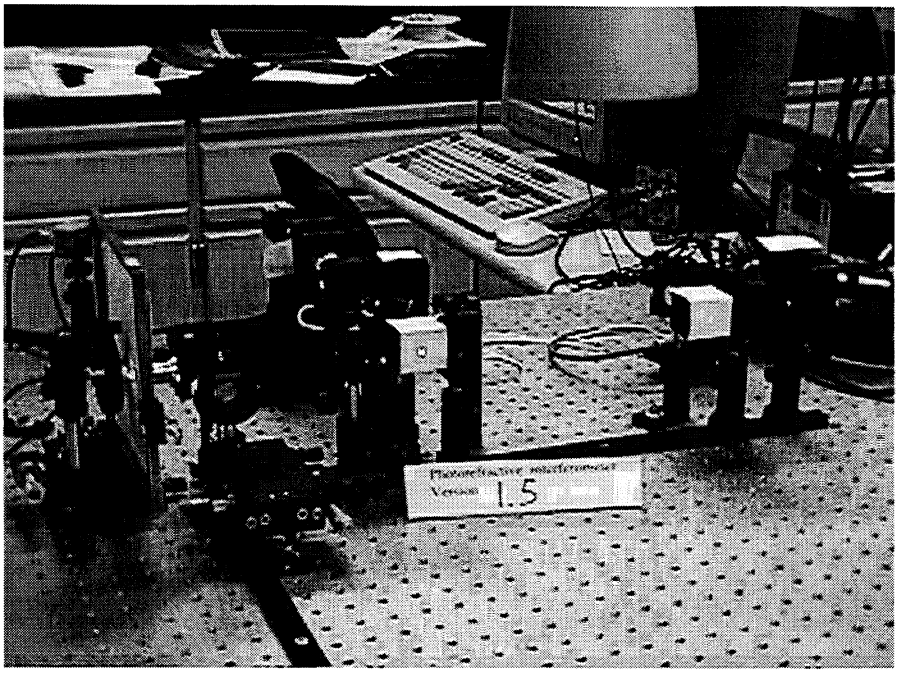

Figure 2.6.47 View of the PRI Version 1.5: Paper sample is on the left, photodiode and crystal with high voltage leads are in the center back.

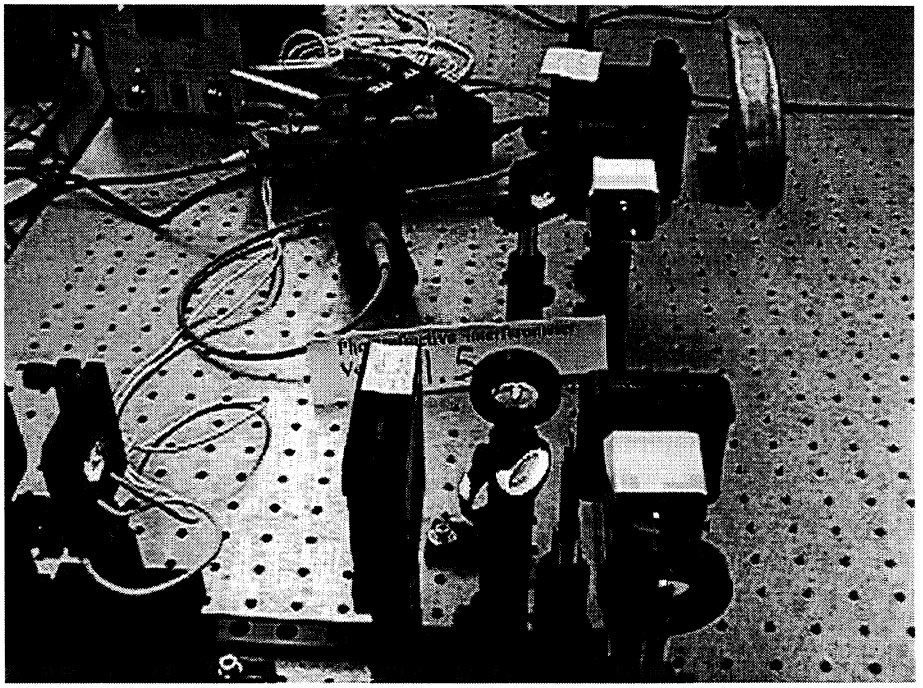

Figure 2.6.48 View of the 45° mirror (center), and of the crystal (white wires to the left).

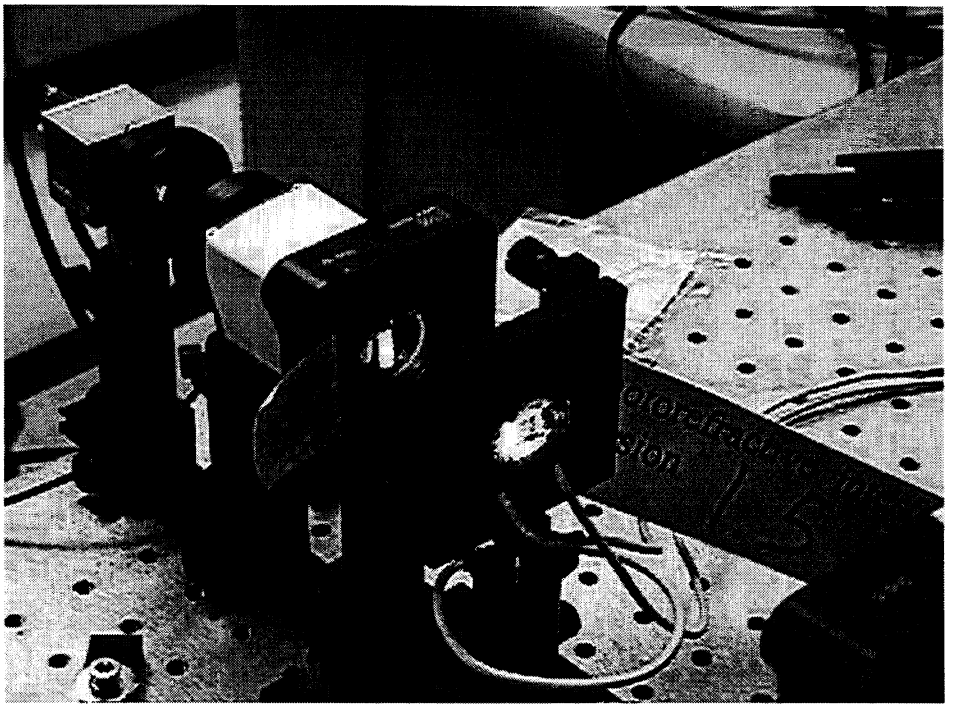

Figure 2.6.49 View of the BSO crystal with its electrodes on the sides (center).

With PRI Version 1.5, the signal to noise ratio became acceptable for laser-ultrasonics measurements. Therefore, data was recorded on static paper samples as a reference database for comparison with contact measurements.

2.6.3.4.2 Experimental setup for laser generation and laser detection on static paper grades

The experimental setup used for measurements on all paper samples was closely related to PRI Version 1.5. To detect both the A_0 and S_0 waves, the incident beam and the collected beam were placed at 40° incidence with respect to the normal to the paper surface. The detection beam was focused on the paper. The power density was kept low to avoid burning the sample.

Table 2.6.1 shows the incident power applied on the paper as a function of power measured at the output of the laser. The power of the reference beam is also shown. However, the collected power of the signal beam was below 1 mW, thus not measurable by the power meter.

Table 2.6.1 Incident power on paper and into the reference beam versus total output power.

Output power of detection laser (mW)	Incident power applied on the paper samples (mW)	type of paper grades	Power into the Reference beam (mW)
105	24.5	Medium 26-lb	67.8
120	28	33-lb linerboard, 42-lb linerboard, 69-lb linerboard, sack, tissue	77.7
140	32.5		90
150	34.8	raw stock	97
170	39.4	copy paper newsprint, art paper, bleachboard	110

On static paper samples, the spot illuminated by the laser beam is stationary so the light generates heat that must be dissipated to prevent burning. A portion of the incident beam is neither absorbed nor reflected by the paper. It just passes through the fibers through the back side of the sheet. This is especially true with low basis weight grades: copy paper, art paper, newsprint, tissue, etc.

If the incident beam is highly focused or the power is too high, it will burn a hole through the sample. The incident beam will then travel freely through the paper sample without creating any reflection and thus the signal beam will disappear.

Figure 2.6.50 shows a schematic of the BSO PRC interferometer. In Figures 2.6.51-2.6.60, a combination of pictures are shown to describe the experimental setup.

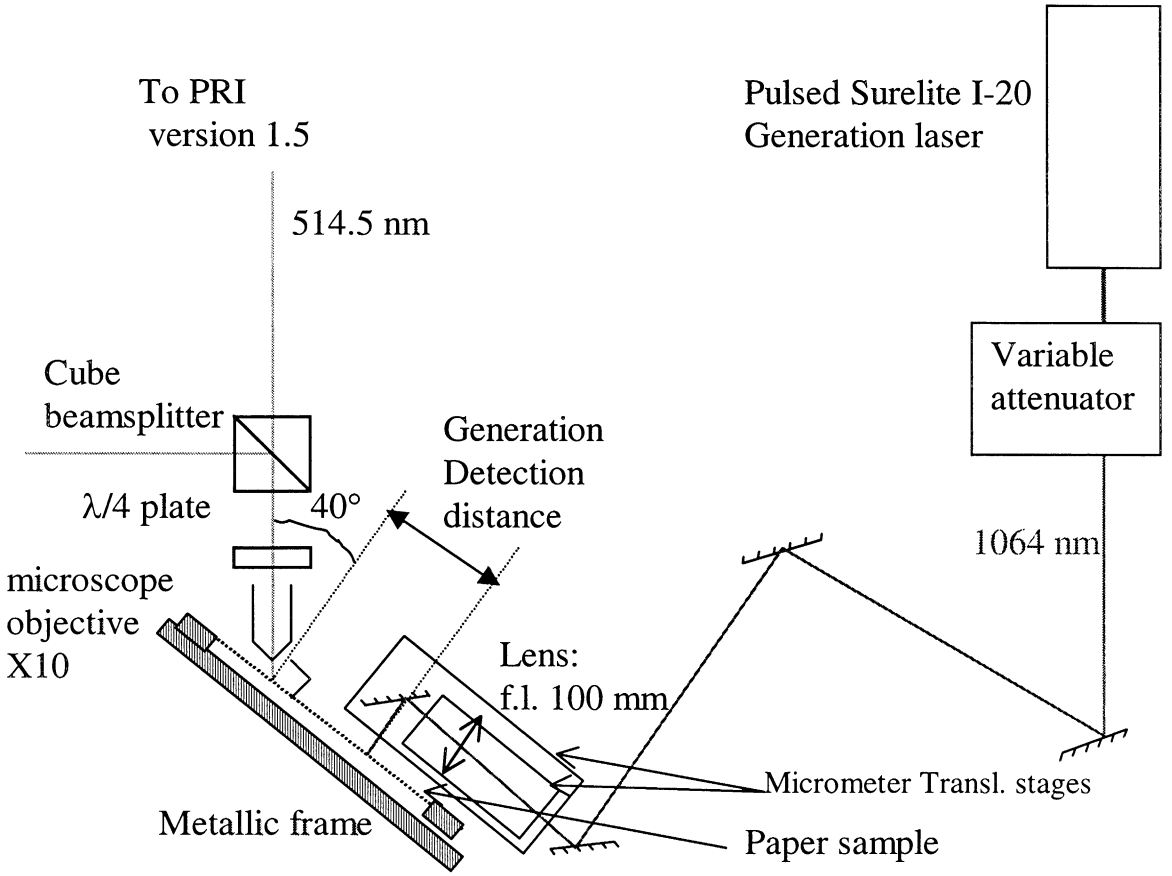

Figure 2.6.50 General schematic of the experimental setup for the tests on paper grades using BSO PRC interferometer.

Figure 2.6.51 General view of the experimental setup for the tests on paper: The detector is placed on left corner of table.

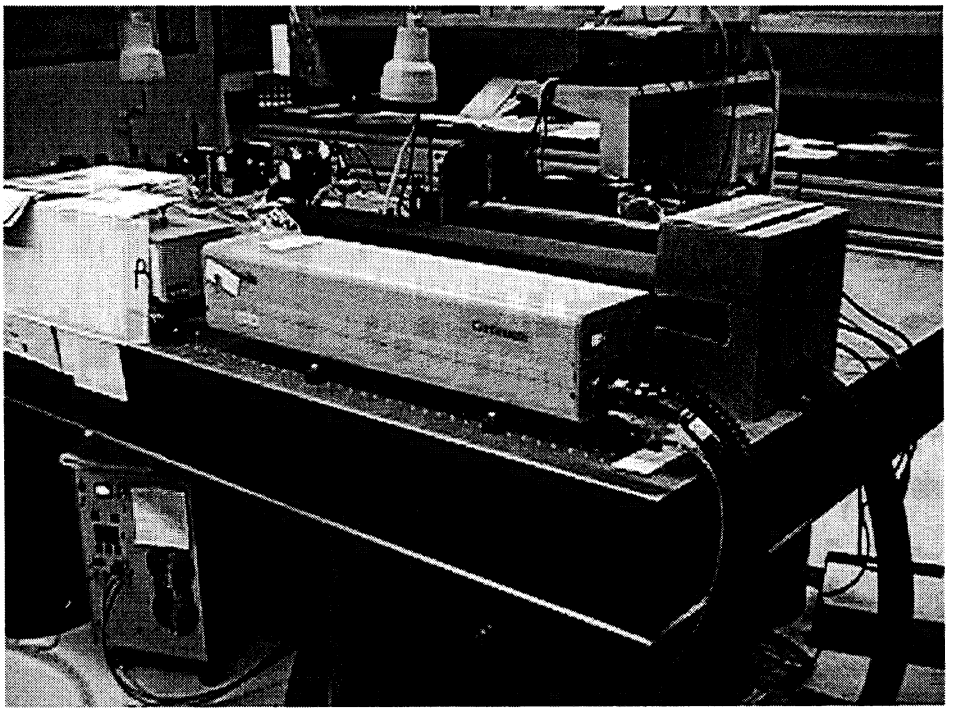

Figure 2.6.52 the table.

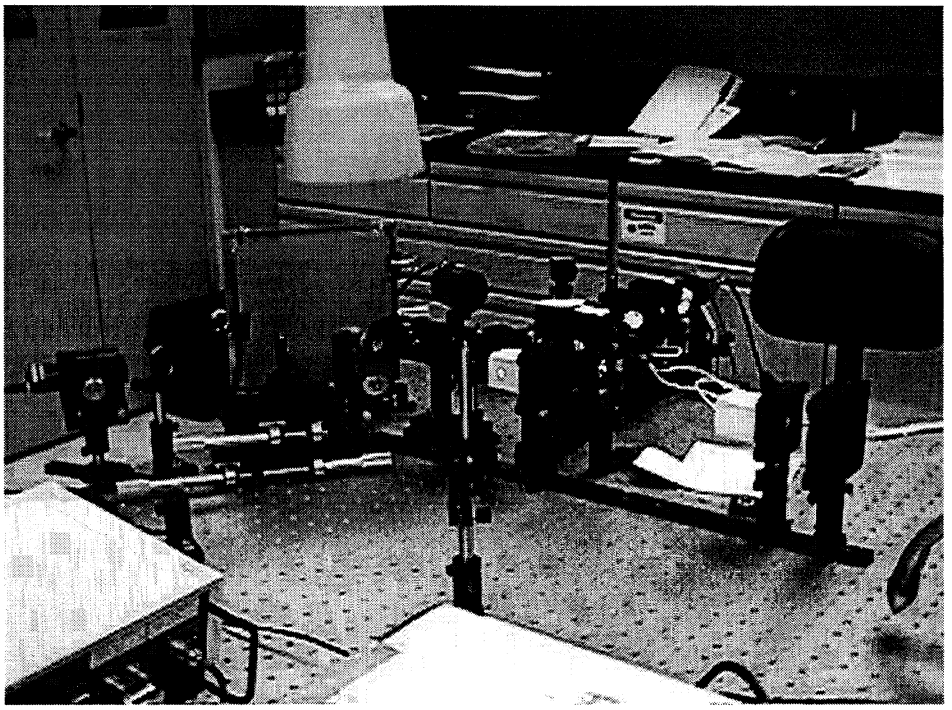

Figure 2.6.53 View of the generation optics and PRI Version 1.5, sample: 42-lb Linerboard.

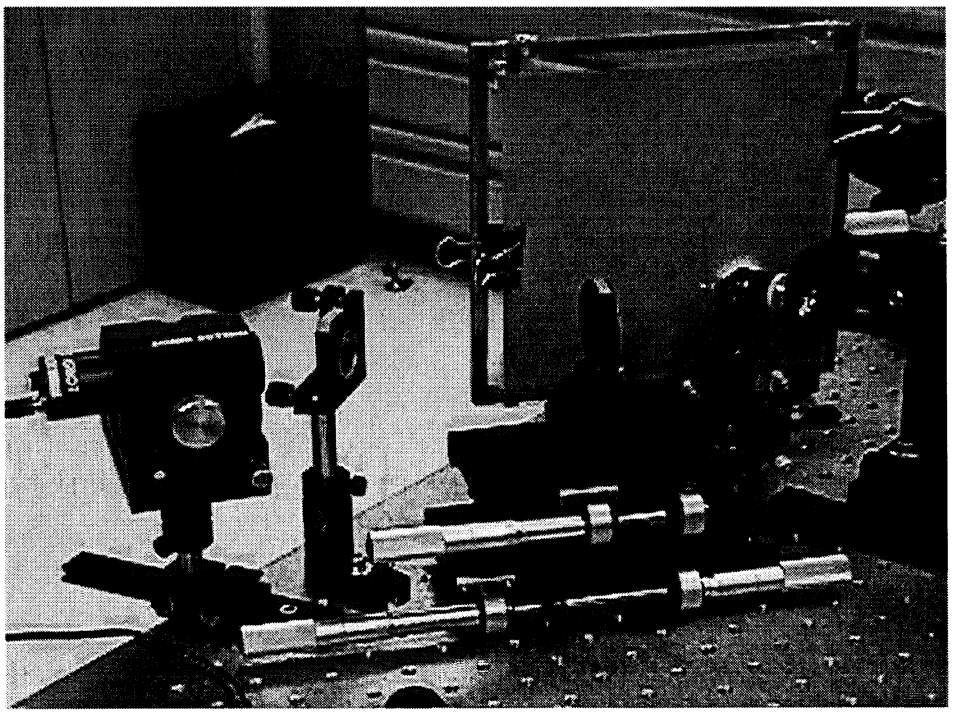

Figure 2.6.54 View of the generation optics. From the left to the right: diode alignment laser, mirror, focusing lens, and last mirror.

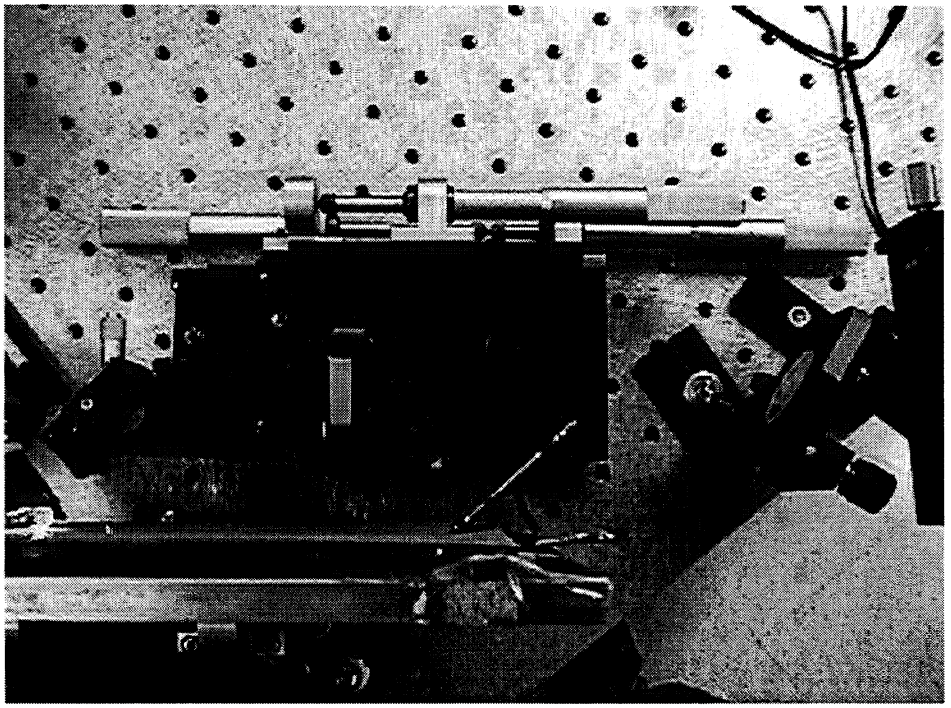

Figure 2.6.55 View from above of the generation optics and paper sample (beam comes in from right side).

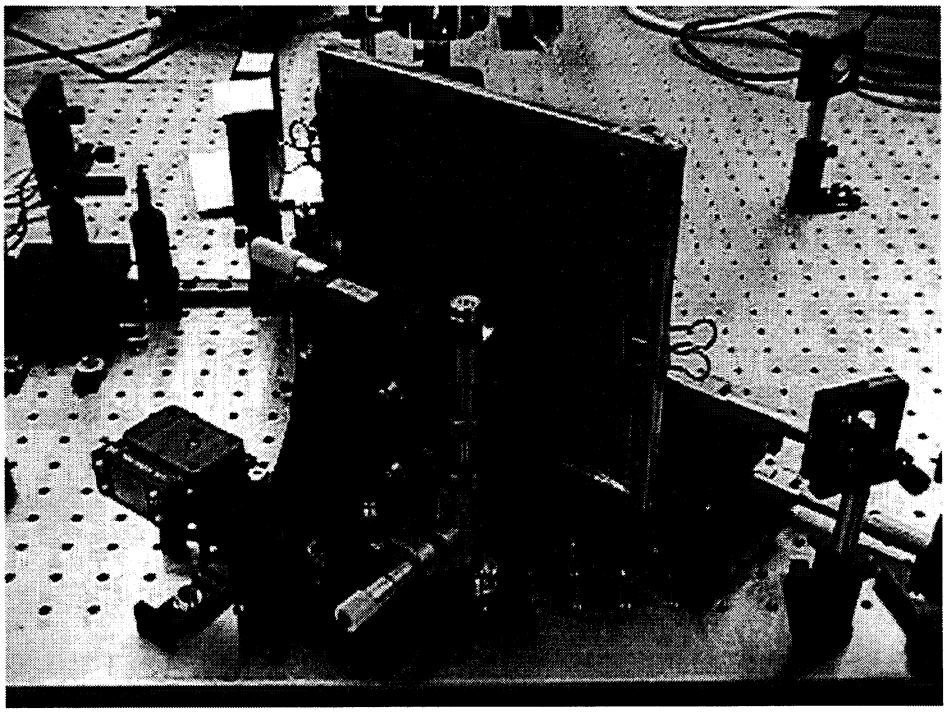

Figure 2.6.56 View from behind the paper sample holder. Edge of the sample is clamped into the brass frame, but the detection area is unsupported.

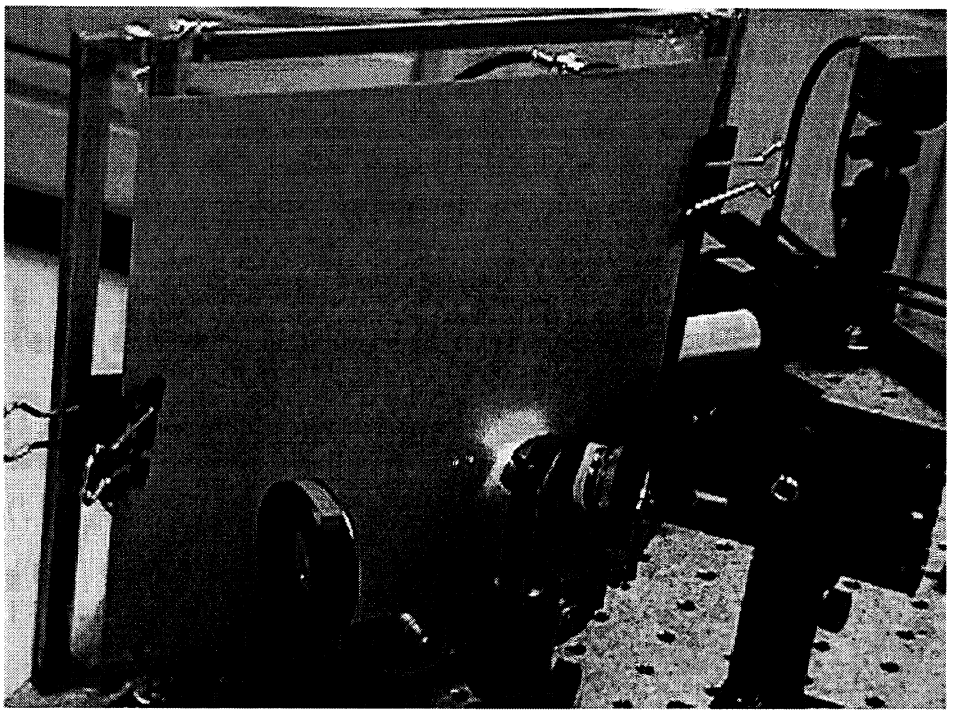

Figure 2.6.57 View of the alignment spot for generation beam (red) and detection beam (green).

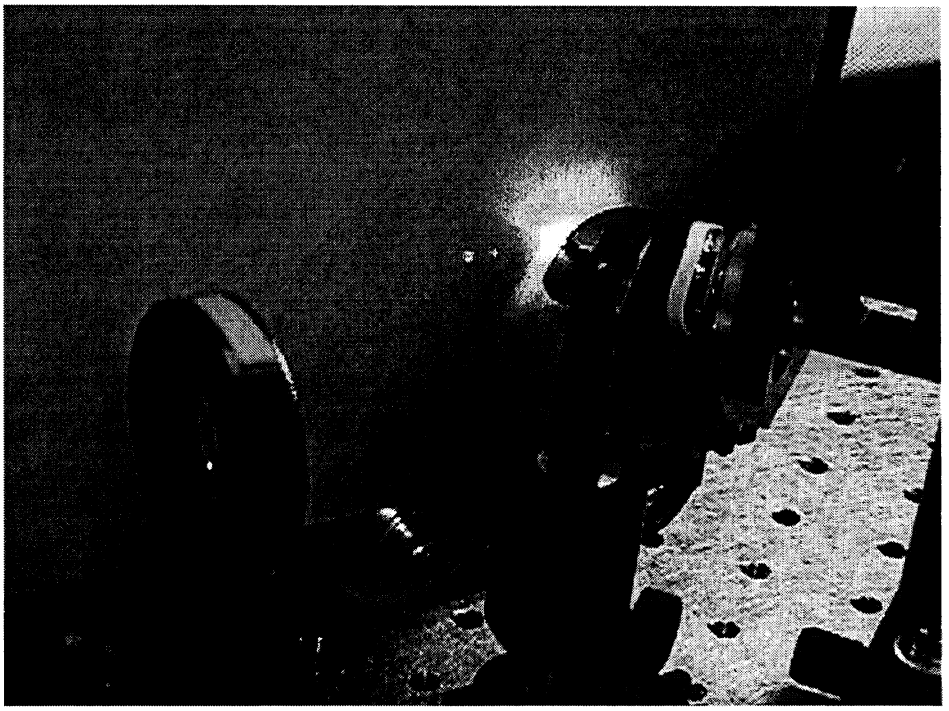

Figure 2.6.58 Close view of generation lens (red stripe), last reflecting mirror at 45°, and microscope objective of the detection beam.

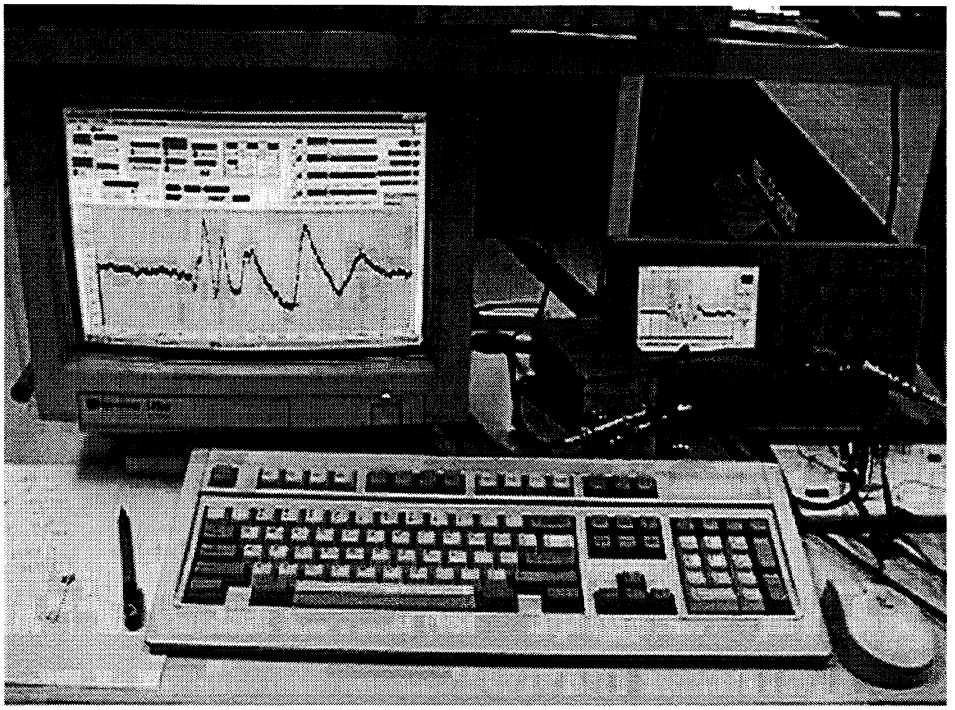

Figure 2.6.59 Laser generated A_0 wave on 42-lb Linerboard displayed with custom data acquisition software.

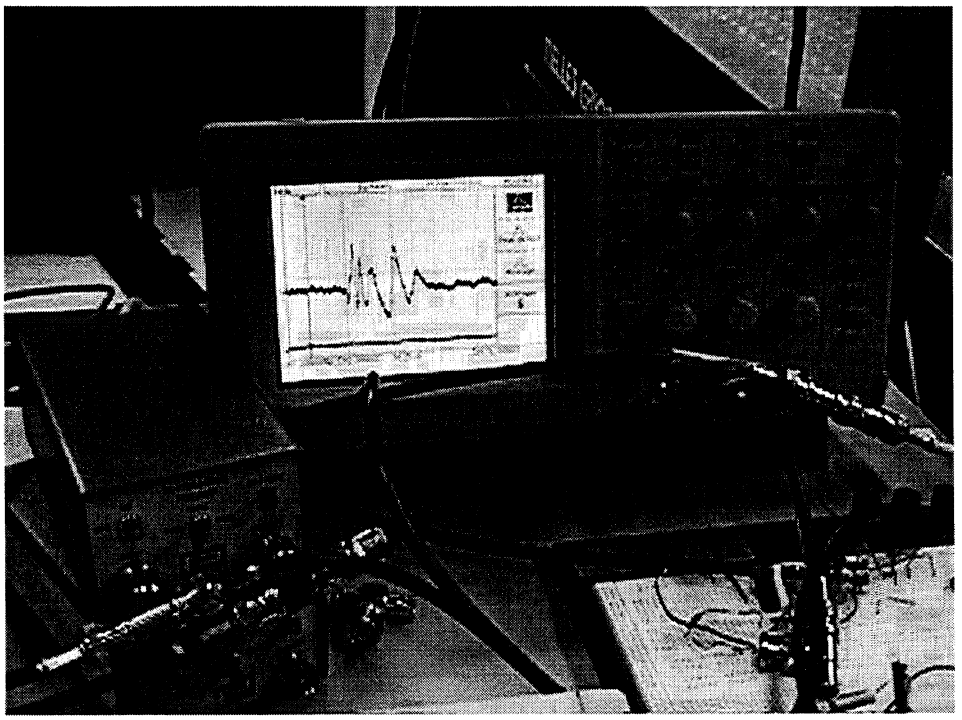

Figure 2.6.60: Laser generated A_0 wave on 42-lb Linerboard displayed on oscilloscope.

2.6.3.4.3 Time Domain Photorefractive Interferometer Results (J. Jong, IPST)

When laser ultrasonic detection is used in paper testing, signals are found to vary. This is evident in the shapes of the waveforms collected when the same configuration is used at the same detection point. The amplitude variance is obvious, however the time of wave arrival remains almost constant.

Johnson (1996) showed that, unlike in metals, some statistical variation of the waveforms in peak amplitudes and arrival time were present in paper. Using a correlation technique, he found that the relative time delay measured at the same point was within 1% difference while the delay became as large as 6% when measured at different detection points.

Figure 2.6.61 shows two examples of typical time signals obtained on copy paper using the current BSO PRC setup (Version 1.5) with the two detection points 5 mm apart. The presence of the zeroth order symmetric (S_0) mode wave is seen first. It is followed shortly thereafter by the zeroth order antisymmetric (A_0) mode wave. There may be a first order antisymmetric mode (A_1) present between the S_0 and A_0 modes as studied by Schumacher et al. (1993) in steel plate. However, this mode is ignored since it is difficult to identify due to low amplitude and of less importance compared to the two fundamental modes.

The S_0 mode is not expected to change its shape as it propagates in paper since it is nondispersive at the frequencies present [Mann et al., 1980; Johnson, 1996]. However, Figure 2.6.61 shows that the shapes of the two S_0 modes vary. A possible reason for this is that the S_0 mode may be affected by the non-uniform local characteristics of the paper at the detection point. As for the A_0 mode, it is dispersive and lasts over a longer time period. The slower components of the A_0 mode is expected to arrive later at the detection point.

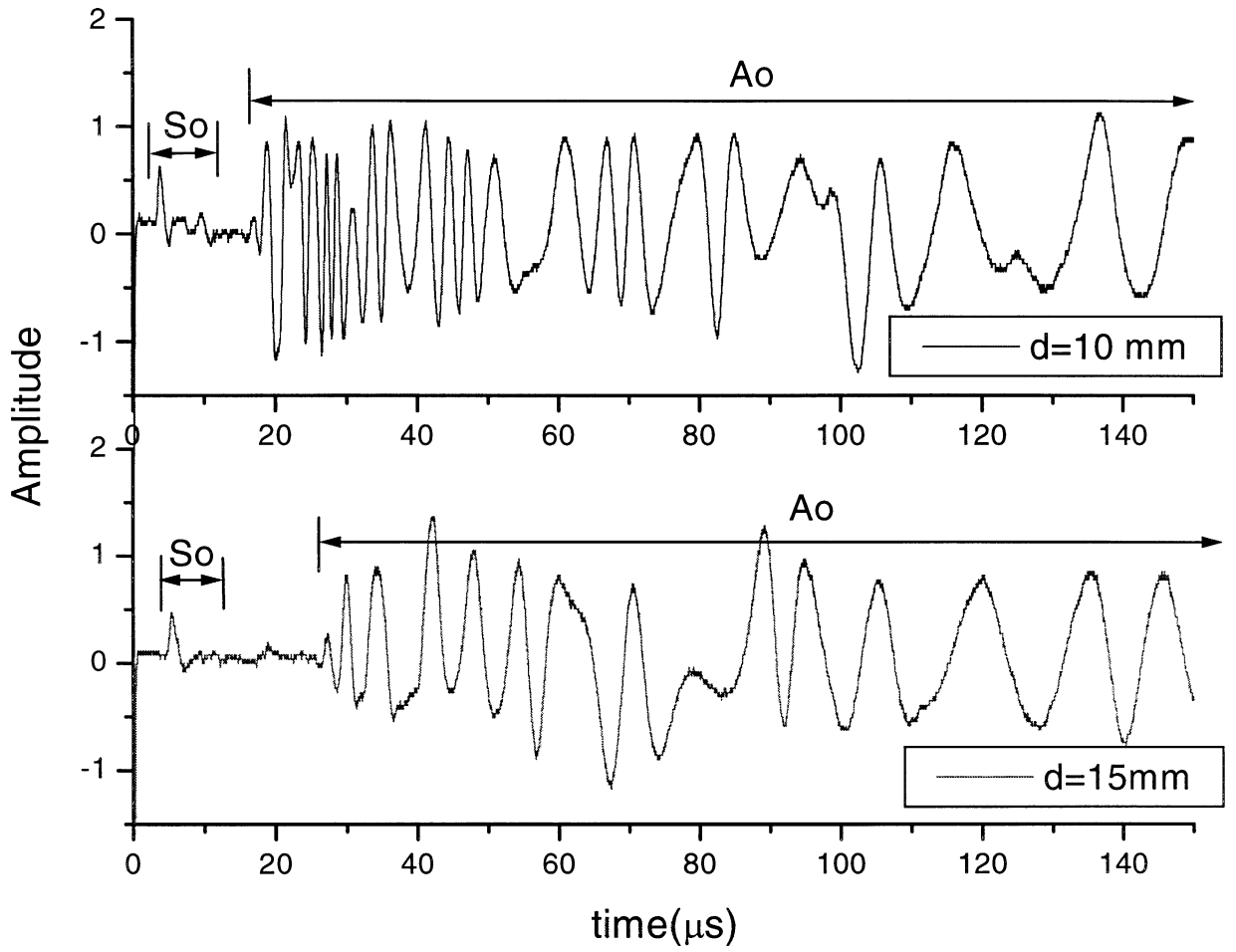

Figure 2.6.61 Typical signals collected with BSO PRC setup for static copy paper in MD: Sampling rate is 50MHz and energy is 7.74mJ. A single shot was used for data collection. The incidence of the detection laser beam is at 40°.

One remarkable achievement of the current signal detection setup using the non-contact ultrasonic laser is the quality of the signals detected without any averaging involved. The signals in Figure 2.6.61 were collected using a single shot and were found to be as good as the typical signals obtained by the contact ultrasonic laser measurements (which are always averaged).

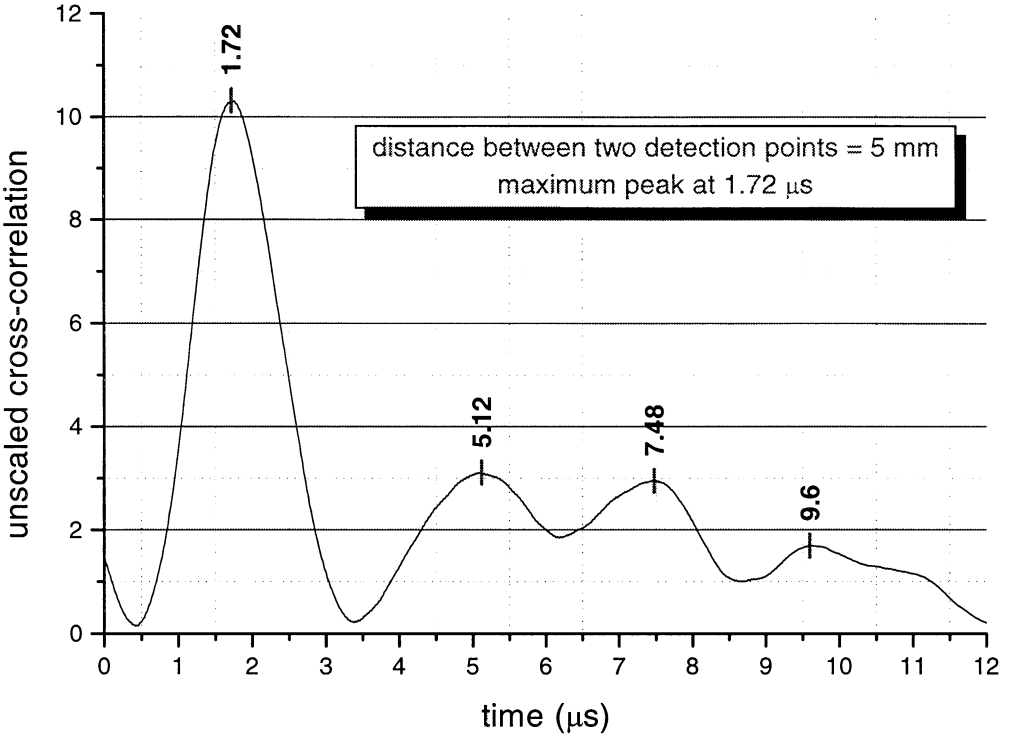

Figure 2.6.62 Cross-correlation of the two S_0 signals shown in Figure 2.6.61: This figure shows that the cross-correlation of the two S_0 waves can be found at the maximum peak of 1.72 μs. This peak corresponds to the relative time delay between the two S_0 waves. The S_0 velocity is calculated by dividing the time delay into the known distance between the two detection points.

To determine the phase velocity of the S_0 mode in MD of the copy paper, a cross-correlation function of the two S_0 signals is taken. Figure 2.6.62 shows the resulting cross-correlation of the two S_0 signals from Figure 2.6.61 with a separation distance of 5 mm. It indicates that there exists a maximum peak at 1.72 μs. Since this peak exists at the relative time delay between the two signals, the resulting S_0 velocity can be found by dividing the time delay into the known distance between the two detection points. It was found to be approximately 2910 m/s for this particular case. To be statistically valid, several trials are required and need to be averaged. Also, the same result can be found for the S_0 mode phase velocity in the low frequency region by using a cross-spectral density technique.

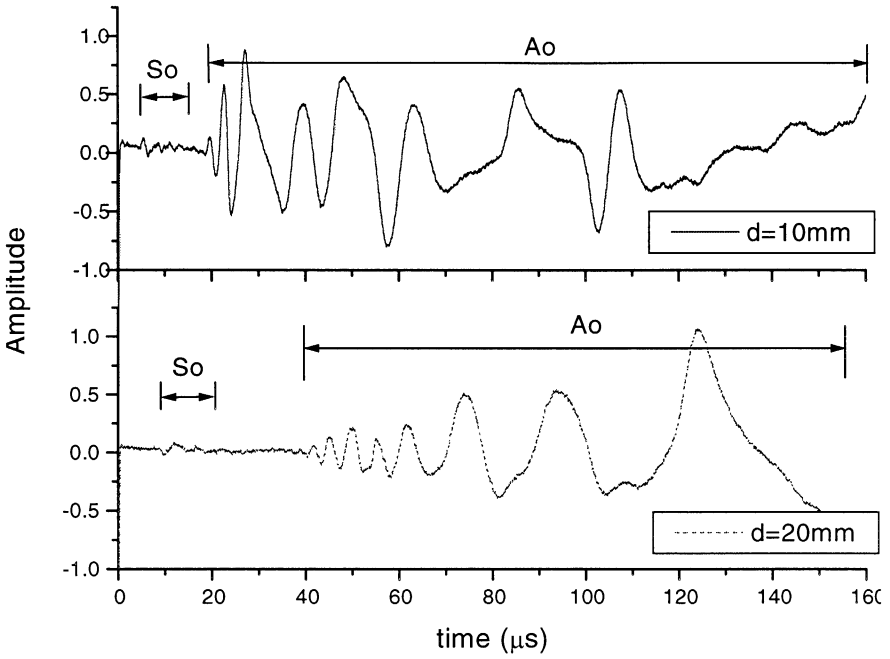

Figure 2.6.63 Signals collected with BSO PRC setup for static copy paper in CD: Sampling rate is 50MHz and energy is 6mJ. The signals were averaged 4 times.

To show the characteristics of the copy paper in CD, Figure 2.6.63 is plotted. Again, the S_0 mode is present but its shape varies noticeably. The cross-correlation function of the two S_0 signals results in the phase velocity of 1957 m/s for this case.

The S_0 mode velocity measurements in the low frequency region can be used to determine elastic stiffness constants, C_{11} or C_{22}, in MD or CD respectively. The error associated with this evaluation method is known to be less than 2% [Mann et al., 1980]. Other information that can be obtained from the S_0 mode is another elastic constant, C_{33}. Ideally, if the S_0 mode can be measured accurately around the cut-off frequency, then C_{33} can be determined independently. Yet, as Johnson (1996) found, the nature of the narrow frequency bandwidth of the CSD spectrum makes it difficult to estimate C_{33} using this method. Further work should be pursued on this matter.

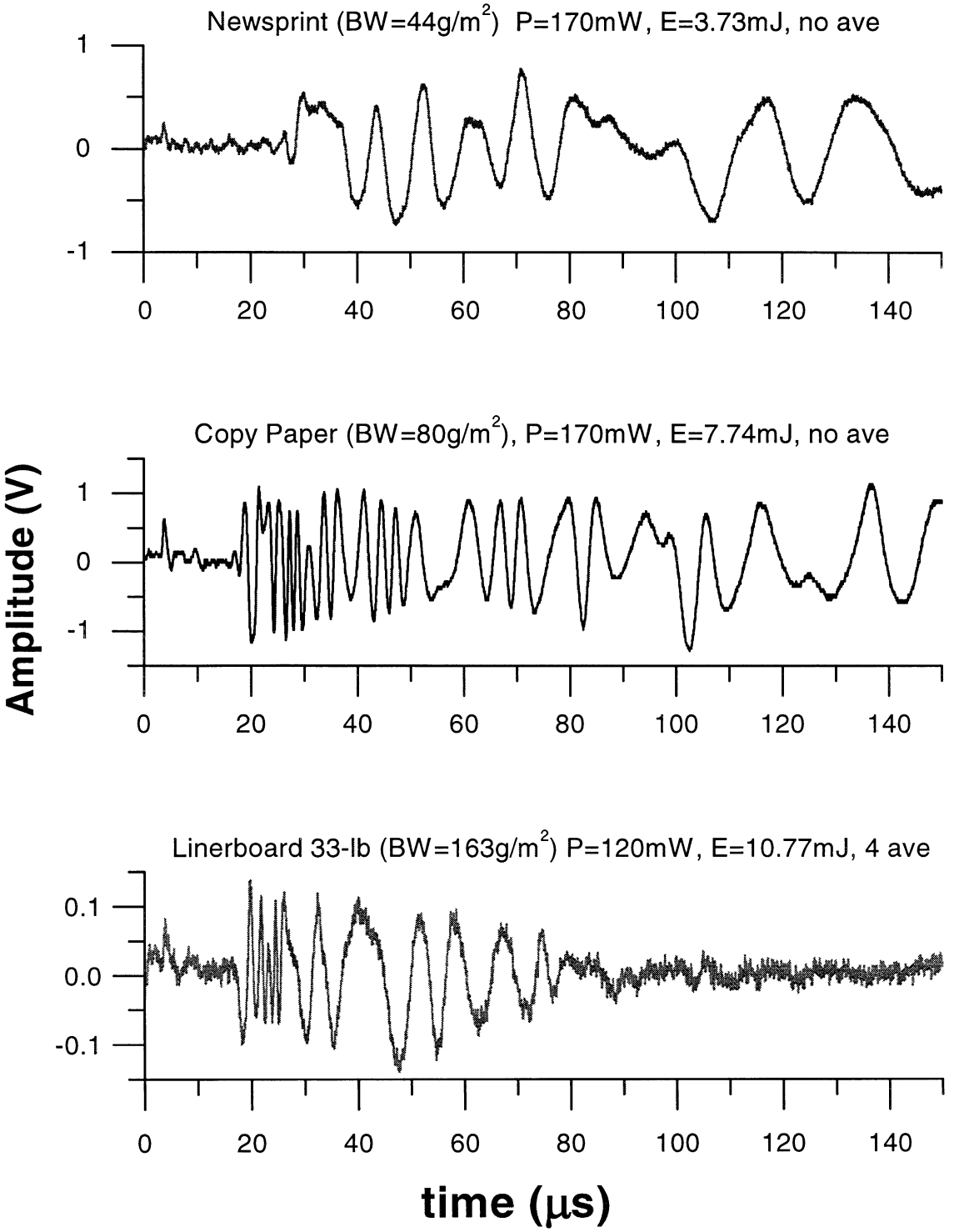

Figure 2.6.64 BSO PRC results on selected static paper samples by grammage in MD: The distance between the source and detection point was maintained at 10 mm apart and the sampling rate of 50 MHz was used throughout.

Figure 2.6.64 shows typical examples of the waveforms in MD obtained on selected static paper grades with the BSO photorefractive interferometer. The distance between the source and detection point was maintained at 10 mm apart and a sampling rate of 50 MHz was used throughout. The results from linerboard 33-lb were averaged 4 times, while the others were single shot measurements. The figure shows that each paper sample tends to respond uniquely to an ultrasonic source based on its stiffness properties. The figure also shows that the A_0 mode can easily be detected in the paper samples due to relatively large amplitudes. The amplitudes of the S_0 mode waves are small relatively. In certain samples with higher grammage, such as bleachboard and linerboard, the S_0 modes were not detected. This suggests that a technique using A_0 mode analysis should be developed rigorously so that the analysis can be based on the A_0 mode waves.

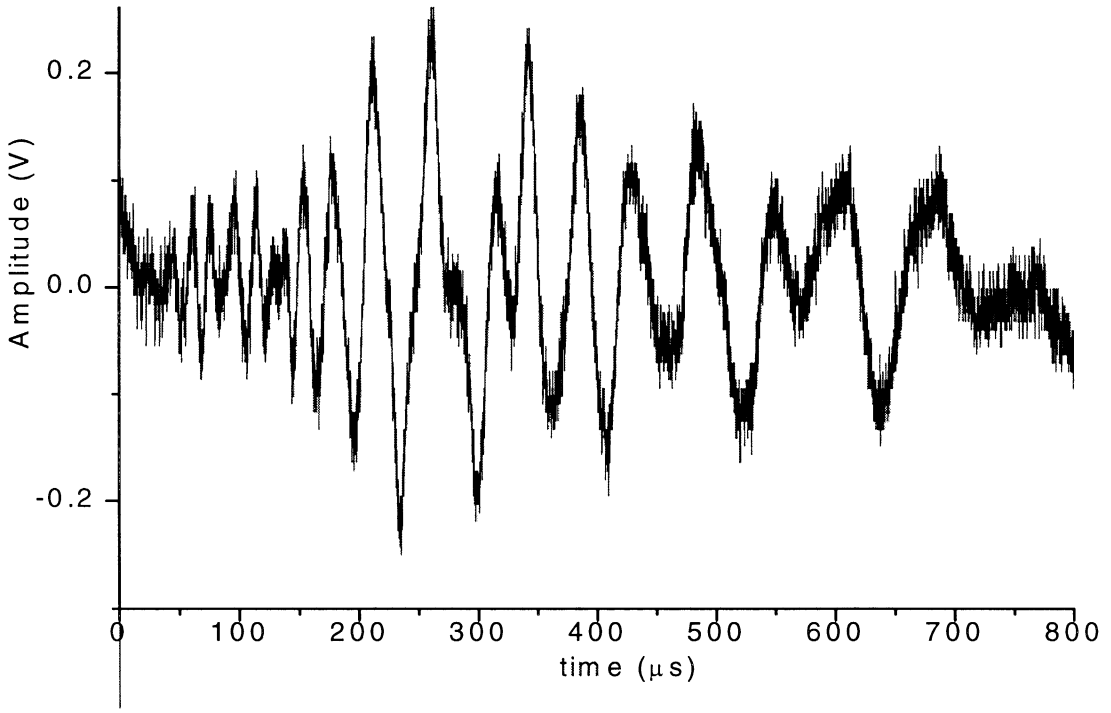

Figure 2.6.65 BSO PRC results on static 1-ply tissue paper in MD: The measurement was taken using P=120 mW and E=1.09 mJ. A single shot was used for the signal.

Figure 2.6.65 shows the BSO PRC results on a static 1-ply tissue paper in MD. Since the testing of tissue was not within the main scope of the project, only a handful of measurements were taken out of curiosity. It is noteworthy that the measurements on tissue showed encouraging results, although the response time was slower compared to other samples due to very low basis weight. So far, contact techniques have not been able to produce reliable measurements on tissue. Therefore, it shows a great potential that the current non-contact technique may be implemented on tissue as well.

The technique used here for the A_0 mode analysis is based on the one originally suggested by Sachse and Pao (1977). Later, Schumacher et al. (1993) applied it to Lamb waves. Since a time-of-flight method is not appropriate to use for the evaluation of dispersive, broadband transient waves, phase velocities are extracted from FFTs and unwrapped phase angles as a function of frequency and distance between two detection points. First, the signal generated at the same source location is recorded at two detection points along the wave path. Second, only the region of the signal corresponding to the A_0 mode is selected and the rest is zero-padded. Then, the signal is windowed using a rectangular window. Third, each signal is processed for spectrum analysis and the FFT is plotted. Finally, the phase angle of the signal is unwrapped and the difference of the two are directly related to the phase velocity of the A_0 mode using the following relationship:

$$c = \frac{-2\pi \cdot f \cdot d}{(\Delta\phi + 2m\pi)}, \qquad (3)$$

where c is the phase velocity of the A_0 mode (m/s), f is the frequency (Hz), d is the distance between the two detection points (m), $\Delta\phi$ is the difference in unwrapped phase angle for a given frequency (radians), and m is an integer associated with a correction of the phase at lower frequency.

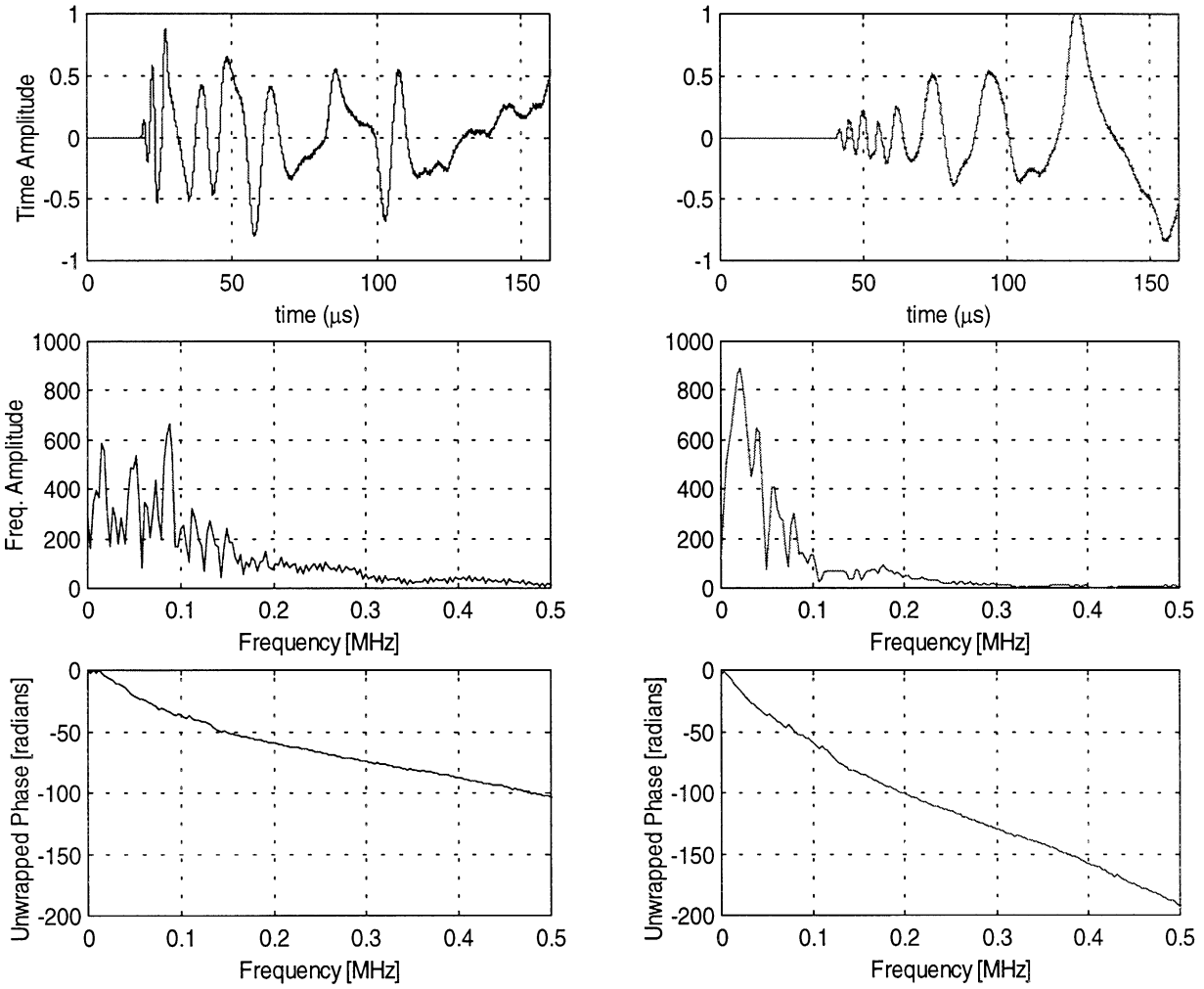

(a) d=10 mm (b) d=20 mm

Figure 2.6.66 A_0 mode analysis of the signals shown in Figure 2.6.63 on static copy paper in CD: The figure showing the portion of the wave not corresponding to the A_0 mode is zero-padded. Then, a rectangular window is superposed onto the signal. The FFT of the signal is computed and the unwrapped phase angle is extracted.

Figure 2.6.66 shows the combination of the steps involved in the technique for evaluating the A_0 mode wave for d = 10 mm and 20 mm, respectively. For each case, the zero-padded A_0 waveform is windowed and processed to compute the FFT spectrum. The unwrapped phase angle is determined. The FFTs of the two signals indicate that the signal energy exists only in the low frequency regions below 0.3 MHz. This trend is consistent throughout the experiments. On the other hand, the results given by Johnson (1996) on static copy paper showed that the energy was still present up to 1 MHz. The reason for not being able to detect higher frequency A_0 component with the current PRC configuration was unclear. Nevertheless, it is not necessary to have the higher frequency A_0 component present to determine the paper stiffness, since the values of the stiffness constants can be evaluated using the low frequency information only.

More immediate concern comes from what value of the integer *m* should be used to correct the phase angle at the very low frequency region where the signal energy is low. As the phase unwrapping is performed from low to higher frequencies, the accuracy of the phase at a given frequency depends on that of the phase at lower frequencies, where discontinuities exist. A small error in phase angle at very low frequency may accumulate and result in a significant difference at higher frequencies.

Figure 2.6.67 shows a comparison between a theoretical A_0 dispersion curve and the results with corrected phase angles. The phase velocity determined without a correction tends to show a somewhat higher prediction in the low frequency region below 0.1 MHz, while the one corrected with -2π seems to match with the theoretical curve. Comparison with other paper samples showed that good prediction seems to come with a correction of -2π or -4π. Nevertheless, further analysis is required to determine the accuracy of the correction term *m* for the A_0 mode analysis.

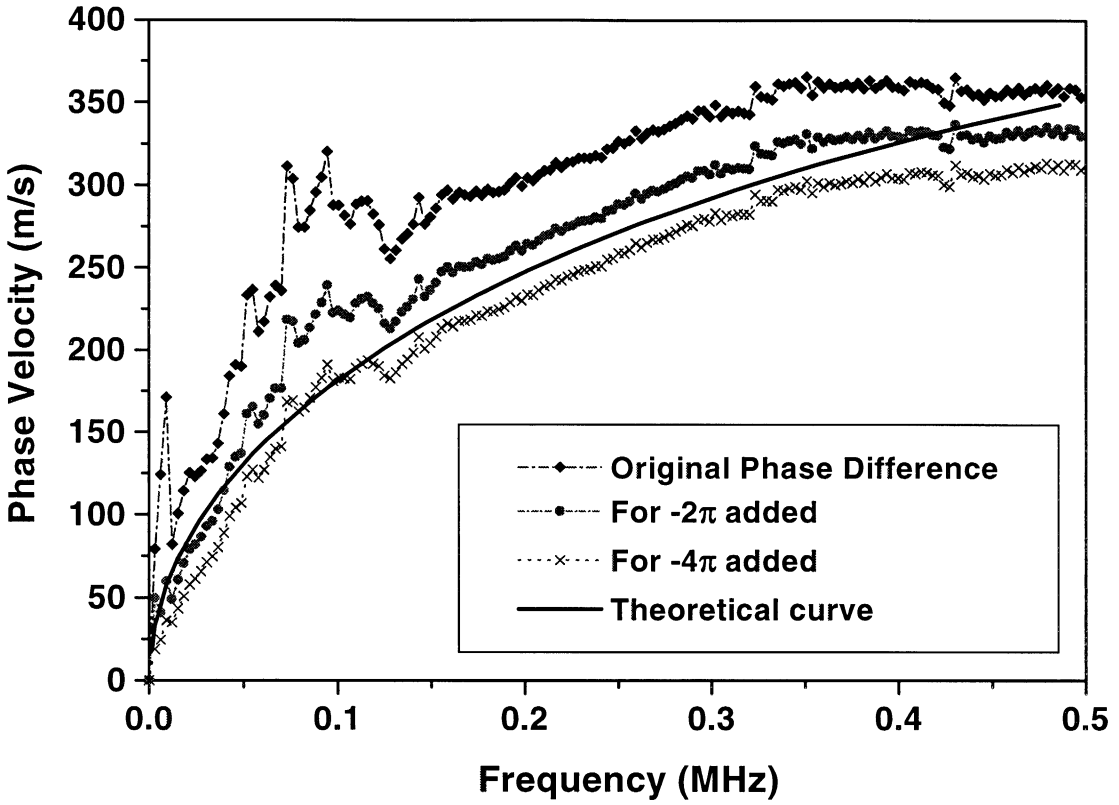

Figure 2.6.67 Comparison of the Ao mode velocities between a theoretical dispersion curve and the velocities with corrected phase angles on static copy paper.

2.6.3.4.4 Improvement of experimental setup on static paper, second round of measurements with 2 paper grades

Most of the measurements on samples were made using a strong ablation mode for generation (around 3-17 mJ/pulse over a spot of ≅ 100 μm diameter) to obtain high amplitude signals. This was not appropriate for two reasons: first, the strong ablation mode damages the paper; second, the strength of the acoustic source varies significantly with the number of shots consecutively made at the same spot. Therefore, for the new interferometer, efforts were made in two directions: reducing the damage to paper by decreasing the power density of the generation beam, and increasing the interferometer sensitivity.

The schematic of the improved version of the photorefractive interferometer (Version 1.6) is shown in Figure 2.6.68.

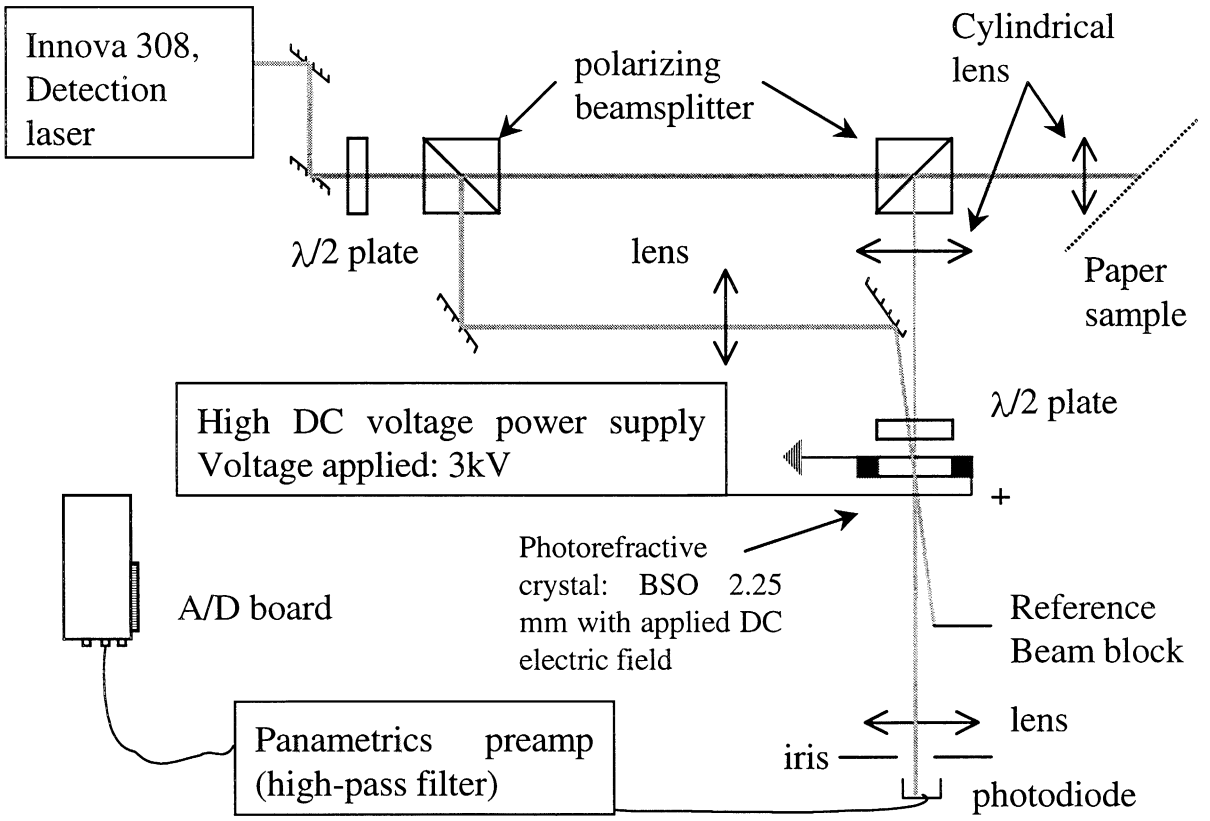

Figure 2.6.68 Schematic of photorefractive interferometer Version 1.6 (line detection).

The cylindrical lens close to the paper sample focuses the circular beam into a line along the vertical direction. The focal length is 48.9 mm at 514 nm and the diameter of the lens is 25.4 mm. It should be noted that this specific lens was intended for use with 1064 nm so was not properly anti-reflection coated for 514 nm, and thus a significant amount of the power was lost. The focused detection spot was a vertical line 2 mm long and 0.5 mm wide. Using this configuration, the interferometer was sensitive to ultrasonic waves propagating in the horizontal direction (i.e., perpendicular to the detection line). This configuration (line detection) presents a

significant advantage over point detection since the total amount of power impinging on the paper can be increased without burning it.

This is especially interesting for the linerboard sample in which the damage threshold and the collected power are very low, resulting in a poor signal to noise ratio. The incoming polarization on the paper was linear horizontal as opposed to circular as in previous interferometers. It was found that the rough surface of paper was depolarizing the back-scattered light. Therefore, a quarter wave plate before the focusing lens was not necessary since the polarizing cube beamsplitter selected only the vertically polarized speckles before sending them to the crystal as a signal beam. Figure 2.6.69 shows a picture of Version 1.6.

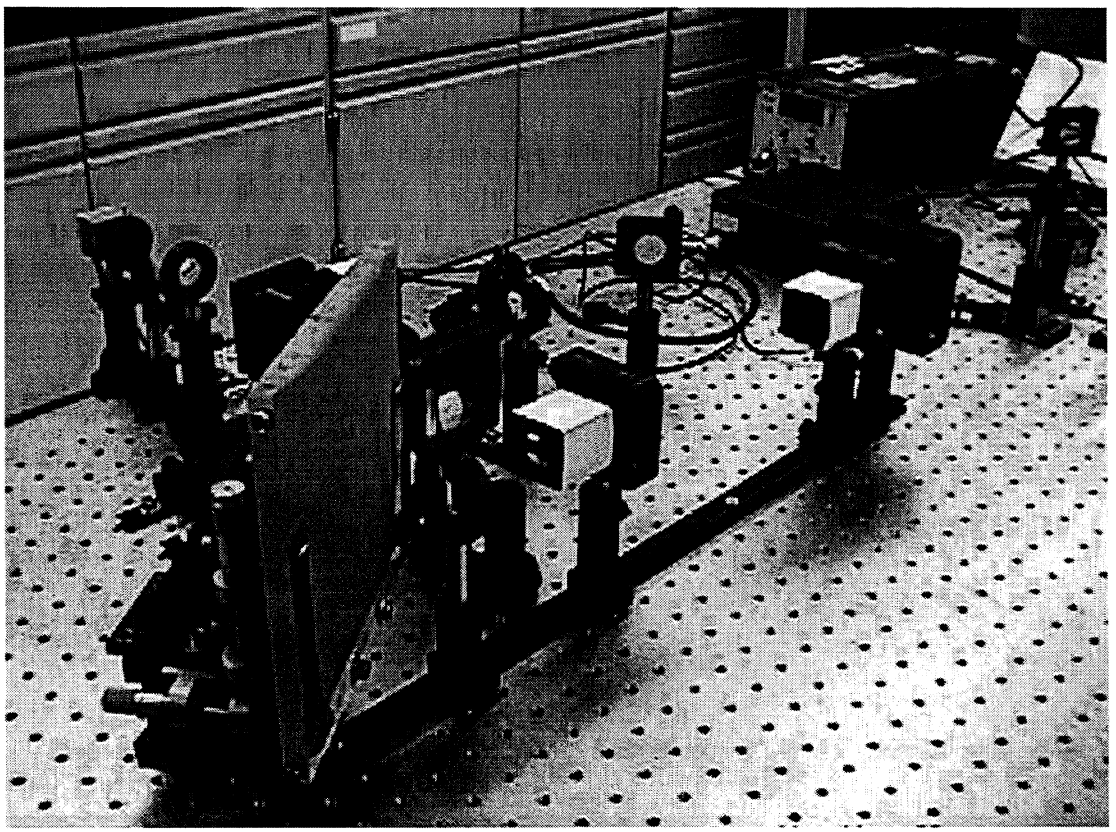

Figure 2.6.69 General view of photorefractive interferometer Version 1.6.

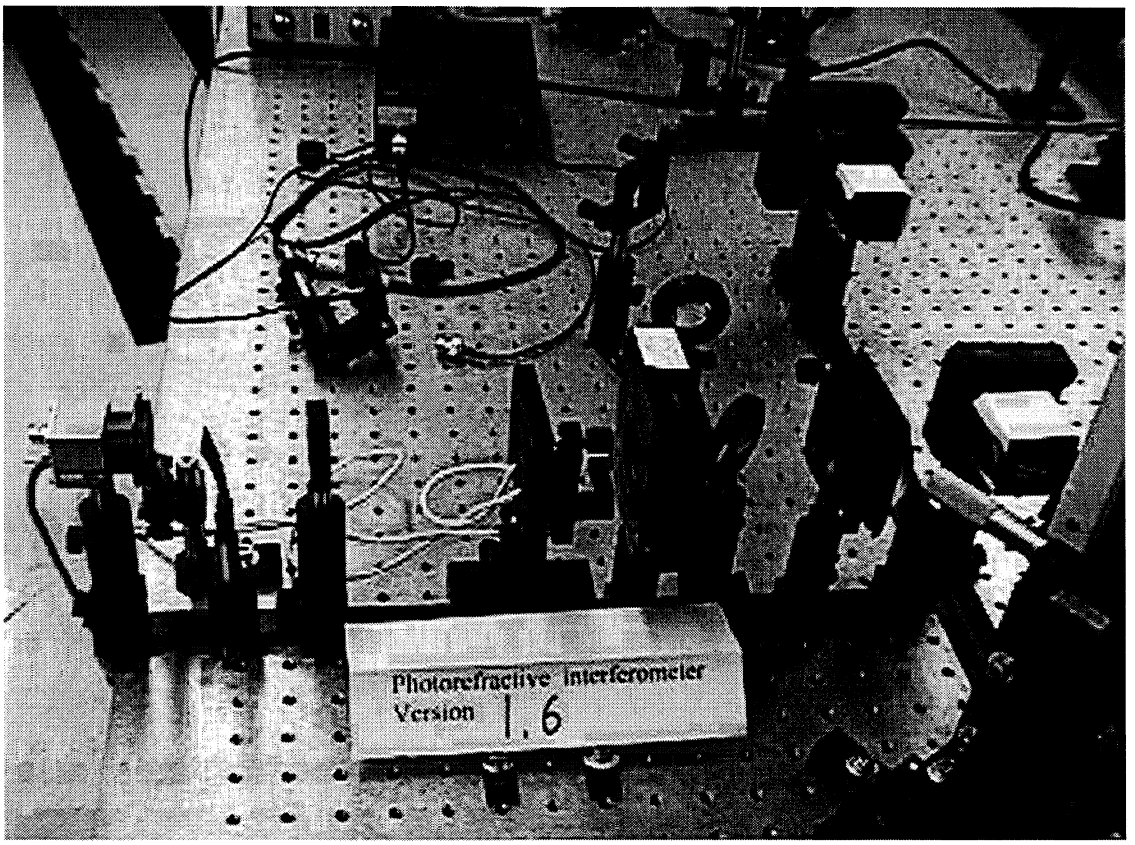

Figure 2.6.70 View from the side of photorefractive interferometer Version 1.6. PRC is the object with the white wires attached to it in the center. The photodiode is to the left, and the sample is bottom right.

As the same cylindrical lens is used to focus and collect the beam, the spot collected by the lens is a line. This line needs to be refocused to a circle by another cylindrical lens (Figure 2.6.70) onto the surface of the photorefractive BSO crystal. This enhances the interference with the reference beam.

Since the phase information (thus the ultrasonic displacements) is written by the photorefractive effect on the signal beam after it passes through the crystal, the signal beam can go directly to the photodiode without a polarizer filtering out the reference beam. Therefore, the polarizing cube beamsplitter after the crystal was removed from this setup in comparison to the PRI Version 1.5.

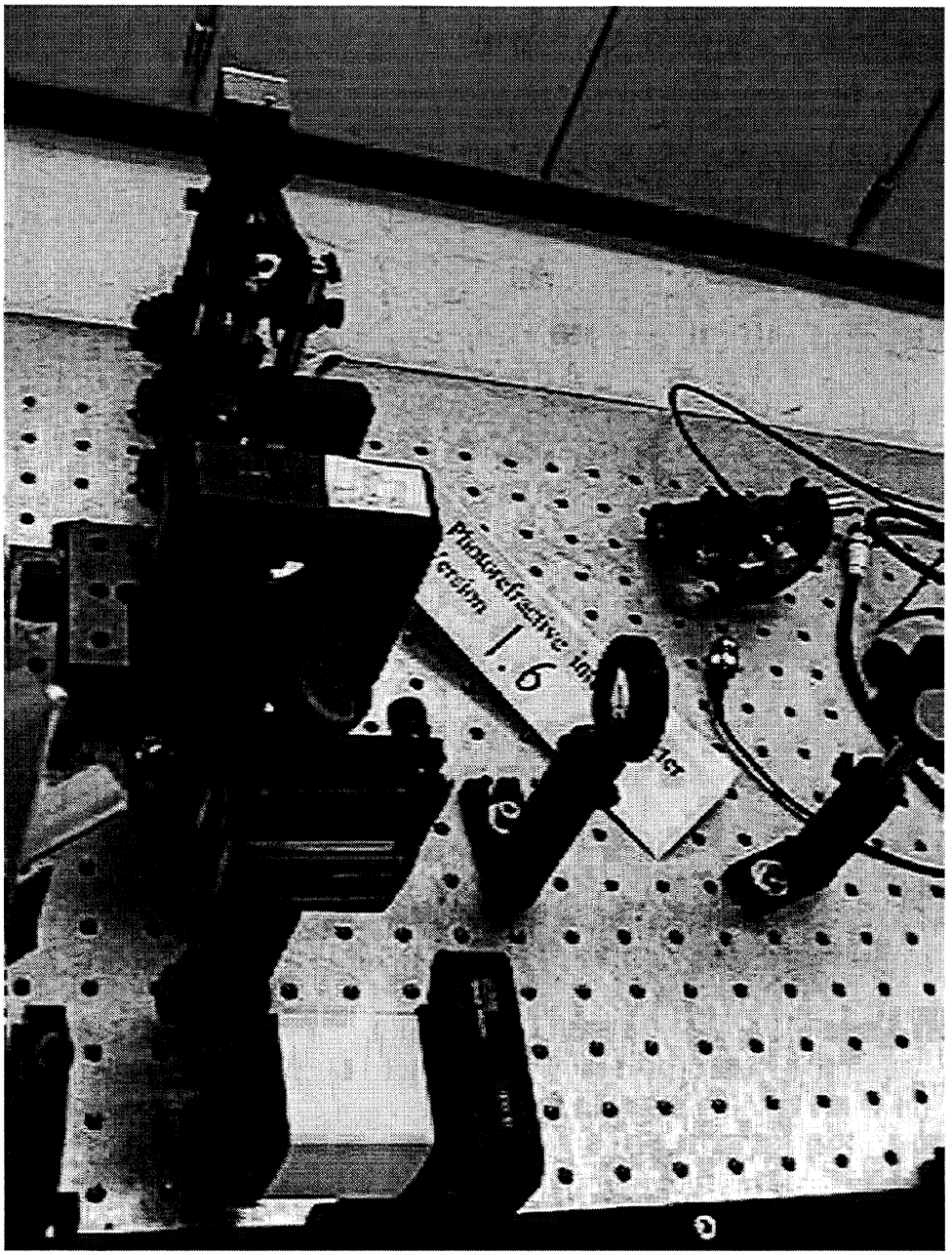

Figure 2.6.71 View of polarizing beamsplitter (bottom) and refocusing large cylindrical lens (just above the beamsplitter).

So far, a comparison between PRI Versions 1.5 and 1.6 under the same conditions has not been made, but it seems that the sensitivity is significantly better for PRI Version 1.6. Figure 2.6.72 shows a schematic of Version 1.6 with an updated set of generation optics.

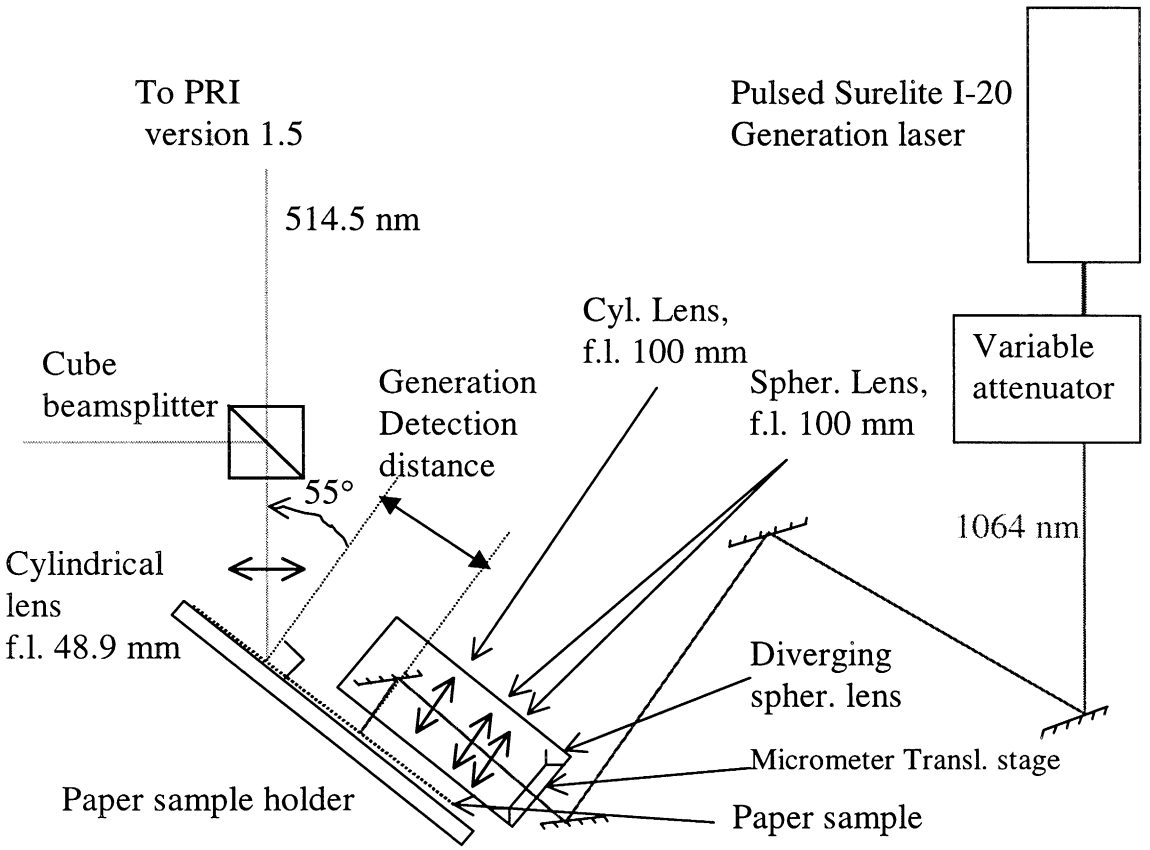

Figure 2.6.72 Schematic of the improved detection and generation systems with PRI Version 1.6.

The generation optics were also changed to generate ultrasound with a line. The advantage is that the attenuation of the amplitude occurs only due to the viscoelastic behavior of paper not due to geometrical circular spreading. This is important for the measurements taken at relatively long generation/detection distances (> 20 mm). Also, another advantage is that it is possible to generate roughly the same amplitude of displacements by putting slightly more energy per pulse without burning the sample, because the laser spot is spread out over a much larger surface (a line instead of a point). Figure 2.6.73 shows a picture of Version 1.6 with a new sample holder. Figure 2.6.74 shows a close-up view of the improved generation optics.

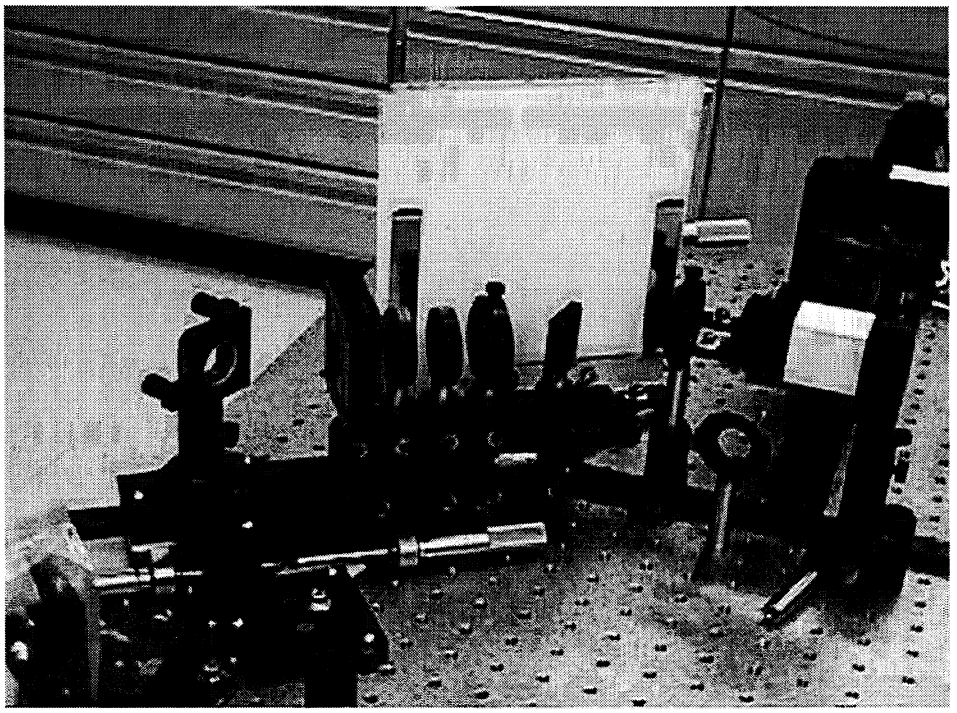

Figure 2.6.73 View of the improved detection and generation systems with PRI Version 1.6 and new paper sample holder.

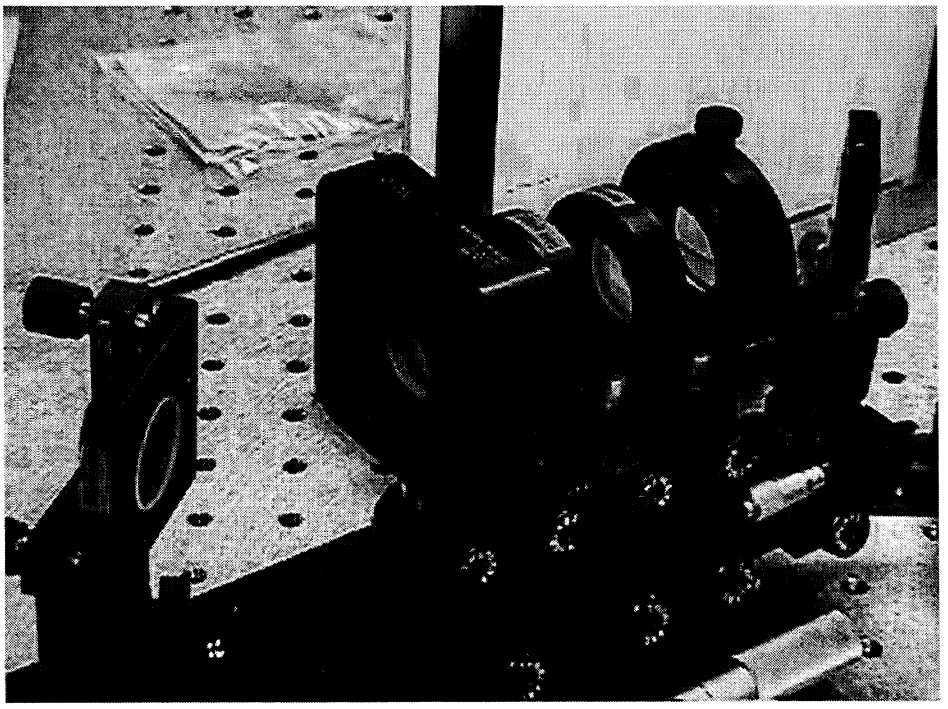

Figure 2.6.74 Close view of the improved generation optics.

The new generation optics include:

- One additional diverging spherical lens with short focal length, to expand the 1064 nm laser beam;
- Two additional converging spherical lens, each with a focal length of 100 mm to compensate for divergence;
- One additional converging cylindrical lens, focal length of 100.5 mm, focusing the beam into a vertical line;
- One mirror at 45° incidence to direct the beam onto the paper.

In Version 1.6, the generation beam is still normal to the paper surface. The dimension of the generation spot was 11 mm long x 0.5 mm large.

2.6.3.4.5 Results of the improved setup

2.6.3.4.5.1 Results on 42-lb Linerboard

Further measurements were obtained for laser generated waves travelling along the cross direction (CD) of the sample. They are presented as a function of distance between the generation and the detection points. The dispersive nature of the A_0 wave is clearly visible. Because of the saturation of the photodiode by the generation laser pulse, the S_0 wave is disguised in the initial noise.

All data presented in Figure 2.6.75 are single shot measurements. Even at relatively long distance between the generation and the detection points (d = 40 mm), the A_0 waveform remains visible on 42-lb linerboard.

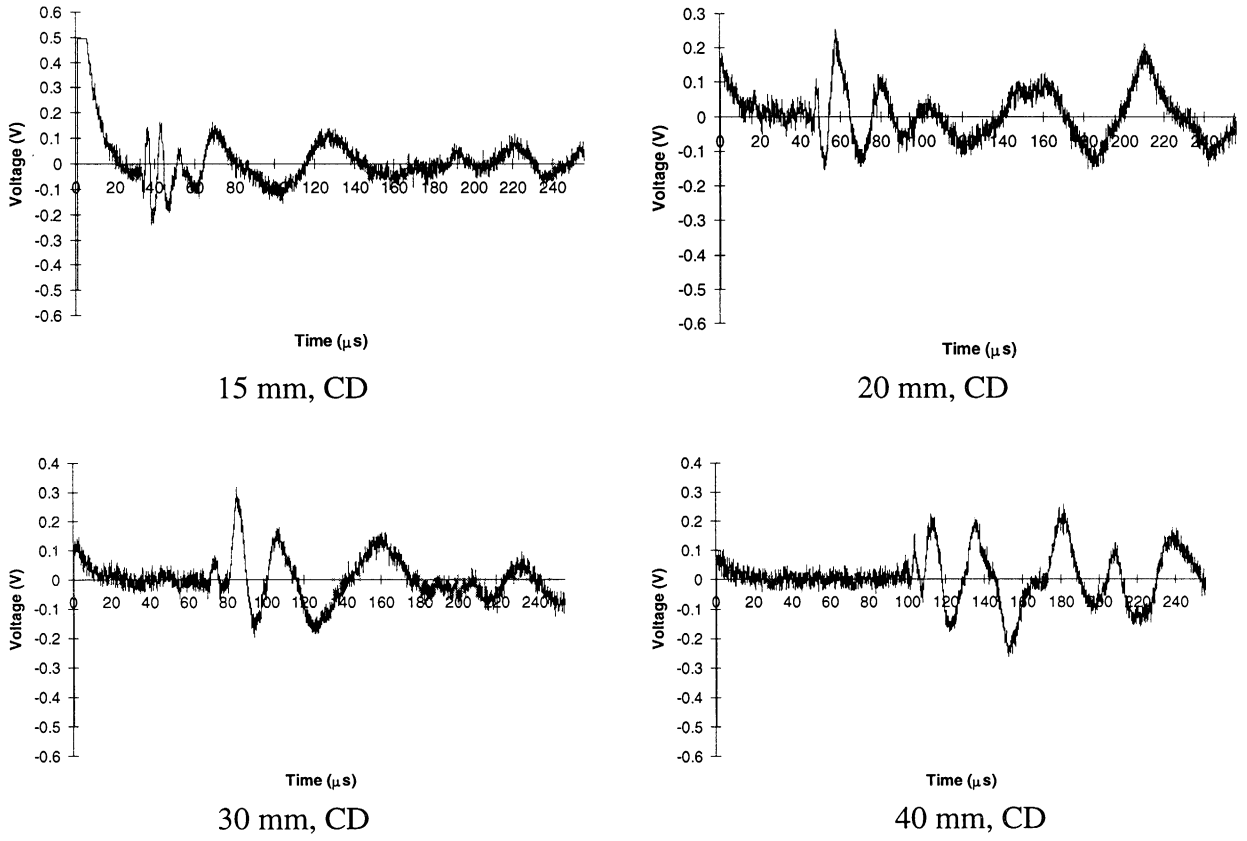

Figure 2.6.75 Laser generated ultrasound on 42lb linerboard , using improved setup. All graphs are single shot measurements.

2.6.3.4.5.2 Results on Copy Paper

Measurements were obtained for laser generated waves travelling along the cross direction (CD) and machine direction (MD) on copy paper. Again, some examples are presented as a function of distance between the generation and the detection points.

All the data presented in Figure 2.6.76 are single shot measurements along CD. The S_0 waveforms are visible but have small amplitudes compared to the A_0 waveforms. The dispersive nature of the A_0 wave is evident.

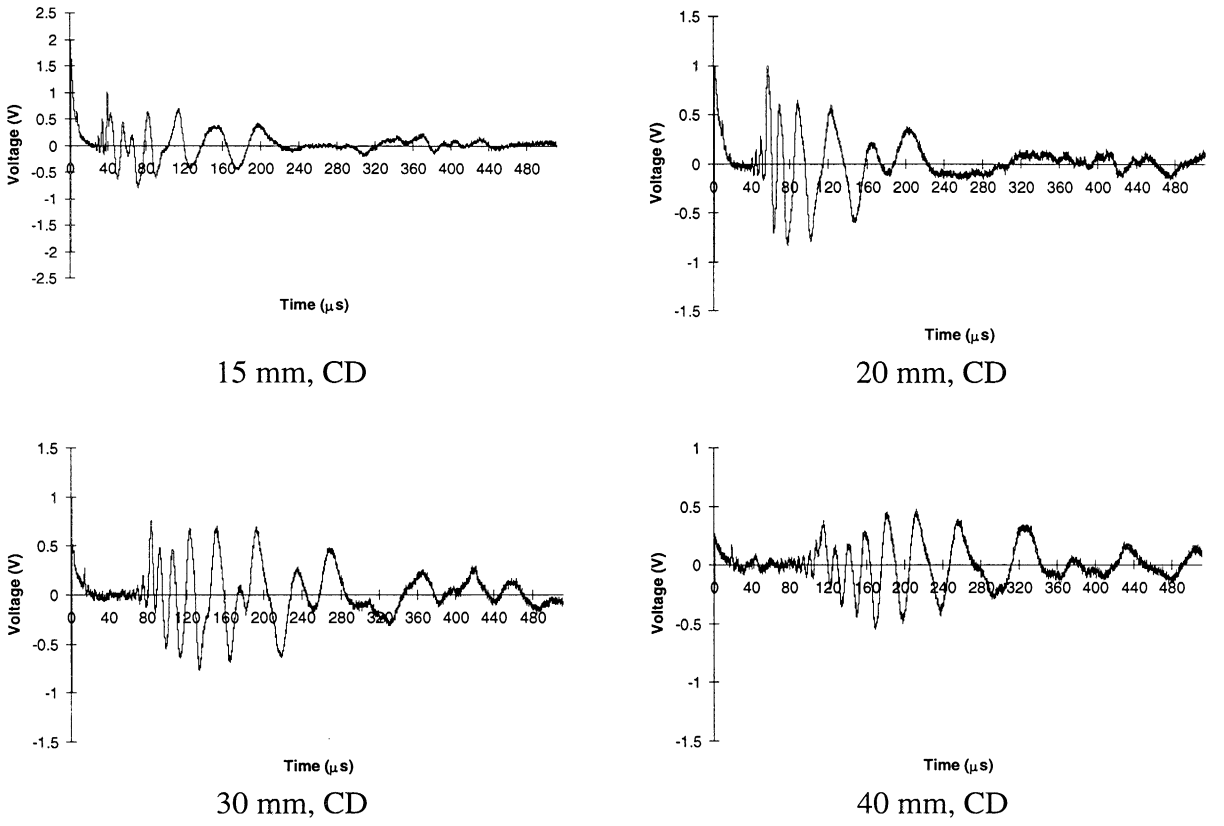

Figure 2.6.76 Laser generated ultrasound on copy paper, along CD, using improved setup. All measurements are single shot.

In Figure 2.6.76, the generation pulse had the same energy level of 40.2 mJ. The S_0 waveform is more clearly visible at longer generation-detection distances because the saturation of the photodiode by the generation pulse is not as strong. There is less 1064 nm parasitic light collected by the detection optics when the two spots are further apart and the arrival time of the S_0 wave is starting to come out of the saturation zone of the first 10 μs.

Figure 2.6.77 shows the results on copy paper along MD. The waveforms traveling along machine direction are very similar in shape to those obtained along cross direction. The time of flight is of course different because the elastic constants are different between machine direction

and cross direction. Indeed, the arrival of both S_0 and A_0 waves in machine direction is earlier than in CD.

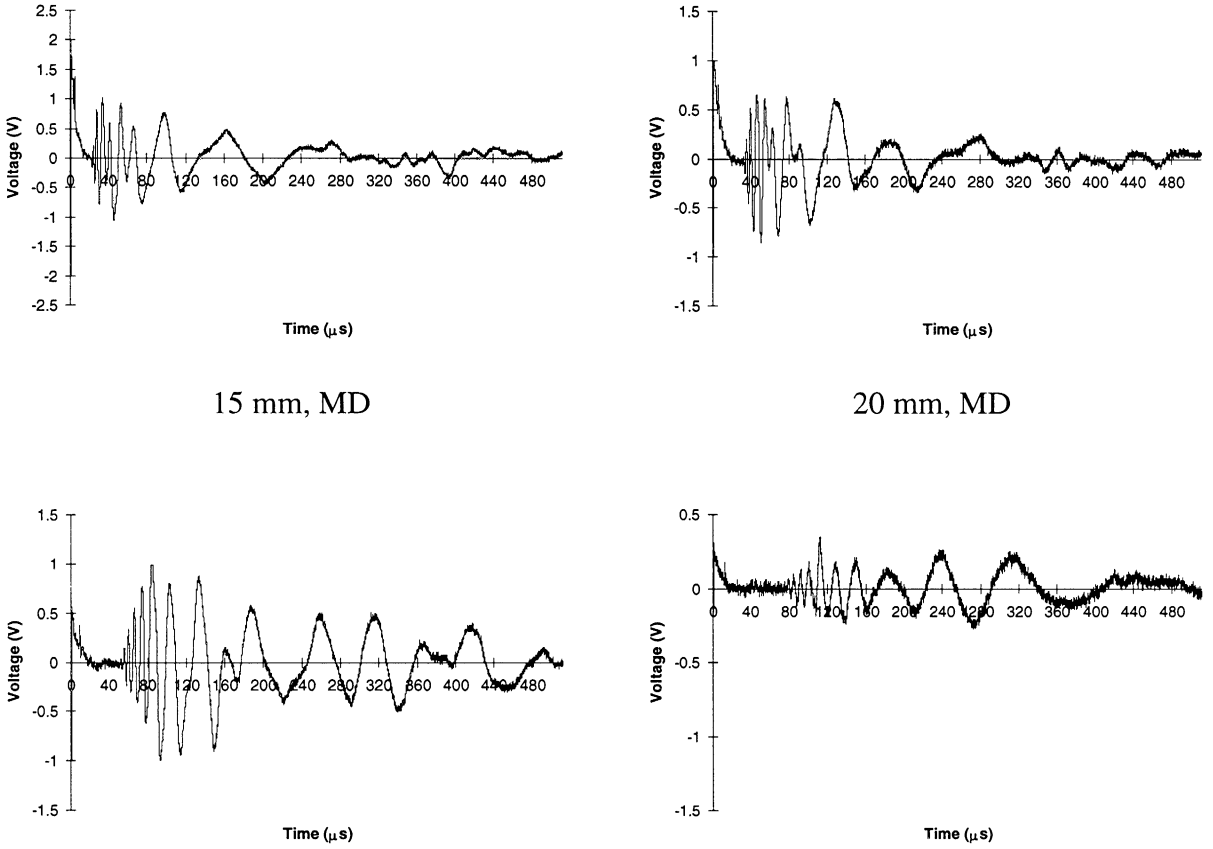

Figure 2.6.77 Single shot laser generated ultrasound on copy paper, along MD, using improved setup.

2.6.3.5 GaAs Photorefractive Setup

At the beginning of Phase II, generation and detection of ultrasound will be investigated on paper using a new photorefractive interferometer which will be developed in-house at IPST. The new interferometer will use a two-wave mixing technique with a GaAs crystal, which is known to be photorefractive in the infrared range. A continuous 600 mW Nd:YAG laser (1064 nm

wavelength) will be used as a detection laser. AC or DC electric fields will be applied to the sides of the crystal to increase gain.

There are a number of reasons to investigate this type of interferometer. First, from a wavelength point of view, paper tends to have a larger reflectivity at 1064 nm than at 532 or 514 nm, as described in Sections 2.2 and 2.6.8. Second, it is interesting to implement fiber optics on the interferometer because of easy beam control. Fiber optics in the near infrared are readily available on the market and inexpensive compared to those in the visible since the fiber-optic telecommunication industry uses near-infrared diodes and this has led to a significant product development in this area. Third, under laboratory conditions, the sensitivity to displacements of two-wave mixing using crystals with an applied electric field is better than the one obtained with the photo-EMF effect. This is probably true on static or slow moving paper but remains to be shown at higher speeds

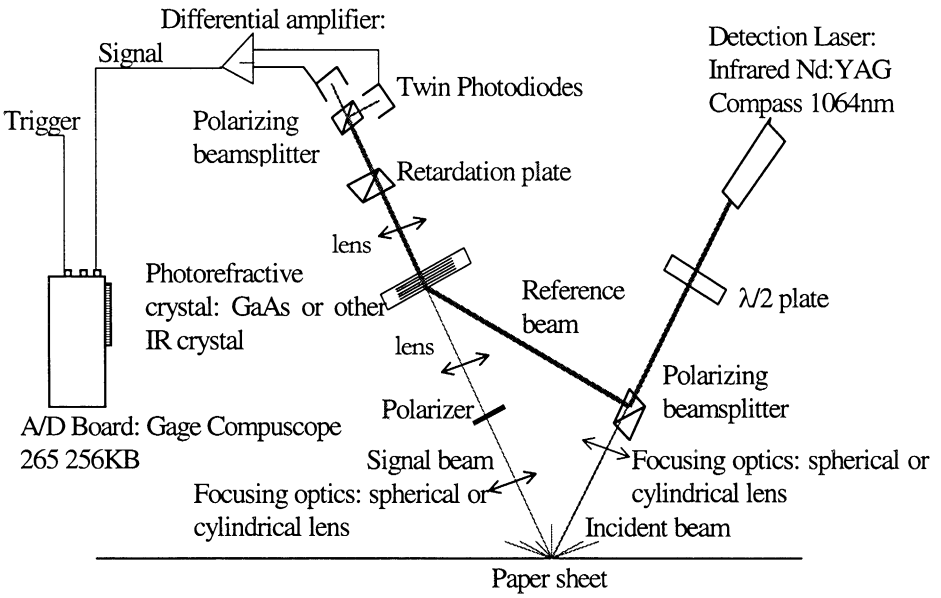

Figure 2.6.78 "V" setup for single-point Photorefractive Interferometer.

The experimental setup that we plan to use is shown schematically in Figure 2.6.78. Two photodiodes, a second polarizing beam splitter and a retardation plate are intended for quadrature detection. Since there is no optical activity (rotation of the plane of polarization with distance) in GaAs, a quadratic detection system will be more sensitive to displacements with this crystal than with a single photodiode.

2.6.4 Frequency Domain Photorefractive Imaging Interferometer Measurements (V. A. Deason, K. L. Telschow, S. M. Watson, and R. S. Schley, INEEL)

2.6.4.1 Imaging vs. Point Measurement

The paper industry has for several years utilized ultrasonic testing to evaluate the orientation and mechanical properties of paper off-line. The usual method involves measurement of sound speed between two contacting points on the paper and at numerous angles, providing data for one angular direction at a time. This information can be compiled to portray the mechanical properties in all directions.

In contrast, the INEEL has developed new technology that provides an image of the ultrasonic motion in the paper simultaneously in all directions over a significant area of paper. The data are optically (as opposed to computationally) processed so as to present a video image of the paper with the ultrasonic wavefronts superimposed on the image. The shape and distribution of the acoustic wavefronts provide information about sound speed and material properties in all directions along the paper simultaneously, thus displaying in a single image such properties as anisotropy, orientation and local inhomogeneities. At the present time, the response time of the system is inadequate for on-line use in paper manufacturing, but several new developments are expected to greatly improve the response time of the system and the system's immunity to general vibration noise. During the first program year, this task has applied this

new technology to the measurement of non-moving paper elastic properties and demonstrated its imaging qualitative and quantitative capabilities.

2.6.4.2 INEEL Imaging Ultrasonic Camera

The INEEL has developed an imaging ultrasonic camera (referred to as the "INEEL camera" in the following discussion, patent pending, Hale and Telschow, 1996; Hale, et al., 1997; Telschow, et al., 1997; Telschow and Deason, 1998; Telschow, et al., 1998). The INEEL camera utilizes optical nonlinear processes in photorefractive materials (PRM) to record optical interferometric information about the state of vibration of the paper, and to extract from this information about the out-of-plane displacements due to vibrations of a surface. This is done in an imaging mode at high rates, so real time video images of the distribution of acoustic waves on the surface can be recorded. Unlike other types of interferometers, where the two interfering waves mix at the detector, this step occurs, in the INEEL camera, in the PRM where one can take advantage of the properties of photorefractivity to perform preprocessing of the data. This approach configures a type of optical analog computer to demodulate and present the ultrasonic motion in the paper.

In operation, the paper is illuminated with a laser beam that has been diverged to cover the area of interest. As the acoustic wave moves through the paper, it causes any given point on the surface to be displaced vertically by a small amount (typically on the order of nanometers or less). This displacement causes the phase of the reflected laser beam to be altered by an equivalent amount. It is this change in phase that is detected by the INEEL camera. The reflected light, usually called the object beam, is collected and focussed by a lens into the PRM, where it mixes with a second, mutually coherent reference beam, and interferes to create a

recorded hologram of the object. The camera operates in what is usually called the non-linear two wave mixing mode (it can also operate in the alternative four wave mode), in which the reference beam reconstructs the hologram. If this were the end of the story, we would simply be slightly amplifying the object beam by adding to it the reconstructed object beam from the hologram. This is the well known non-linear amplification effect. However, in the INEEL camera, the reference beam has been phase modulated at a rate very close to but different from the frequency of the acoustic wave in the paper. The physical effect of this is to cause the holographic interference pattern in the PRM to move at a speed related to the frequency difference between the object and reference wave modulation rates. Since the PRM has an intrinsic response time, and holograms are both written and erased at approximately this rate, the offset frequency must be chosen so that the details of the hologram do not move so rapidly that the PRM cannot record the change. This whole process is sometimes called dynamic photorefractive holography.

The final effect is that paper vibrations at the chosen frequency contribute to the strength of the hologram and to the reconstructed wave, while others do not. Thus, the intensity (brightness) of the reconstructed holographic image of the paper is everywhere related to the amplitude of vibration of the corresponding point on the paper at the chosen frequency. This means that a video camera (or even the human eye) viewing the paper through the PRM will see a large fixed background image and a superimposed weak image that varies in intensity as the paper vibrates. These are sometimes referred to as the DC and AC components of the optical signal, respectively, in analogy to electrical signals. The frequency of the AC component is not at the original ultrasonic frequency but has been demodulated by mixing with the reference beam which has been independently modulated at a slightly different frequency. To have useful data,

the DC and AC components must be separated. This is done in two wave mixing in a bismuth silicon oxide (BSO) PRM by taking advantage of the optical activity of BSO which causes the DC and AC components to have differing polarizations. Several other methods to further improve the quality of the data are under development.

Since the hologram cannot be refreshed faster than the response time of the PRM, any changes in the object wave whose frequency is significantly faster than this will not be recorded, while changes slower than the response time will be automatically compensated for. This provides one of the main advantages of the INEEL camera: the potential for immunity to large but slow (by ultrasonic standards) vibrations caused by other equipment or activity in the environment. Investigation is underway to incorporate this environmental adaptation capability into the camera operation.

When thin sheet materials are ultrasonically excited, there are potentially several ultrasonic modes of vibration excited. In particular, symmetric (S_0) and antisymmetric (A_0) modes will usually be generated. The velocity of the S_0 mode is faster than that of the A_0, and its amplitude is usually smaller. It has been traditional with ultrasonic methods to measure the S_0 mode because it is non-dispersive, providing simple determination of the elastic properties of the paper. However, pulsed laser excitation of ultrasound generates a broadband signal highly susceptible to dispersion effects: this can broaden the signals, and reduce the accuracy of the data. In contrast with continuous excitation as used in the INEEL imaging approach, the A_0 mode can be utilized because it is larger and slower, and therefore easier to detect, and also dispersion is no longer a difficulty. The usual experimental setup is shown in Figure 2.6.79.

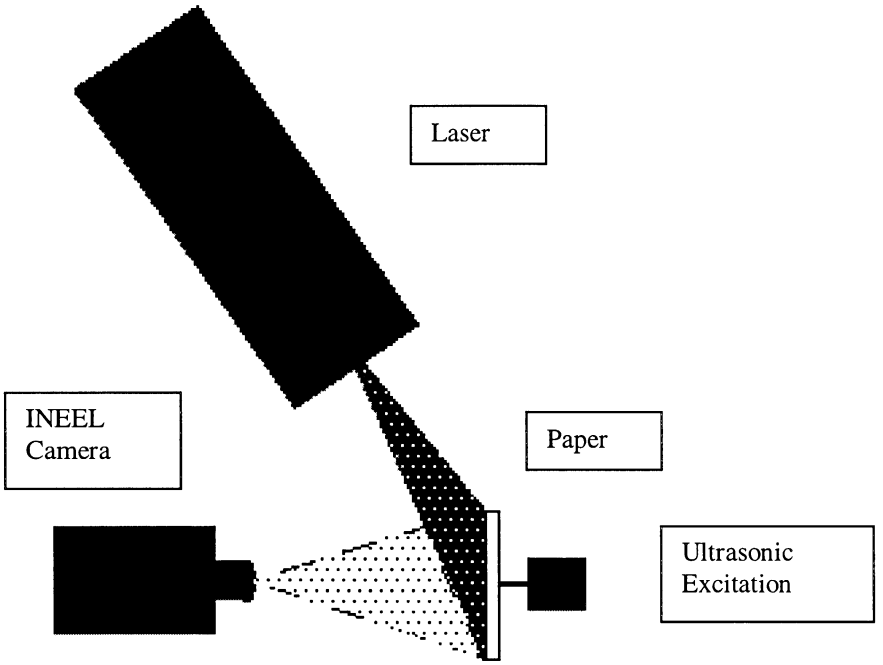

Figure 2.6.79 Schematic of the INEEL Photorefractive Ultrasonic Camera.

The IPST team has provided the INEEL with a number of well characterized paper samples. The properties of these samples were determined using methods established within the paper industry at the IPST. At the INEEL, these samples were tested using the imaging laser ultrasound system, whereby the sound speed (wavelength) in all directions of the antisymmetric (A_0) wave could be determined. The paper samples were vertically supported in an 18 cm diameter aluminum ring. Ultrasonic travelling waves were excited near the center by a point contacting piezoelectric transducer. Images of the travelling wave pattern were acquired by either an analog or digital video camera and transferred to computer disk for analysis. Analysis involved determination of the major and minor diameters of the traveling wave front and its angle relative to machine direction. Use of 2 dimensional FFT on the wavefront pattern provided an easy and useful method for analyzing the entire pattern at once. The concentric wavefront pattern of the travelling waves transforms into a single ring in the spatial frequency domain. The

major and minor diameter of this ring and its orientation provide a measure of the relevant wavelength and asymmetry in the travelling wavefront.

Measurements were taken on IPST RSK59 and LNR42 samples with an analog video camera and 8 bit video digitizer. IPST provided physical properties and all but two of the anisotropic elastic constant matrix values for these paper samples. The remaining two were estimated using data for comparable materials. These values are shown in Figure 2.6.80.

RSK59 (data from IPST)
Density = 0.818 g/cm^3
Thickness = 110 μm

Cmatrix (GPa)

9.85	**1.77**	0.10	*0.00*	*0.00*	*0.00*
1.77	**4.95**	0.15	*0.00*	*0.00*	*0.00*
0.10	0.15	**0.14**	*0.00*	*0.00*	*0.00*
0.00	*0.00*	*0.00*	**0.20**	*0.00*	*0.00*
0.00	*0.00*	*0.00*	*0.00*	**0.21**	*0.00*
0.00	*0.00*	*0.00*	*0.00*	*0.00*	**2.53**

Note: C_{13}, C_{23} approximated

CS_0(MD) = 3.46 mm/μs
CS_0(CD) = 2.42 mm/μs

LNR42 (data from IPST)
Density = 0.742 g/cm^3
Thickness = 288 μm

Cmatrix (GPa)

10.3	**1.82**	0.10	*0.00*	*0.00*	*0.00*
1.82	**3.70**	0.15	*0.00*	*0.00*	*0.00*
0.10	0.15	**0.10**	*0.00*	*0.00*	*0.00*
0.00	*0.00*	*0.00*	**0.14**	*0.00*	*0.00*
0.00	*0.00*	*0.00*	*0.00*	**0.16**	*0.00*
0.00	*0.00*	*0.00*	*0.00*	*0.00*	**2.23**

Note: C_{13}, C_{23} approximated

CS_0(MD) = 3.71 mm/μs
CS_0(CD) = 2.16 mm/μs

Figure 2.6.80 Elastic constants used for calculating the plate wave modes in selected papers. Data and samples provided by the IPST.

Using these values, and appropriate plate mode theory (Habeger, et al., 1979), the speed of the A_0 and S_0 modes as a function of frequency was computed for both machine and cross direction (MD and CD). The results for a 112 μm thick RSK59 paper sample in both the MD & CD is shown in Figure 2.6.81. Note the predicted dispersion of the A_0

mode due to frequency dependent sound speed. For the INEEL method, this is unimportant as operation is at a single frequency. The imaging method is thus able to take advantage of the larger amplitude and lower sound speed of the A_0 mode. Figures 2.6.82a and 2.6.82b show the predicted wavelengths of the A_0 and S_0 modes for the MD and CD. Figures 2.6.83a & 2.6.84a shows an image taken with the INEEL Camera of the ultrasonic wavefronts at 40 and 100 kHz, respectively. Note that the ultrasonic wavefronts are clearly shown in all directions at once over an 80 x 80 mm region. Each is a single frame of camera data: no averaging has been done.

Figures 2.6.83b and 2.6.84b show the corresponding two dimensional magnitudes of the two dimensional Fourier transform, obtained using the Fast Fourier Transform (FFT).

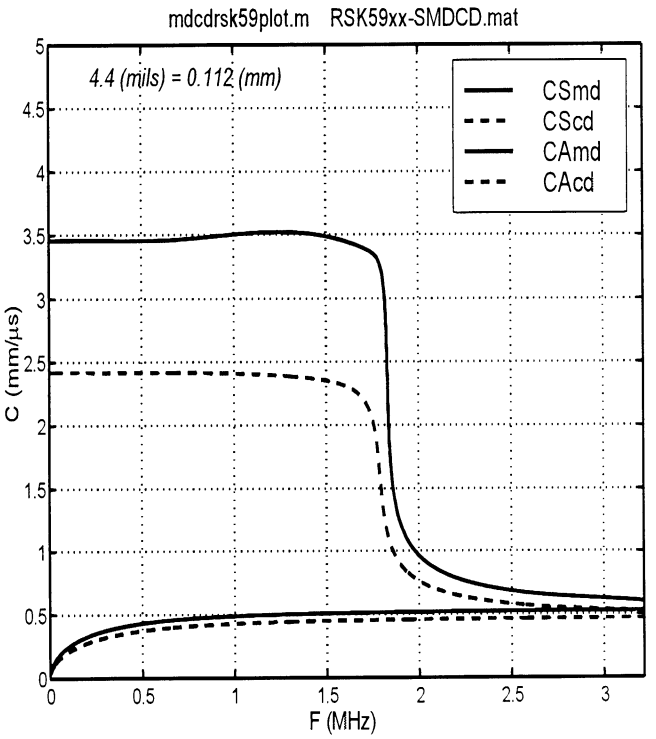

Figure 2.6.81 Calculated S_0 and A_0 mode velocities for paper sample RSK59 in the cross and machine directions.

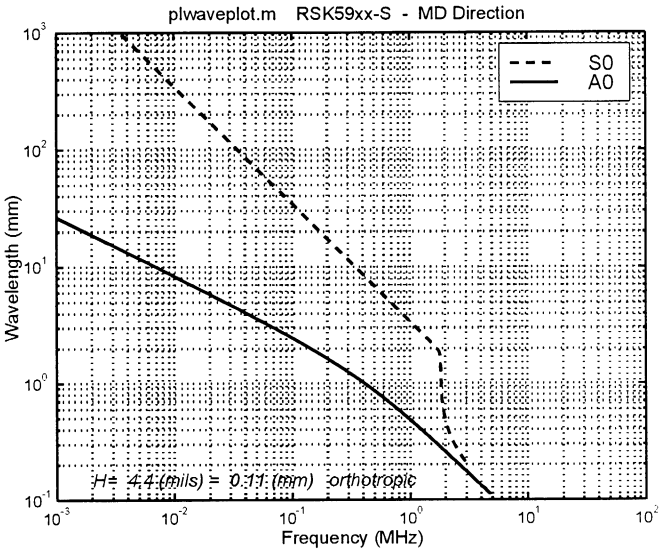

Figure 2.6.82a Calculated S_0 and A_0 mode wavelengths for paper sample RSK59, machine direction.

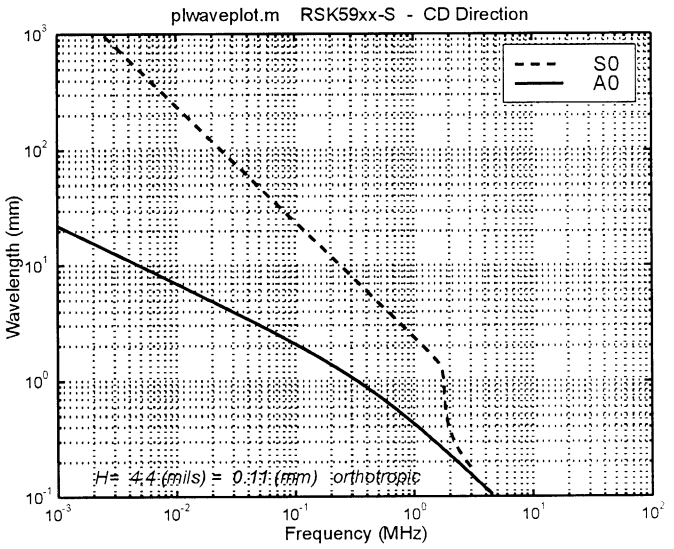

Figure 2.6.82b: Calculated S_0 and A_0 mode wavelengths for paper sample RSK59, cross direction.

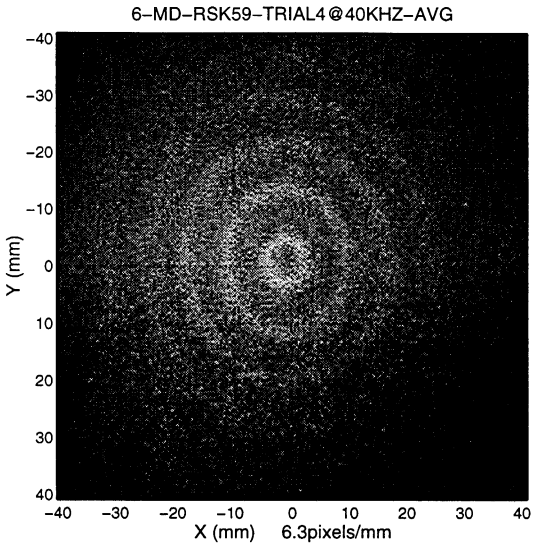

Figure 2.6.83a INEEL Camera image of ultrasonic waves in paper sample RSK59 at 40 kHz, machine direction is vertical.

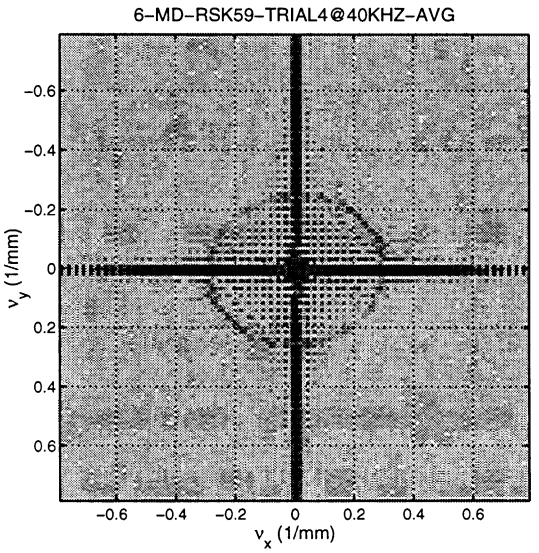

Figure 2.6.83 b Magnitude of the Fourier transform of Figure 2.6.83a showing the MD direction.

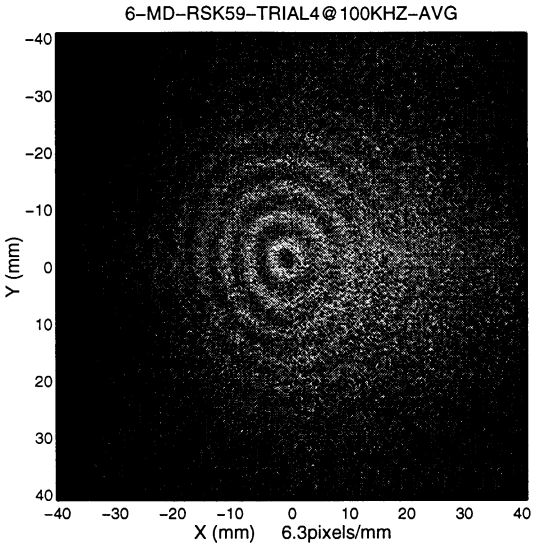

Figure 2.6.84a INEEL Camera image of ultrasonic waves in paper sample RSK59 at 100 kHz.

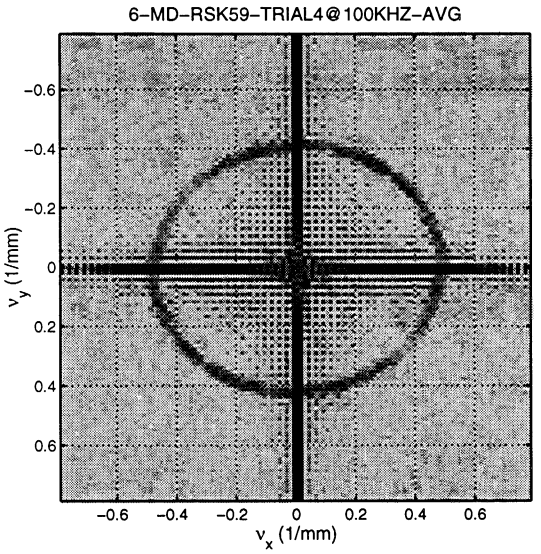

Figure 2.6.84 b Magnitude of the Fourier transform of Figure 2.6.84a showing the MD direction to be oriented approximately +5 degrees with respect to the vertical.

This FFT processing step utilizes all of the information in the image to extract wavelength data. It can be shown that the Fourier transform of a single outward traveling wave is a single ring in the transform domain that shows explicitly the wavelength anisotropy in all directions

along the paper simultaneously. The somewhat elliptical form near the center of this figure shows the average wavelength in all directions, the orientation (tilt), and the MD/CD sound speed asymmetry (major and minor axis). This single figure contains all of the data normally obtained by performing multiple measurements at many angles around the paper and plotting the results in polar form.

Figures 2.6.85a and 2.6.85b show the ultrasonic A_0 mode wavelengths obtained from the FFT image data for RSK59 and LNR42 paper types respectively. Results from the calculations for these paper types using the elastic data provided independently by the IPST are shown also. Very good agreement is evident, which illustrates the quantitative capability of the imaging ultrasonic method.

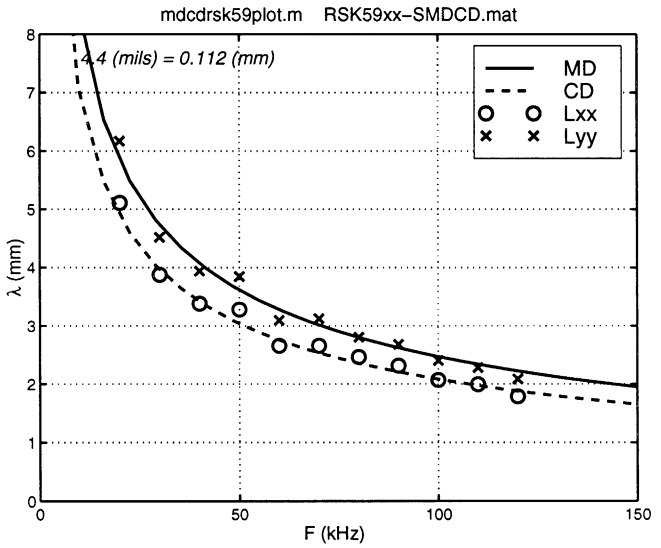

Figure 2.6.85a Comparison of calculated and experimental wavelength data for sample RSK59 in MD and CD directions.

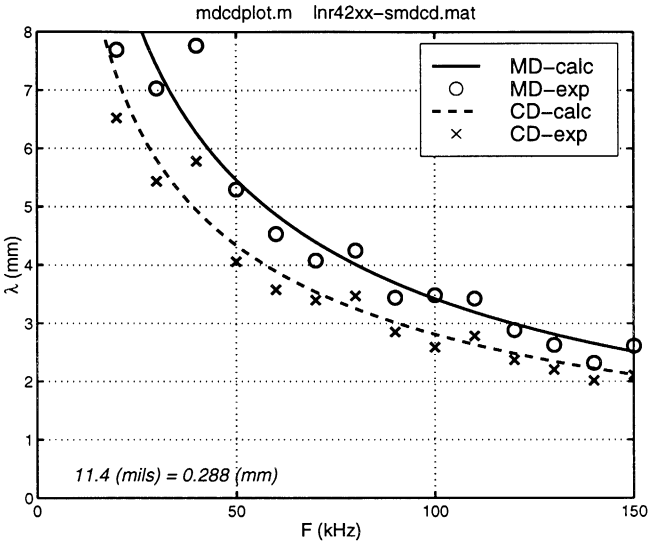

Figure 2.6.85 b Comparison of calculated and experimental wavelength data for samples LNR42 in MD and CD directions.

2.6.4.3 S_0 & A_0 MD/CD Velocity Ratio Determination

It has been traditional to use the S_0 modes for determination of certain paper properties due to the non dispersive nature of this mode. For the S_0 mode in a plate of thickness h, the wavevector is $k_{S0} = \frac{2\pi}{\lambda_{S0}}$, $for\ k_{S0}h << 1 \Rightarrow h << \frac{\lambda_{S0}}{2\pi}$ the phase velocity is given by

$$C_{S0} = \frac{\omega}{k_{S0}} = f\lambda_{S0} \approx \sqrt{\left(\frac{C_{11} - C_{13}^2/C_{33}}{\rho} \right)} \equiv C_0 \quad \Rightarrow \quad \left[\quad \lambda_{S0} = \frac{C_0}{f} \quad \right] \qquad (1)$$

However, it can be shown that the A_0 mode can be used also. For the A_0 mode in a plate of thickness h, the wavevector is $k_{S0} = \frac{2\pi}{\lambda_{A0}}$, $for\ k_{A0}h << 1 \Rightarrow h << \frac{\lambda_{A0}}{2\pi}$ the phase velocity is given by

$$C_{A0} = \frac{\omega}{k_{A0}} = f\lambda_{A0} \approx \frac{k_{A0}h}{\sqrt{3}}\sqrt{\left(\frac{C_{11} - C_{13}^2/C_{33}}{\rho}\right)} = \frac{k_{A0}hC_0}{\sqrt{3}} = \frac{2\pi hC_0}{\lambda_{A0}\sqrt{3}} \tag{2}$$

with the consequence that the wavelength $\lambda_{A0} = \sqrt{\frac{2\pi hC_0}{f\sqrt{3}}}$ and

$$\lambda_{A0}^2 = \frac{C_0}{f}\left(\frac{2\pi h}{\sqrt{3}}\right) = \lambda_{S0}\left(\frac{2\pi h}{\sqrt{3}}\right) or C_{A0}^2 = \left(\frac{2\pi fh}{\sqrt{3}}\right)C_{S0} \tag{3}$$

Therefore, the square of the MD/CD ratio for the A_0 mode can yield the same information about $\left(\frac{C_{11} - C_{13}^2/C_{33}}{\rho}\right)$ as the MD/CD ratio for the S_0

$$\frac{C_{S0}(MD)}{C_{S0}(CD)} = \frac{C_{A0}^2(MD)}{C_{A0}^2(CD)}, for h << \frac{\lambda_{A0}}{2\pi} \tag{4}$$

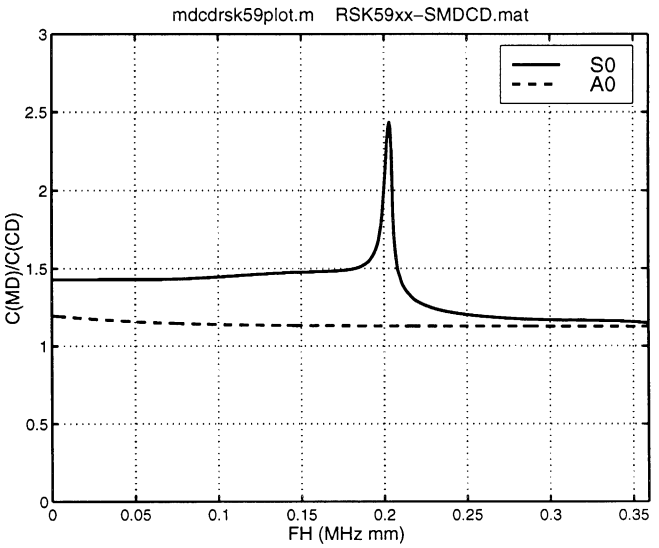

Figure 2.6.86 Calculated ratios of MD to CD velocities for A_0 and S_0 modes in sample RSK 50.

Figure 2.6.86 shows the predicted S_0 mode and A_0 mode MC/CD velocity ratios as a function of frequency. The S_0 mode ratio is approximately constant at low frequencies which is why this mode is preferred for characterization of the paper stiffness. However, the A_0 mode ratio is only slightly dependent on frequency and can also be used for characterization if the frequency is well defined. Figure 2.6.87 shows the predicted and measured A_0 mode velocity ratio. Good agreement is seen for the characterization of this paper sample.

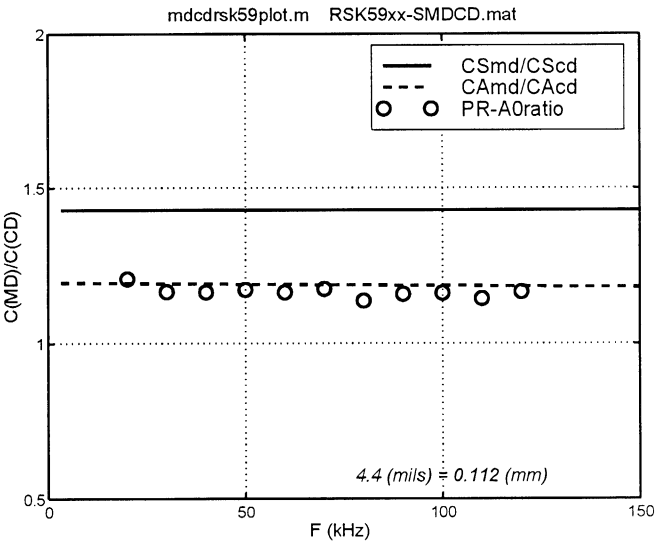

Figure 2.6.87 Comparison of calculated and experimental ratio of the MD to CD velocity of the A_0 mode at low frequency (the S_0 ratio is shown for comparison).

Figure 2.6.88 shows the predicted and experimentally measured values for the corresponding values for the S_0 mode ratio and the square of the A_0 mode ratio obtained in RSK59 paper. Generally good agreement is seen for all the photorefractive imaging measurements with a deviation systematically appearing at the higher frequencies, as

predicted. The calculated values show the amount of deviation between the two ratios to be expected as a function of frequency and indicate that the two ratios agree to within about 4% for frequencies up to 150 kHz.

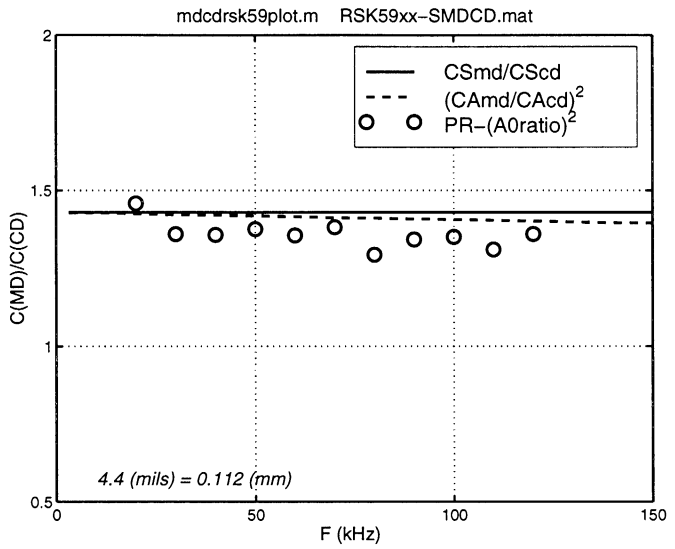

Figure 2.6.88 Calculated and experimental ratios of MD to CD velocity compared for A_0 and S_0 modes.

2.6.4.4 Frequency Domain Photorefractive Imaging Interferometer Measurements (Summary)

The INEEL photorefractive imaging ultrasound approach offers a powerful new method for performing non-contact measurements of elastic waves in paper. The imaging approach offers an obvious improvement in measurement speed and ease over the point measurement methods. Data have been provided that show the imaging method is sensitive and quantitative, yielding the complete A_0 mode wave speed anisotropy and paper orientation in one quickly obtained image form a CCD camera. However, this technology is not yet ready for on-line implementation. Several deficiencies concerning adaptation to the moving paper web, including sensitivity, wave excitation, speed of

response and adaptation to speckle noise, are yet to be resolved during future years of this research program. However, if successful, this effort will result in a unique and useful diagnostic technique for on-line process control for the paper industry.

2.6.5 Photo-induced EMF Interferometer (E. Lafond, IPST)

2.6.5.1 Experimental Setup

2.6.5.1.1 Operating principle, basics of the Photo-EMF interferometer

The photoinduced-EMF interferometer is also a photorefractive interferometer but it is quite different from the BSO photorefractive interferometer. It is designed to detect out-of-plane displacements of a surface. Under certain specific conditions, it can also detect in-plane displacements with a much smaller signal to noise ratio than for the out-of-plane configuration. In the following, the in-plane configuration is not detailed since the signal to noise ratio happened to be too poor for measurements on moving paper. Instead we will focus on the out-of-plane configuration. The core of the detection system on loan from Lasson Technologies that has been tested and improved with the IPST generation and acquisition system and IPST web simulator is the GaAs:Cr detector itself. In this system, the GaAs:Cr photorefractive crystal is used both as:

- a photoconductive beam mixer since it is a photorefractive crystal;
- a photodiode because of the current generated between the electrodes placed on its surface due to ultrasonic signals.

The amplitude of the detected signal is directly proportional to the power collected in the signal beam. So the amplitude of the signal is also proportional to the output power of the detection laser, in addition to the ultrasonic signal. The detection laser was an Ar:ion laser of which the wavelength was 514.5 nm and the maximum output power was 1.33 W.

The frequency bandwidth of the Lasson system itself was DC to 2 MHz (at -3 dB). When the current generated by the detector was too small it was amplified with a Panametrics

ultrasonic preamplifier (+39.2 dB). The bandwidth of the amplifier was 13 kHz to 6 MHz (at -3 dB). The version of the Lasson detector used for the trials was not optimized for the speckles coming from paper. The bandwidth will be adapted in the future by changing the electronic filters inside the detector box (both high pass and low pass filters). Figure 2.6.89 shows the frequency response of the Panametrics preamplifier used in the setup.

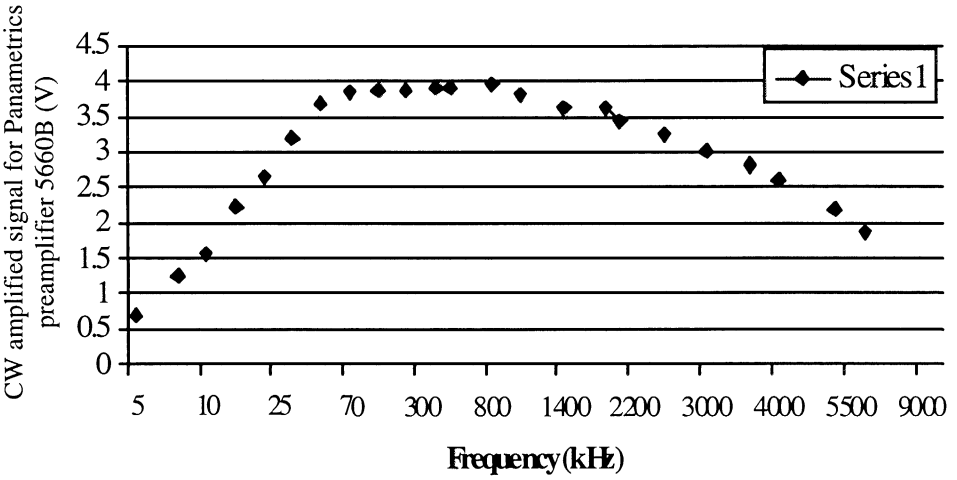

Figure 2.6.89 Frequency response of the preamplifier used for signals of small amplitude.

An improved bandwidth range would be from 20 kHz to 5 MHz. The detection system incorporating this frequency range is planned to be built and tested during Phase II.

In all experiments that were done with this interferometer, the optical system was forming an image of the spot on the paper illuminated by the detection laser onto the surface of the photorefractive crystal. The image of the spot was between the two vertical electrodes and the maximum current generated (thus the maximum signal to noise ratio) was obtained when the image covered the smallest percent of the crystal's surface (see Figure 2.6.90).

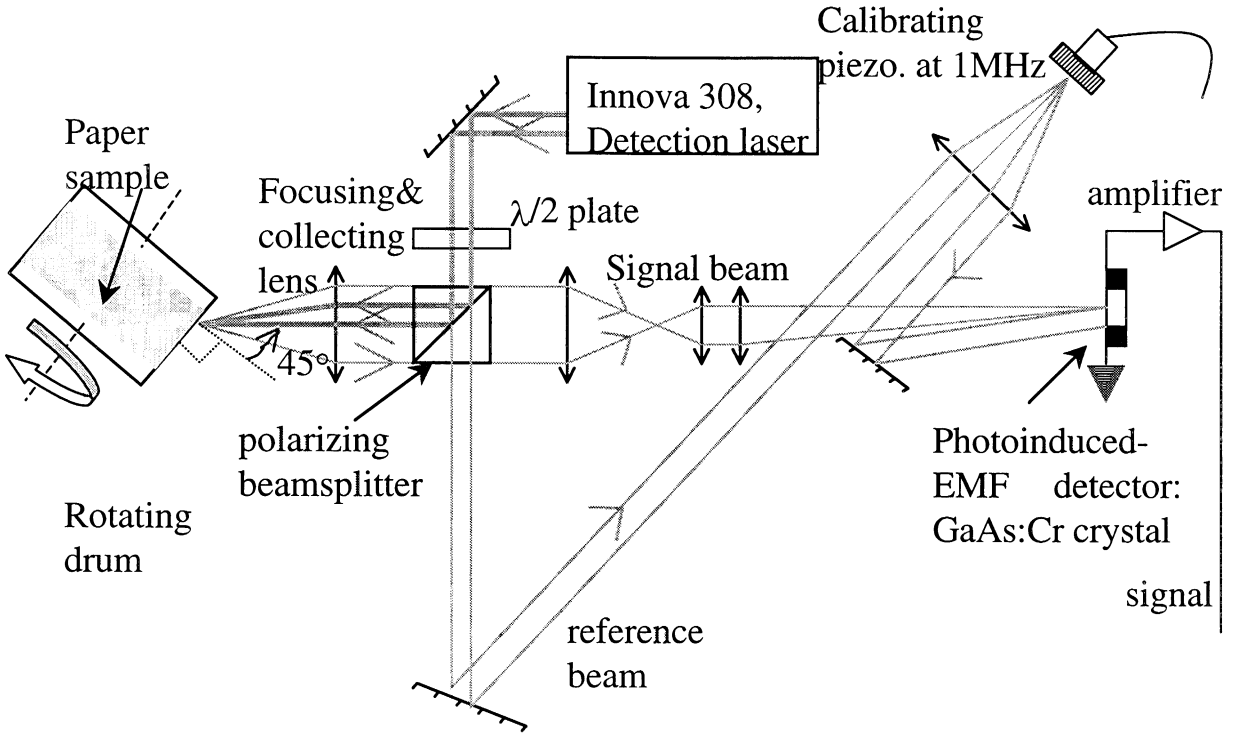

Figure 2.6.90 Photoinduced-EMF interferometer with web simulator shown at 45° incidence.

The front focusing lens for the incoming beam was used also as a collecting lens for the signal beam ("T" type measurement head) and its focal length was 100 mm. This means that when the paper surface was not in the focal plane of the focusing/collecting lens, the image on the detector was unfocused resulting in a loss of sensitivity of the interferometer. This was indeed observed at speeds over 2 m/s with the original configuration of the web simulator.

During moving paper measurements, the wobbling of the web simulator increased significantly with the rotation speed and caused the surface to shift both in the direction of the beam and perpendicularly to it for at least several mm. The original configuration of the web simulator was thus introducing some artificial fluttering whose frequencies were well above the

tens of hertz encountered on a real paper web. The second configuration almost completely eliminated this artificial fluttering and the rotating drum and paper sample stayed in the same position relative to the front lens even up to 25 m/s.

The photorefractive properties of the crystal insure that the interferometer adapts to the changing speckle pattern of the paper surface. But as with any photorefractive or Fabry-Pérot interferometer, the signal decreases with the speed at which the speckle pattern changes. Thus as the web surface speed increased, the signal strength decreased.

2.6.5.1.2 Noise in the system

Fluttering caused a defocusing of the signal beam onto the GaAs:Cr detector thus resulting in a decrease of the signal (not in an increase of the noise itself in reality). The influence of fluttering can be taken care of if we use a different optical system for light collection on the signal beam.

On this setup (photoinduced-emf interferometer + web simulator + A/D board), the noise can be seen as coming from 4 different sources.

The first source is the speckle noise (or texture noise) caused by the rough surface of paper. This noise comes from the coherent nature of laser light reflected from the material's surface, interfering constructively and destructively along certain directions (speckles) in an almost random way. It is also called "pseudo signal" in the area of interferometric detection on moving parts. The higher the speed of the paper, the higher are the frequencies found in the spectrum of the pseudo signal. Above 10 m/s on paper, the highest frequencies are in the 1 MHz range. Texture noise is typically broadband.

The second source comes from the feedback of the light back-scattered by the paper surface into the cavity of the detection laser. As opposed to metallic materials, paper webs behave as depolarizing surfaces. Even with a cube beam-splitter placed just before the focusing and collecting lens, part of the light reflected off the paper comes back along the optical path into the laser cavity. Laser cavities are sensitive to speckles coming back into their amplifying medium and it results in fluctuations of the laser output power, thus in fluctuations of the amplitude of the photo-EMF signal. This noise has a spectrum that is made of narrow peaks – it is not broadband at all.

The third source is the electronic noise from the Lasson GaAs:Cr detector since the current generated by the photo-EMF effect is very small (in the nano-amp range) and has to be amplified before being converted into an output voltage. The electronic noise comes from the built-in amplifier for the detector. The electronic noise coming from the Panametrics preamplifier that is used when the signal of the detector is very small is negligible compared to other noise sources. The frequency spectrum of the electronic noise should be broadband.

The fourth (and unexpected) source of noise comes from the A/D board in the computer. By comparing the ultrasonic signals displayed on the computer (thus coming from the A/D board) and on the oscilloscope, we found that the A/D board was much more noisy that the oscilloscope. The spectrum of this noise is in the MHz range and is a problem that needs to be addressed in the future on the industrial prototype. It may come from this A/D board specifically.

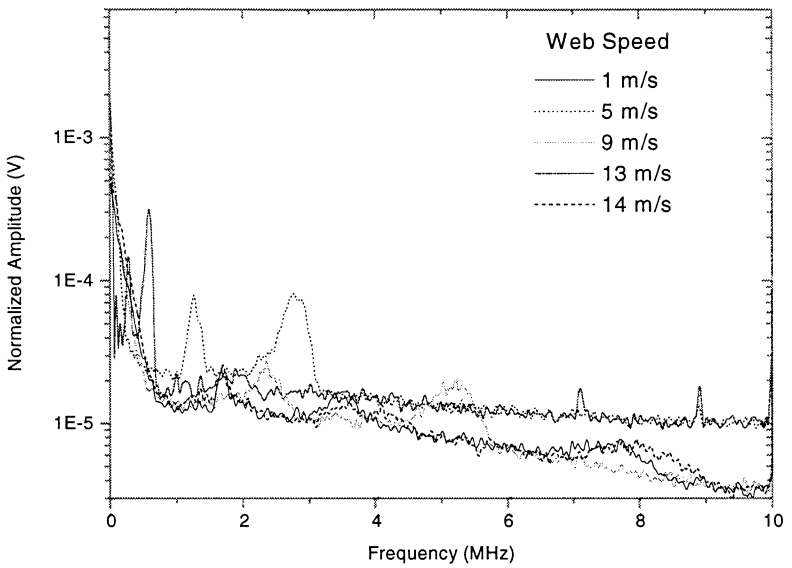

(a) Spectrum of photo-EMF detector voltage without any ultrasonic signal

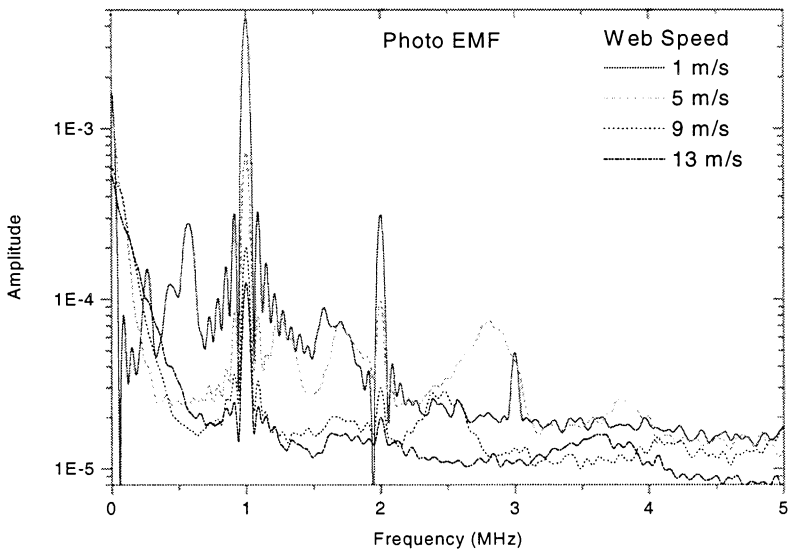

(b) Spectrum of photo-EMF detector voltage with a 1 MHz CW ultrasonic signal

Figure 2.6.91 Frequency domain noise spectra of the photoinduced–EMF on bleachboard using the Photo EMF at different web speeds.

Figure 2.6.91 shows typical noise spectra in the frequency domain obtained on a moving bleachboard using the photo-EMF detector. Figure *a* shows the amplitude and frequency of the

noise without any signal present. Figure *b* was obtained with an ultrasonic signal artificially generated at 1 MHz in a CW sine wave mode using a calibrating piezoelectric transducer. Two harmonics of the 1 MHz wave can be seen in Figure *b*. It is evident from the graph that the noise peak shifts towards higher frequencies as the web speed increases from 1 m/s to 14 m/s. For each noise spectrum, there are several small peaks that exist and this indicates a number of minor sources of noise. Most likely, the big peaks at 7 and 9 MHz in the 1 m/s curve are either coming from the perturbation of the detection laser cavity by back-scattered light or from the A/D board.

The noise does not increase with the web speed. Instead the amplitude of the signal decreases thus the signal to noise ratio decreases as function of the increasing web speed, which is what is expected. This is a normal photorefractive phenomena since the faster the web goes the faster the speckle pattern changes and the less the crystal has time to adapt to the changing wavefront.

2.6.5.1.3 Configurations for the experiments

Three different configurations for detection on moving paper and one for detection on static paper were used. Static paper measurements were done first to prove the concept of a photo-EMF interferometer on paper. A circular spot was used for the generation at 1064 nm wavelength, and a circular spot for detection. On the optical head of the interferometer, a second lens was added in front of the focusing/collecting lens (see Figure 2.6.90).

This second lens had the same diameter as the focusing/collecting lens but the resulting focal length of the two lenses was 50 mm instead of 100 mm. This increased the étendue of the interferometer but reduced the depth of focus. Thus it was in fact not really suitable for moving paper (defocusing of the image of the paper surface on the GaAs:Cr detector) and we removed it

after tests on static paper were done. Below are displayed some photos of the experiments with the photoinduced-EMF interferometer on static paper (Figures 2.6.92-94).

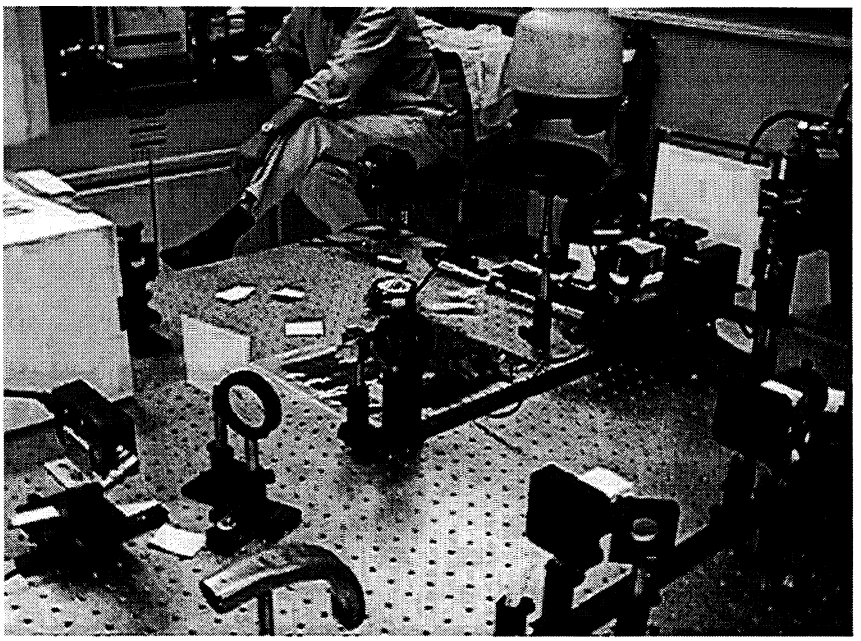

Figure 2.6.92 General view of the photo-EMF interferometer for measurements on static paper (optics in the lower right corner are not part of this setup).

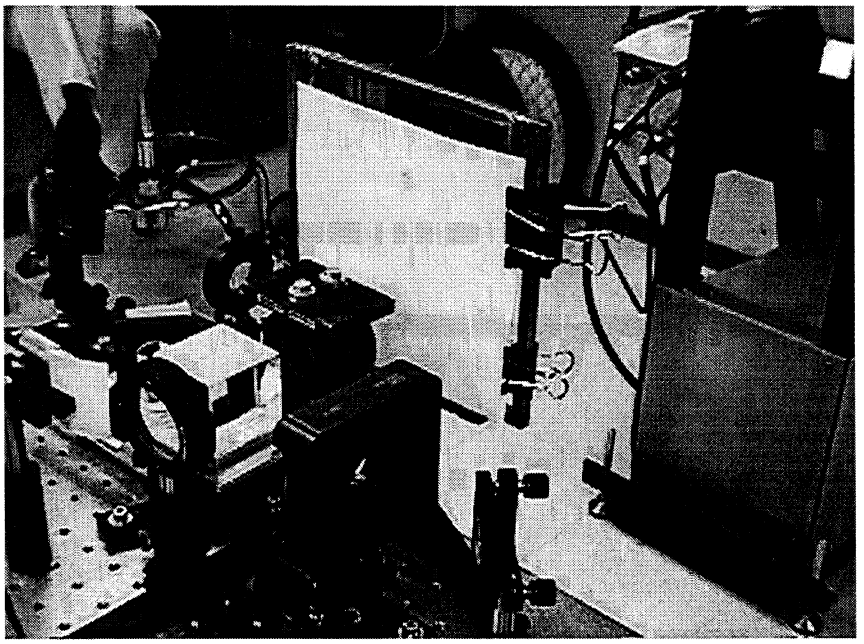

Figure 2.6.93 Close view of the optical head of the photo-EMF interferometer for measurements on static paper .

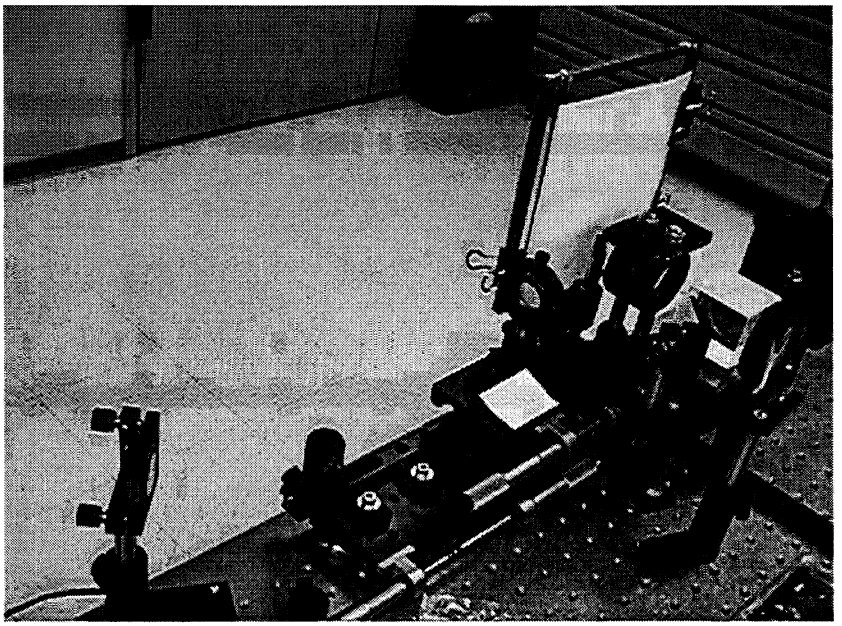

Figure 2.6.94 View of the generation optics (red tags) and paper sample holder for measurements on static paper (sample shown is copy paper).

After completing the proof-of-concept measurements on static paper, measurements were performed on moving paper. Because the paper was moving, the power of the detection laser was able to be increased significantly because the impinged spot was constantly moving so it could not burn the paper.

In Table 2.6.2 is presented a comparison among the different configurations we used for the trials on moving paper.

Figure 2.6.95-97 were taken of the setup used on July 9 & 10, 1998, with the configuration #1 of the web simulator.

Table 2.6.2 Summary of the different experimental configurations used for tests on moving paper.

Date	Generation spot and **detection incidence angle**	Paper grade investigated	Meas. along	Web simulator used for the trials
July 9 & 10, 1998	Point or 0.5 x 2 mm line, **0° (normal inc.)**	Copy paper, 42-lb linerboard Bleachboard Raw stock	CD	Configuration #1
August 13 & 14, 1998	0.5 x 11 mm line **45°**	Copy paper 42-lb linerboard Bleachboard	CD	Configuration #1
August 21, 1998	0.5 x 12 mm line **45°**	Copy paper 42-lb linerboard	CD	Configuration #2
August 24 & 25, 1998	0.5 x 14 mm line **45°**	Copy paper 42-lb linerboard Bleachboard	MD	Configuration #2

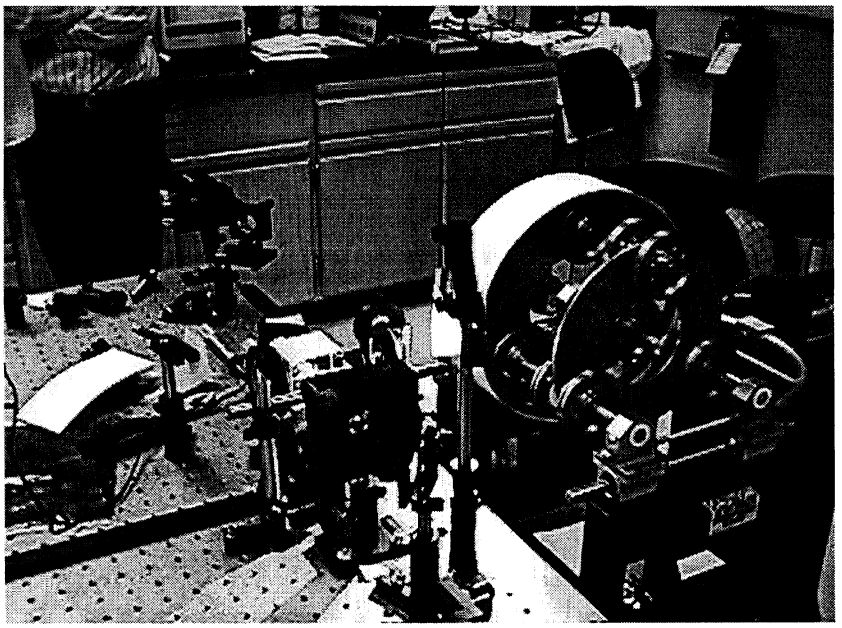

Figure 2.6.95 View of the detection system and web simulator for on-line detection of laser generated ultrasound on paper.

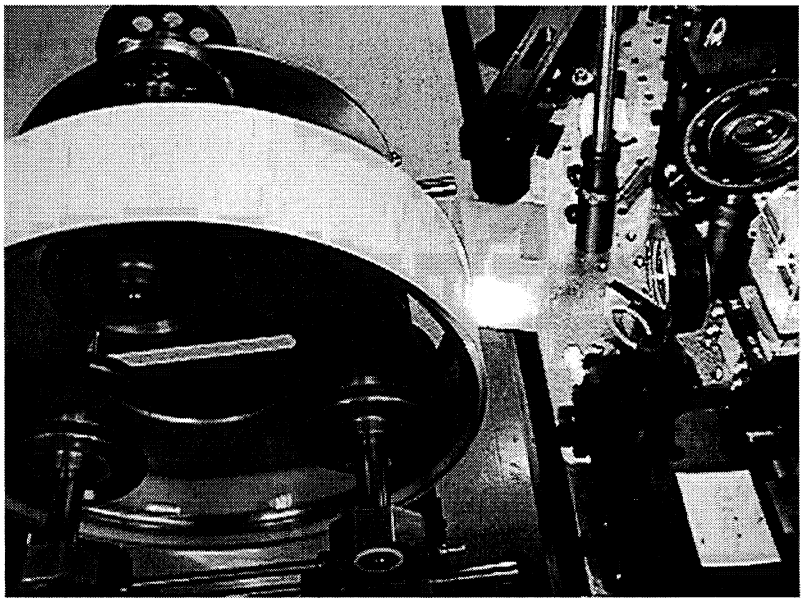

Figure 2.6.96 Detection optical head, running web simulator and 45 ° mirror in the generation system.

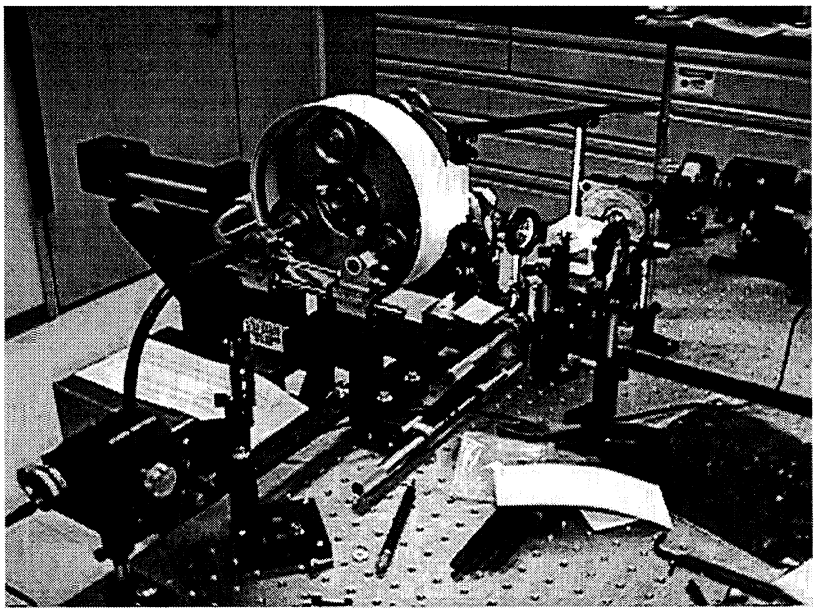

Figure 2.6.97 Detection and generation systems and running web simulator, view from the left side.

Figures 2.6.98-101 are pictures taken during the tests of August 13 & 14, 1998. It was decided to change the incidence angle for detection from 0° (normal incidence) to 45° incidence, in order to be able to detect both in-plane and out-of-plane displacements. This was done since the out-of-plane component of the S_0 wave is very small compared to the in-plane component and it had not been observed on moving paper with the 0° setup.

Another improvement consisted in using a long line for the generation spot instead of a point, in order to generate roughly the same amplitude for the ultrasonic waves but with a much smaller laser power density on paper. This change was done because the ablation damage on paper made with the circular generation spot used in the previous trials happened to be unacceptable especially on copy paper and raw stock.

Figure 2.6.98 shows a vertical piece of beige cardboard can be seen next to the sheet. It has been put between the generation and detection spots in order to prevent a possible shock wave in the air (which may occur at the generation spot) from overlapping with the ultrasonic wave traveling in the paper. Such a shock wave was seen when using the previous setup (point generation).

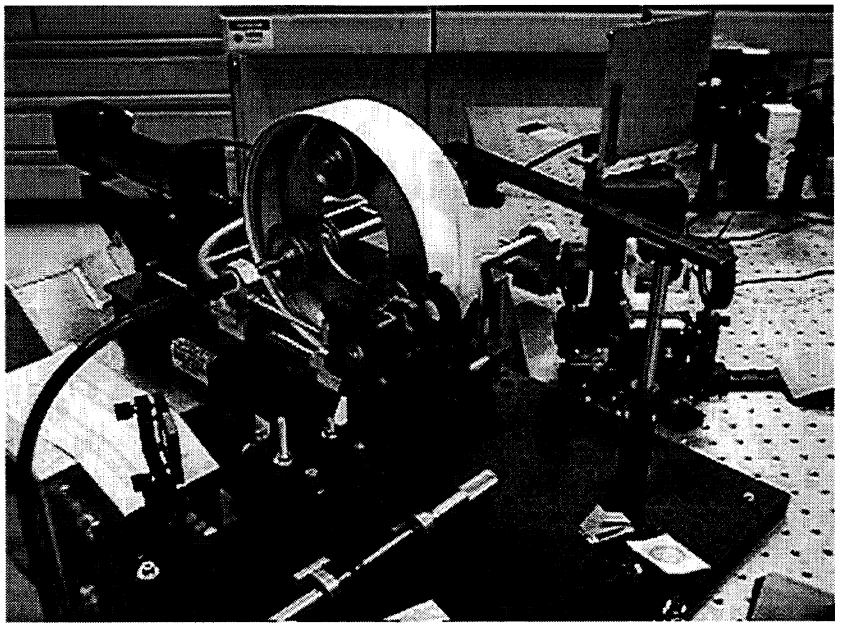

Figure 2.6.98 Detection and generation systems and web simulator #1, configuration for tests made on August 13 & 14, 1998.

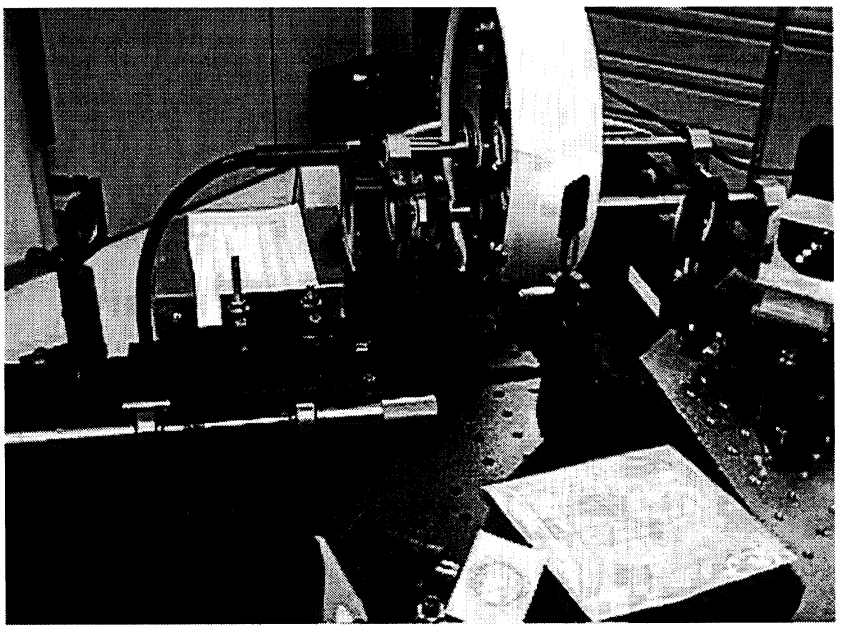

Figure 2.6.99 View of the generation system and web simulator, configuration for tests made on August 13&14, 1998.

The lenses that are part of the generation system which is used to produce a line source instead of a point source for the generation spot can be seen in Figures 2.6.99 and 2.6.101. One spherical diverging lens, then two spherical converging lens then one cylindrical lens were used. The paper strip was cut along the machine direction (as all paper strips used on the rotating drum) and the direction of rotation of the sheet was along machine direction like on a real paper web. The waves were travelling along cross direction (horizontal). An averaged signal showing the dispersive A_0 wave on moving copy paper is displayed in Figure 2.6.100.

Figures 2.6.102-107 show pictures taken from the trials with copy paper and 42-lb-linerboard on August 21, 1998. The optical configuration for both generation and detection systems was identical to the one used in the tests on August 13 and 14, except that this time configuration #2 of the web simulator was used instead of configuration #1.

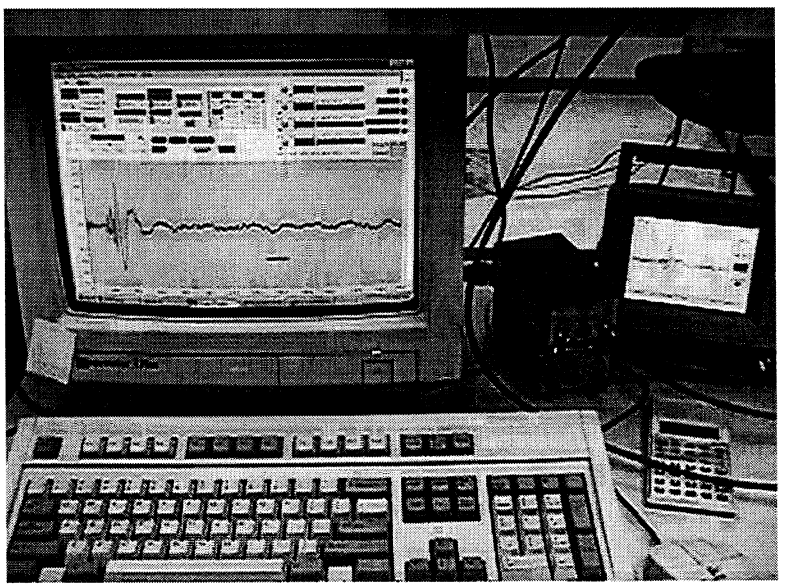

Figure 2.6.100 A_0 wave on copy paper, line generation, averaged signal.

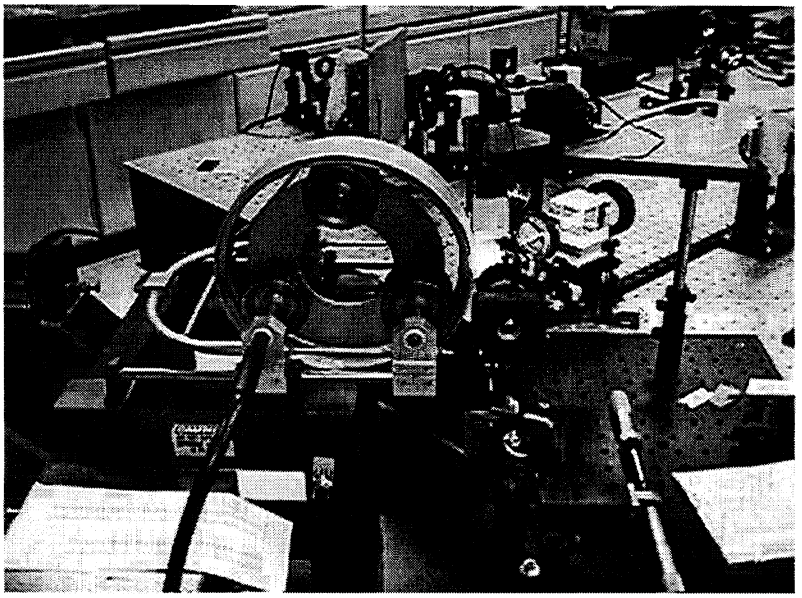

Figure 2.6.101 Tests on 42-lb-linerboard, trials made on August 13&14, 1998, with configuration #1 of web simulator.

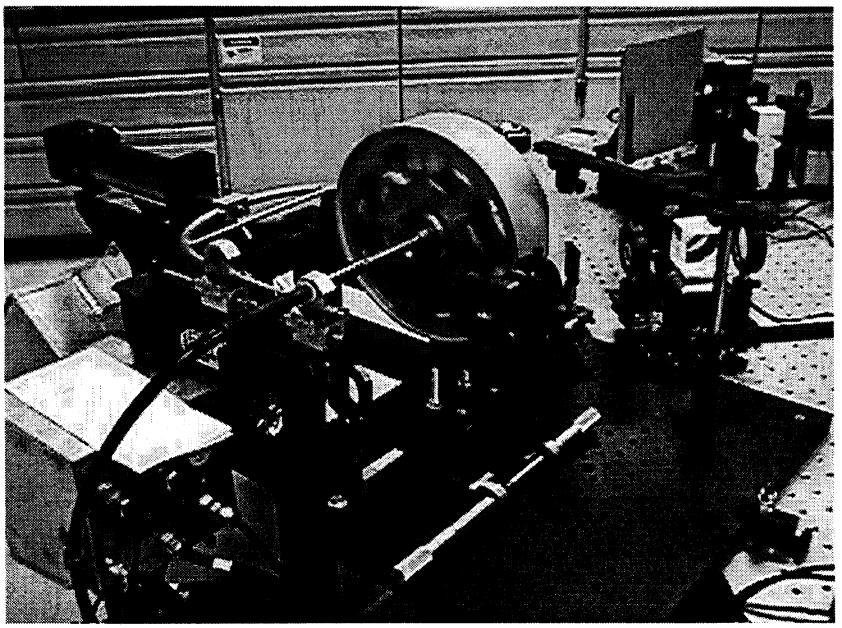

Figure 2.6.102 Tests on 42-lb-linerboard made on August 21, 1998 with configuration #2 of the web simulator (detection laser is off).

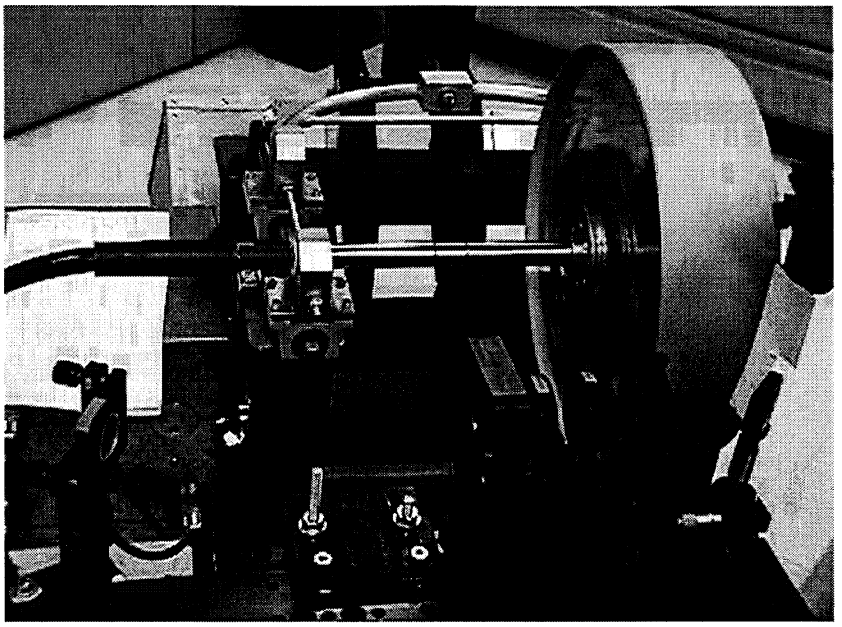

Figure 2.6.103 Close view of the running web simulator with 42-lb-linerboard, August 21, 1998 (generation optics in the foreground).

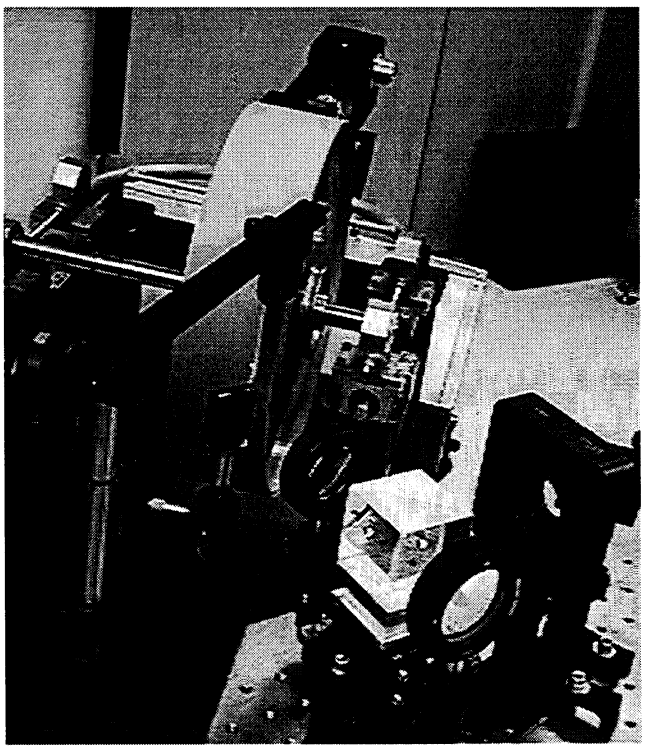

Figure 2.6.104 View of the running web simulator with 42-lb linerboard paper grade, and of the optics of the detection head.

Measurements were also made along machine direction with the same copy paper and 42-lb linerboard samples used on August 21, plus a new sample of bleachboard. The generation line was set horizontally above the detection point and the ultrasonic waves were thus travelling along MD. Apart from that, the generation and detection systems were the same as on the 21st.

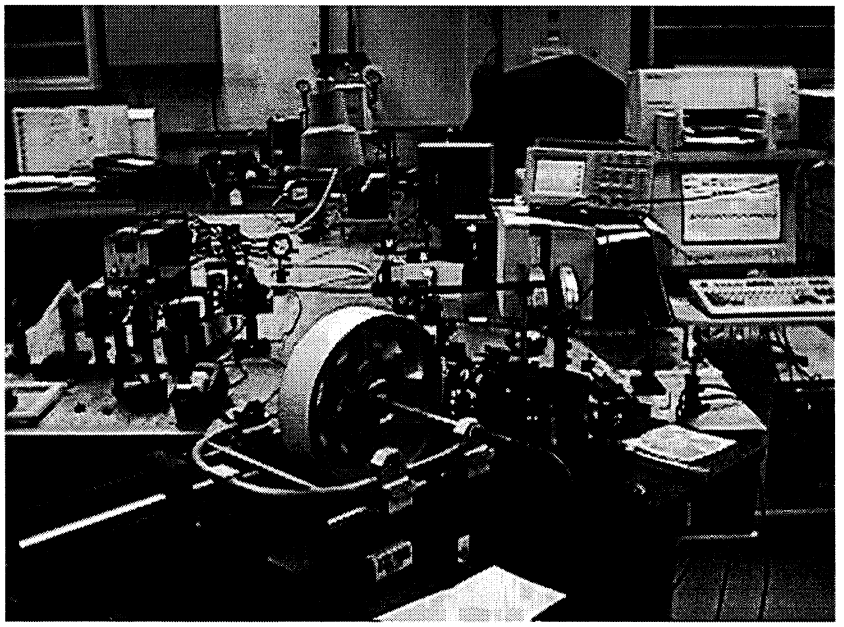

Figure 2.6.105 General view of the running web simulator (bottom), laser generation (right), detection (center) and data acquisition (right). Optics on the left are not part of the setup.

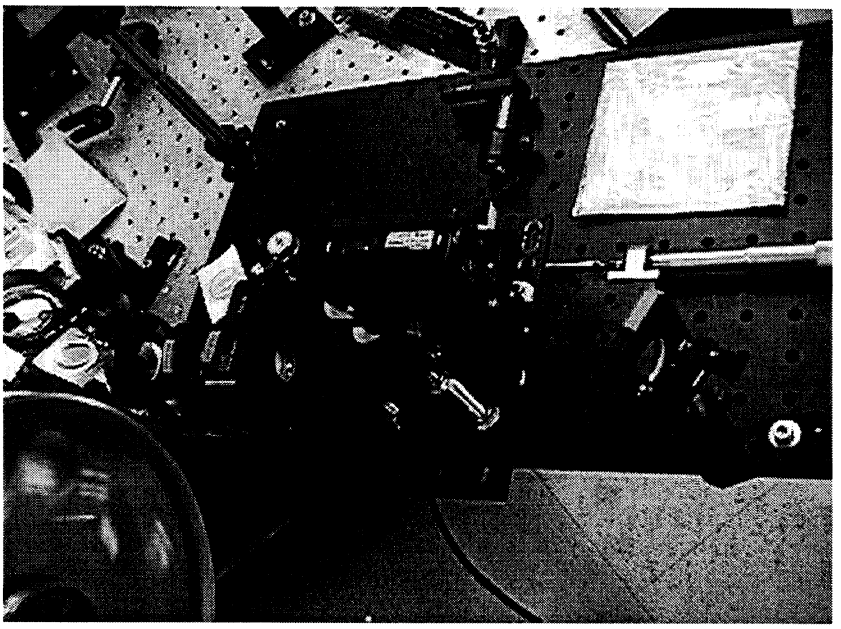

Figure 2.6.106 View of the rotating drum (bottom left) and laser optics (optics with red tags).

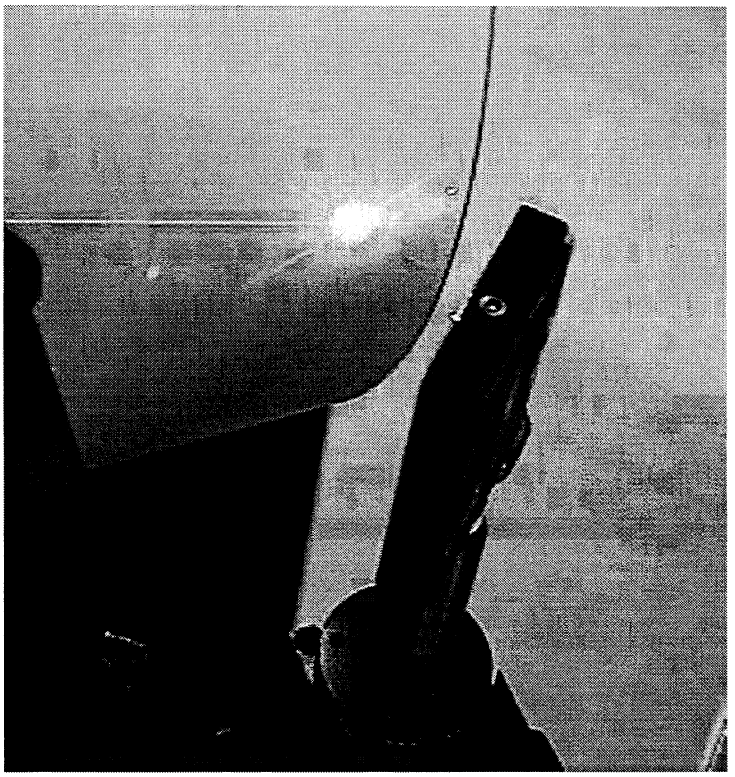

Figure 2.6.107 Detail of the generation mirror and detection spot on moving copy paper.

On the copy paper sample, signals were also recorded at 30 m/s, which is about 20% above the current production speed for copy paper (see Figures 2.6.108-109). This was done in order to see if the detection system was still able to detect the A_0 wave at this very high speed.

At this speed, the signal to noise ratio is very poor. Thus it is difficult to tell if the waveform that is observed is actually an A_0 wave or a shock wave travelling in the air at 30 m/s. Further analysis of the frequency content of the detected waveform should positively identify the wave.

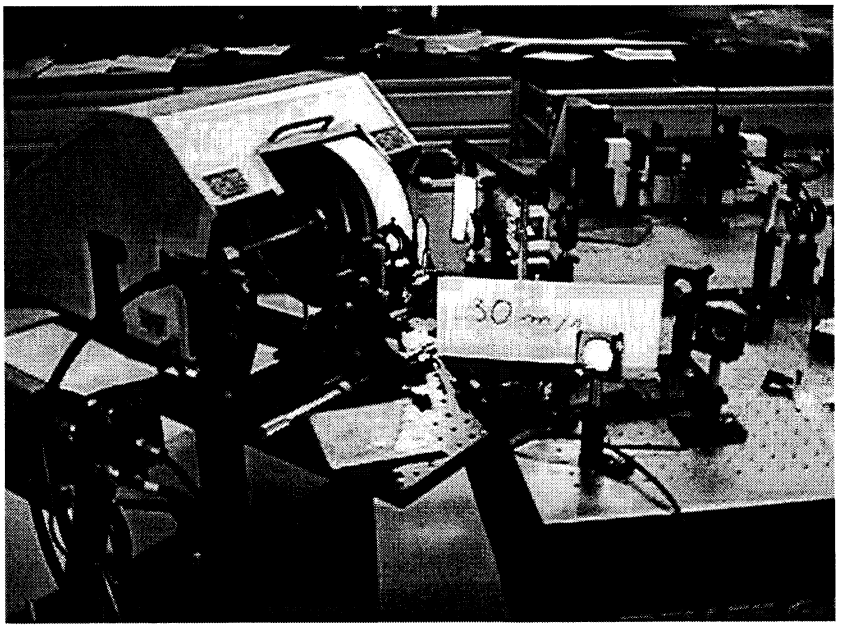

Figure 2.6.108 General view of the system running at 30 m/s on copy paper.

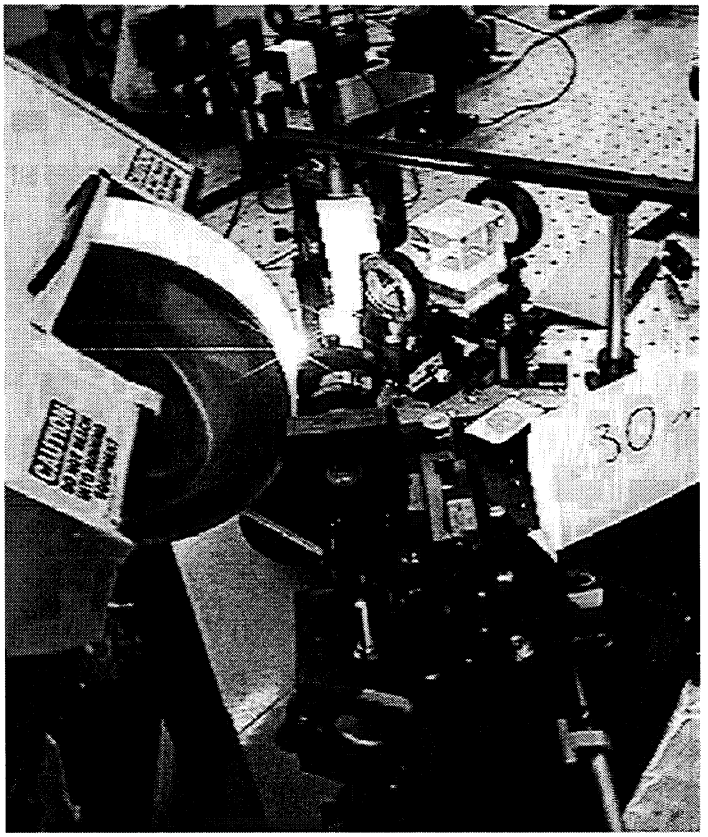

Figure 2.6.109 Close up of the system at 30 m/s on copy paper.

2.6.5.2 Results on Static Paper (J. Jong, IPST)

The photo EMF detector was used to detect a signal generated by a source laser on static paper. Figure 2.6.110 shows typical signals recorded by the photo EMF setup at 45° incidence on a static copy paper. The top graph shows that the S_0 and A_0 mode waves are clearly detected using an out-of-plane detection configuration. On the other hand, the bottom plot shows that the signal to noise level decreases significantly using an in-plane detection configuration. The presence of the S_0 mode wave with the in-plane system is no longer obvious.

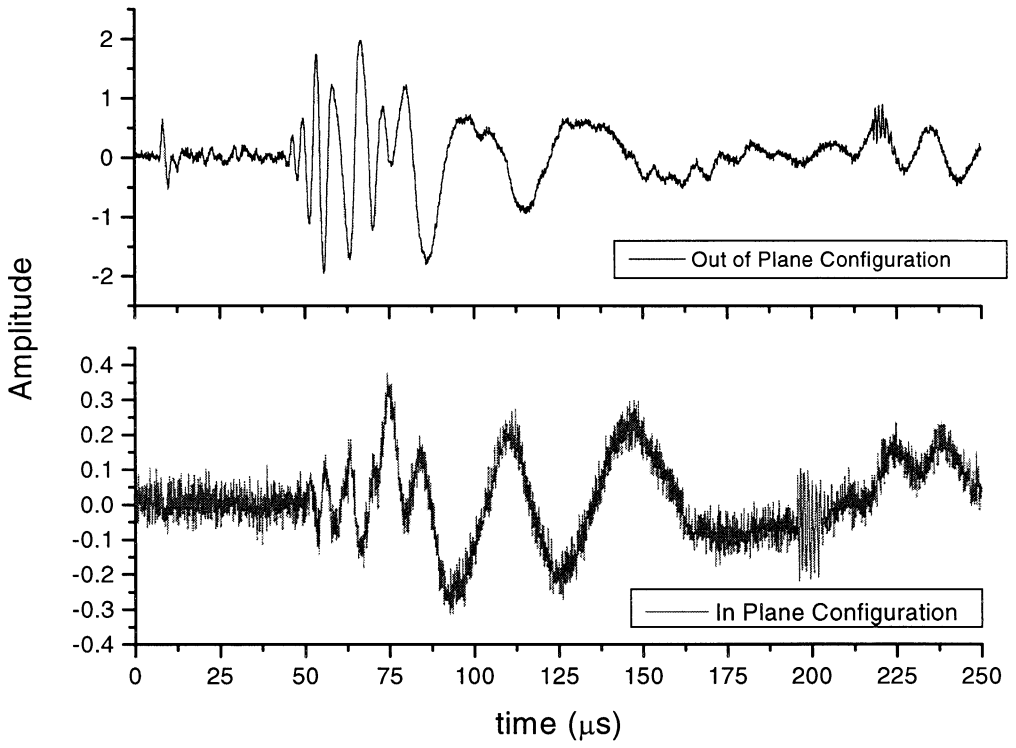

Figure 2.6.110 Photo EMF signals on static copy paper using out-of-plane (top) and in-plane (bottom) configurations: The detection laser was aimed at 45° incidence with respect to the normal to the surface.

Figure 2.6.111 shows the spectra of the signals in Figure 2.6.110 using the out-of-plane and in-plane configurations. The signal energy is mostly present in the low frequency range below 0.5 MHz. This is in agreement with the results obtained earlier by the BSO PRC setup.

Figure 2.6.112 shows ultrasonic signals on a fairly thick bleachboard sample (grammage of 262 g/m^2). The S_0 mode wave is not easily detected and the A_0 mode wave tends to dampen out quickly. This behavior is in agreement with the results obtained using the BSO PRC setup earlier. The noise level is very high in the in-plane configuration.

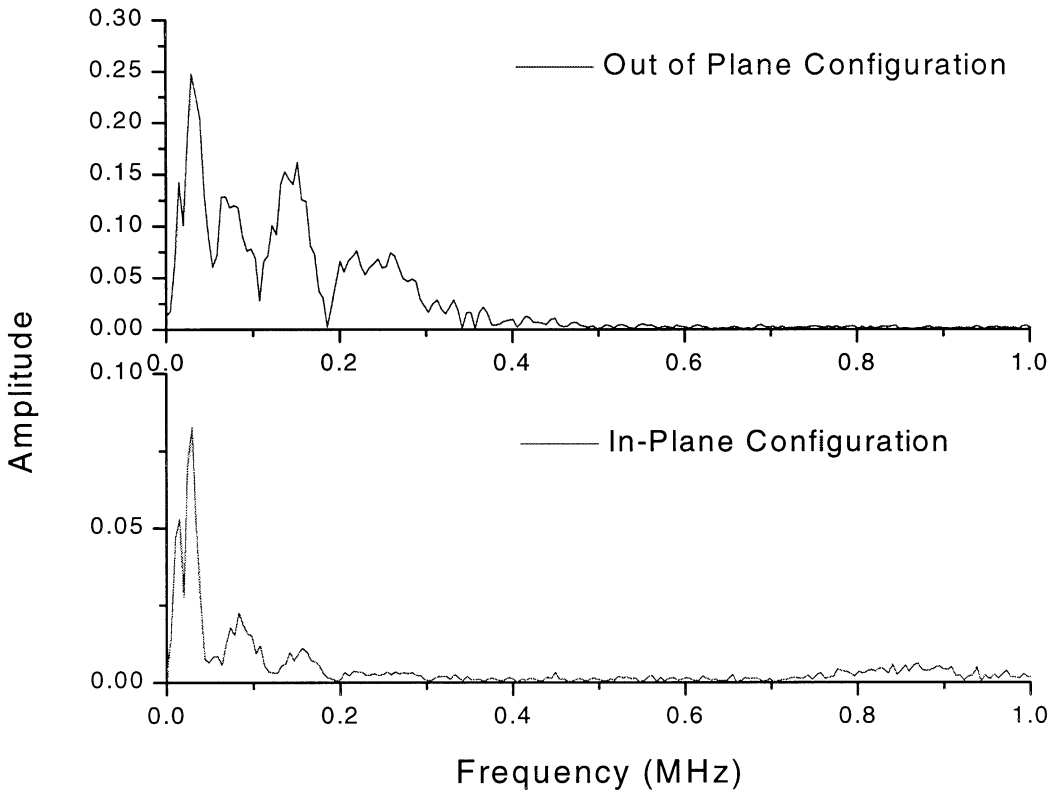

Figure 2.6.111 Frequency spectra of the signals shown in Figure 2.6.109 using the out-of-plane and in-plane configurations: The detection laser was aimed at 45° incidence with respect to normal to the surface.

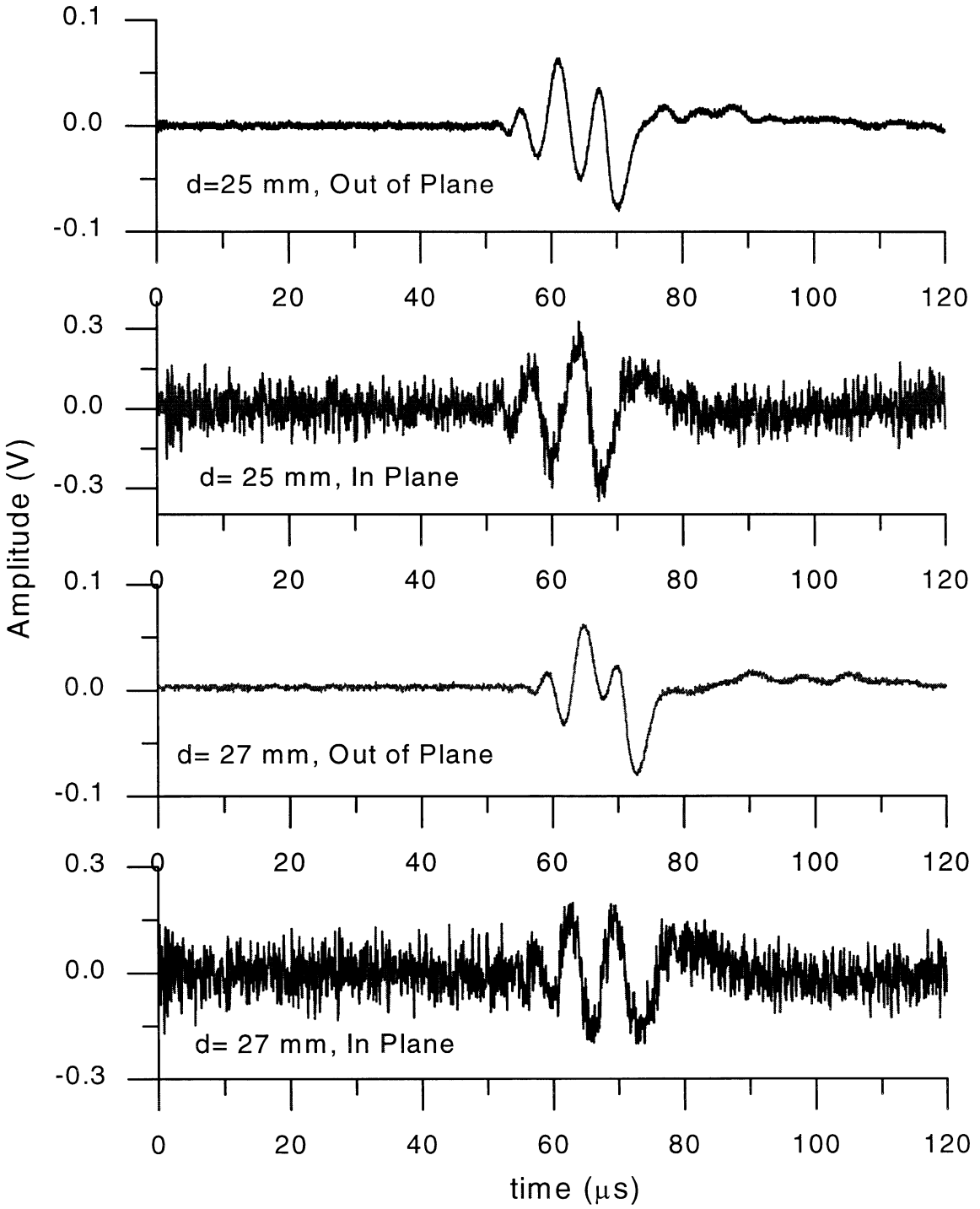

Figure 2.6.112 Signals on bleachboard sample using the out-of-plane and in-plane configurations: The grammage is 262 g/m^2. A single shot was used for the signal. The S_0 mode wave is not visible and the A_0 mode wave dampens out quickly.

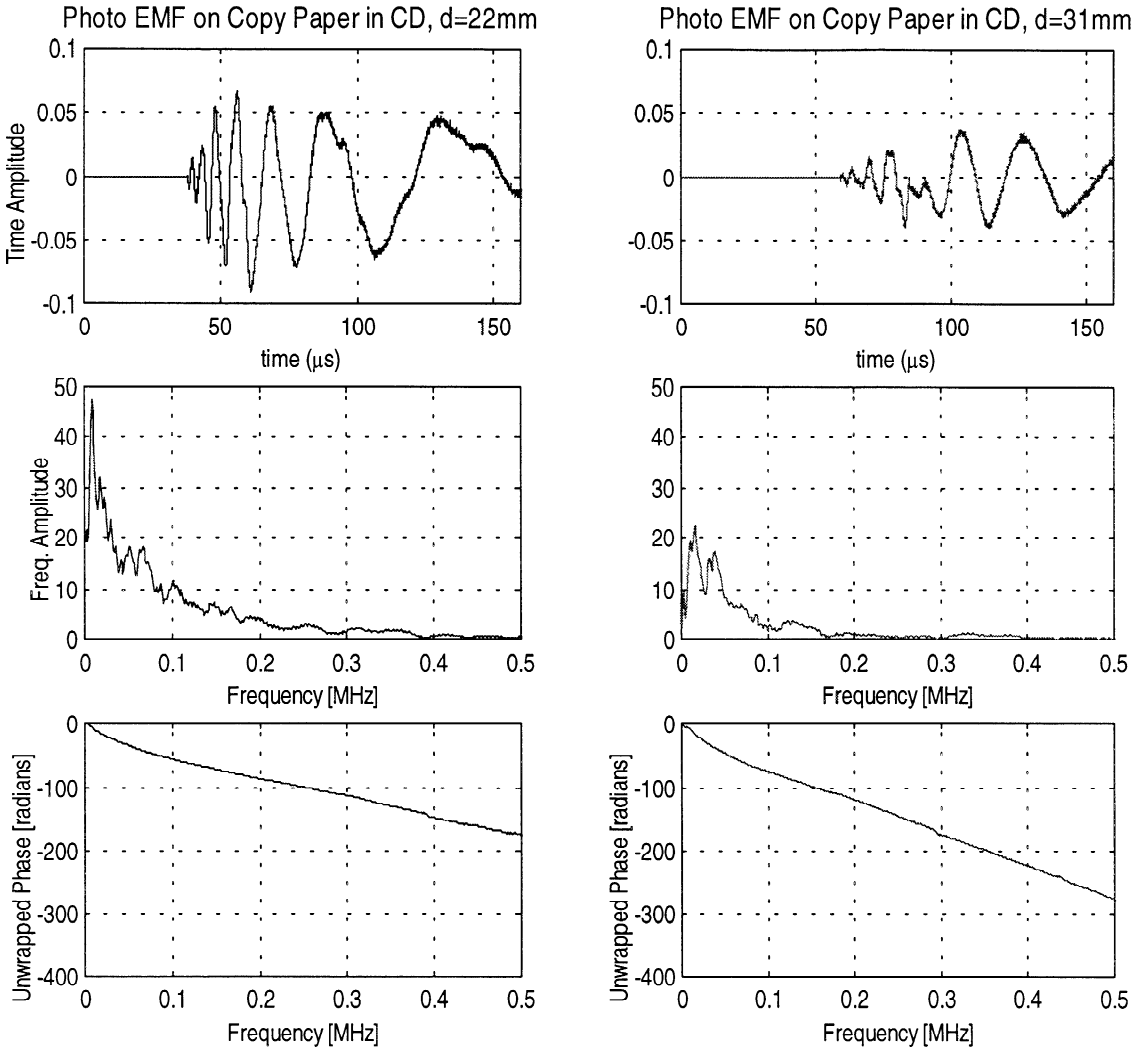

(a) d=22 mm (b) d=31 mm

Figure 2.6.113 A_0 mode analysis of the photo EMF signals on static copy paper in CD.

In Figure 2.6.113, the A_0 mode waves on static copy paper in the CD were detected at two different distances between the source and detector (d=22mm and 31mm) and were analyzed using the same technique described in Section 2.6.1.1. The FFTs of the signals are calculated and the phase angles are unwrapped. It is important to keep in mind that the phase angle information is reliable only within the frequency range where significant signal energy is present.

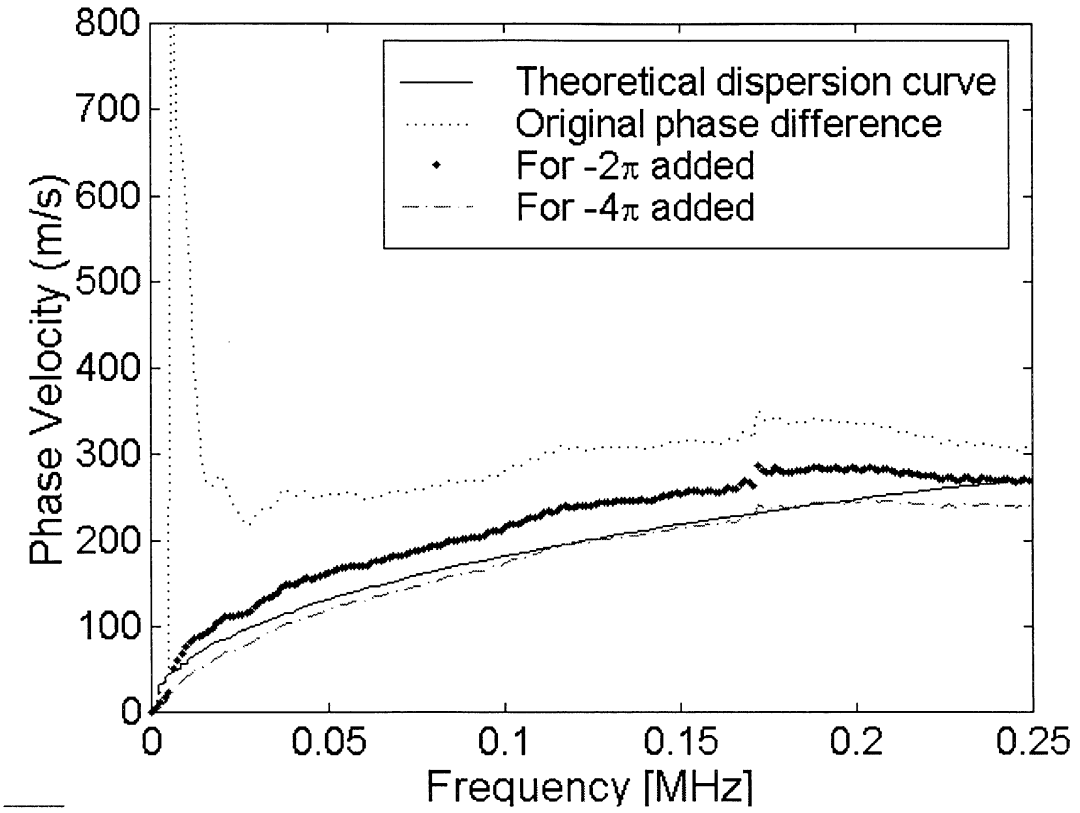

Figure 2.6.114 Comparison of the A_0 mode velocities using the photo EMF setup on static copy paper in CD.

In Figure 2.6.114, the resulting A_0 phase velocities with the corrected phase angles are plotted against the theoretical dispersion curve corresponding to the A_0 mode for static copy paper in the CD. The phase velocity with the -4π correction shows good agreement with the theoretical curve up to 0.2 MHz in frequency. This range also corresponds to the region where signal energy exists. Therefore, we can only be confident of the accuracy of the phase velocity in this region. In the frequency region over 0.2 MHz, the phase velocities deviate from the theoretical curve due to the lack of energy present. Hence, the results in this region are not reliable. Also, when the phase angle is not corrected, the result plotted in Figure 2.6.114 shows that significant error may occur at very low frequency. In order to circumvent this error, Johnson

(1996) suggested using a simplified low frequency approximation for the A_0 mode. Nevertheless, this method is not feasible in the current analysis since it requires the information of the S_0 mode wave, which may or may not be available.

2.6.5.3 Moving Paper Results (J. Jong, IPST)

Figure 2.6.115 shows an assortment of typical results obtained by the photo EMF interferometer on moving bleachboard in the CD at increasing speeds. The distance between the source and detection spot was maintained at 15 mm. The power of the detection laser was kept at 1.33 W and the energy level of the source laser was 25.1 mJ. The detection beam was at 45° incidence. At speeds up to 6 m/s, the shapes of the A_0 mode waveforms are clearly noticeable. As the web speed increases further, the magnitude of the A_0 signal decreases; that is, the A_0 signal becomes harder to distinguish from the noise. At 14 m/s, the A_0 signal becomes almost indistinguishable from the texture noise present. For the S_0 mode, the signal is detectable at 1 m/s, although it disappears quickly as the speed increases.

Figure 2.6.116 shows the corresponding FFT spectra of the signals shown in Figure 2.6.115. Most of the A_0 signal energy is present below 0.5 MHz. The broadband noise, as discussed in the previous noise analysis, appears to shift to higher frequency as the web speed increases up to a certain speed. That is, at 2 m/s, the broadband noise peak is approximately at 0.7 MHz. At 4 m/s, it is at 1.2 MHz. At speeds higher than 6 m/s, it exists at 1.6 MHz. Also noticeable is the sharp peak at approximately 1.75 MHz for higher web speeds. It results from the burst of energy that exists within the first 10 μs and is related to the saturation of the photodetector by the generation laser.

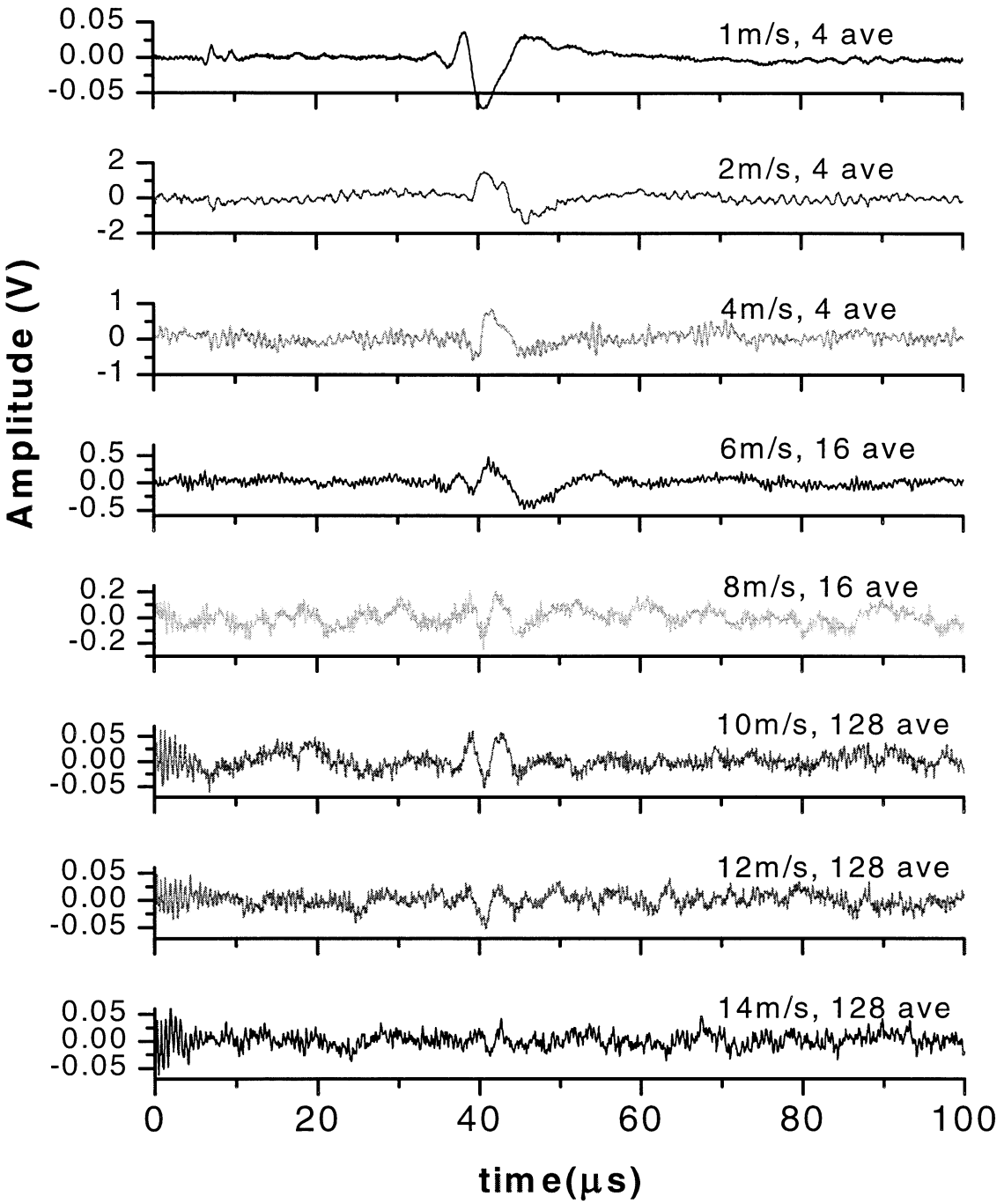

Figure 2.6.115 Comparison of the Photo EMF signals on bleachboard in CD at different web speeds: d=15mm, P=1.33W, E=25.1mJ using a line generation in ablation mode. The incidence of the detection beam is at 45° with respect to normal to the surface. The amplifier was not used for the signal at 1 m/s. Then, the signals were amplified at 39.7 dB. Data taken August 14th.

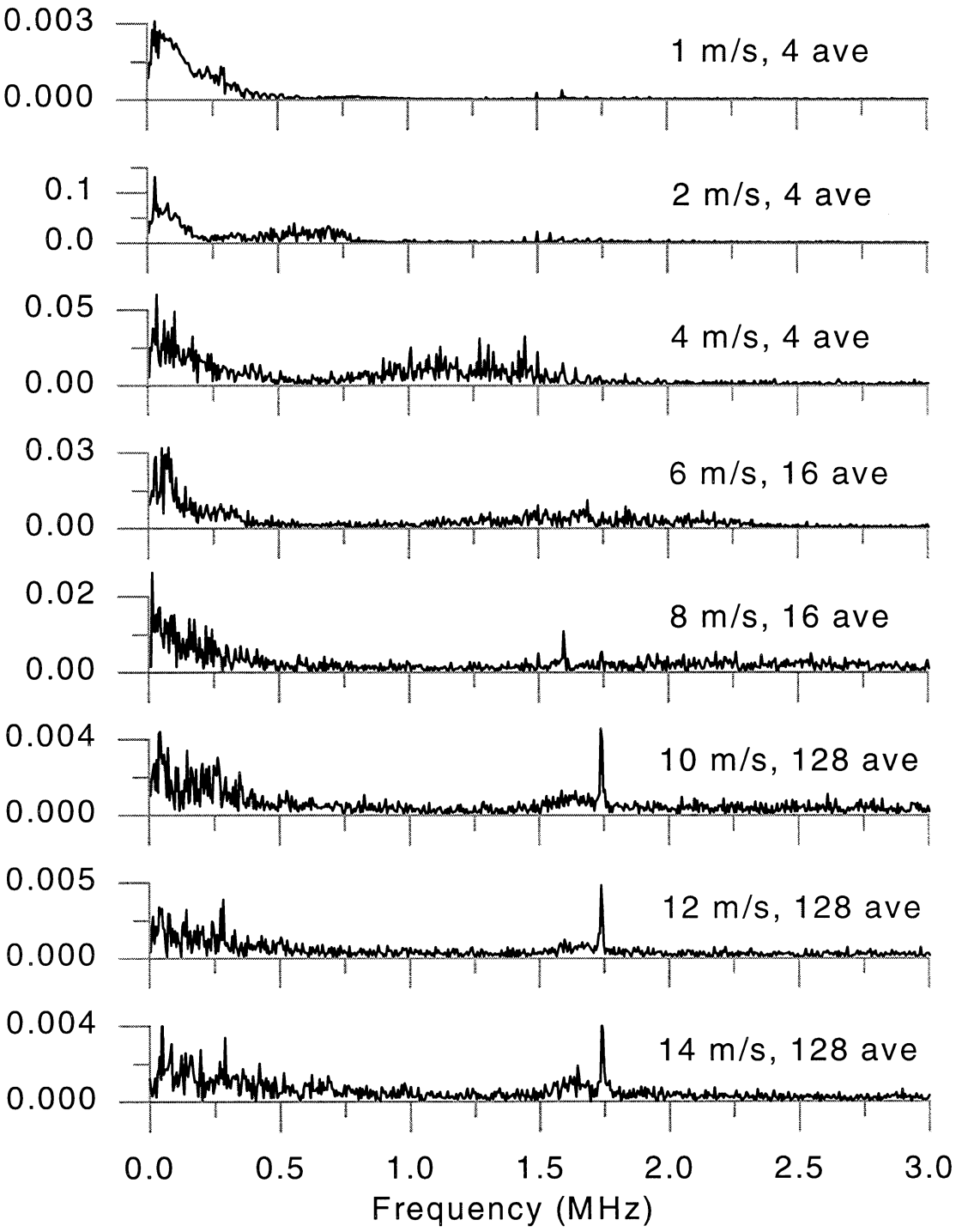

Figure 2.6.116 FFT spectra of the Photo EMF signals shown in Figure 2.6.112 on bleachboard in CD at different web speeds: d=15mm, P=1.33W, E=25.1mJ using a line generation in ablation mode. The incidence of the detection beam is at 45° with respect to normal to the surface.

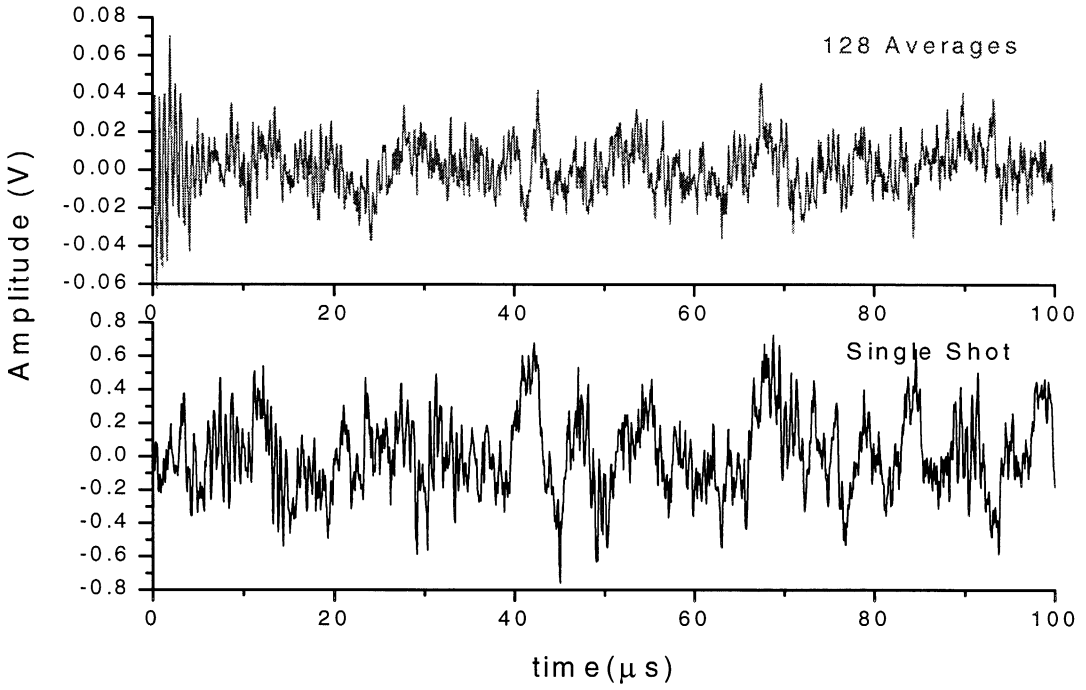

Figure 2.6.117 (a) Comparison of signals at 14 m/s using 128 averages and a single shot on bleachboard: The figure indicates that the amplitude becomes one order of magnitude smaller when signal is averaged at 128 times.

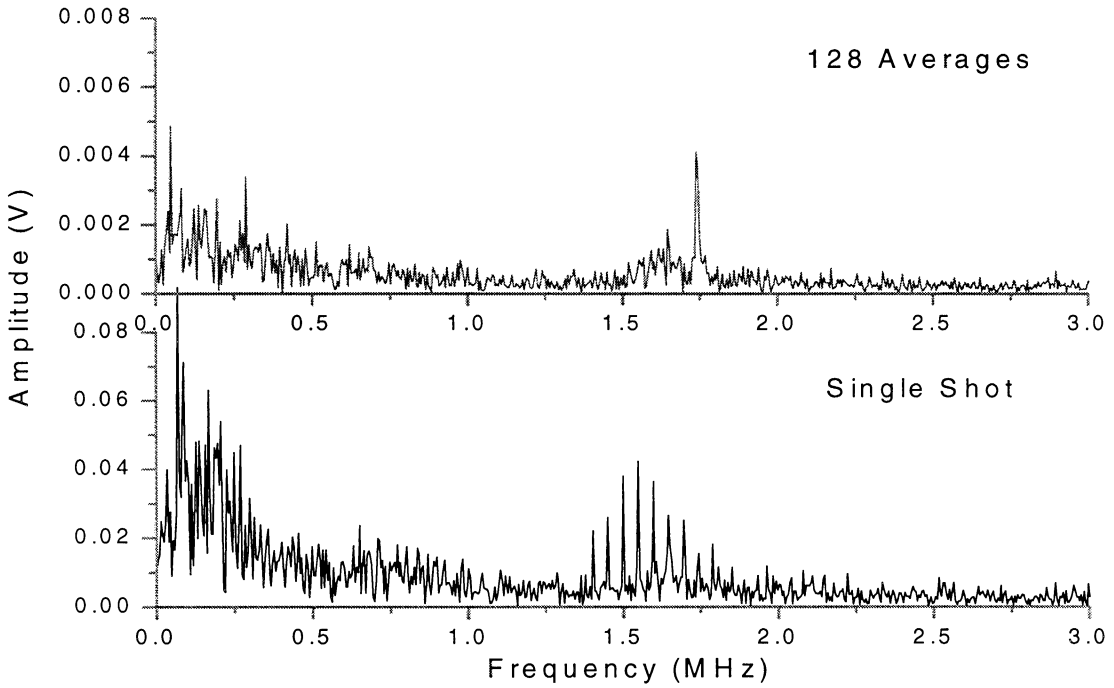

Figure 2.6.117 (b) FFT Spectra for Figure 2.6.117 (a).

The characteristics of bleachboard are very different from those of copy paper. The grammage is very high at 262 g/m^2. Signals are not expected to be well formed. Nevertheless, the results at high speeds are very promising.

The plots in Figure 2.6.117a and b compare two signals obtained on bleachboard at 14 m/s with the setup as of August 14th. For *a* and *b*, the top signal is averaged at 128 times while the bottom one is obtained by a single shot. The signal with the 128 times average has an amplitude magnitude that is one order smaller than that of the single shot. This is caused by extreme variability in the sample and hence variability in the signal (therefore averaging causes the signal to disappear). The A_0 in contained in the frequency range below 0.5 MHz. The frequency analysis shows that there appears to be a noise peak existing at 1.6 MHz. Most likely, the set of peaks around 1.5 MHz in the single shot data is laser noise (feedback into the laser cavity).

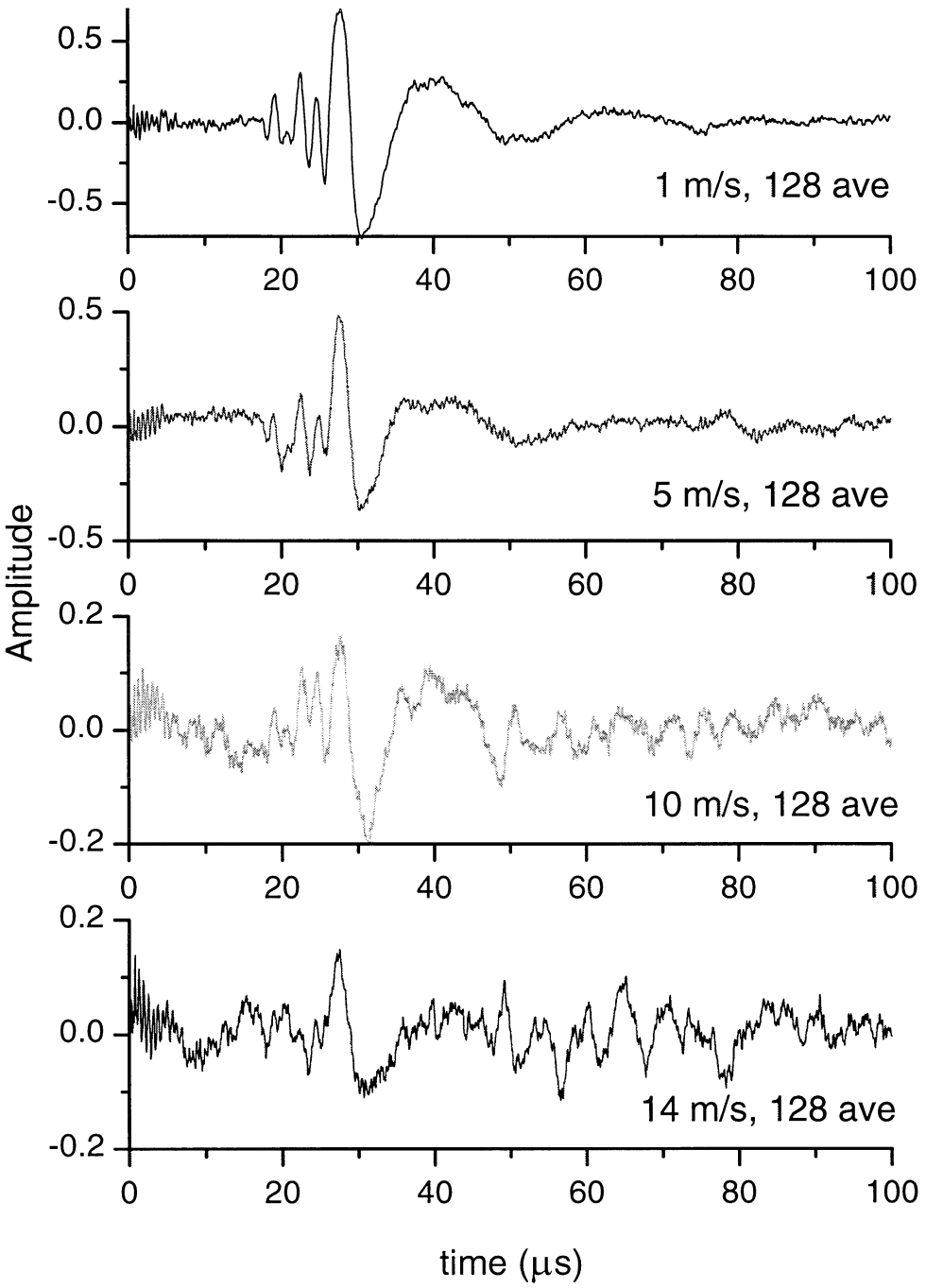

Figure 2.6.118 Change of signal amplitudes against web speeds on copy paper in CD: d=10mm, E=25.1mJ, and P=1.33W using a line generation in ablation mode. All signals are averaged 128 times. The incidence of the detection beam is at 45°. Data taken on August 14.

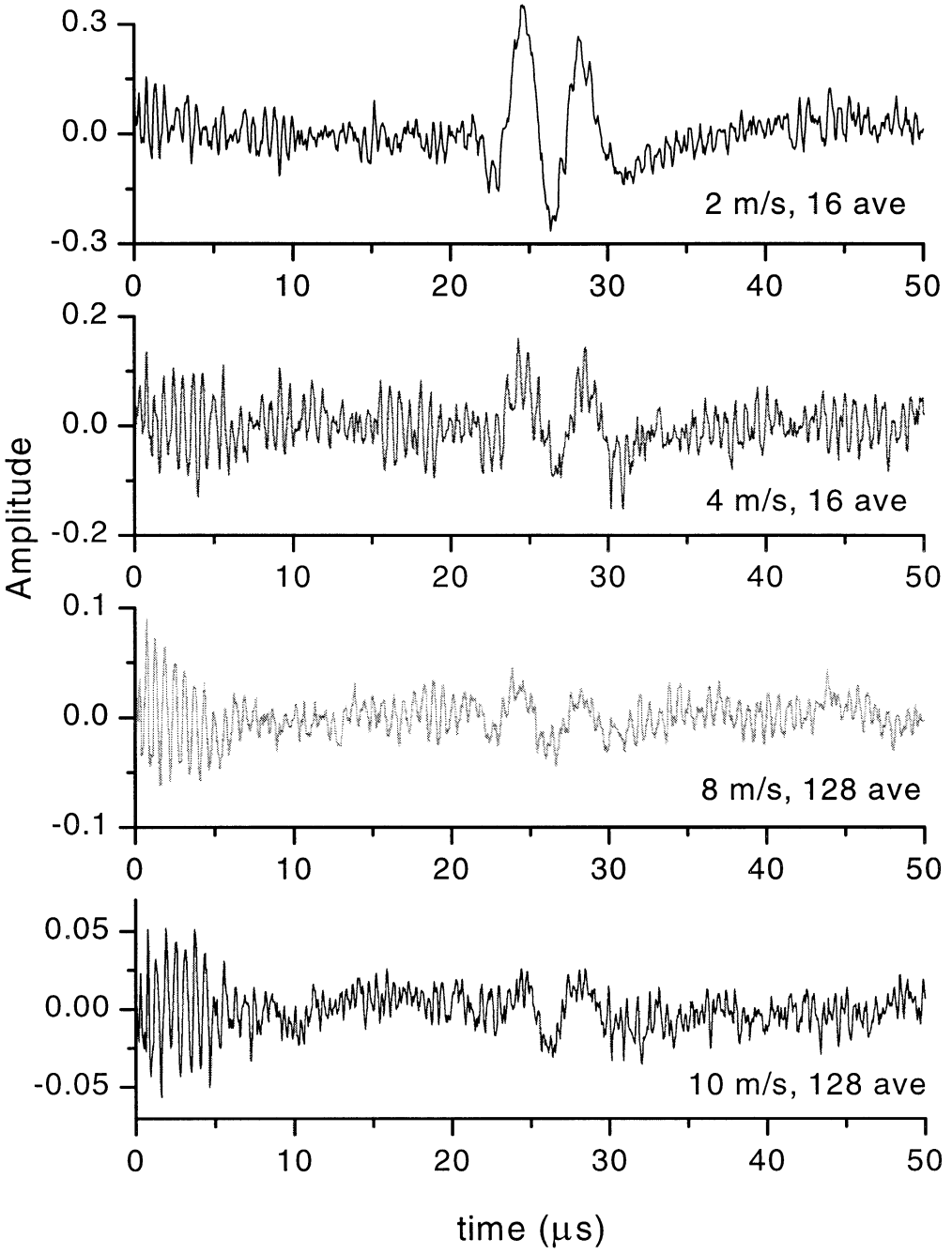

Figure 2.6.119 Change of signal amplitudes vs. web speeds on linerboard 42-lb in CD: d=10mm, E=25.1mJ, P=0.72W using a line generation in ablation mode. The incidence of the detection beam is at 45°. Data taken on August 14.

Typical waveforms obtained with copy paper and 42-lb linerboard are plotted in Figures 2.6.118 and 2.6.119, respectively. The distance *d* between the source and the detection spot was maintained at 10 mm for both figures. The energy level of the source laser was 25.1 mJ using a line generation in ablation mode. The incident angle of the detection beam was at 45° with respect to the normal to the surface. The power of the detection laser was at 1.33 W for copy paper and 0.72 W for 42-lb linerboard.

As previously described with the bleachboard sample, the signal amplitude decreases as the web speed increases. The overall signals on the copy paper are fairly clean without much noise present up to 14 m/s. On the other hand, the signals on the 42-lb linerboard tend to contain more texture noise and dampen out quickly. At web speeds higher than 8 m/s, the S/N ratio becomes very low. Notice that the results shown in Figures 2.6.115, 2.6.118 and 2.6.119 so far were obtained with the web simulator in the original configuration limited to the maximum speed of 14 m/s.

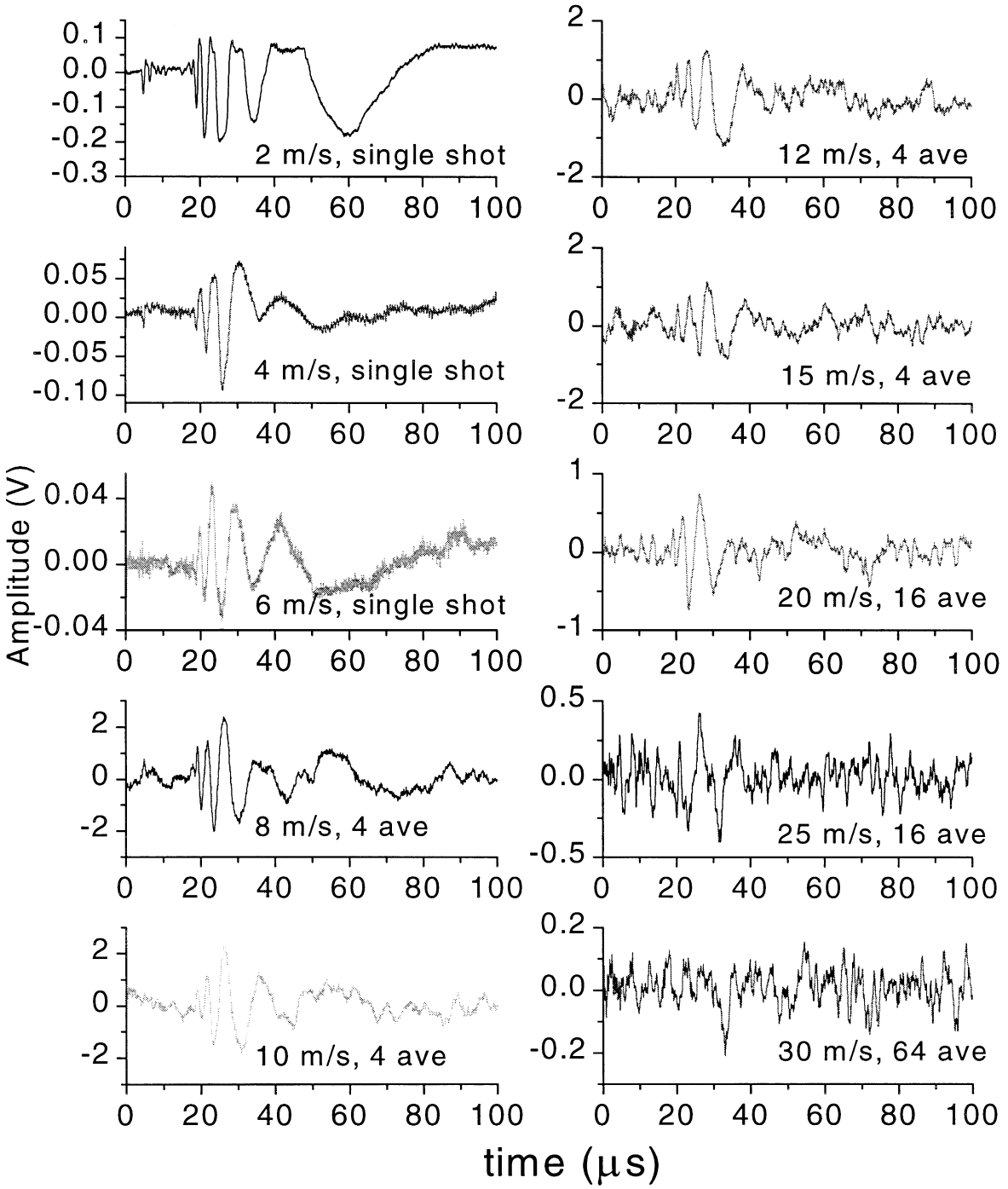

Figure 2.6.120 Comparison of the signals on copy paper in CD at different web speeds after modification of the web simulator: d=10mm, P=1.33W, E=25.6mJ using a line generation in the intermediate regime. Data taken on August 21.

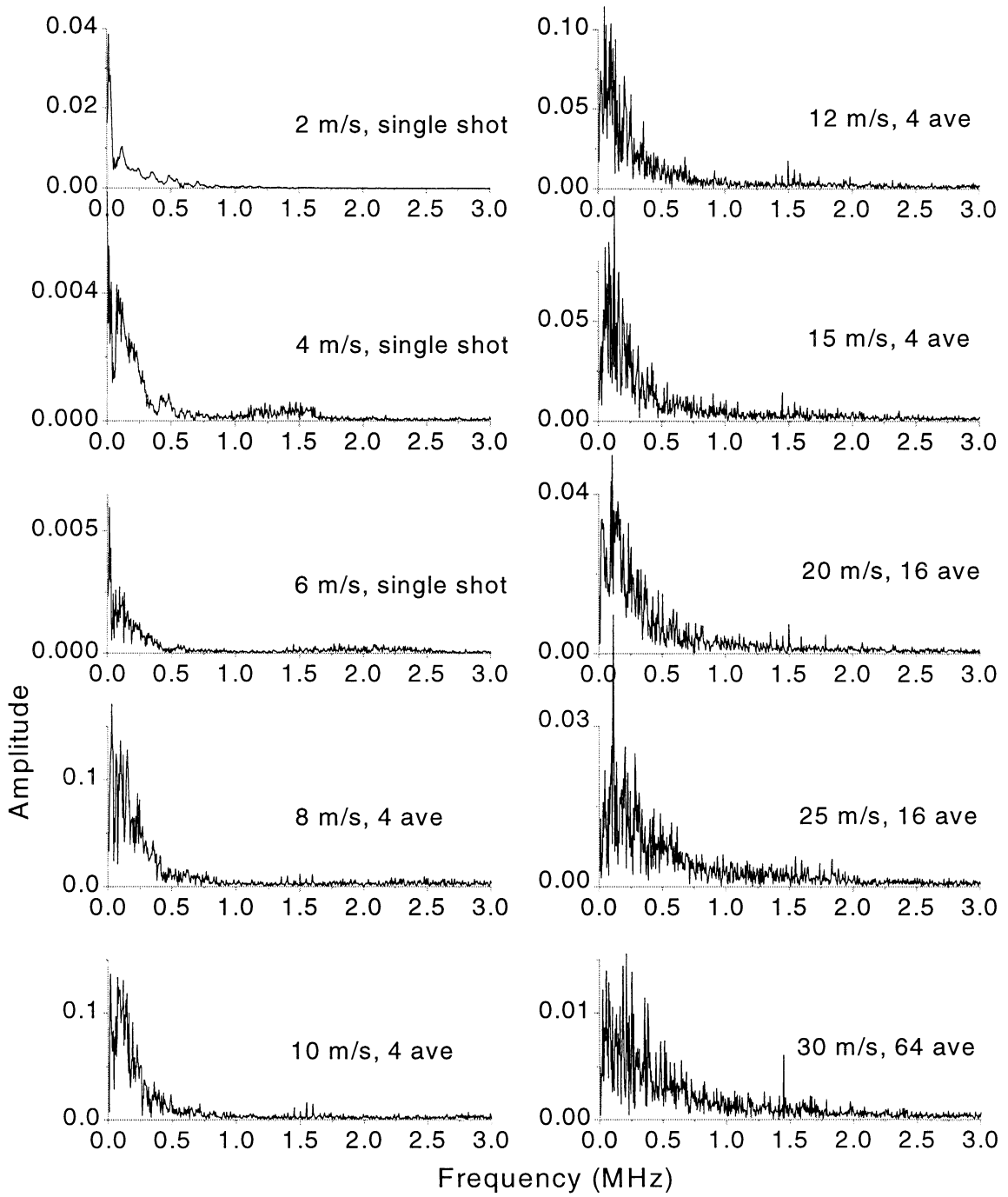

Figure 2.6.121 FFT spectra of the signals shown in Figure 2.6.120 on copy paper in CD at different web speeds after modification of the web simulator: d=10mm, P=1.33W, E=25.6mJ using a line generation in the intermediate regime. Data taken August 21st.

Figure 2.6.120 shows the combination of signals obtained on copy paper in the CD after the web simulator was modified to increase the maximum speed to 30 m/s. The distance, the power and the energy per pulse were maintained at 10 mm, 1.33 W and 25.6 mJ, respectively. The source laser was operated in intermediate regime using a line generation.

Since a typical papermaking machine can run as fast as 30 m/s, Figure 2.6.120 shows the remarkable possibility of implementing the current non-contact laser ultrasonic technique on a real papermaking machine. For typical copy paper, machine speed runs at 18.5 m/s (3650 ft/min) (Biermann, 1993). At that speed, the waveform can be detected clearly using the current setup as shown in Figure 2.6.120. By improving the current configuration and optimizing the laser optics, the S/N ratio can be further improved.

Figure 2.6.121 shows the corresponding FFT spectra of the signals on copy paper in CD shown in Figure 2.6.120. Again, the signal energy is mostly present in the low frequency region. The noise level appears to be relatively low after the web simulator was modified. There still seems to be noise present at approximately 1.5 MHz for high speeds.

In order to investigate what effect the modification of the web simulator has on the signal, two FFT spectra of the signals on copy paper before and after the modification are compared in Figure 2.6.122. The figure shows that the noise level has decreased and the noise peak has shifted slightly from 1.6 MHz to 1.5 MHz. Therefore, it is likely that the noise is related to the web simulator.

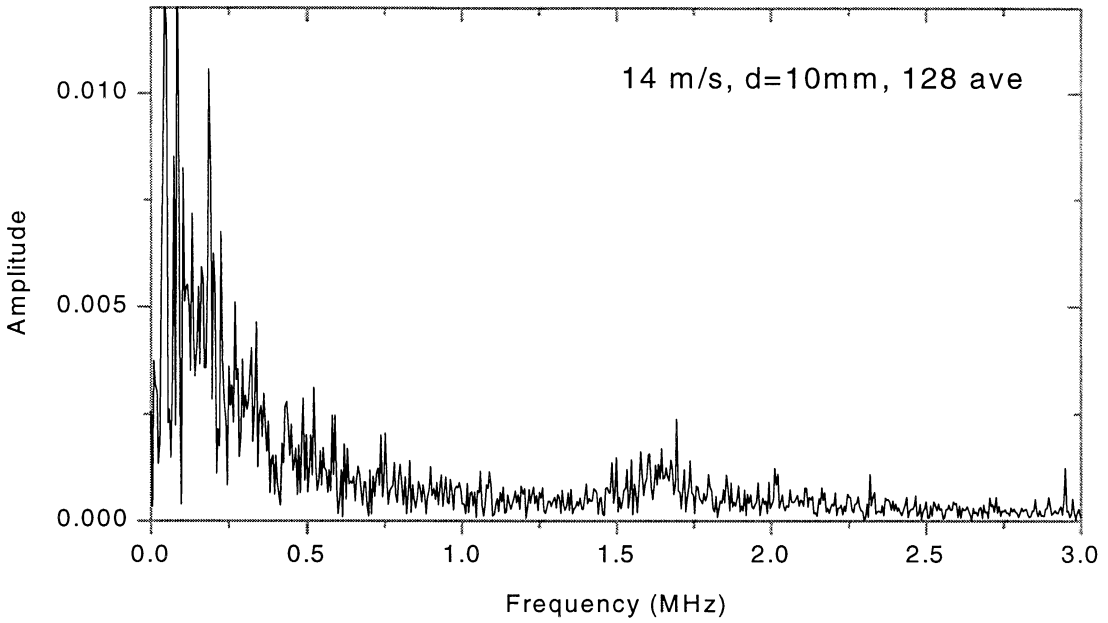

(a)before modification

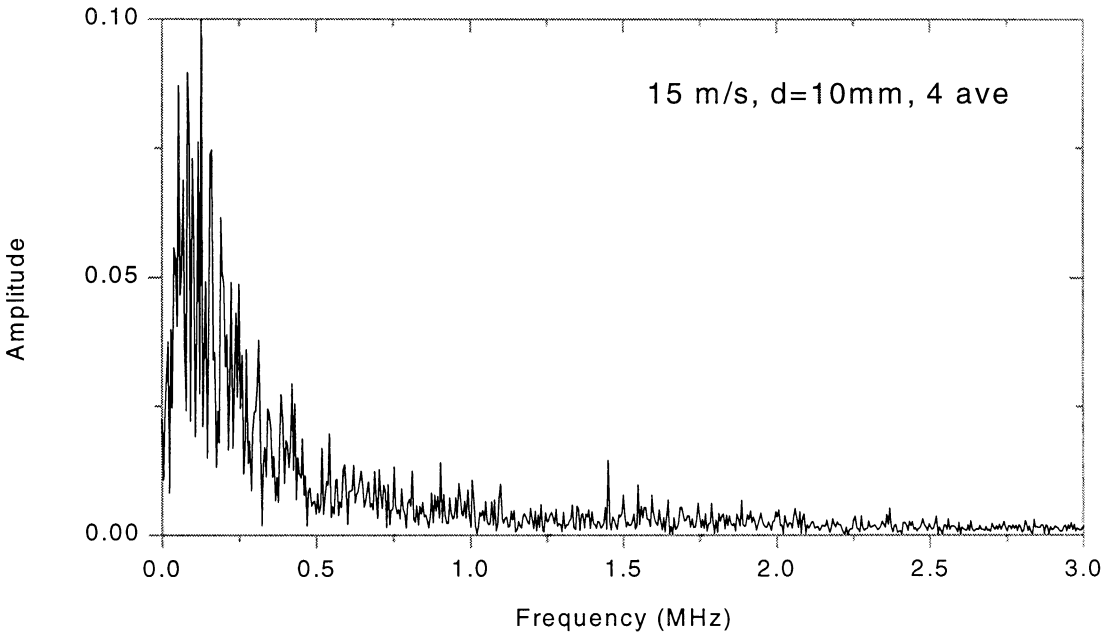

(b) after modification

Figure 2.6.122 Comparison of FFT spectra on copy paper before and after the modification of the web simulator.

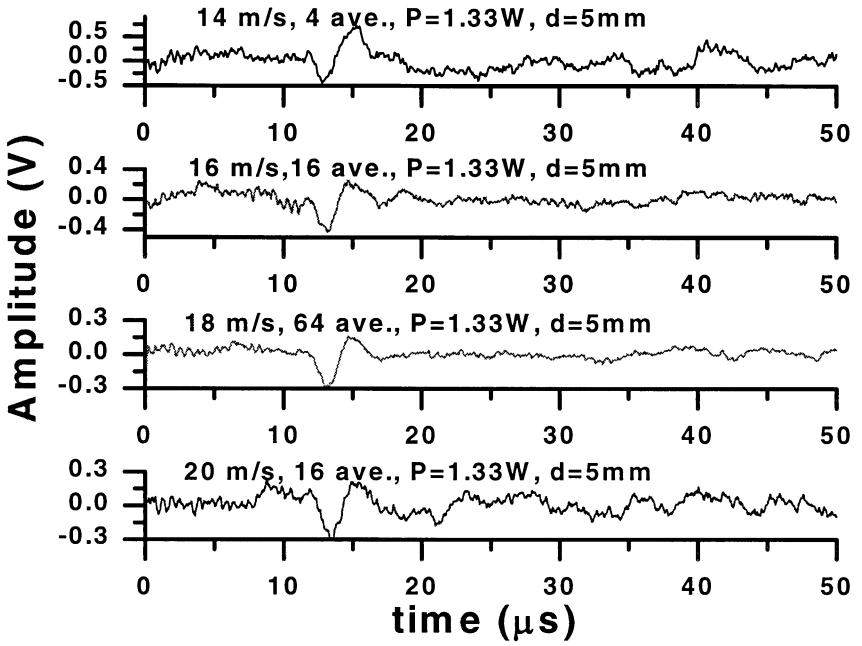

Figure 2.6.123 Time signals in CD obtained by the photo EMF at speeds higher than the typical machine speed of 11.6 m/s for linerboard 42-lb: d=5mm, P=1.33W, E=25.6mJ using a line generation in the intermediate regime. Data taken on August 21.

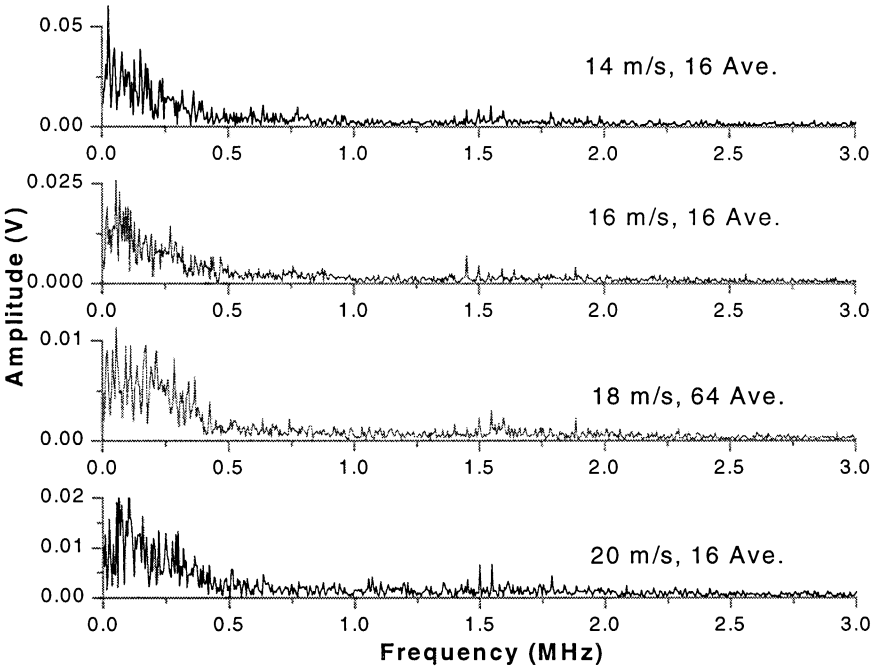

Figure 2.6.124 FFT spectra corresponding to the signals in Figure 2.6.123: The signals were obtained in CD by the photo EMF at speeds higher than the typical machine speed of 11.6 m/s for linerboard 42-lb; d=5mm, P=1.33W, E=25.6mJ using a line generation in the intermediate regime. Data taken on August 21.

Figure 2.6.123 shows time signals obtained in CD by the photo EMF at speeds higher than the typical machine speed for 42-lb linerboard, which is approximately 11.6 m/s (2290 ft/min) (Biermann, 1993). Figure 2.6.124 shows the corresponding FFT spectra of the signals obtained in Figure 2.6.123. The spectra show that, even at speeds higher than the typical machine speed, the A_0 mode can still be detected in the frequency region below 0.5 MHz where most of the energy is present. Noise is found approximately at 1.5 MHz, as previously indicated for the results obtained with the modified web simulator. The comparison of the FFT spectra between copy paper and 42-lb linerboard suggests that the fluttering noise may be independent of paper grade since the noise exists at the same frequency range for both copy paper and 42-lb linerboard. Further tests are required to confirm this.

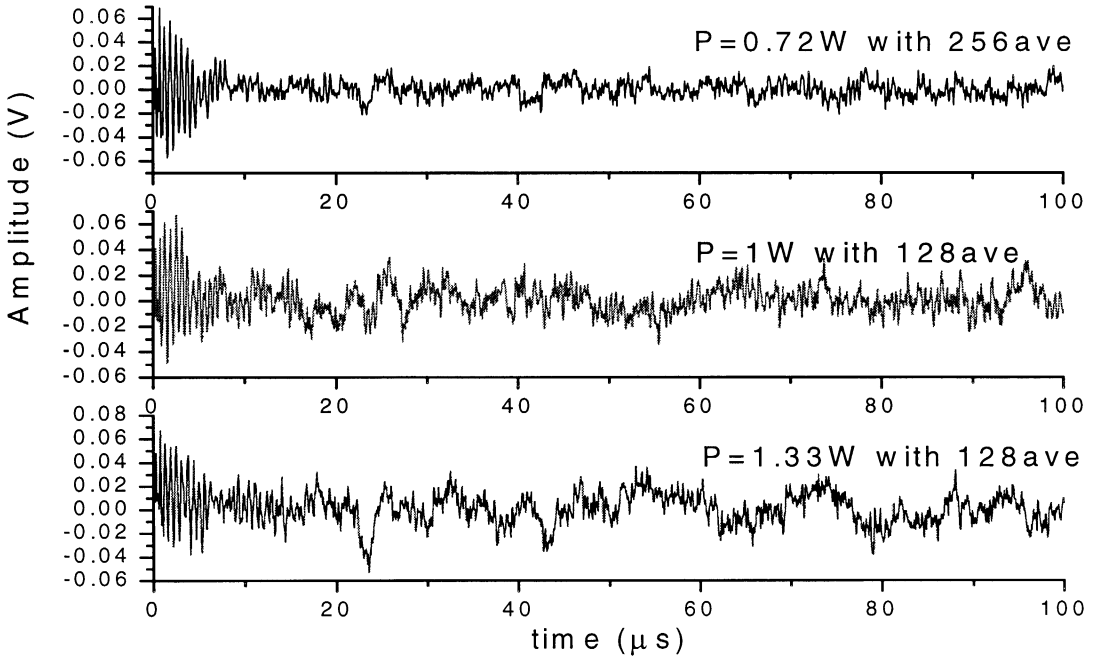

Figure 2.6.125 Recorded signals on 42-lb linerboard in CD when the detection power was increased: The signals were obtained before the web simulator was modified. Web speed, source energy and distance were maintained at 14 m/s, 25.1mJ and 9mm respectively. Data taken on August 14.

In order to improve signal detection at high speed, the power of the detection laser was varied. Figure 2.6.125 shows selected signals recorded on 42-lb linerboard before the modification of the web simulator as the power increased from 0.72W to 1.33W. The web speed was maintained at 14 m/s. Within the first 10 μs, there was a burst of signal associated with generation laser saturation of the GaAs:Cr detector. This was also present in the bleachboard at the same speed, but not evident in the copy paper. A similar noise pulse was detected in the work by Brodeur et al. (1997), who attributed the cause of the noise to electromagnetic interference generated during the firing of the Nd:YAG laser. The initial noise is bound to interfere with the detection of the S_0 mode wave for small generation/detection distances.

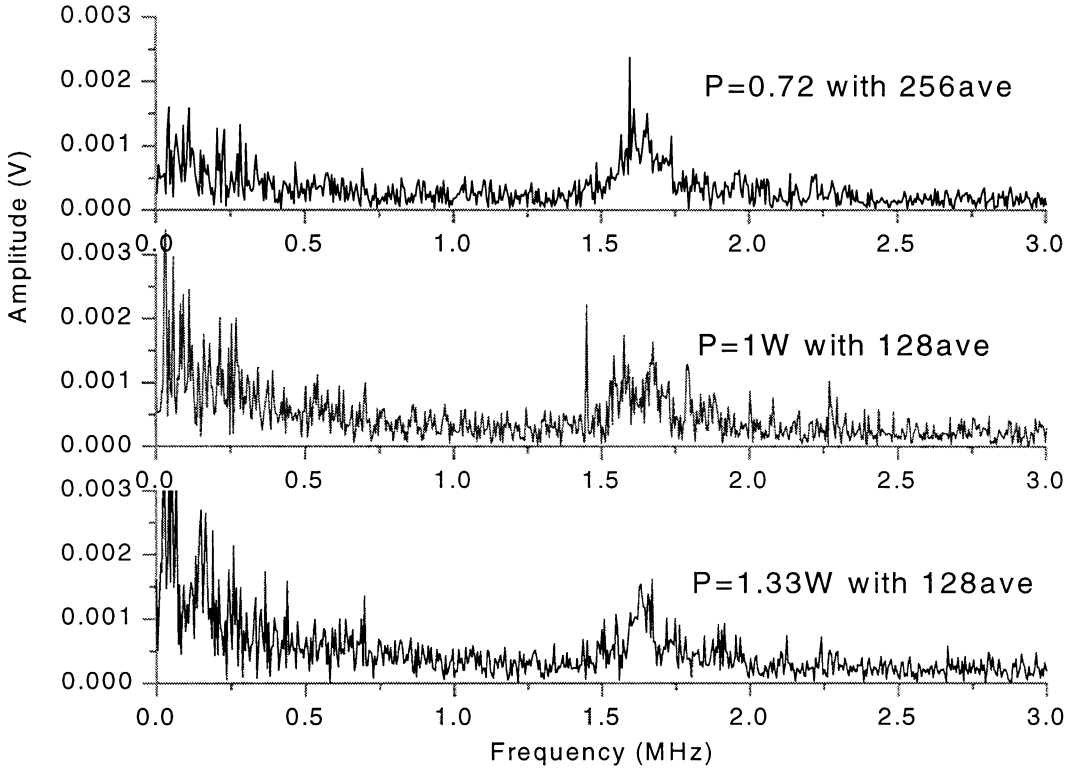

Figure 2.6.126 Corresponding FFT spectra on 42-lb linerboard in CD for the increase of the detection power: The signals were obtained before the web simulator was modified. Web speed, source energy and distance were maintained at 14 m/s, 25.1mJ and 9mm respectively. There is a noise peak at ≈1.6 MHz. The source of the peak is possibly related to fluttering.

When the FFTs of the above signals are computed, some interesting results are observed. Figure 2.6.126 shows the corresponding spectra of the same signals obtained on 42-lb linerboard before the web simulator was modified. Again, there exists a peak approximately at 1.6 MHz. The peak does not change its magnitude with increasing the detection power. Therefore, the source of the noise peak is not related to the detection laser. More tests are required to investigate possible sources of this noise. It is also important to determine how to suppress the noise as well as how to improve the S/N ratio.

Some results were obtained along MD on moving paper samples by modifying the experimental setup on August 24th and 25th. The detection beam was fixed at the same point as previously. The generation line was rotated 90° and move above the detection point. Figures 2.6.127-129 show the signals in MD for copy paper, 42-lb linerboard and bleachboard, respectively. The results in MD are similar to those in CD for the three samples. The S_0 mode was not visible, however the system still needs to be optimized.

Overall, the preliminary results obtained by the Photo EMF technique on moving paper are very promising. We have demonstrated non-contact laser ultrasonics at commercial machine speeds.

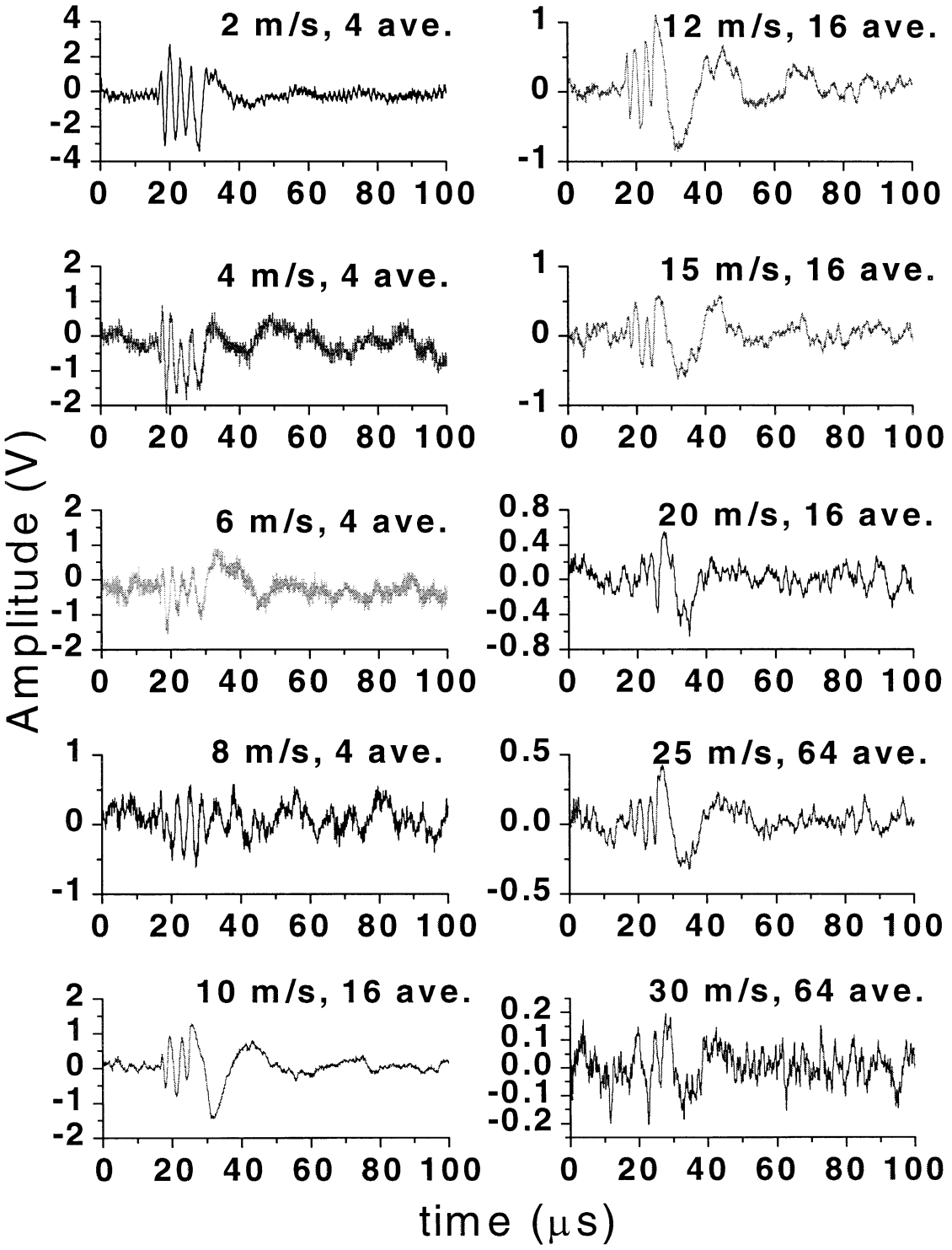

Figure 2.6.127 Comparison of the signals on copy paper in MD at different web speeds: d = 10 mm, P = 1.33 W, E =26.7mJ using a line generation in the intermediate regime up to 8 m/s and in the ablation mode from 10 m/s. Maximum power density was used at 30 m/s by decreasing the generation spot diameter. Data taken August 24th and 25th.

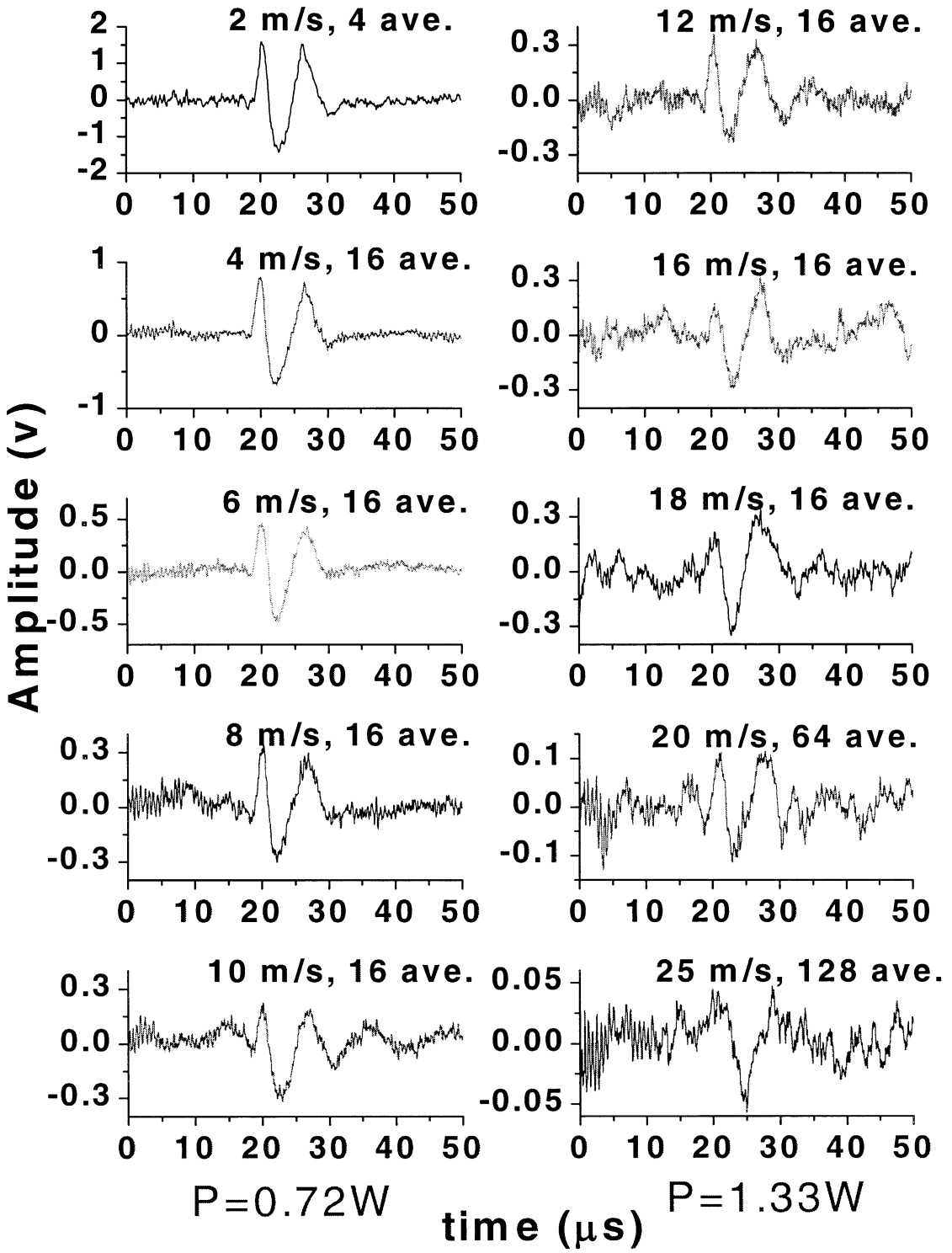

Figure 2.6.128 Comparison of the signals on linerboard 42-lb in MD at different web speeds: d = 10 mm and E =26.7mJ using a line generation in the intermediate regime. Power was increased from 0.72 W to 1.33 W at speeds from 12 m/s. Data taken on August 24 and 25.

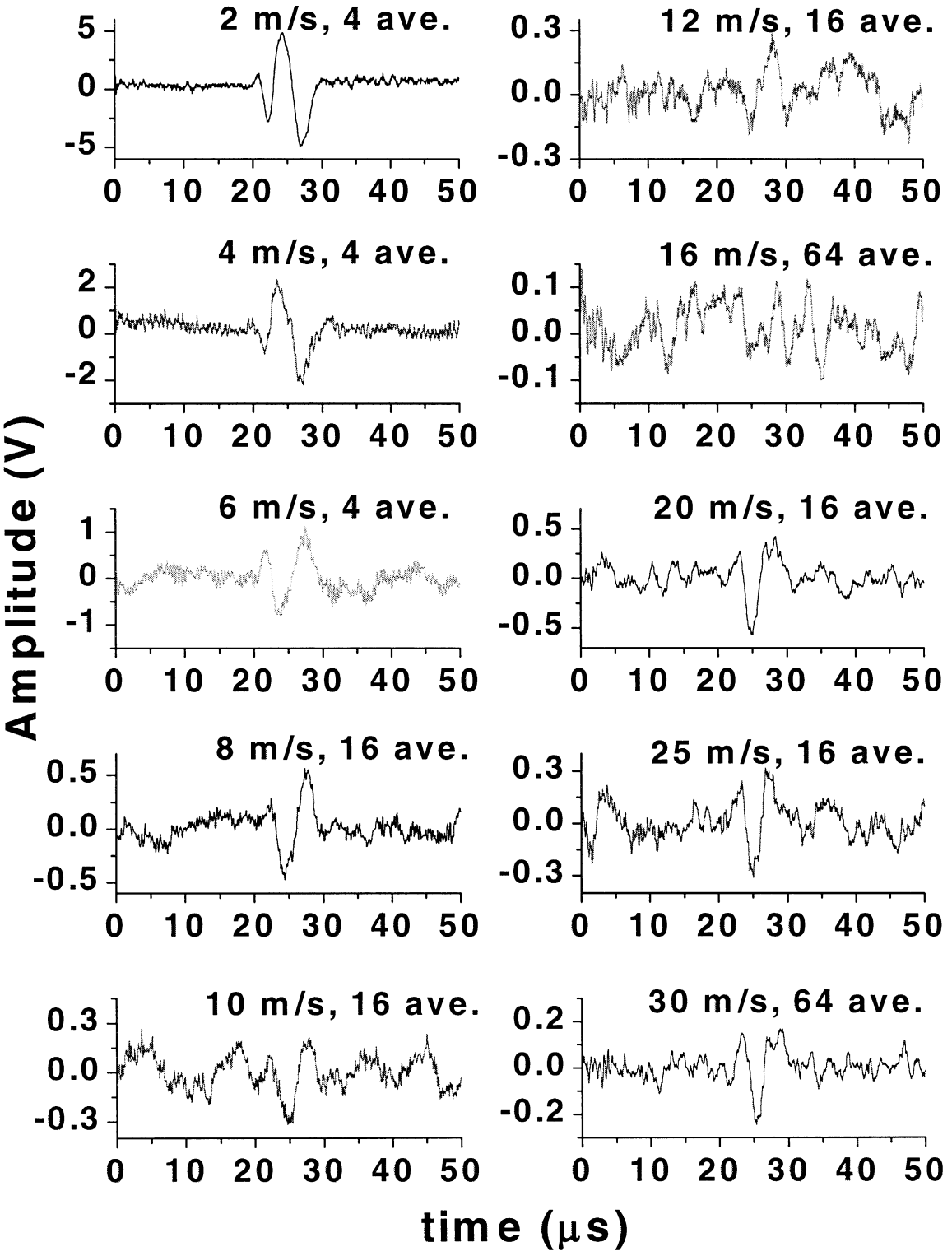

Figure 2.6.129 Comparison of the signals on bleachboard in MD at different web speeds: d = 10 mm, P = 1.33 W, E =26.7mJ using a line generation in the intermediate regime up to 16 m/s and in the ablation mode from 20 m/s. Data taken on August 24 and 25.

2.6.6 Self-mixing interferometer (E. Lafond, IPST)

2.6.6.1 Experimental setup

2.6.6.1.1 Operating principle of the self-mixing interferometer

A laser beam is emitted from the front mirror of a diode laser or another laser (for instance, a low-power Helium-Neon) and is focused onto the surface of the object to investigate (see Figure 2.6.130).

The vibrations of the surface of the object induce a phase shift on the back-scattered speckles caused by the Doppler effect. The back-scattered speckles come back and follow the same optical path toward the laser cavity, after having their phase shifted by the displacement of the surface. A speckle comes into the laser cavity and it interferes with the laser wave oscillating in the cavity and shifts the operating point of the atomic gain curve of the amplifying media.

The shift modifies the output power of the laser, which is monitored by a photodiode put either behind the rear mirror of the laser cavity or (in a configuration not shown on this schematic, see Figure 2.5.6 instead) after a beam splitter in front of the front mirror. The intensity of back-scattered light should be low in order to stay in a range where the time-dependent power variations of the laser are linearly related to the time-dependent displacements of the target surface, at least for low frequencies.

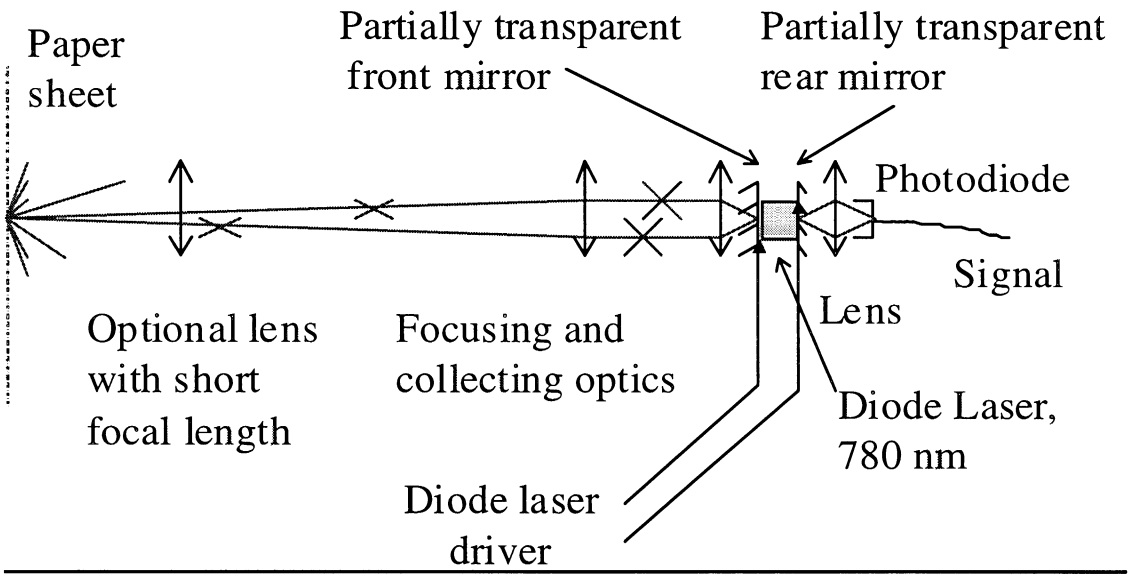

Figure 2.6.130 Schematic of the self-mixing interferometer.

The advantage of a self-mixing interferometer, compared to a Mach-Zehnder interferometer for example, is that it can work easily on scattering surfaces and needs very little light back-scattered since the oscillation of the laser wave inside the cavity is very sensitive to any small perturbation.

One of the main drawbacks is poor signal to noise ratio because of the instabilities inherent to the laser amplifying medium (especially with diode lasers) that creates artificial phase-shifts adding to the one caused by surface displacement.

This method works only with one speckle at a time and when the speckle is aligned with the incident beam because the beam needs to be coherent with itself. If the speckle pattern changes (for example on a moving web) and this particular speckle becomes misaligned, the interferometer will lose the ultrasonic signal. When another speckle comes into alignment, the perturbation of the amplifying medium will resume and provide the displacement of the surface again.

2.6.6.1.2 Bandwidth of the self-mixing interferometer

For evaluation, a high frequency version of a commercially available vibrometer working with the self-mixing principle was used. This high frequency version is a prototype built very recently and the bandwidth, which had not been verified, was supposedly DC to 2 MHz. It was discovered during the trials at IPST that the bandwidth was in fact DC to 200 kHz at –3 dB. Displacements can, however, be detected around 1 MHz providing they are huge, probably in the 100 nm range which is far from the laser generated displacements on paper. Above 100 kHz, the sensitivity to displacements starts to decrease sharply.

The useful bandwidth for measurements on paper with this vibrometer is DC to 200 kHz, which seems too narrow for the ultrasonic waves to be detected on paper. Thus in reality, the prototype used should be classified as a vibrometer instead of an ultrasonic interferometer.

The output power of the laser in this vibrometer was 5 mW at a wavelength of 780 nm, situated in the upper limit of the visible spectrum. This is (almost) an "eye safe" laser, which is not the case of lasers used by the other methods that have been investigated.

2.6.6.1.3 Experimental configurations used for the trials

The vibrometer was first used by aiming the beam directly onto the paper surface without any additional optics, which is the normal way to use it. It was discovered during the trials that the "signal strength" output of the interferometer absolutely required to be maximized (maximum sensitivity to displacements) in order to detect small amplitude ultrasonic waves that are generated on paper. This was done using a focusing lens between the vibrometer and the

sample to increase the étendue of the system (see Section 2.5.3). The laser beam needed to have the focal point be the paper surface.

The first trials were with a 100 mm focal length, 1" diameter lens which was antireflection coated for 1064 nm, which is not too far away from the laser wavelength. The signal strength output was about 2.5 V on static copy paper but started to decrease quickly as soon as the paper web was moving. So the 100 mm focal length lens was replaced with a 25 mm focal length lens to increase the étendue and stay above a 2 V output signal on moving paper. A few trials at normal incidence on paper were performed, but most of the experiments were done at 45° incidence to try to see the S_0 wave. There was not much difference between signals at 0° and 45° incidence. For tests on static paper, the web simulator was used without rotation instead of the static paper sample holder.

The generation system was the same as the one used on August 24th, 1998 with the photoinduced-EMF interferometer. It produced a 0.5 x 13 mm line source generating ultrasonic waves along the cross direction of the paper samples. In order to generate A_0 waves with sufficient amplitude, the beam was focused to the minimum spot to work in a strong ablation mode. This caused significant damage to the paper sheet. The average energy per pulse was maintained at 25.1 mJ at all times. Some pictures of the experimental setup with the detection at normal incidence are presented in Figures 2.6.131-133.

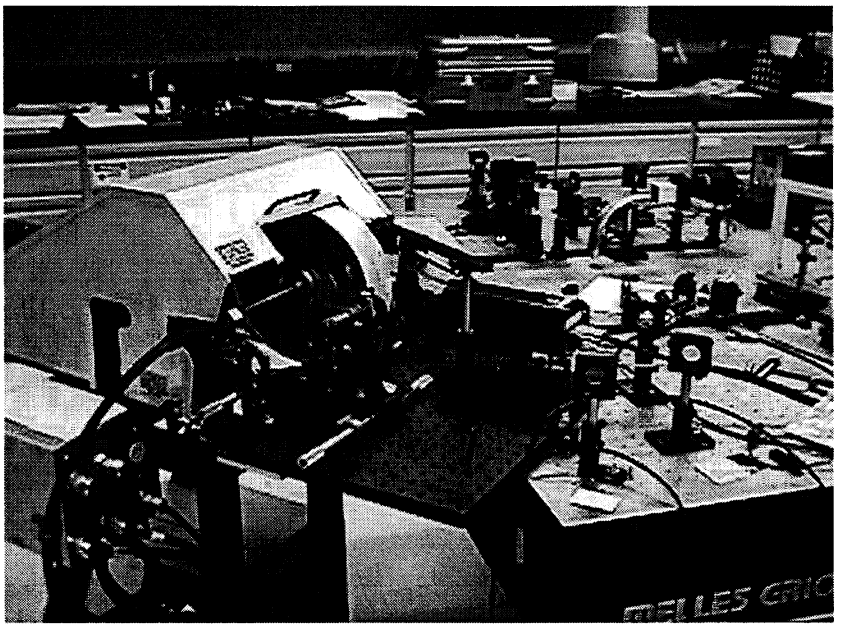

Figure 2.6.131 General overview of the experimental setup at normal incidence with the self-mixing interferometer.

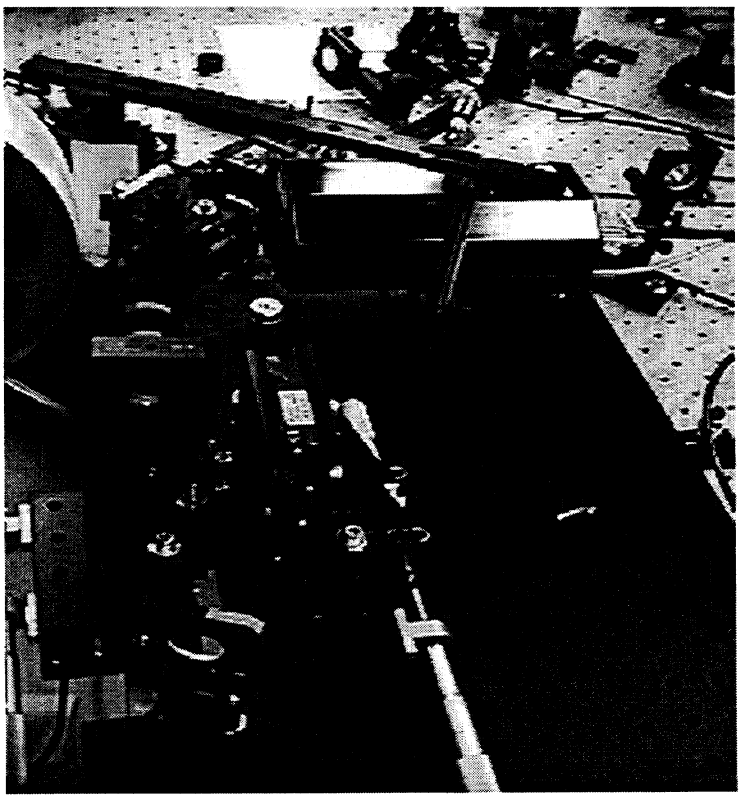

Figure 2.6.132 View of the experimental setup for normal incidence (self-mixing interferometer head is the black box in the upper third of the picture).

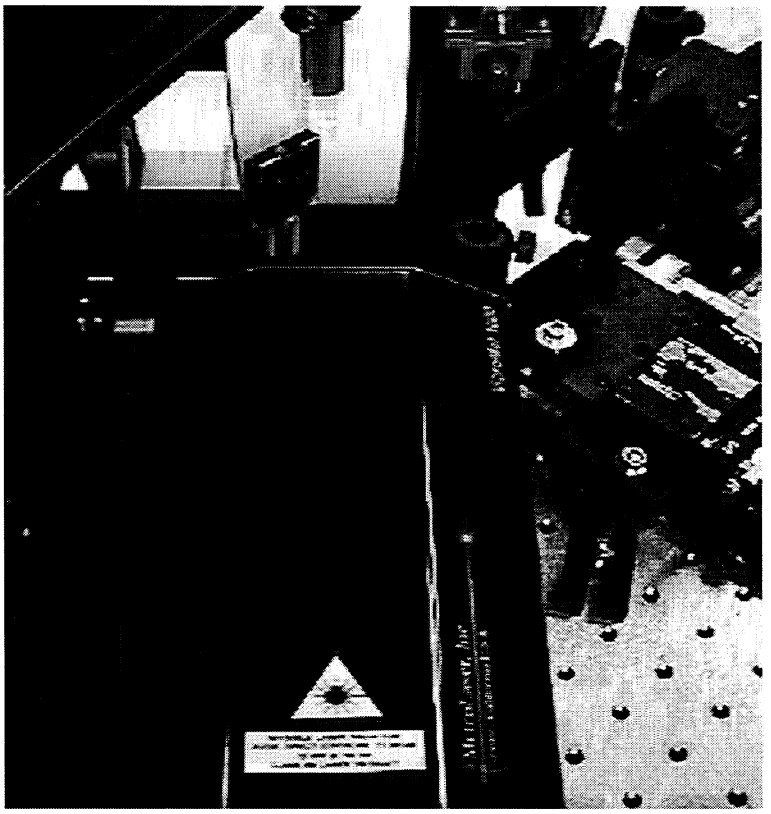

Figure 2.6.133 View of the self-mixing interferometer head at normal incidence without the additional focusing lens.

The pictures of the trials that were done at 45° incidence for the detection beam are presented on Figures 2.6.134-136. The 25 mm focal length lens was added in front of the interferometer for tests on moving paper samples (copy paper and 42-lb linerboard).

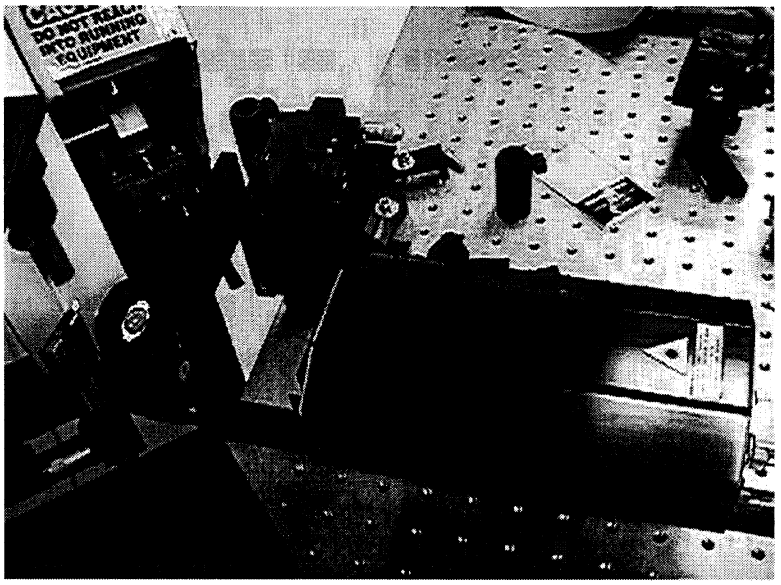

Figure 2.6.134 Self-mixing interferometer head at 45° incidence with additional 25 mm focal length lens shown on the left.

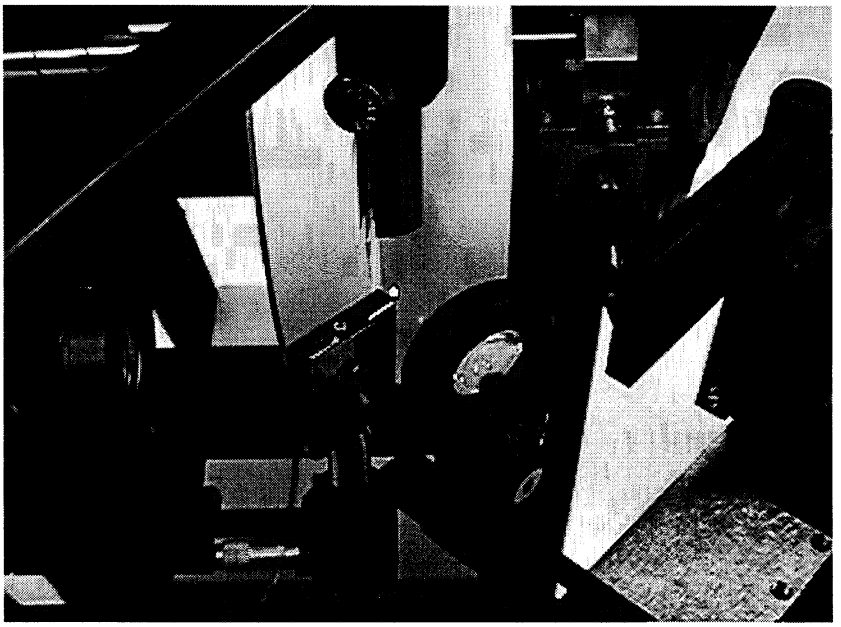

Figure 2.6.135 Detail of the self-mixing interferometer (not shown) with additional lens in the center and last mirror of the generation system.

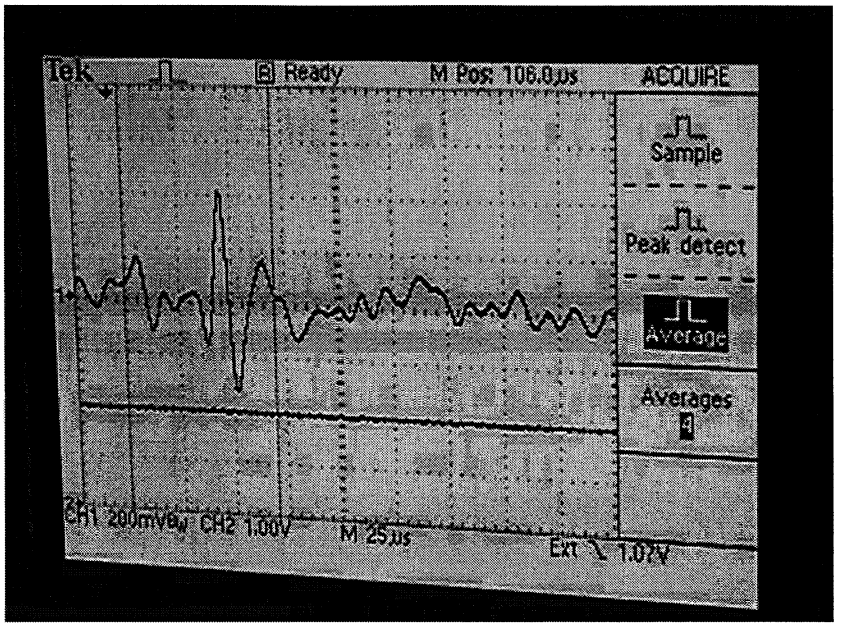

Figure 2.6.136 A_0 wave on copy paper moving at 2 m/s, detected with the self-mixing interferometer.

Trials at 45° incidence did not show an S_0 wave either on copy paper or on 42-lb linerboard. This is not so surprising, considering the high frequency content and much lower amplitude of the S_0 wave compared to the A_0 wave.

2.6.6.2 Non-moving paper results

Figure 2.6.137 presents results among the best available on static copy paper with the self-mixing interferometer.

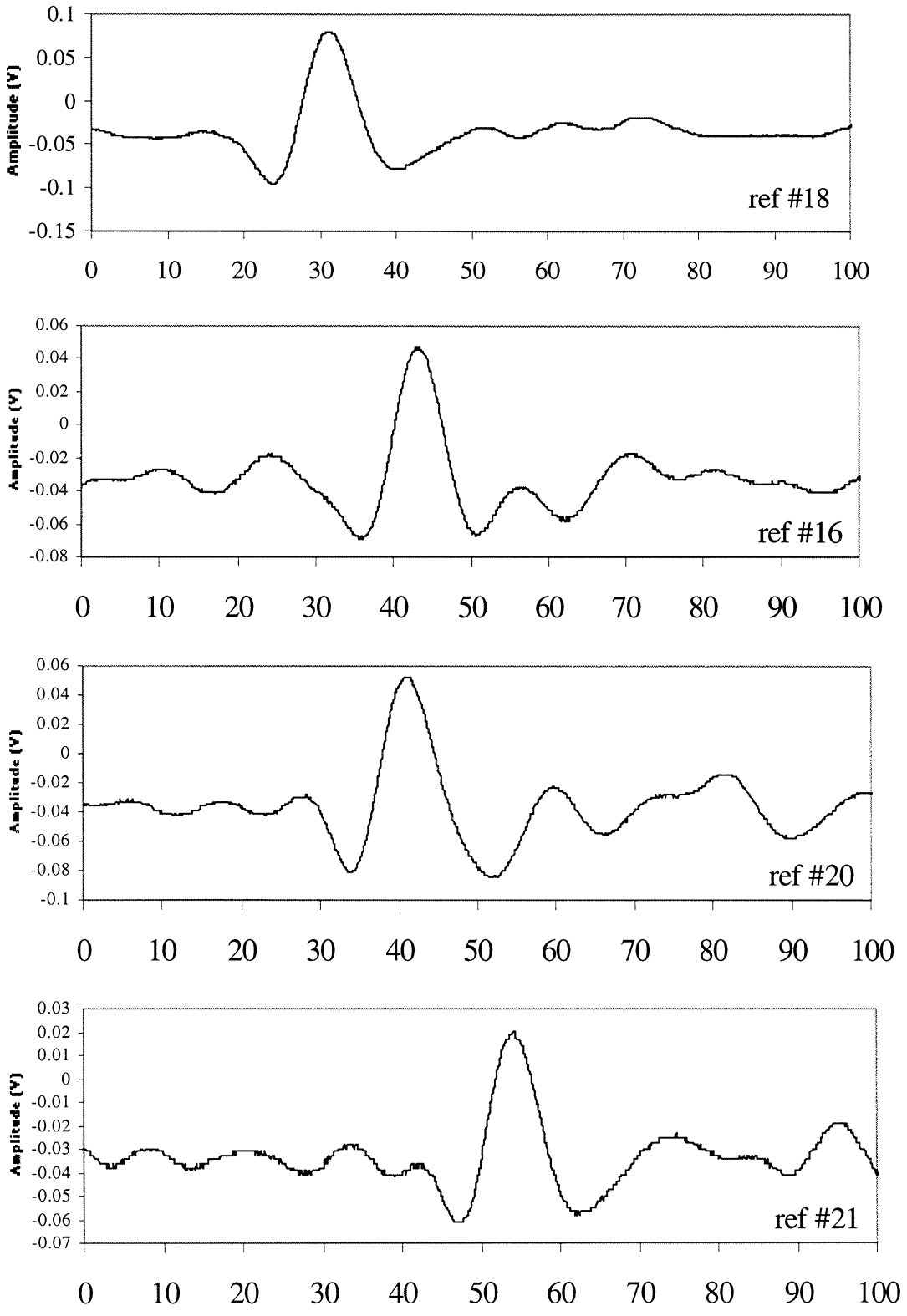

Figure 2.6.137 Data taken on static copy paper with the self mixing vibrometer.

Figure 2.6.137 ref #18 was for a generation-detection distance of 11 mm, ref #16 for 14 mm, ref # 20 at 16 mm, and ref # 21 at 20 mm. All data were taken in single shot, 25.1 mJ per pulse, with the detection performed at 45° of incidence. The Y axis shows voltage and the X axis shows time in μs.

As can be seen by comparing #16 and #20 there was a problem of triggering when we recorded these waveforms, coming from the fact that a different A/D board was used.

Nonetheless, the arrival of the A_0 wave can be clearly seen. The dispersive nature of the A_0 wave has been completely washed out by the narrow bandwidth of the interferometer. The highest frequency present in these signals is around 100 kHz, so a huge amount of information in the wave is lost compared to measurements made with a Fabry-Pérot, photorefractive or Photo-EMF interferometer.

2.6.6.3 Dynamic copy paper results

Figure 2.6.138 shows waveforms at 2 m/s on copy paper. A generation-detection distance of 10 mm with single shot was used for ref #35, and 20 mm, averaged 16 times, for # 40. Note the scale change on the y-axis – ultrasonic waves are disappearing into the noise of the interferometer already.

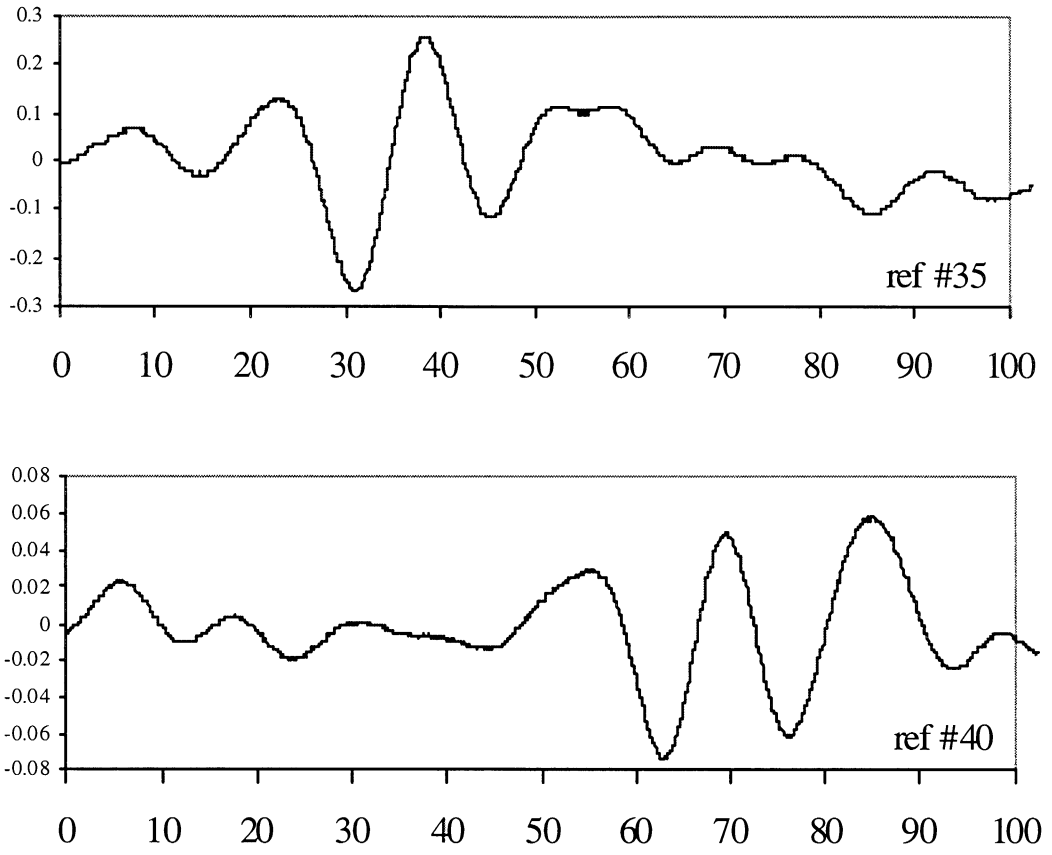

Figure 2.6.138 Ref #35 and 40 shows waveforms at 2 m/s on copy paper. Generation-detection distance of 10 mm single shot for ref #35, and 20 mm, averaged 16 times, for # 40. Note the scale change on the y-axis – ultrasonic waves are disappearing into the noise of the interferometer already.

On the curves in Figure 2.6.139 are ref #43: 16 averages, travel distance 10 mm and ref # 42: 16 averages, 15 mm. The trigger time was shifted, so the A_0 wave does not appear at the expected time in ref #43. The web speed was 12 m/s for both recordings. At this speed the measurements are already unreliable and the A_0 wave continuously appears and disappears more or less randomly in the noise. Averaging more than 16 times doesn't seem of any help since the base line of the signal fluctuates too much and the digitization of the voltage is done over only 256 levels (8 bits).

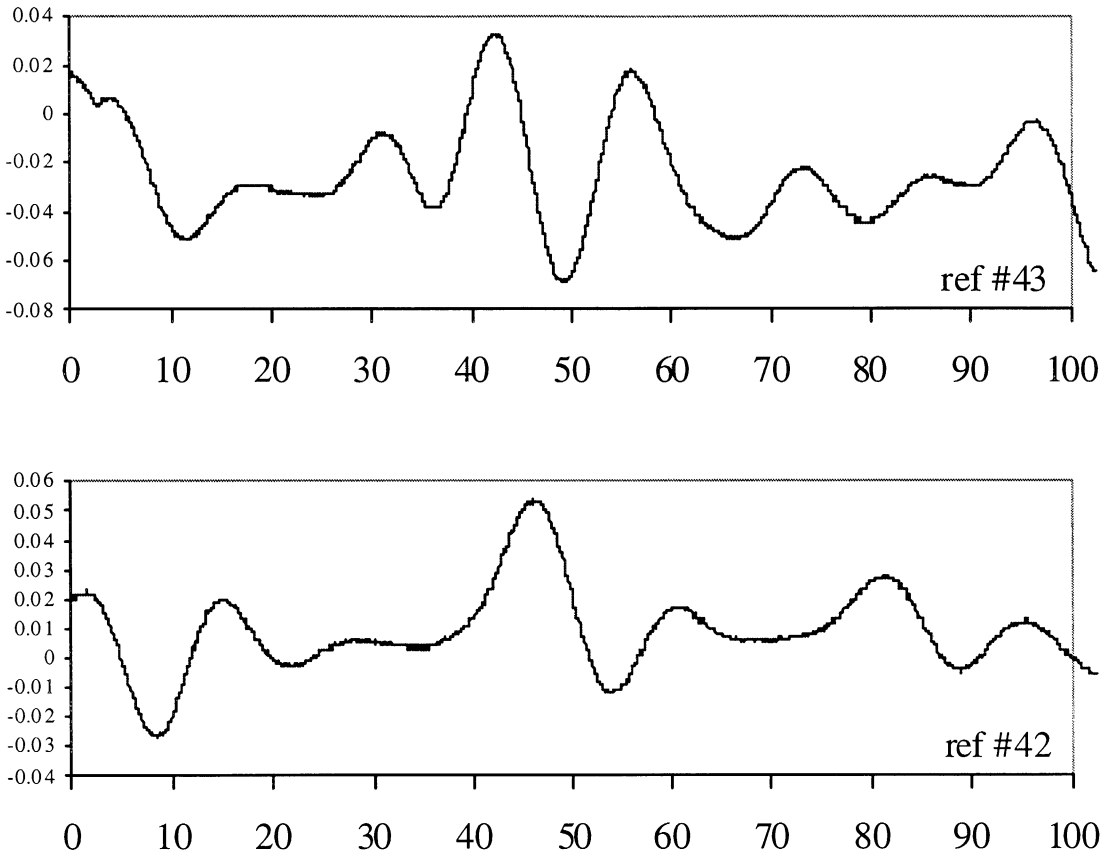

Figure 2.6.139 Self-mixing interferometer results on copy paper at 12 m/s. Ref#43: 16 averages, generation/detection distance of 10 mm. Ref # 42: 16 averages, 15 mm. The trigger was not working properly, so the A_0 wave does not appear at the expected time in ref #43.

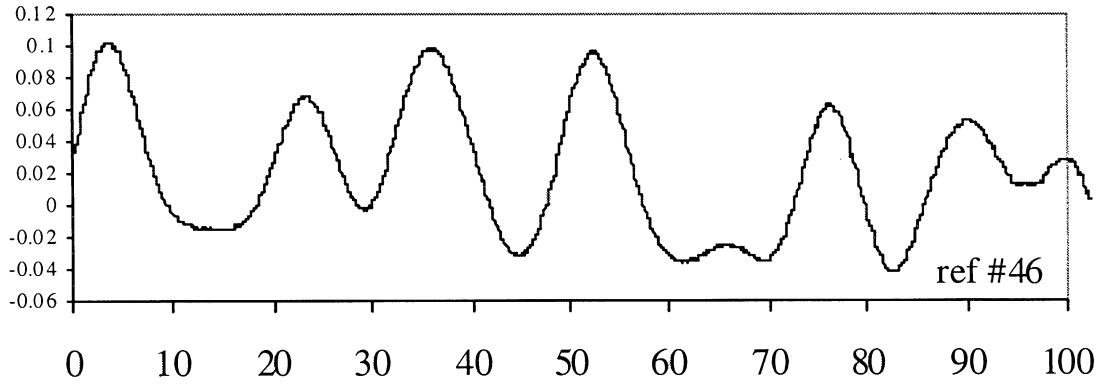

Figure 2.6.140 Copy paper: 16 averages, generation/detection distance of 10 mm, typical of the waveforms we obtained at 25 m/s. The ultrasonic signal has totally disappeared into the noise at this speed.

Figure 2.6.140 shows waveform #46 taken on copy paper with 16 averages and a generation/detection distance of 10 mm, typical of the waveforms we obtained at 25 m/s. The ultrasonic signal has completely disappeared into the noise at this speed.

2.6.6.4 Dynamic 42-lb linerboard results

The 42-lb linerboard reflects less light than the copy paper previously investigated so the signal to noise ratio is even lower, as expected.

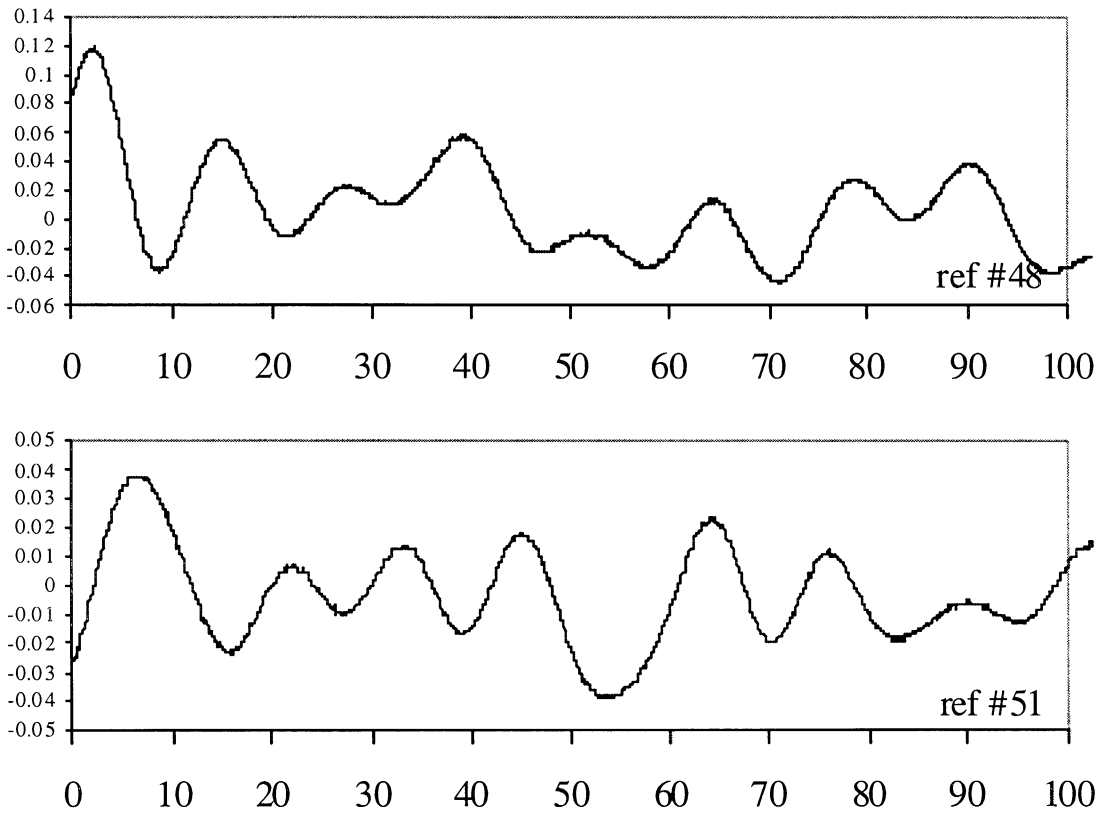

Figure 2.6.141 42-lb linerboard with the self-mixing interferometer at 2 m/s. Ref #48 shows the signal averaged 4 times with a generation/detection distance of 10 mm, and Ref # 51 is averaged 16 times for a Generation-Detection distance of 20 mm. The A_0 wave is completely lost on 42-lb Linerboard at this speed and at 14 m/s (not shown).

Figure 2.6.141, ref #48 shows the signal of the interferometer averaged 4 times with a generation/detection distance of 10 mm, and ref #51 is averaged 16 times with a generation/detection distance of 20 mm. Both waveforms were taken at 2 m/s. The A_0 wave is completely lost on 42-lb linerboard at this speed and also at 14 m/s.

2.6.6.5 Conclusion on Self-Mixing interferometric method

The self-mixing interferometer that was tested seems interesting for detecting low frequency (under 100-200 kHz) ultrasonic waves on paper having a high amplitude, probably around one hundred nanometers. Also the interferometer uses an "eye safe" laser. The price of the prototype is significantly lower than the price of other interferometers (estimation: $15,000), so it is a low cost system. It is also a very compact system because the detection laser is so small.

But it has some significant drawbacks for our application:

- Poor sensitivity to displacements:

  → very small signal to noise ratio for A_0 waves.

  → impossible to detect S_0 waves which have an amplitude of only a few nm.

- Required to work in strong ablation mode to generate a signal large enough to be detected:

  → destructive testing (damage to sample).

- Bandwidth too small for measurements on paper (DC to 100 kHz):

  → loss of all the information contained in high frequencies, including the S_0 mode.

  → loss of dispersive nature of the A_0 wave.

  → impossible to see the S_0 wave because it is a high frequency ultrasonic wave.

- Signal to noise ratio decreases significantly on moving paper compared to static paper:

  → impossible to detect A_0 wave a 25 m/s, very difficult above 2 m/s.

It is possible that another interferometer working on the principle of self-mixing could work better than the one used for these trials if it was using an improved optical system for the collection of light from the sample. The manufacturer of this interferometer believes it would be possible to increase the bandwidth up to 1 MHz by changing the electronics of the low pass filter.

A detection laser having a power comparable to the laser used for the photorefractive interferometer would probably help the signal to noise ratio, too. But in that case the advantage of using an "eye safe" laser is lost. Above 100 kHz, the sensitivity to displacements is really quite low.

To summarize, it seems that even though self-mixing interferometers are cheap and thus attractive compared to other interferometers, the bandwidth and poor sensitivity to displacements make them unsuitable for the specific needs of paper.

2.6.7 Moving Paper Texture Noise Reduction Method (J. Gerhardstein, IPST)

2.6.7.1 Introduction

Noise due to trying to make measurements on a rough, moving surface has been a serious design consideration since the inception of this project. One possible solution is to scan the detection laser, thereby reducing the apparent speed of the surface. This is analogous to moving the detection spot into the same frame of reference as the surface.

Several methods exist for scanning a laser beam. O'Shea (1985) lists 5 principal types, along with certain attributes, shown in Table 2.6.3.

Table 2.6.3 Classes of scanners and attributes, from O'Shea (1985).

Type	Scan Angle	Approx. Maximum Frequency	Scan Type
Galvanometer	30 deg.	10 kHz	Random
Rotating Prism (including holographic)	90 deg.	50 kHz	Periodic
Taut-band (resonant)	30 deg.	1 kHz	Harmonic
Piezoelectric	2 deg.	500 kHz	Harmonic
Acousto-Optic	<1 deg.	20 MHz	Random

The following criterion were used to narrow the list:

1) To accommodate variable web speeds, the scanner must be able to scan over a range of speeds. A random scan path most closely fits this need, but a periodic one may be able to work as well.

2) If the scanner must hold the sheet "stationary" for a typical measurement time of around 300 microseconds on a web moving 25 m/s, this gives a scan distance of 7.5 mm. If the scanner stands off the sheet a distance of 50 mm, it must be able to scan through an angle of 8.5 degrees (minimum).

3) If the scan time is 300 microseconds, the scanner must be able to scan the above distance at a frequency of 3333 Hz.

From these criterion, the taut-band (resonant) is eliminated due to slow speeds and harmonic scans, and piezoelectric and acousto-optic scanners are eliminated due to small scan angles. Holographic scanners are capable of scanning complex paths, but they require a large capital outlay to produce the first one (copies after the first are inexpensive, however). Rotating prisms and holographic scanners also suffer from synchronization problems in trying to time their scanning speed and scanning time with the arrival of the ultrasonic waves. This leaves galvanometer scanners as the first choice.

2.6.7.2 Scanning System

After contacting several galvanometer scanning companies, a prototype of a flexure-mounted galvanometer was chosen. This scanner is specified to scan a maximum angle of 30 degrees, at speeds of up to 20,000 degrees/second (though higher speeds were obtained during actual testing). Typical installation of the scanner is shown in Figures 2.6.142 and 2.6.143.

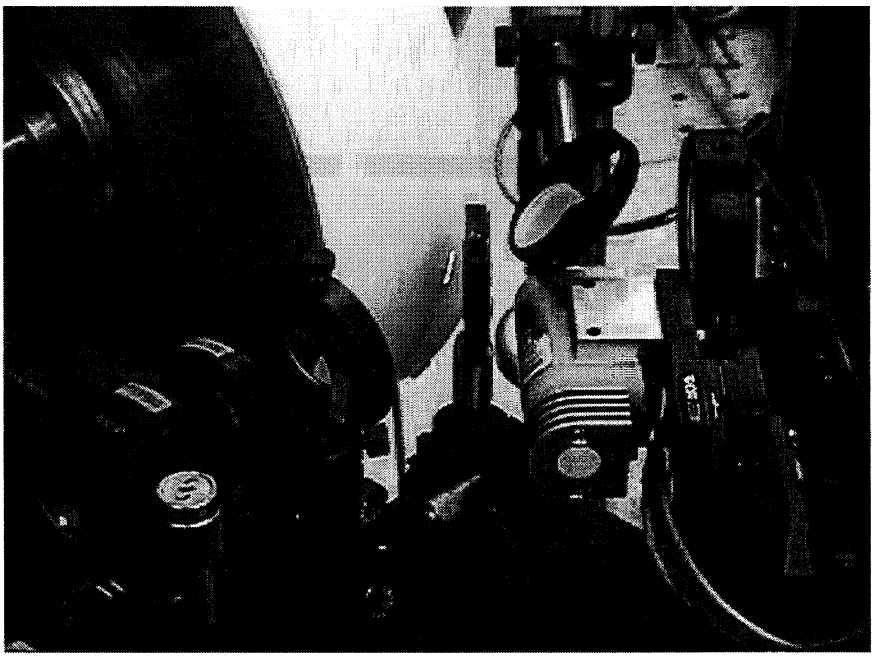

Figure 2.6.142 Galvanometer scanner on linerboard on the rotating drum. Scanner is at center right, with the mirror hidden.

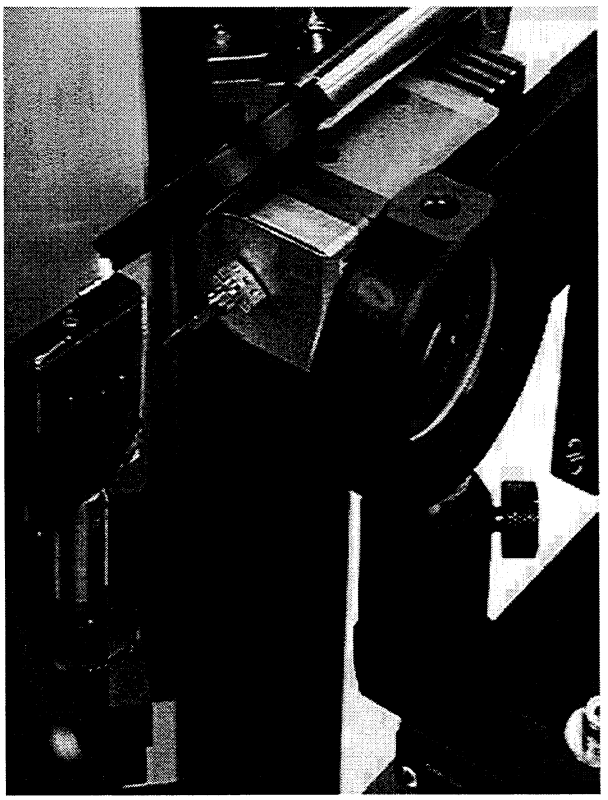

Figure 2.6.143 Galvanometer scanner (center) on rotating drum (left). Edge of mirror is visible at this angle.

The galvanometer is equipped with a 10 mm diameter mirror. A larger mirror would be preferable from a light collection standpoint, but would reduce the speed of the scanner due to inertia. Standoff distance between the scanner and the web is an important parameter as well. Placing the scanner a short distance from the web improves light collection, but requires the scanner to run at a faster speed and larger angle to match the web speed for the specified period of time.

The command signal to the scanner is a time-varying voltage. A built-in control loop attempts to keep the angular position of the scanner proportional to the instantaneous voltage of the command signal (the proportionality constant is approximately 4.9 degrees/volt). A typical command signal for scanning is shown in Figure 2.7.144. The scanner starts out at +10 degrees at 0 μs, rotates to -10 degrees in 1000 μs, and then returns to +10 degrees from 1000 μs to 3000 μs. The shape of the scan during the first 1000 μs is a straight line with the ends rounded slightly using a moving average. This provides a constant angular velocity scan (in this case, 20,000 degrees/second). The 2000 μs return path is sinusoidal in shape, which is an easier path for the scanner to follow. The scanner is synchronized to the detection system such that detection occurs during the first 1000 μs of the scan.

The scanner provides position, velocity and error output signals which can be used to determine how closely the scanner is following the command signal. Agreement is good up to 20,000 degrees/second. Velocities up to 28,000 degrees/second have been seen, but position typically lags behind the command signal by several 10's or 100's of μs. This is acceptably as long as this lag is accounted for in the scanner timing.

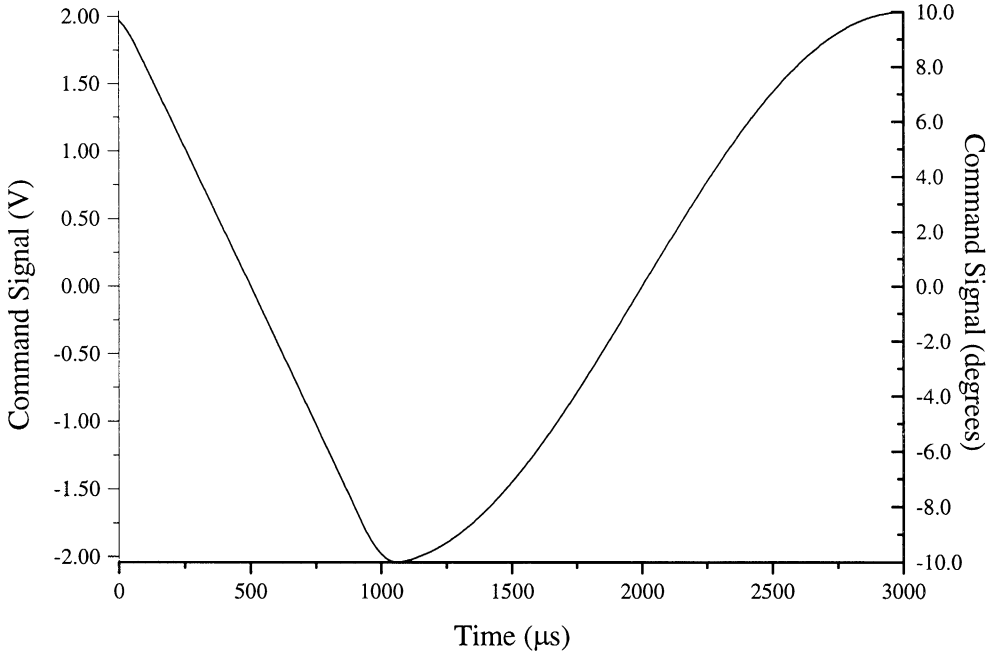

Figure 2.6.144 Typical command signal for scanner for 1000 μs scan at 20,000 degrees/second.

Preliminary measurements were made with the scanner on copy paper and linerboard up to speeds of 25 m/s using the photo-EMF system with a piezoelectric transducer in the path of the reference beam to simulate ultrasound waves. The photo-EMF combined with the piezoelectric transducer allows evaluation of signal strength using a continuous uniform "wave" with a moving rough surface. Signal strength with and without scanning provides an estimate of the increase in signal strength due to scanning. All data below was collected at 20 MSamples/sec. The scanner was placed 2.3 cm from the web.

2.6.7.3 System Evaluation

Figures 2.6.145 and 2.6.146 show results at 8 m/s on copy paper. Figure 2.6.145 shows typical single shot signal strength without scanning. The piezoelectric transducer is running at 1 MHz and 15 V_{pp} producing a continuous sine wave signal that is recorded by the detector (sample

time is too long to see individual sine wave cycles). Variations in the amplitude are due primarily to surface noise and web flutter as the copy paper sample rotates on the drum. Average signal strength is 0.892 V_{RMS}.

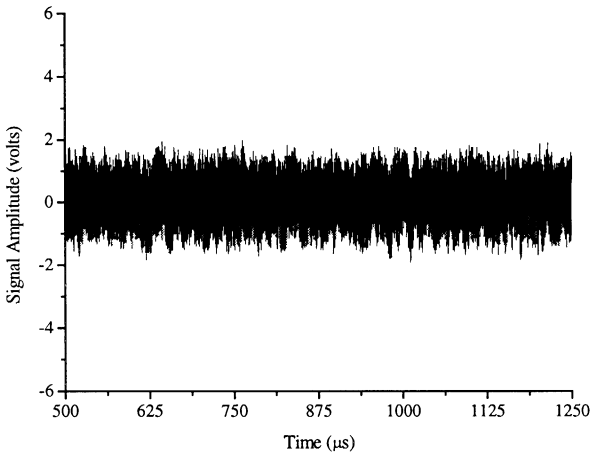

Figure 2.6.145 Single shot measurement with the Photo-EMF system at 8 m/s on copy paper without scanning.

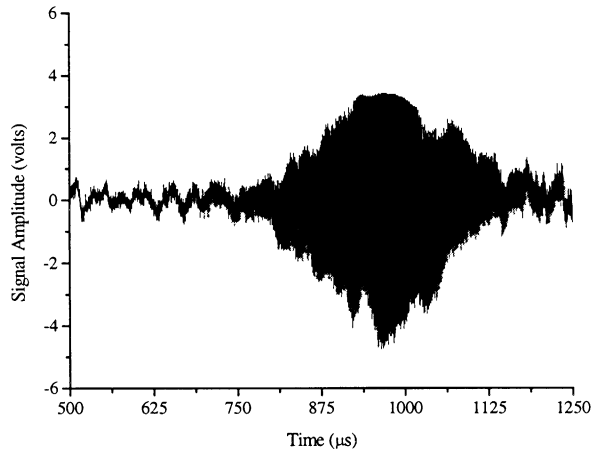

Figure 2.6.146 Single shot measurement with the Photo-EMF system at 8 m/s on copy paper, scanning at 18,000 degrees/second.

Figure 2.6.146 shows the same setup with the galvanometer scanner used to improve the signal to noise ratio. The scanner is set to scan at 18,000 degrees/second for 1000 μs (18 degrees of scanning), starting at time = 0 μs. Two regions are seen in Figure 2.6.146. Up to 800 μs, the signal is quite weak with an average strength of just 0.256 V_{RMS}. From 800 to 1100 μs, the signal is much stronger, with an average strength between 950 and 1000 μs of 2.92 V_{RMS}. Two effects are occurring here. First, the signal strength up to 800 μs is much lower than the unscanned signal see in Figure 2.6.145. This is due to the detector being out of focus. Between 800 to 1100 μs, the detector comes into focus, and the improvement in the signal due to the scanner can be seen. If we compare the signal strength in Figure 2.6.145 (0.892 V_{RMS}) to the signal strength from 800 to 1100 μs in Figure 2.6.146 (2.92 V_{RMS}), there is a signal increase of 3.3 times.

Figures 2.6.147 and 2.6.148 show the same setup, but with a web speed of 12 m/s. Scan speed in Figure 2.6.148 is approximately 27,000 degrees/second, well in excess of the rated speed of the scanner. Signal strength in Figure 2.6.147 is 0.628 V_{RMS}. Signal strength in Figure 2.6.148 is 2.21 V_{RMS} between 925 and 975 μs, and 0.204 V_{RMS} between 500 and 700 μs. Again, the lower signal for the first part of Figure 2.6.148 is due to the detector being out of focus. Nonetheless, this is a signal to noise ratio improvement of 3.5 times between the unscanned signal in Figure 2.6.147 and the latter part of Figure 2.6.148.

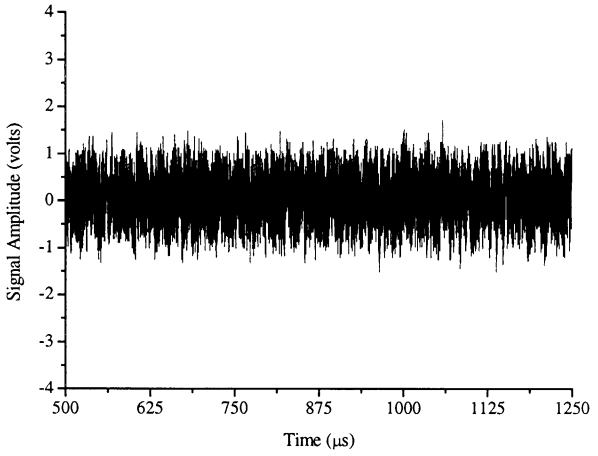

Figure 2.6.147 Single shot measurement with the Photo-EMF detector on copy paper, without scanning, at 12 m/s.

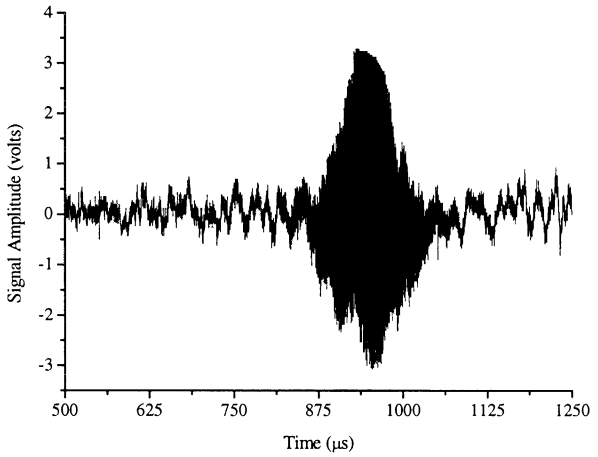

Figure 2.6.148 Single shot measurement with the Photo-EMF detector at 12 m/s on copy paper, scanning at 27,000 degrees/second.

Figures 2.6.149 and 2.6.150 again show the same setup, but at a web speed of 25 m/s and four-times signal averaging. Scanner speed is set at 30,000 degrees/second, which is the maximum set point for a 1000 μs scan (30 degrees in 1000 μs). This speed, however, is significantly less than what is required for a 25 m/s web speed at a 2.3 cm standoff distance. The

scanner does not actually reach the commanded 30,000 degrees/second, but somewhere closer to 28,000. Hence, for these runs, the scanner will not reach the web speed of 25 m/s.

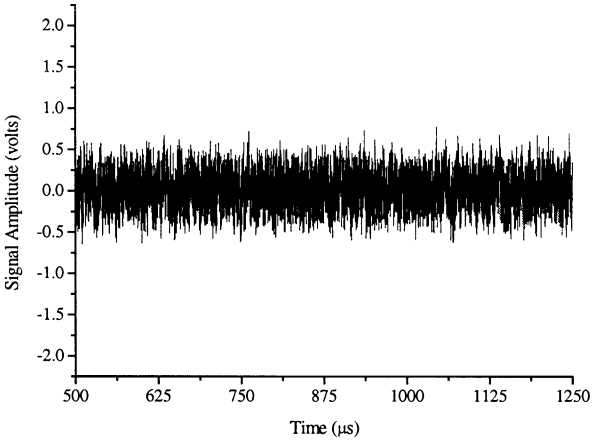

Figure 2.6.149 Four-times averaged measurement with the Photo-EMF detector on copy paper, without scanning, at 25 m/s.

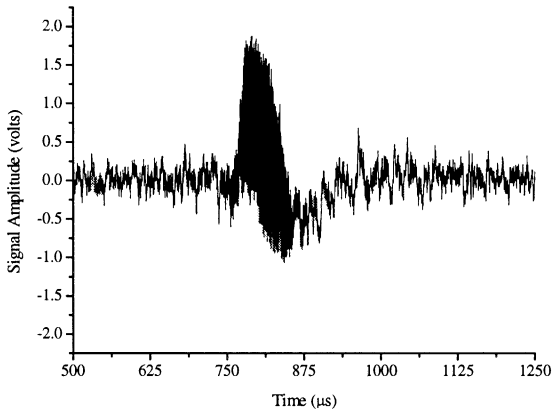

Figure 2.6.150 Four-times averaged measurement with the Photo-EMF detector on copy paper at 25 m/s, commanded scan speed of 30,000 degrees/second (maximum scan speed reached is closer to 28,000 degrees/second).

Limitations of the scanner are evident by the shorter time over which the signal strength increases. Strong signal is only seen for about 50 μs in Figure 2.6.150, where as it was seen for 200-300 μs at lower scan speeds (see Figures 2.6.146 and 2.6.148). Higher speeds require longer

acceleration times, but since the range of motion of the scanner is limited, the amount of time that the scanner is "at speed" is reduced.

Signal strength in Figure 2.6.149 without scanning is 0.240 V_{RMS}. Signal strength in Figure 2.6.150 with a commanded scan speed of 30,000 degrees/second is 0.121 V_{RMS} between 500 and 700 μs, and 0.888 V_{RMS} between 785 and 835 μs. This is a signal to noise improvement of 3.7 between the unscanned signal in Figure 2.6.149 and the scanned signal with the detector in focus in Figure 2.6.150, even though the scanner was not able to match the web speed. The time period over which the signal amplitude is increased (780-850 μs) is likely too short to accurately record ultrasound waves.

Preliminary measurements were also made on 42-lb linerboard using the same setup as above. Signal to noise ratio increases of approximately 4 were observed to speeds of 14.5 m/s.

Measurements were attempted using the pulse laser for excitation. Precise timing of the scanner to the arrival of the ultrasound waves was found to be more difficult than originally thought as the scanner tends to lag behind the command signal, especially at higher scan speeds. Unfortunately, time limited the experiments with the scanner and adequate testing with the pulse laser was not complete at the time this report was written. However, we expect to see similar results with the pulse laser excitation.

Scanner technology appears to be promising. Signal strength on a moving web of copy paper was measured between 3.3-3.7 times stronger with the scanner than without. Significant signal strength improvements were achieved even when the maximum speed the scanner reached was less than the speed of the sample. The galvanometer scanner is limited to scan speeds of around 28,000 degrees/second, but in order to achieve sufficient "time at speed", slower scan speeds are

required. For the setup used in these experiments, the galvanometer was placed approximately 2.3 cm from the surface of the web. At this distance, the 10 mm diameter mirror was not the limiting aperture of the system (the mirror just above it in Figures 2.6.142 and 2.6.143 was the limiting aperture). If the galvanometer is moved further back from the web, the maximum web speed at which the scanner can keep up with will be increased. However, moving the scanner back will also decrease the amount of light collected from the web since the scanner mirror will become the limiting aperture, reducing signal strength.

2.6.8 Multi-wavelength generation

2.6.8.1 Experimental setup

For the generation and comparison of ultrasonic waves at different wavelengths, the generation laser of IPST with its doubling and tripling non-linear crystals was used as well as a contact "bender" transducer especially designed for detection of in-plane waves (primarily S_0 waves). Despite the fact that a contact transducer does not have the advantage of being broadband like an optical interferometer, it allowed us to make a first evaluation of generation at different wavelengths. This transducer was also able to detect the in-plane component of A_0 waves on paper, which is still larger than the in-plane component of the S_0 wave. The schematic of the experimental setup is presented in Figure 2.6.151.

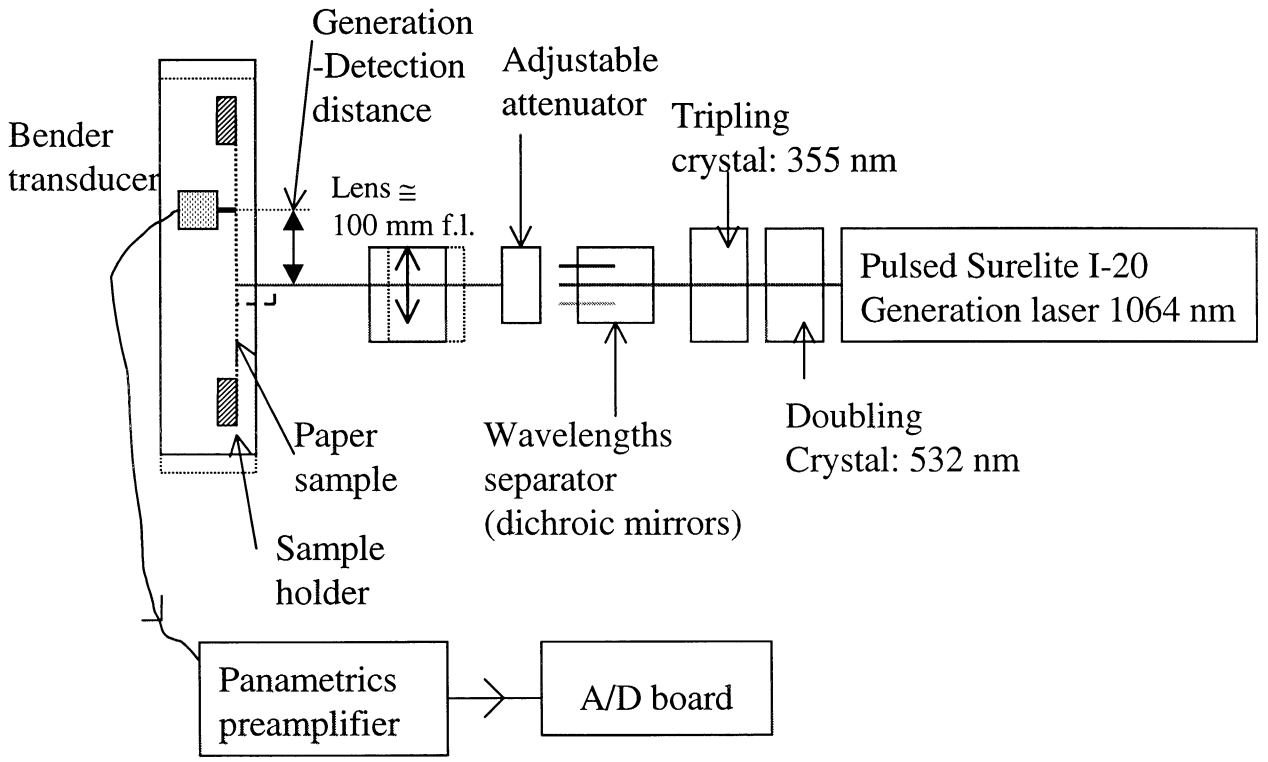

Figure 2.6.151 Schematic of the experimental setup for laser generation, and detection with the bender transducer.

When the signal voltage was sufficient, the Panametrics preamplifier was not used and the signal was digitized directly by the A/D board. The amplification factor of the preamplifier is 93.5x (≅ +39.4 dB) near 60 kHz (one of the resonance frequencies of this transducer).

We present two graphs in Figure 2.6.152 in the frequency domain displaying the frequency response to the laser pulse of the transducer and preamplifier combination. Before taking its Fourier transform, the signal was averaged 4 times in order to reduce the noise.

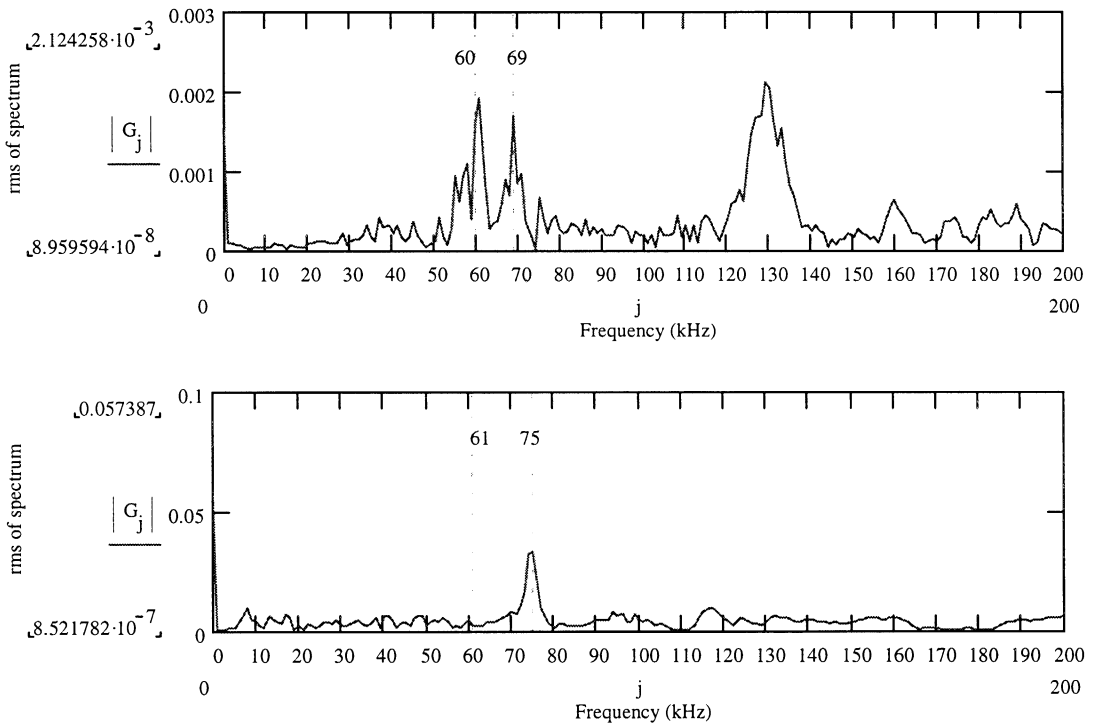

Figure 2.6.152 Frequency response of the preamplifier and bender piezoelectric transducer.

As can be seen from the two graphs in Figure 2.6.152, the transducer has two resonance frequencies, one at 60 kHz and one around 70-75 kHz. The peak at 130 kHz is not really significant. The transducer and the paper sample were fixed on the same translation stage

moving perpendicularly to the laser beams so that the contact between the transducer and the paper did not change when we changed the distance between generation and detection.

The wavelength of the laser generation was switched by putting the doubling and tripling optical crystals inside the laser head, using the standard procedure described by the laser manufacturer. The output energy was optimized for each wavelength in order to ensure that the laser pulse duration was in its normal range (5-7 ns for 1064 nm, 4-6 ns for 532 nm and 355 nm). The fact that the pulse duration is 1 ns shorter for these last two wavelengths than at 1064 nm will not significantly change the frequency content of the generated pulses. Indeed a paper web filters the high frequencies (above 10 MHz) corresponding to this pulse duration anyway, so high frequencies are never observed in paper.

Due to the optical attenuator, we were able to keep the energy per pulse (value from 40 averages) almost constant for each wavelength: 4.89 mJ at 1064 nm, 4.93-4.72 mJ at 532 nm, and 4.89-4.50 mJ at 355 nm. Hence, the only parameter changed for the generation was the wavelength of the generation laser and the spot diameter.

The lens used at each wavelength was a spherical lens, 100 mm focal length, thus producing a circular spot. The beam was focused to the minimum diameter onto the paper samples in most cases. The paper grades investigated were copy paper and 42-lb linerboard, the most relevant for the project and very different both from a mechanical and optical point of view.

2.6.8.2 Results of laser generation at different wavelengths

2.6.8.2.1 Influence of the Generation/Detection distance for 42-lb linerboard at 1064 nm

The results shown in Figure 2.6.153 were obtained with the fundamental wavelength of 1064 nm.

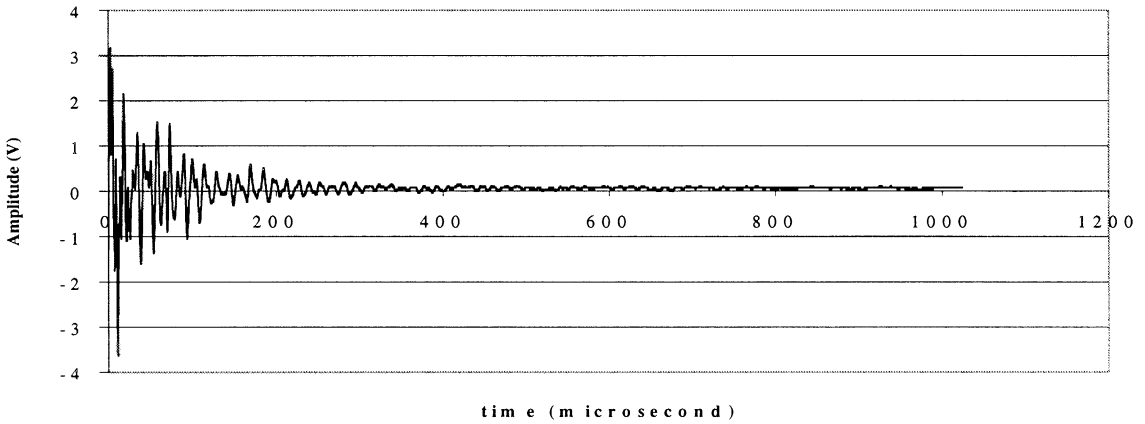

(a) Generation/detection distance of 0 mm.

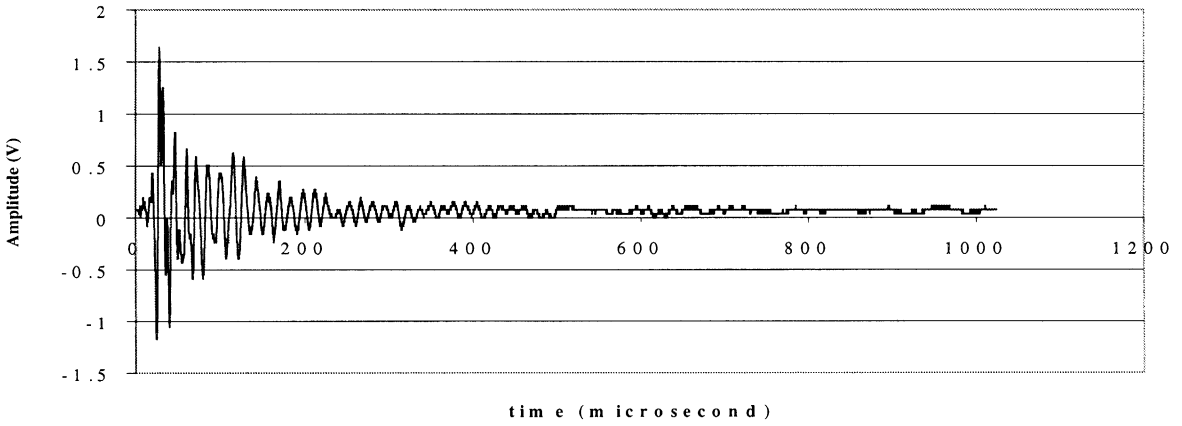

(b) Generation/detection distance of 10 mm.

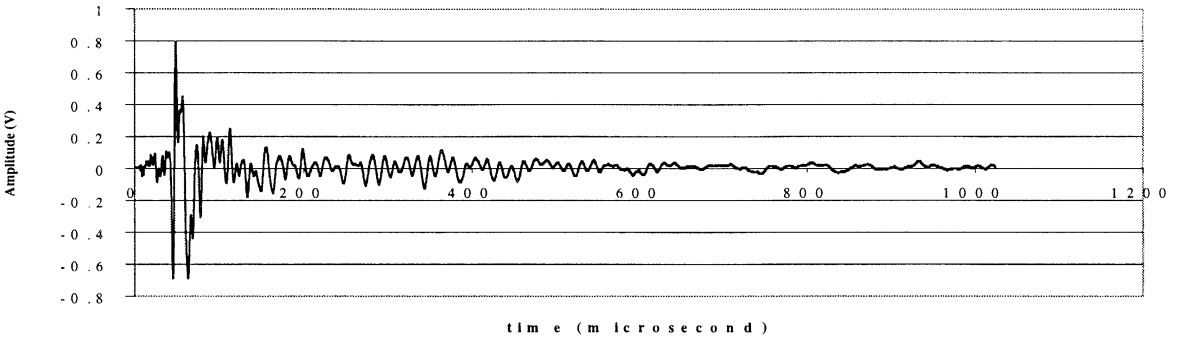

(c) Generation/detection distance of 20 mm.

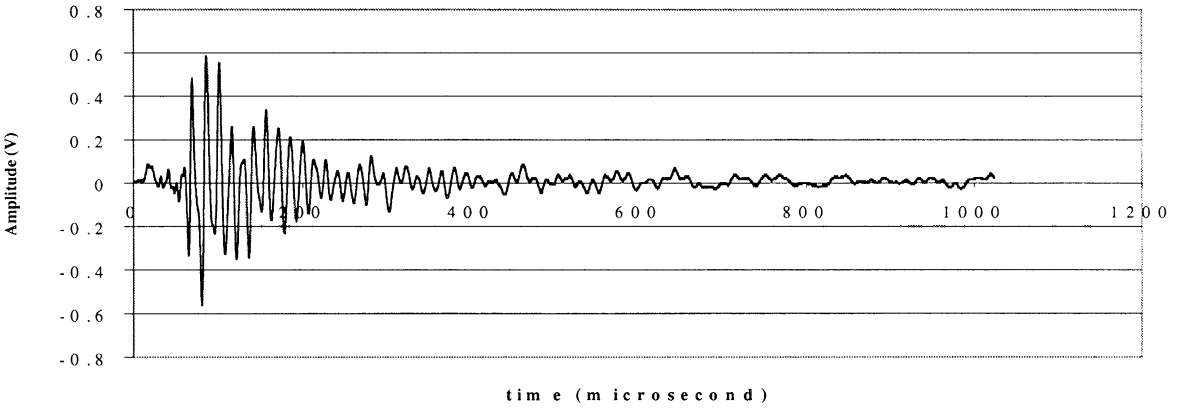

(d) Generation/detection distance of 30 mm.

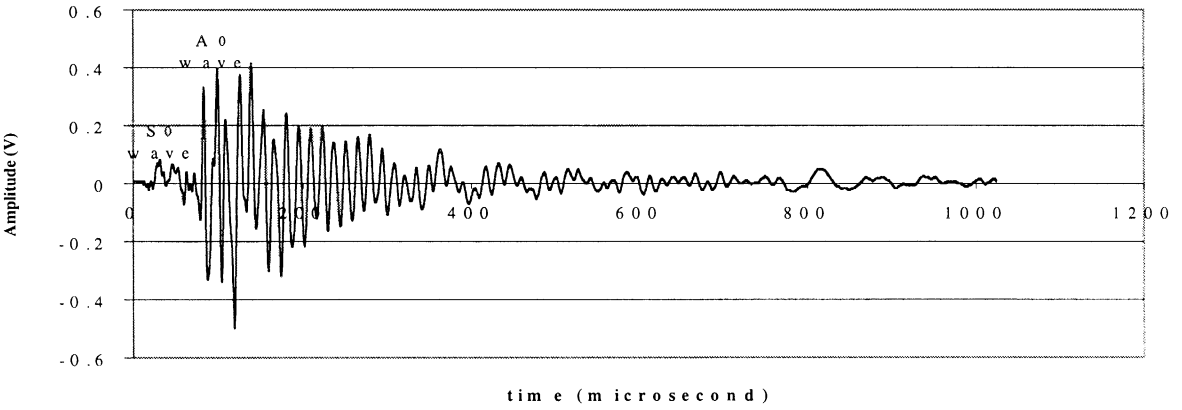

(e) Generation/detection distance of 38 mm.

Figure 2.6.153 (a-e) Ultrasonic waves as function of the Generation-Detection distance along MD for 42-lb Linerboard at 1064 nm.

At 0 mm the laser generation pulse hits almost directly over the transducer so the signal is not really representative of the generation in the paper. The first waveform to appear is the S_0

wave, and its amplitude is 10 times smaller than the large oscillations after it which are the A_0 wave

The machine direction of the samples was horizontal, so the ultrasonic waves were traveling along MD for all the measurements. A contact piezoelectric transducer is much more sensitive to displacements than an optical interferometer in most cases. The fact that the S_0 wave is so small in 42-lb linerboard even with a transducer specially designed for detecting it explains why we had so much difficulties to see it on moving and static linerboard with the interferometers we used.

2.6.8.2.2 Influence of the Generation-Detection distance for Copy Paper at 1064 nm

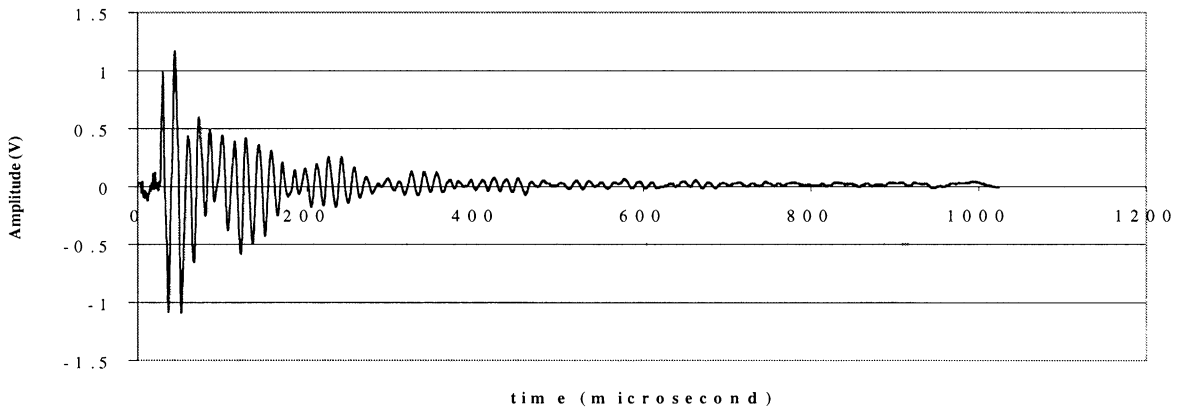

(a) Generation/detection distance of 10 mm

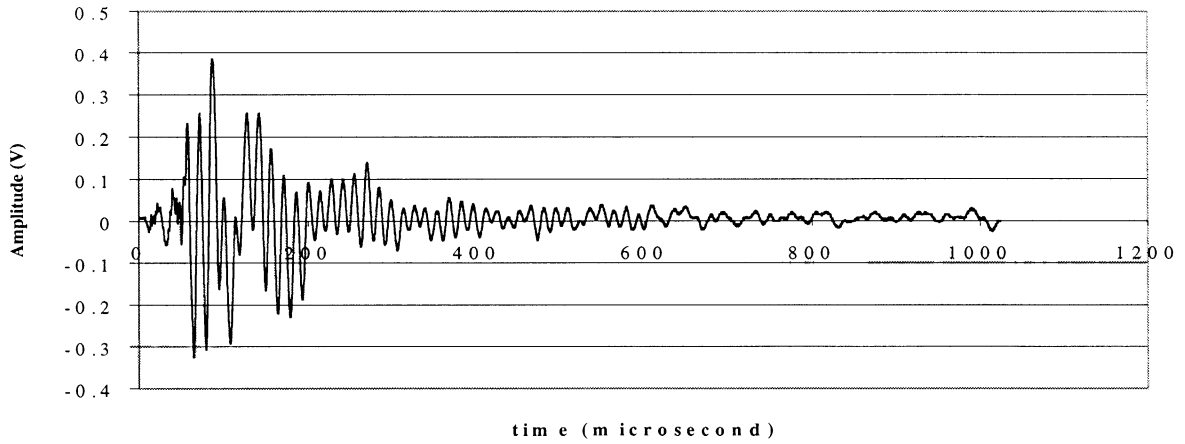

(b) Generation/detection distance of 20 mm

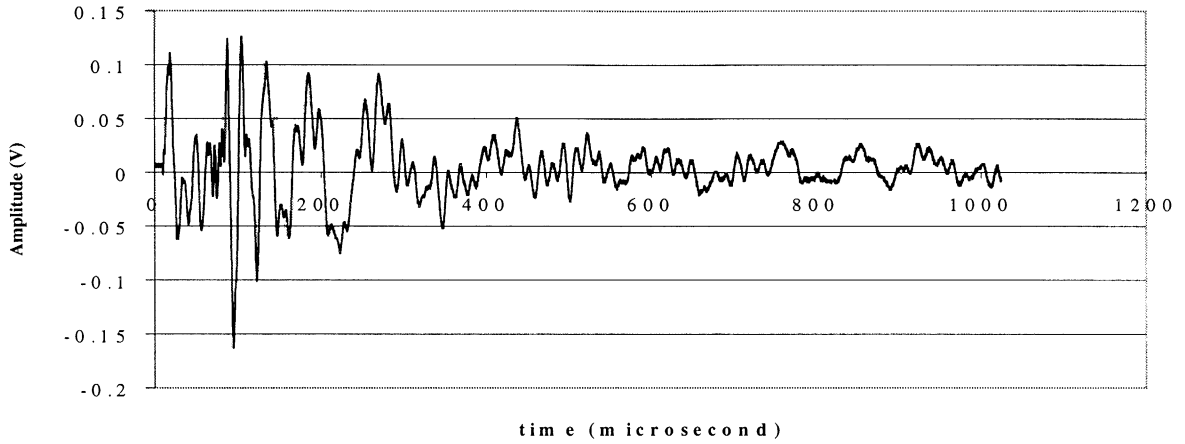

(c) Generation/detection distance of 30 mm

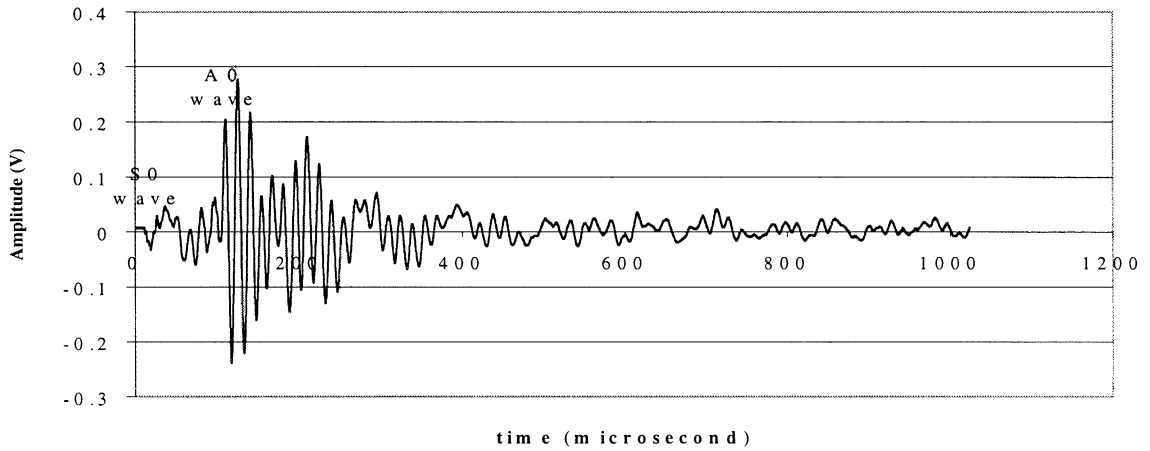

(d) Generation/detection distance of 38 mm

Figure 2.6.154 (a-d) Ultrasonic waves as function of the generation/detection distance along MD for copy paper at 1064 nm.

Figure 2.6.154a-d show results on copy paper as a function of generation/detection distances for 1064 nm generation. Figure 2.6.154a is a bit different from other waveforms since the amplitude ratio of S_0 waves over A_0 waves is not the same as the other waves. But overall, even if this ratio is not as small as in the case of 42-lb linerboard, we can see that the laser pulse generates much more antisymmetric A_0 waves than symmetric S_0 waves at least for frequencies under 100 kHz. The fact that S_0 waves have a larger amplitude for copy paper than for 42-lb linerboard probably comes from copy paper being thinner than linerboard. This is a hypothesis

that we will be able to prove or disprove in the future by comparing more paper grades of different thickness between themselves, using laser generation and piezoelectric detection.

2.6.8.2.3 Influence of the Generation-Detection distance for Copy Paper at 532 nm

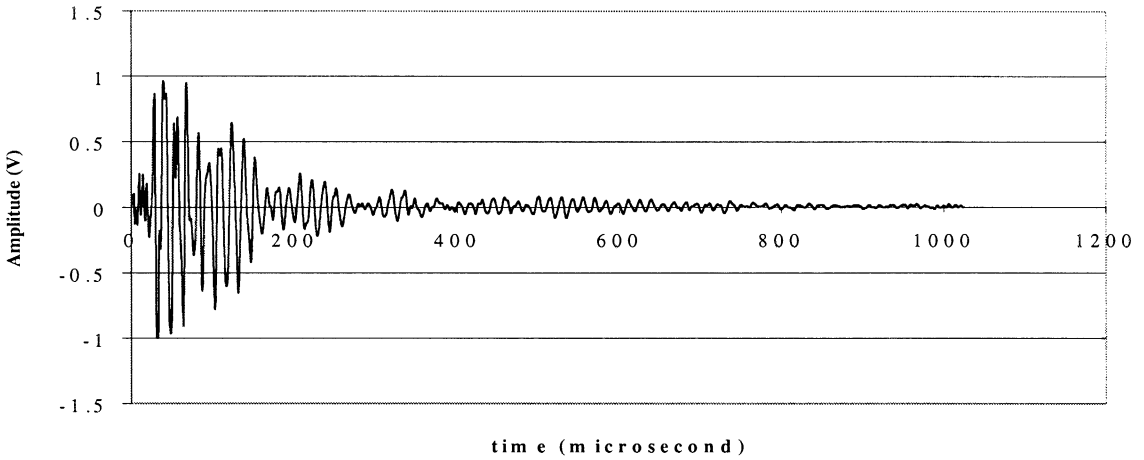

(a) Generation/detection distance of 10 mm

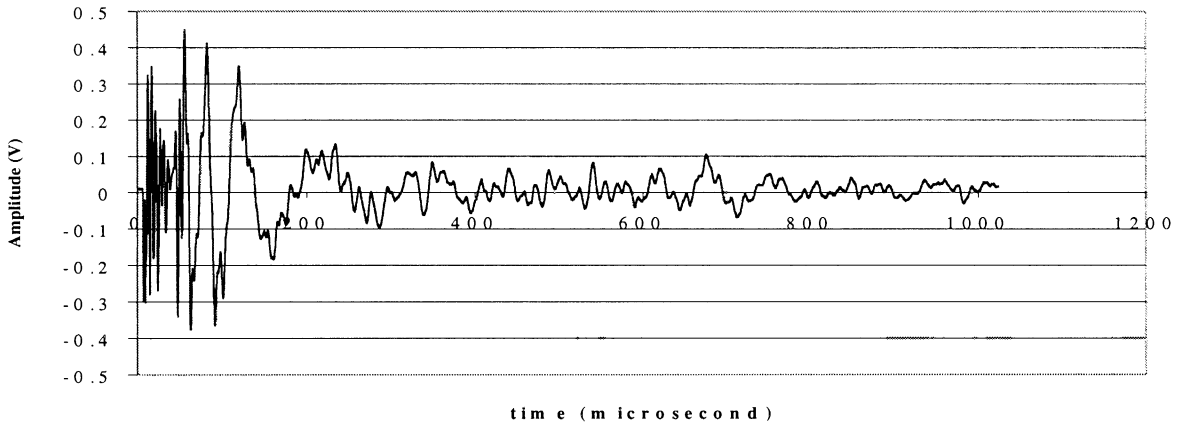

(b) Generation/detection distance of 20 mm

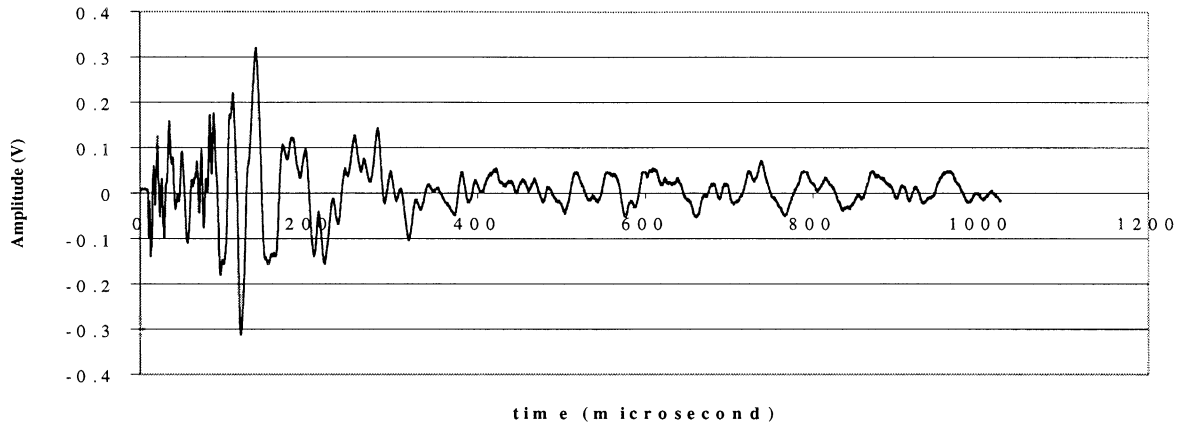

(c) Generation/detection distance of 31 mm

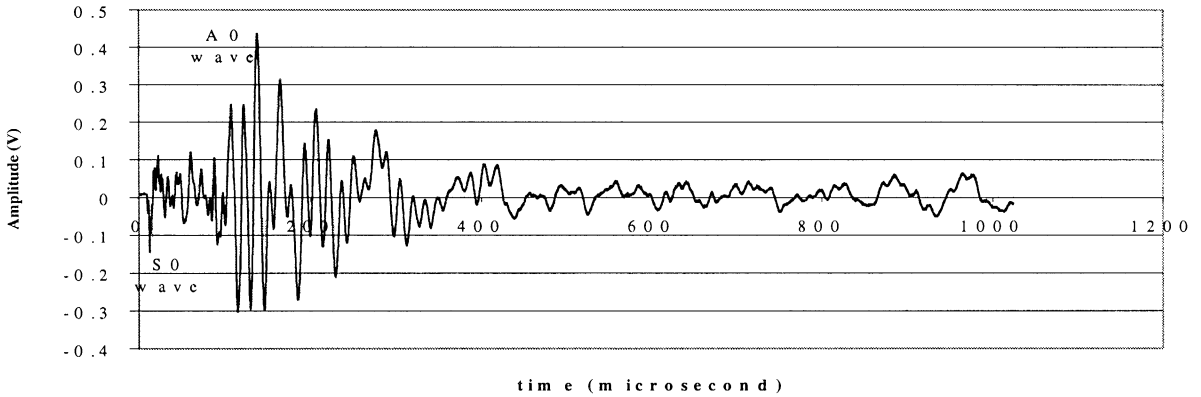

(d) Generation/detection distance of 38 mm

Figure 2.6.155 (a-d) Ultrasonic waves as function of the Generation/Detection distance along MD for copy paper at 532 nm.

Figure 2.6.155a-d show signals on copy paper as a function of generation/detection distances at 532 nm. As expected, both A_0 and S_0 are decrease quickly with distance when the generation is made with a 532 nm spot. Compared to what is observed at 1064 nm, the S_0 wave is much larger at 532 nm. Also the amplitude of the S_0 remains significant even at 38 mm.

What is observed visually during the experiments is that 532 nm light creates much more damage both on copy paper and 42-lb linerboard than 1064 nm wavelength for the same pulse energy. It almost drills holes in copy paper, which makes it no better than destructive testing.

It is possible that the mechanism of generation is different at 532 nm from 1064 nm, working in ablation regime at 532 nm and in intermediate regime at 1064 nm. However, we would expect an ablation regime to generate more A_0 waves in paper than S_0 symmetric waves, since only one side of the sheet receives the pressure from the vaporized material. So this explanation would mean that there would be stronger S_0 waves at 1064 nm. In fact we observe the opposite result.

Another possibility is that the optical pulse penetrates more deeply inside the paper at 532 nm than at 1064 nm. If it is the case, the acoustical source resulting from the ablation/thermal dilatation process would be a buried source, and such a source is more likely to generate S_0 wave than A_0 waves.

2.6.8.2.4 Influence of the Generation-Detection distance for 42-lb linerboard at 532 nm

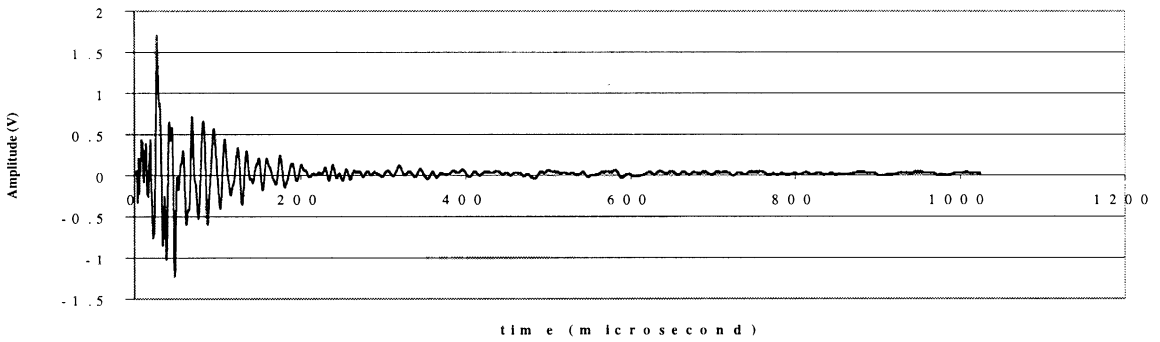

(a) Generation/detection distance of 10 mm

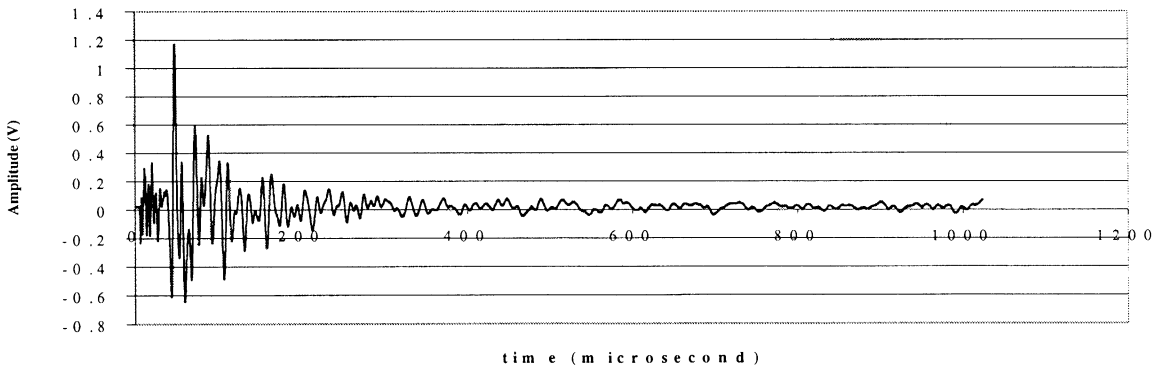

(b) Generation/detection distance of 20 mm

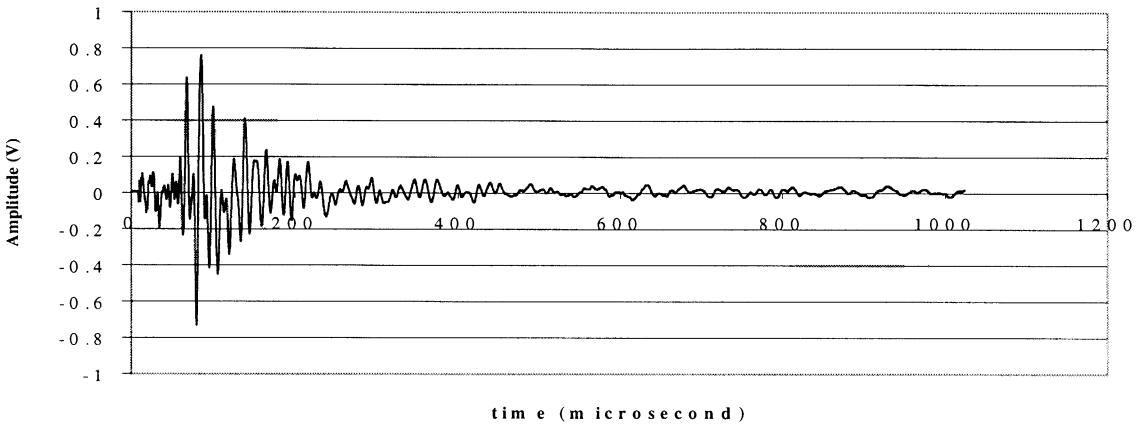

(c) Generation/detection distance of 30 mm

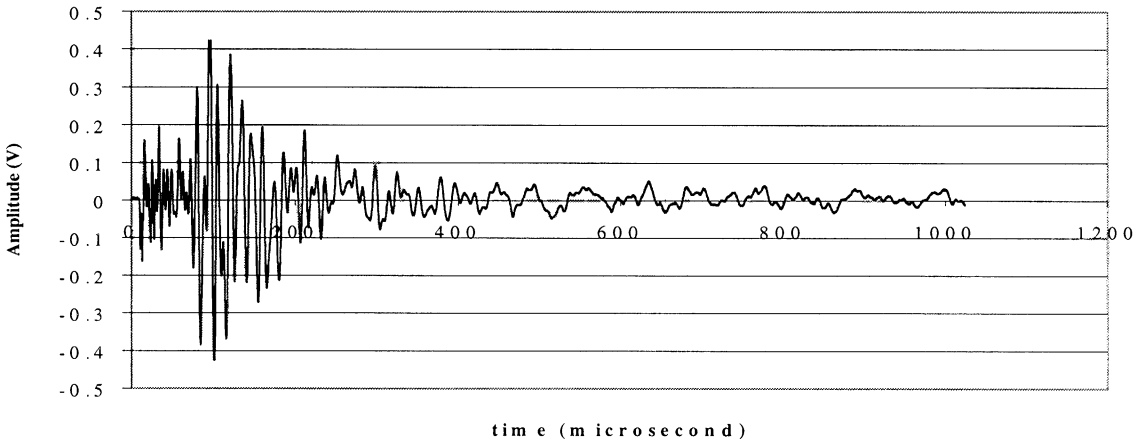

(d) Generation/detection distance of 37 mm

Figure 2.6.156 (a-d) Ultrasonic waves as function of the Generation/Detection distance along MD for 42-lb Linerboard at 532 nm.

Figure 2.6.156a-d shows signals for 42-lb linerboard as a function of generation/detection distance at 532 nm. The S_0 waves seems to be stronger than at 1064 nm. The reasons why this phenomenon occurs are probably the same as for copy paper (ablation instead of intermediate regime or wavelength penetrating deeper inside the sheet).

The amplitude of the A_0 wave remains the same at 532 nm compared to 1064 nm for 42-lb linerboard.

2.6.8.2.5 Influence of the Generation-Detection distance for 42-lb linerboard at 355 nm

For the tests at 355 nm, the distance between the lens and the paper surface was reduced by 9 mm (new distance approximately 91 mm). The generation source is now 0.3-0.5 mm, larger than previously.

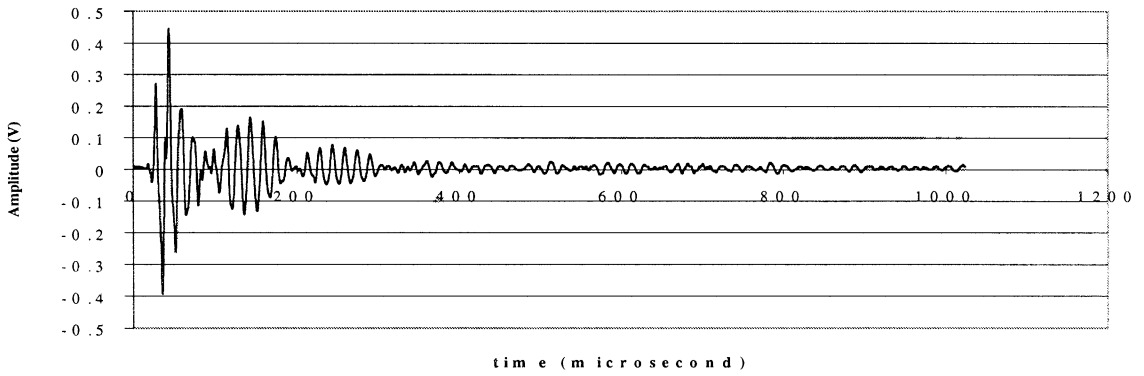

(a) Generation/detection distance of 9 mm

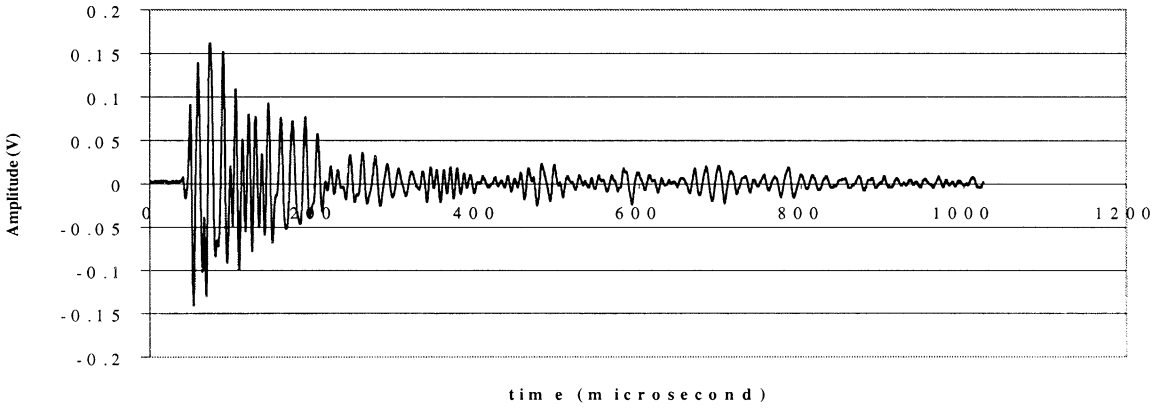

(b) Generation/detection distance of 20 mm

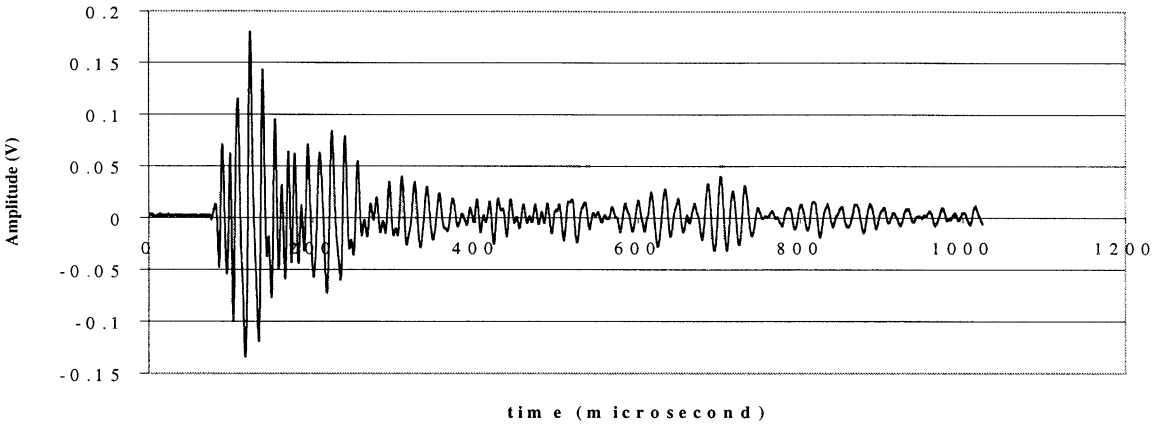

(c) Generation/detection distance of 30 mm

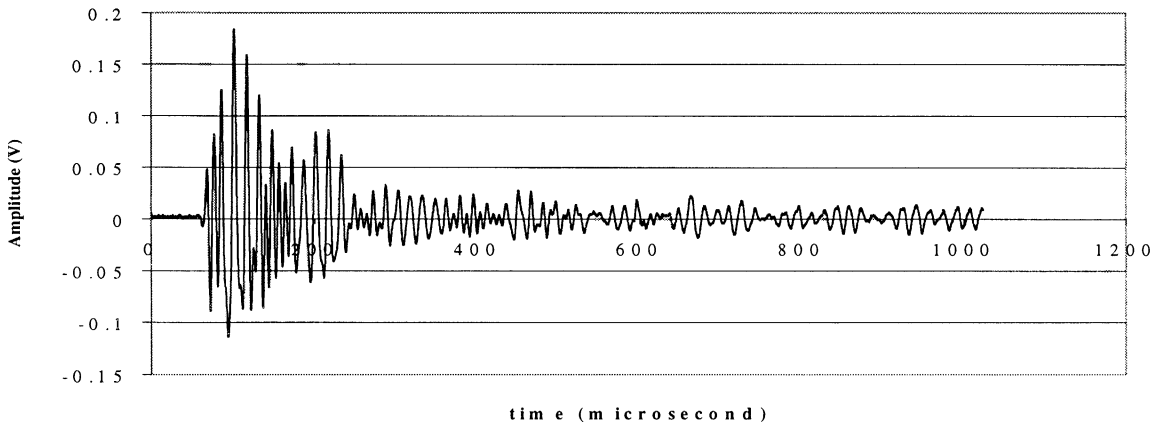

(d) Generation/detection distance of 38 mm

Figure 2.6.157 (a-d) Ultrasonic waves as function of the Generation-Detection distance along MD for 42-lb Linerboard at 355 nm.

As can be seen on the curves in Figure 2.6.157, the S_0 wave has totally disappeared from the waveforms but the A_0 is still there. This effect could be linked to the increased size of the generation spot, or to a smaller absorption of 355 nm wavelength compared to 532 nm by the 42-lb linerboard sample. The amplitude of the A_0 wave has been divided by a factor between 2 and 4. The decrease in the amplitude of the antisymmetric wave is not sufficient to explain the total disappearance of S_0 wave.

2.6.8.2.6 Influence of the Generation-Detection distance on copy paper at 355 nm

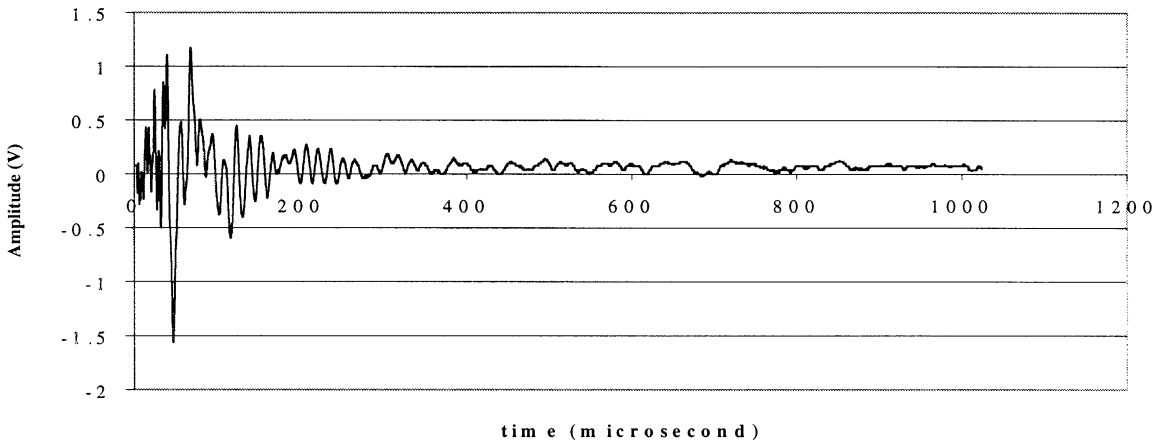

(a) Generation/detection distance of 9 mm

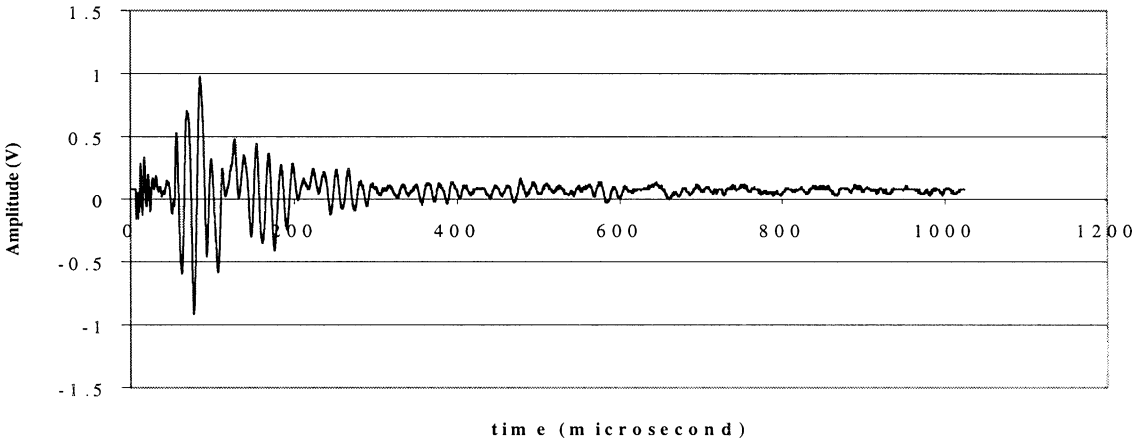

(b) Generation/detection distance of 20 mm

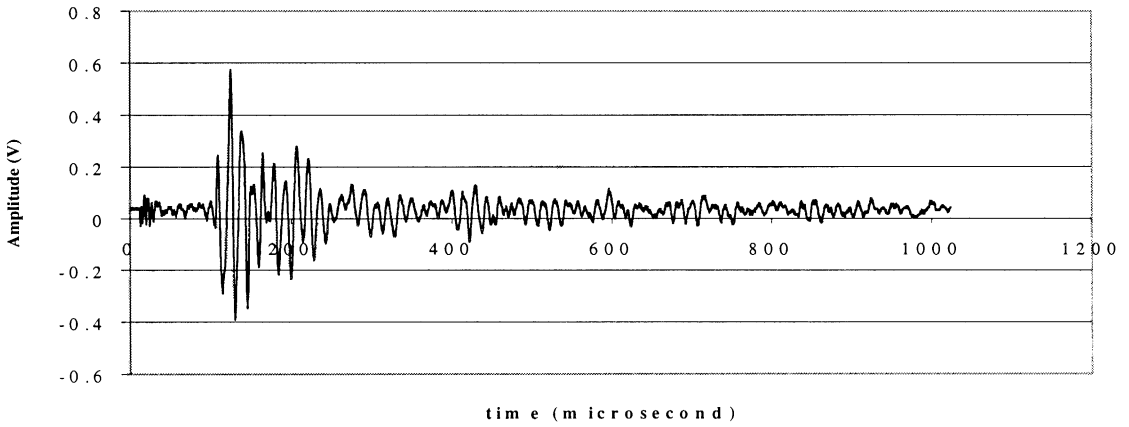

(c) Generation/detection distance of 30 mm

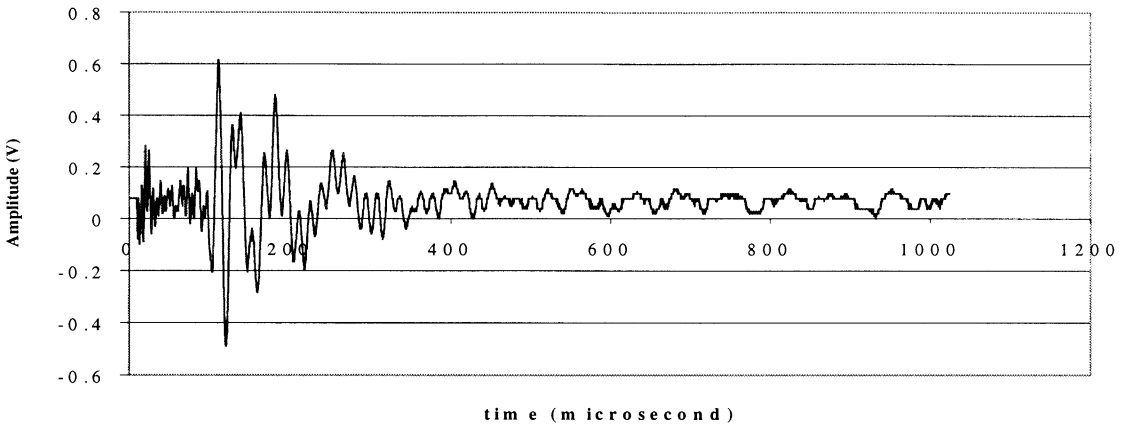

(d) Generation/detection distance of 38 mm

Figure 2.6.158 (a-d) Ultrasonic waves as function of the Generation/Detection distance along MD for copy paper at 355 nm.

We can see in Figure 2.6.158 on copy paper that the S_0 wave is still there, as opposed to what happened for linerboard. The ratio of the amplitude of S_0 and A_0 appears to vary much more at 355 nm than at 1064 nm and 532 nm from one shot to another. It seems to be very dependant on the generation conditions.

Both for copy paper and 42-lb linerboard, the damage caused to paper is worse at 355nm than at 1064 nm. However, the amplitude of the A_0 wave is only slightly bigger at 355 nm than at 1064 nm for copy paper.

2.6.8.3 Conclusions about laser generation at different wavelengths

Concerning the amplitude of the antisymmetric A_0 wave, we can say it seems larger at 1064 and 532 nm than at 355 nm, both for 42-lb linerboard and copy paper.

It appears that there is an improvement in the amplitude of S_0 waves at 532 nm compared to 1064 nm and 355 nm. This could be caused either by a different absorption coefficient of paper at different wavelengths or by a different optical penetration depth. Either way, this

increase of the wave amplitude is obtained by working further in the ablation regime, which damages the paper samples which is not allowed in reality. Alternately, since the generation appears to be more energy efficient at shorter wavelengths, a less powerful (and less costly) laser could be used to take advantage of this.

The comparison we made between wavelengths with the bender piezoelectric transducer needs to be further assessed by using an interferometer for detection in order to get results with a broadband receiver.

Also, we need to test other paper grades to see the influence of the thickness and reflection coefficient of paper on the ratio of the amplitudes of the A_0 and S_0 waves.

At present it seems that the intermediate generation regime at 1064 nm is still the best way to go for generating both S_0 and A_0 waves in a paper web without damaging its surface. Most of the measurements that we did with the interferometers were done using this intermediate generation regime at 1064 nm.

3 PAPER PHYSICS PROGRAM

3.1 *Introduction*

In parallel to the research program aimed at demonstrating the concept of laser ultrasonics on moving paper, we initiated the paper physics program. Tasks performed during Phase I are preliminary steps to the Phase II investigation of the relationships between mechanical properties and machine variables. They included the development of an advanced image analysis method to perform direct reference measurements of the geometrical fiber orientation distribution (FOD), and an experimental setup to performed indirect FOD measurements using a visible light scattering method was developed. Also, research work was undertaken to investigate the effect of moisture content and temperature on laser ultrasonic velocity measurements.

3.2 *Direct FOD Measurement Using an Image Analysis Method (B. Pufahl, IPST)*

3.2.1 Introduction

A novel, dyed fiber based image system was developed to determine fiber orientation distribution and evaluate the relationships between fiber orientation distribution and light scattering measurements. Although other systems had been previously developed, including one at IPST (Hess and Brodeur, 1996), these were based on older camera and lens technology and required repeated and time consuming testing of samples to obtain accurate data. The goal of the new system was to provide accurate automated fiber orientation measurements utilizing robust data analysis techniques.

The system consists of a high resolution (1520x1024 pixel) Kodak MegaPlus 1.6I camera capable of 10-bit (1024 levels) grayscale, a telecentric lens, a computer-controlled XY table, and adjustable front and back lighting (see Figure 3.2.1). The camera was chosen due to its high resolution and the fact that the pixels are square (9 μm by 9 μm) and have 100% fill factor (no gaps between pixels). A camera of this type, in conjunction with a telecentric lens, guarantees that the image being processed has not been modified by any of the elements in the imaging system. The image is transferred from the camera, through a frame buffer, and into the IMAQ for LabVIEW programming environment. A custom LabVIEW interface provides all system control, including camera settings and XY table position.

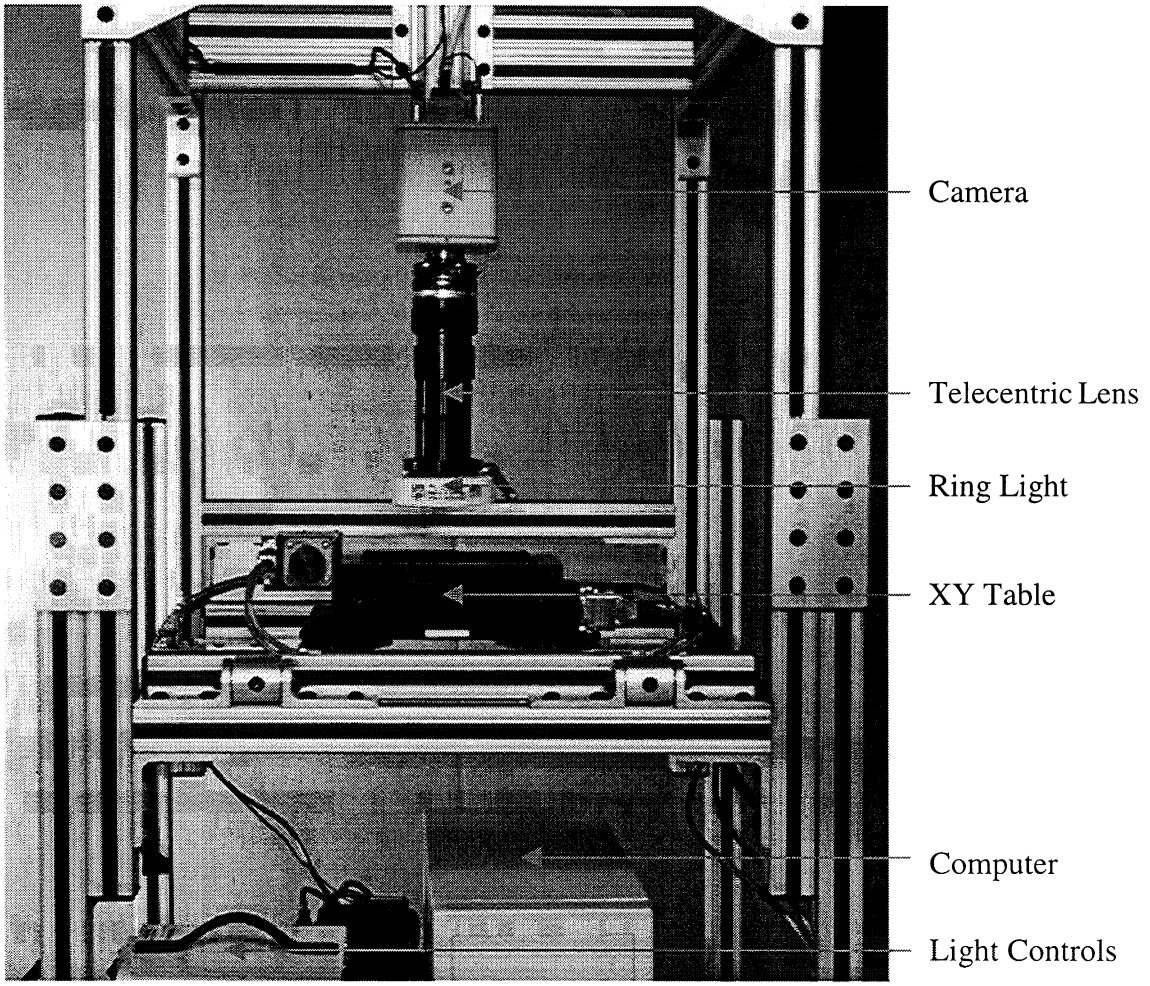

Figure 3.2.1 Image analysis system.

Since the field of view of the camera is much smaller than the paper sample, 48 images are captured for a single sample. These images are, in turn, split into six distinct areas during Fourier processing. The software used to extract orientation information from each image consists of two algorithms: one to improve signal to noise ratio; the other to process orientation information. Signal to noise ratio improvement is achieved by automatically compensating for lighting variations throughout images of the sample. In this regard, fixed thresholds are not employed and the algorithm requires no input from the user for locating fibers. The final step in the signal improvement algorithm is a morphological transformation that adjusts fiber width to 3

pixels with pixel values of 255. This last step is necessary as variations in pixel intensity or fiber width do not necessarily provide results that correlate to actual orientation.

The two dimensional Fourier transform of an image determines the spatial frequency of particles (in this case, fibers) in the image (Pourdeyhimi, 1993). With this technique, high frequencies correspond to fiber widths while lower frequencies correspond to the fiber lengths. The Fourier technique is being utilized as a method to eliminate the need to segment fibers (which is time consuming and does not address the issue of fiber curl), provide scalability to the system (eliminates the need to change program settings dependent on image magnification), provide higher resolution to the orientation data (actual measurements are recorded to within 0.5° before curve fitting), and provide a path to analysis of paper samples that do not contain dyed fibers. Current processing of a sample of 48 images requires 19.5 minutes on an Intel Pentium MMX 233MHz computer or 6.75 minutes on an Intel Pentium II 350MHz computer.

3.2.2 Image Analysis Results

A 15 cm by 15 cm paper sample containing dyed fibers was used for image analysis testing. Due to the nature of the sample holder, the actual processed area was 14 cm machine direction by 12.75 cm cross machine direction. The telecentric lens system used for testing provided a resolution of 15 microns per pixel. A combination of transmitted and reflected light was utilized to further enhance fibers that were embedded in the sheet. The ratio of this lighting was approximately 3:1 reflected to transmitted light.

The original image of a paper sample with dyed fibers is shown in Figure 3.2.2. This image is approximately 25% of the total image which is, in turn, 2.1% of the entire sample. The image is then processed through the signal enhancing and morphological algorithms to produce the

image in Figure 3.2.3. A Fourier transform is then performed on the processed image resulting in the image in Figure 3.2.4 (note that Figure 3.2.4 does not necessarily correspond to the same field of view of Figure 3.2.3). Finally, orientation data is gathered from the Fourier image and graphed in Figure 3.2.5. This process is continued until all 48 images have been processed with the result in Figure 3.2.6. For this sample, a total of 2,985 fibers were processed to provide the orientation data (an average of 62 fibers per image). Figure 3.2.7 shows the orientation distribution of all images within a sample. This technique is useful for determining the uniformity of the sample and shows that, if a sample is indeed uniform, only 5 to 10 images are needed to provide an average of fiber orientation distribution for the entire sample.

The resolution of the orientation data is a function of the angle measured. As the angle approaches either machine direction or cross machine direction, the resolution of the processing approaches 0.4° with a resolution of close to 0.75° at minimum resolution. The resolution of the system can be further improved by interpolating the Fourier data to provide results to within 0.1°.

In addition to reporting raw fiber orientation distribution, the software is also configured to report constants related to cosine, von Mises, and wrapped Cauchy distribution functions. These constants are used for determining amount of correlation between dyed fiber measurements and light scattering measurements.

Figure 3.2.2 Original image of dyed fibers.

Figure 3.2.3 Enhanced signal to noise ratio.

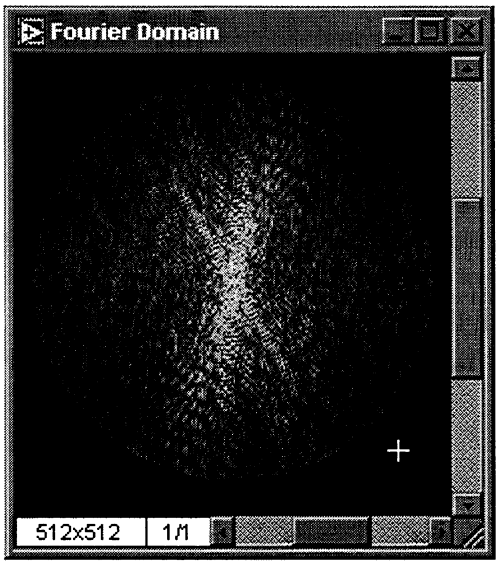

Figure 3.2.4 Fourier representation of enhanced image.

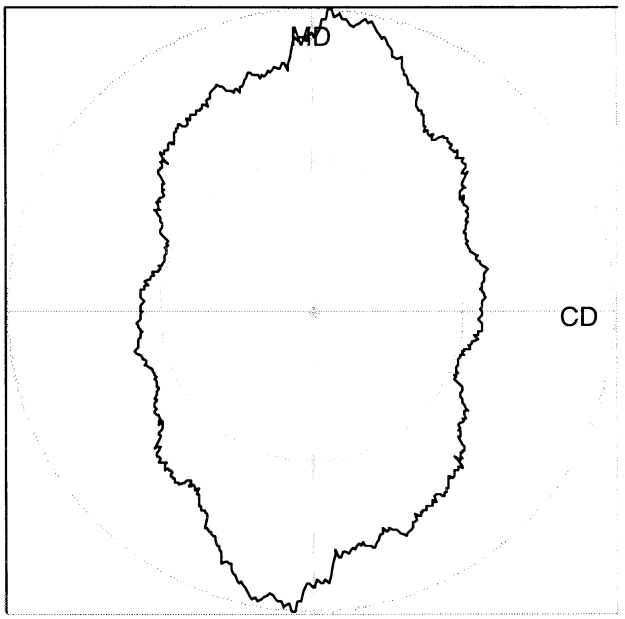

Figure 3.2.5 Fiber orientation distribution (FOD) for single image.

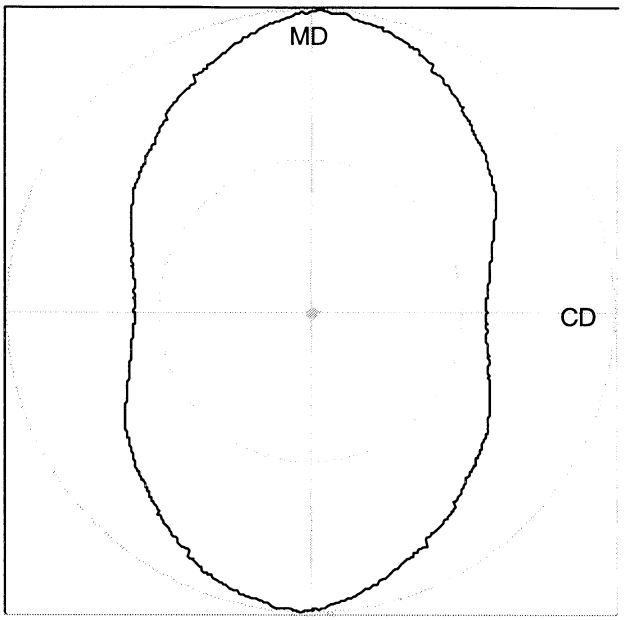

Figure 3.2.6 Fiber orientation distribution (FOD) for entire sample.

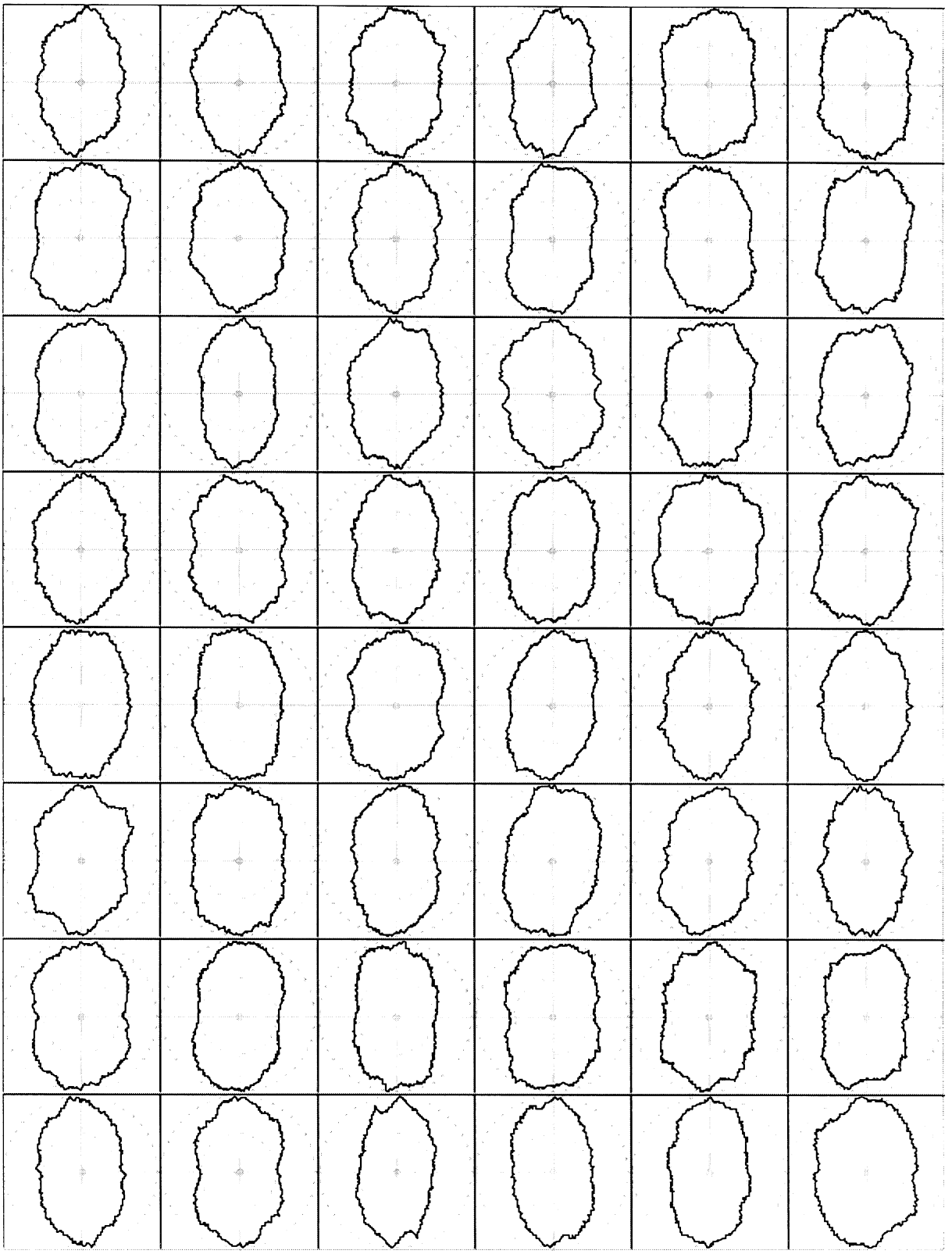

Figure 3.2.7 Fiber orientation distribution (FOD) for subsets of a sample (MD is vertical)

3.3 *Indirect FOD Measurement Using a Visible Light Scattering Method (J. Jong, J. Gerhardstein, IPST)*

3.3.1 Introduction

Previous studies have shown that the geometrical fiber orientation distribution (FOD) as typically measured using the image analysis of dyed fibers can indirectly be determined using a visible light scattering method (Kohl and Hartig, 1985; Niskanen and Sadowski, 1987). This approach is of course suitable for determining the fiber orientation distribution in machine-made paper. Silvy (1982) provided an analysis of the relation between the geometrical fiber orientation distribution and light scattering distribution of fiber orientation.

In this work, we are interested in further investigating light scattering measurements first in a transmission mode, then in a reflection mode. Light scattering results are fundamental to determining information about paper structure that is independent of built-in stresses. A detailed concept of the light scattering method is well documented by Kohl and Hartig (1985), Syre and Hagen (1995), and Ishisaki (1997). Also Niskanen and Sadowski (1987) suggested that the light scattering gave a reliable measurement of fiber orientation based on the samples ranged from 60 g/m^2 to 180 g/m^2.

In a typical light scattering method, a circular laser beam is focused on the surface of the sample, some of the light is scattered and diffused along the in-plane direction and the rest is transmitted through the z-direction of the paper. The light scattering occurs preferably in the direction of oriented fibers. Therefore, the resulting shape of the transmitted light becomes elliptical with the major axis oriented in the direction of the fiber orientation. The Max/Min

FOD anisotropy ratio can also be determined from the ratio of the major to minor axis of the ellipse. For a handsheet, the shape of the light should be circular due to random fiber orientation.

3.3.2 Experimental Methodology

A schematic diagram of the light scattering experimental setup for the transmission configuration is shown in Figure 3.3.1. A 150 mW Ar:ion laser at 514.5 nm is used as the light source. The beam exiting the laser is not particularly round or clean. So upon leaving the laser, it is sent through a spatial filter consisting of a 10x microscope objective which focuses the laser to the aperture of a 20 μm pinhole, and a 6.4 mm focal length collimating lens placed on the other side of the pinhole which re-collimates the beam. After the spatial filter, an iris is used to remove diffraction rings from around the primary beam, followed by a neutral density filter that can be used to attenuate the beam if the CCD becomes saturated. Following the filter, the beam is focused to a point on the paper sample with a typical spot size 1 mm in diameter. Care must be taken with the laser as to not burn holes through the sample. A CCD camera on the back side of the sample records the shape of the transmitted light. A computer which controls the CCD camera performs image analysis in order to extract the information of interest. This allows the computer to save only the information of interest for each spot instead of a large image file.

The sample is mounted in an XY table which is controlled by the same computer which operates the CCD camera. Custom software written in LabVIEW allows the computer to scan a sample and take an array of measurements without operator intervention.

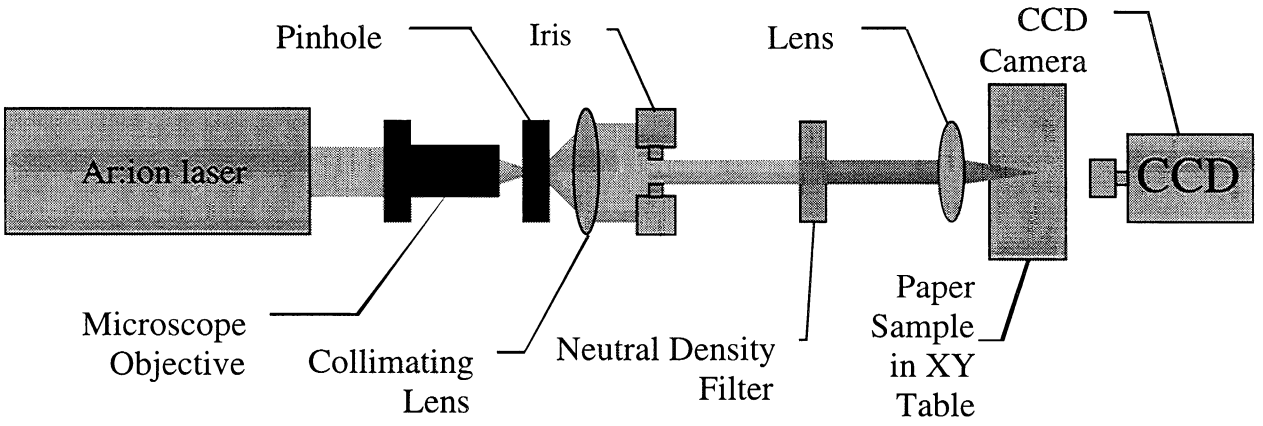

Figure 3.3.1 Schematic diagram of the light diffusion setup in transmission configuration.

Typical image analysis for the transmitted light is shown in Figure 3.3.2 *a-f*. Step *a* shows an example of a raw image. This image is thresholded to produce the binary image shown in *b*. The edge of the image in *b* is quite rough and the image contains points which are not connected to the largest object. In order to clean up the image, a closure is performed and shown in *c*. An edge detection routine is run, and leaves only the edge points around the ellipse, as shown in *d*. The edge points are extracted from the binary image and form an array in Cartesian space, *e*. A curve fit to any of a number of functions can then be performed. The curve fit in *f* is the cosine distribution.

A set of thirteen measurements is taken on each sample in the pattern shown in Figure 3.3.3. The first set of measurements was taken with MD facing vertically. The second set of measurements was obtained after the sample was rotated 90° counterclockwise for verification of the first set of data. Sample size was 18 cm by 18 cm.

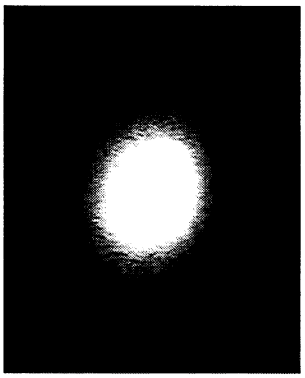

a) The original image.

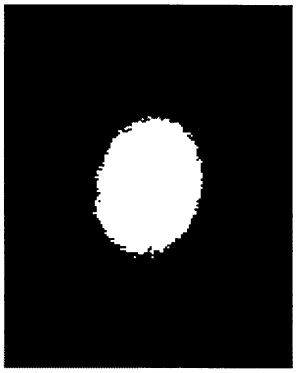

b) After thresholding.

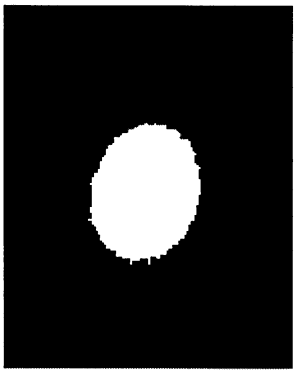

c) After closure.

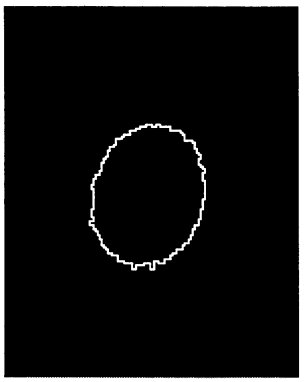

d) After edge detect.

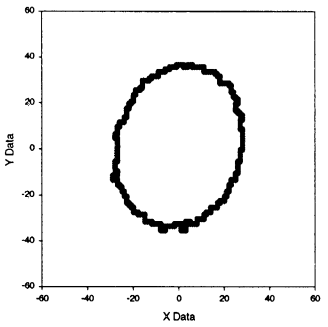

e) After extracting.

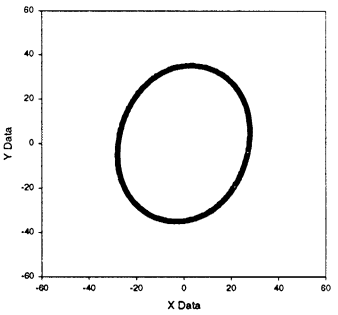

f) After curve fit.

Figure 3.3.2*a-f* Images through the analysis process. *a*) raw gray scale image from camera; *b*) binary image formed from thresholding *a*; *c*) after closure is performed on *b* to clean up the edge; *d*) only the edge points are then kept; *e*) edge points are extracted from the image into Cartesian space; *f*) curve fit to the points in *e*, in this case the cosine distribution. Ishisaki, 1997.

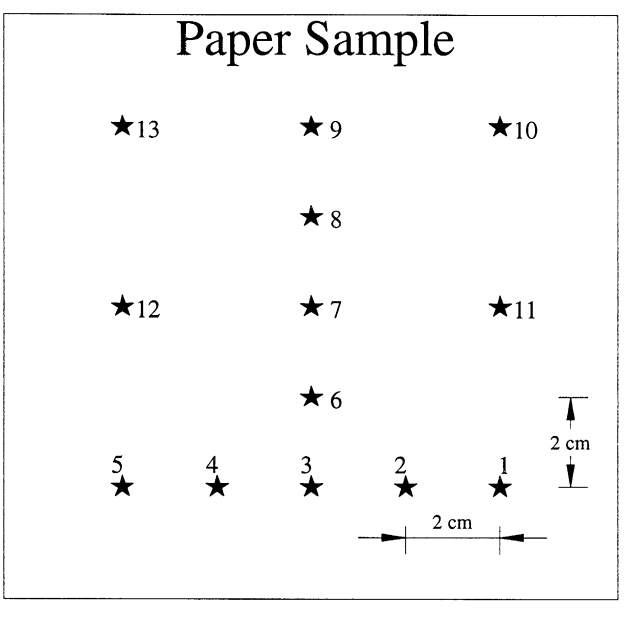

Figure 3.3.3 Location of the measured points with light scattering technique: each measured point is indicated by the star and the corresponding number.

To quantify the results, three mathematical functions can be used to characterize the fiber orientation distribution: the cosine function, the von Mise Function and the wrapped Cauchy function as follows (Baum et al., 1984; Schulgasser, 1985):

- Cosine Distribution Function :

$$f(\phi-\theta) = a_0 \cdot (1 + a_1 \cos[2(\phi-\theta)] + a_2 \cos[4(\phi-\theta)]) \qquad (1)$$

- Von Mises Distribution Function :

$$f(\phi-\theta) = a_0 \cdot Exp[a_1 \cos[2(\phi-\theta)]]/(\pi \cdot \mathrm{I}_0(a_1)) \qquad (2)$$

- Wrapped Cauchy Distribution Function :

$$f(\phi-\theta) = a_0 \cdot \frac{1-a_1^2}{1+a_1^2-2a_1\cos[2(\phi-\theta)]} \qquad (3)$$

where a_0, a_1 *and* a_2 represent shape parameters that fit raw fiber orientation data, $I_0(a_1)$ (in Equation 2) is a modified Bessel function of the first kind and zeroth order, ϕ is the independent variable (the measured angle), and θ is the angle of fiber orientation deviated from MD.

Schulgasser (1985) made a comparison of the three distribution functions. He reported that the wrapped Cauchy distribution would best fit the fiber orientation mechanism involved in a papermaking process because of the rapid process which fibers in the headbox undergo as they leave the slice and deposit on the fast moving wire. This argument still requires experimental verification.

3.3.3 Results

Figure 3.3.4 (a) shows an example of a light scattered image on a calibrated sample generated by a dynamic sheet former. The sample was originally prepared by Ishisaki (1997). The fiber orientation angle of the sample is initially known to be 0° and is compared with the current results to verify the accuracy of the light diffusion setup. The nominal stiffness anisotropy ratio R of the sample was 2.8. The grammage was 100 g/m^2. Figures 3.3.4 (b), (c) and (d) show the curve fitted shapes in polar coordinates obtained by regression using the cosine function, the Von Mise function, and the wrapped Cauchy function distributions, respectively. The scattered image from location 1 (see Figure 3.3.3) with MD vertical was arbitrarily chosen.

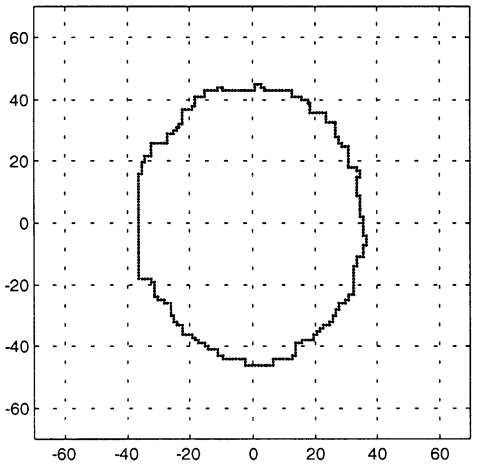

(a) Original image

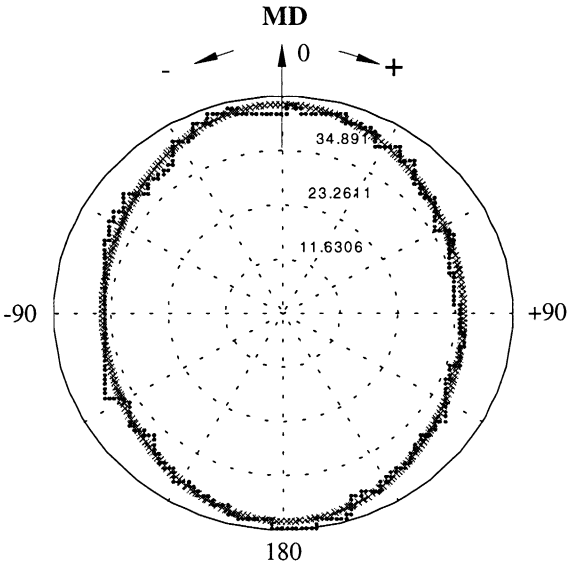

(b) Cosine distribution: -1.29°

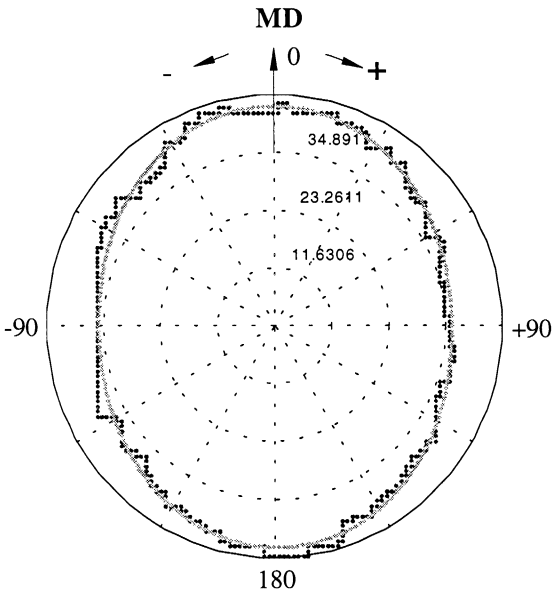

(c) Von Mise distribution: -1.51°

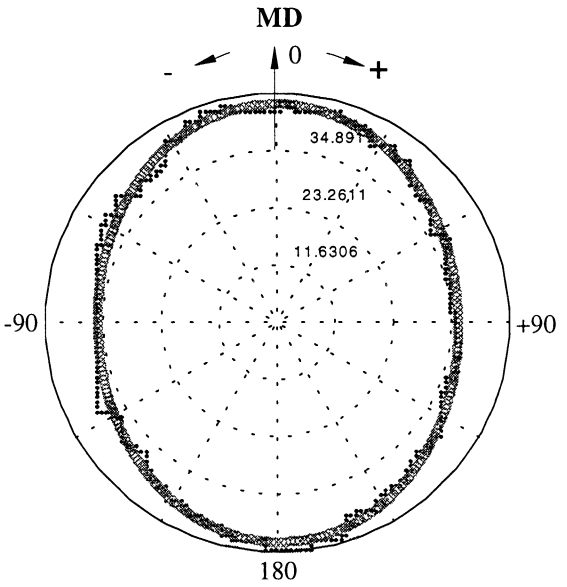

(d) Wrapped Cauchy distribution: -1.46°

Figure 3.3.4 Example of the light scattered image on a calibrated sample made by a dynamic sheet former and the curve-fitted shapes using the cosine function, the von Mise function, and the wrapped Cauchy function distributions. An arbitrary image at location 1 (see Figure 3.3.3) with MD vertical was selected. The sample had a grammage of 100 g/m^2 and a nominal stiffness anisotropy ratio *R* of 2.8.

All three distribution functions in Figure 3.3.4 predict the fiber orientation angles reasonably. Schulgasser (1985) suggested that the wrapped Cauchy distribution would best fit the fiber orientation mechanism involved in a papermaking. The results in Figure 3.3.4 neither support nor refute this statement.

Table 3.3.1 describes the results obtained by the light scattering method for all 13 position on the calibrated sample with R=2.8. The fiber orientation angles are obtained from the three function distributions and the averages are calculated. The Max/Min anisotropy ratio is calculated based on the regression from the cosine function. The table shows that the three functions predict similar orientation angle based on the averages. It is interesting to see that the angles measured at certain positions (e.g. 2, 8, 10) are more orientated than the others. This suggests that the fiber orientation distribution varies locally depending on the local characteristics at the time of papermaking. It is practical with the current equipment to investigate a whole profile of the fiber orientation distribution along CD, so that any local characteristics can be detected.

The light diffusion method was also applied to machine-made samples. It was observed that the effect of local orientation distribution was strongly present. For example, in copy paper, the local fiber orientation angles varied from -20° to +20°. This local variation was also present in other machine-made samples. Nevertheless, as long as the measurements are averaged sufficiently, the global fiber orientation distribution measured by the current light diffusion technique should compare well with more traditional FOD measurements (which perform measurements over large areas), such as with dyed fibers.

Table 3.3.1 Fiber orientation measurements on the calibrated sample with R=2.8: Fiber orientation angles are based on the curve fitted results using the cosine, the von Mise, and the wrapped Cauchy function distributions. Averages of the three angles are computed for each measured point. Averages for each function are also calculated.

Measured Location	Max/Min Anisotropy Ratio	Fiber Orientation Angles deviated from MD (degrees)			
		Cosine	Von Mise	Wrapped Cauchy	**Average**
1	1.22	-1.29	-1.52	-1.46	**-1.42**
2	1.27	-6.19	-6.27	-6.24	**-6.23**
3	1.25	-0.44	-0.37	-0.45	**-0.42**
4	1.18	-1.47	-1.03	-1.12	**-1.21**
5	1.17	-3.60	-2.14	-2.35	**-2.70**
6	1.24	3.91	3.93	4.04	**3.96**
7	1.24	2.77	0.11	0.35	**1.08**
8	1.23	11.59	11.97	11.83	**11.80**
9	1.20	-4.33	-4.32	-4.33	**-4.33**
10	1.14	-9.69	-9.91	-10.03	**-9.88**
11	1.28	-1.44	-0.77	-0.89	**-1.03**
12	1.20	2.66	2.62	2.51	**2.60**
13	1.23	4.37	4.73	4.66	**4.59**
Average	**1.22**	**-0.24**	**-0.23**	**-0.27**	**-0.25**

The light diffusion technique is in the process of being upgraded for on-line application. During the next phase of the project, the light diffusion in the reflection mode will also be developed.

3.4 *Effects of Moisture Content and Temperature on Ultrasonic Propagation in Paper (Y. Berthelot, GIT)*

3.4.1 Introduction

The objective of this research effort is to determine experimentally the influence of temperature and moisture content on the propagation of ultrasound in paper. The motivation is that one can determine important mechanical properties of paper samples from ultrasonic measurements (e.g., Baum, 1987) but the influence of temperature and moisture must be accurately determined before attempting to characterize the paper. This is especially important in the context of on-machine measurements because corrections must be applied to the velocity measurements. This research was originally planned for Phase II of the project, but considering the importance of these measurements, it was decided to initiate the work during Phase I.

The originality of the research lies in the experimental methodology, which should yield some of the most complete and accurate data to date. The experimental approach is based on laser ultrasonics (Scruby and Drain, 1990), a technique in which ultrasound is both generated and detected by lasers. The method is quasi-noninvasive, noncontact, with point source and point receiver precision. The technique is now well established and laser ultrasonics in copy paper has been demonstrated as a useful laboratory technique for paper characterization (Johnson, 1996).

3.4.2 Experimental arrangement

3.4.2.1 Overview

A sample is placed in a holder inside a controlled environmental chamber, as sketched in Figure 3.4.1. An Nd:YAG pulsed laser placed outside the chamber is used for generation of ultrasound. An Argon:ion laser interferometer is used to detect the ultrasonic waveform. The detecting probe head is inside the environmental chamber, close to the paper sample. An optical fiber is used to bring the Argon:ion laser light in and out of the chamber.

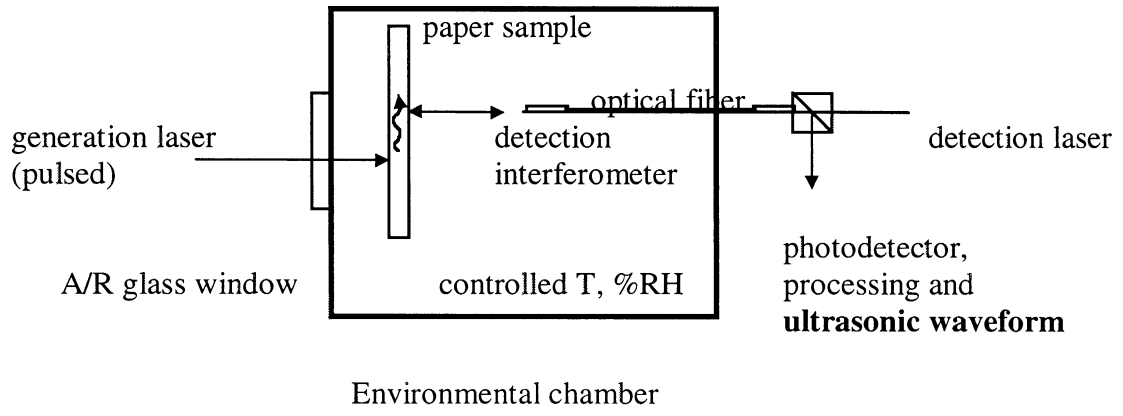

Figure 3.4.1 Sketch of the experimental arrangement.

3.4.2.2 Optical Generation

The generation laser is a Q-switched Nd:YAG with a 6 ns pulse duration and full energy of 460 mJ. The light is vertically polarized. The amount of energy actually delivered to the sample is controlled by polarization optics. A sketch of the generation setup is shown in Figure 3.4.2. A reflecting mirror is placed on a translation stage which provides a 13 mm scanning range over the sample. It is easier to scan the generation spot with a fixed laser detection spot than the reverse.

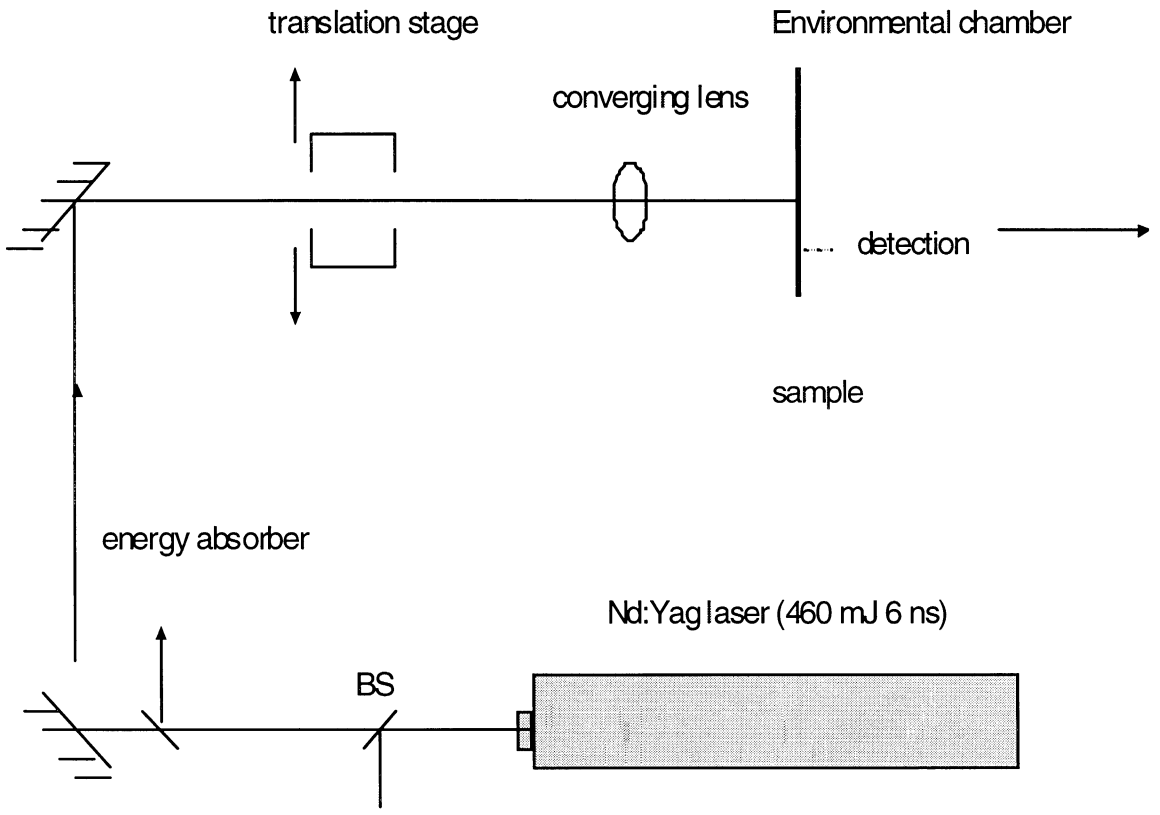

Figure 3.4.2 Block diagram of the optical generation system.

3.4.2.3 Detection Optics

The detection system is a standard Mach-Zehnder heterodyne interferometer. The laser is a CW Argon:ion laser with an output of 1.7 W at 514.5 nm. A block diagram of the setup is shown in Figure 3.4.3. The vertically polarized light passes through an acousto-optic Bragg cell which splits the beam into two parts: the signal beam, and the reference beam which is shifted by 40 MHz. The signal beam is sent to the chamber via a multimode small core (50 μm) fiber. The light is coupled in and out of the fiber by a miniature cylindrical lens with graded index of refraction (quarter pitch GRIN lens). The light is focused to a tight spot on the paper sample (50 to 100 μm) by means of a microscope objective. The polarization of the reference beam is shifted to horizontal with a quarter-wave plate and mirror combination, and the signal is passed through a polarized beam splitter to direct it towards the mixer where it interferes with the signal beam reflected from the sample. The signal reflected from the sample is Doppler shifted by the surface velocity component normal to the paper surface (out-of-plane component). The signal and the reference beams interfere and produce a frequency modulated signal whose carrier frequency is 40.0 MHz and with modulation directly proportional to the out-of-plane surface velocity of the paper measured at the detection spot. The optical signal is detected by an avalanche photodiode and it is demodulated by a standard FM discriminator. The signal is then amplified and filtered, sent to a digital oscilloscope and transferred via a GPIB IEEE 488 interface to a computer for data storage and analysis. Both the detection and the generation optics are placed on the same 4' x 6' optical bench. A photograph of the generation/detection optical bench is shown in Figure 3.4.4.

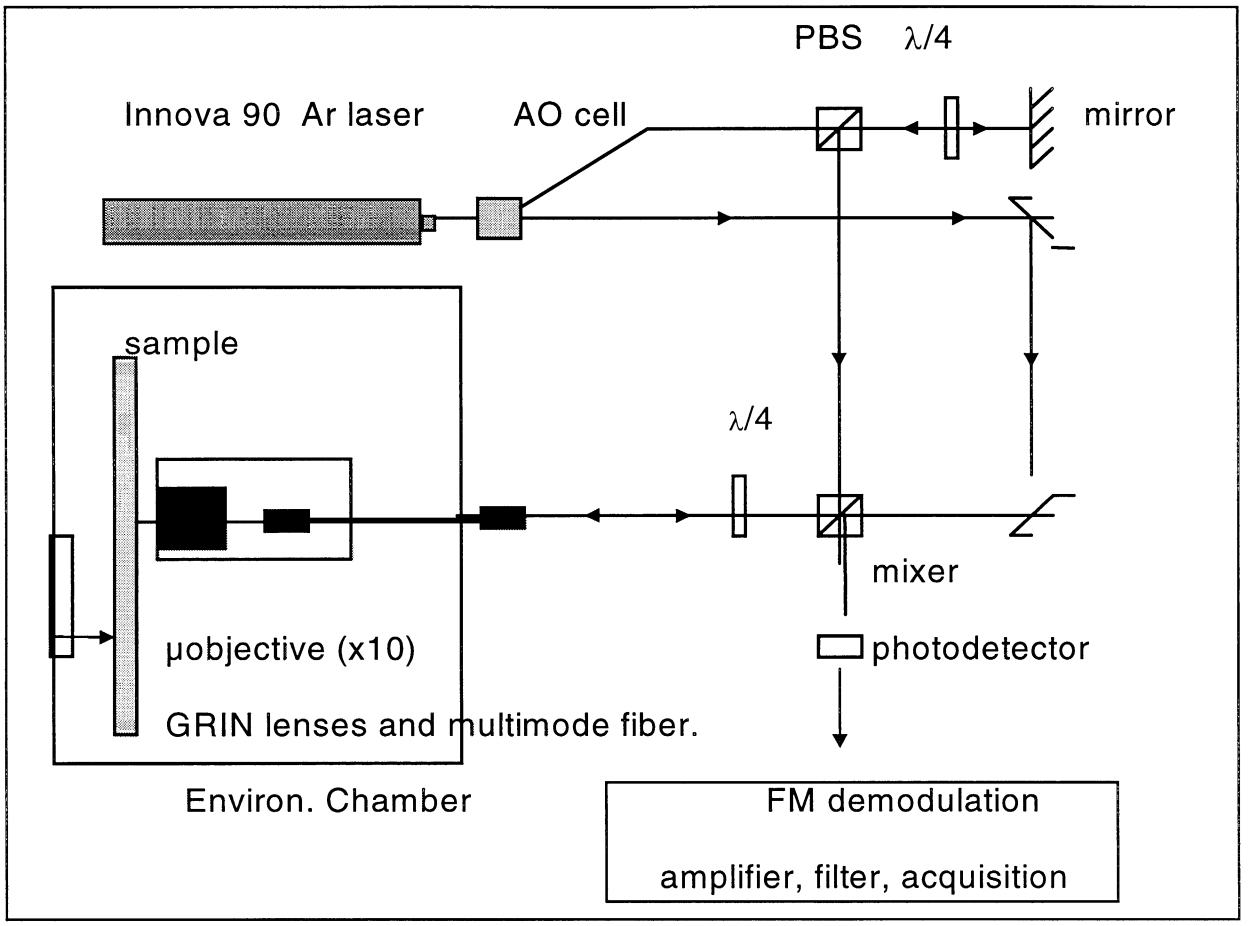

Figure 3.4.3 Block diagram of the optical detection arrangement.

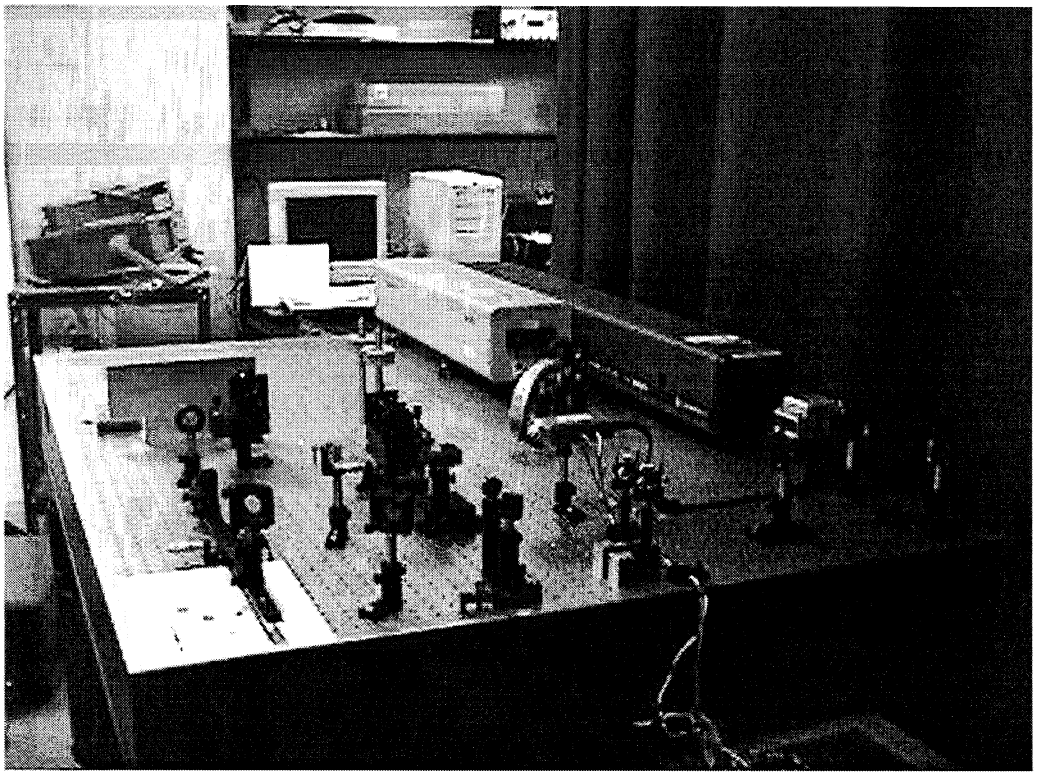

Figure 3.4.4 Generation/detection optical bench.

3.4.2.4 Chamber

The environmental chamber has interior dimensions of 16.5" x 20" x 15.75". The temperature range is -12 °C to +93 °C, and the relative humidity ranges from 20% to 98% in the dry bulb range of +20 °C to +85 °C as limited by a 3°C dew point. A photograph of the chamber is shown in Figure 3.4.5. The paper sample is placed in a holder similar to the ones used at IPST so as to standardize the size of samples and the clamping technique. Moisture content in the sample is to be determined experimentally by measuring the weight of the paper sample in the chamber and comparing with an equivalent dry sample.

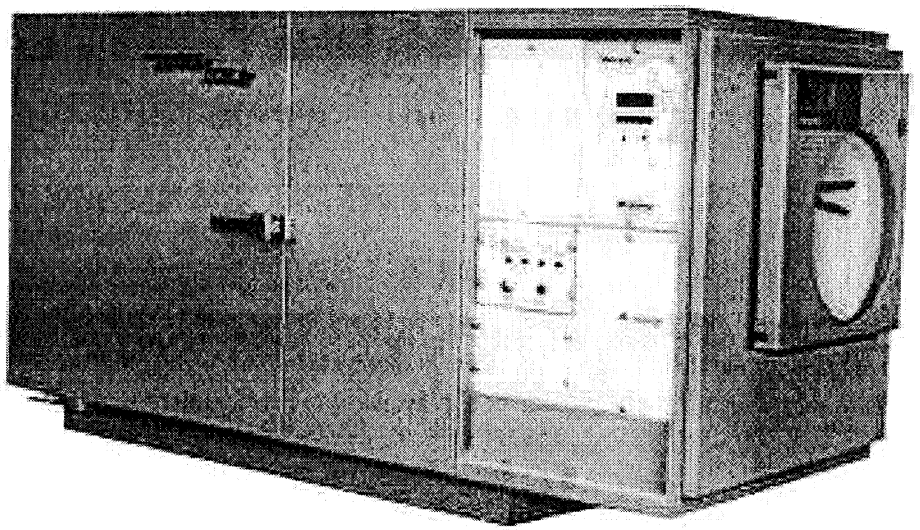

Figure 3.4.5 Environmental chamber.

3.4.2.5 Data analysis

The data acquisition and analysis is based on previous work at Georgia Tech (Johnson, 1996). It consists in the following steps:

- Acquire ultrasonic waveforms for each set of temperature and moisture content in MD and CD.
- Process data to obtain phase velocity versus frequency (dispersion curves)
- Obtain elastic constants C_{55} and C_{11} (MD), and C_{44} and C_{22} (CD).

3.4.3 Status

The optical generation system is operational and the environmental chamber is on order. The laser detection system is partially completed and should be fully operational before 9/30/98 so that preliminary data on samples (without the chamber) can be obtained. The data acquisition system is in place but it is being upgraded with LabVIEW.

The graduate Research Assistant position has not been filled at this point. It is anticipated that it will be filled no later than early October 98.

4 CONCLUSIONS

At the end of Phase I, we are proud to announce that all goals for the first year have been met or exceeded, and the ultimate goal of the control of a paper machine appears reachable. These goals included:

1. *Laboratory demonstration of laser ultrasonic characterization of moving paper.*

- Two web simulators capable of web speeds over 40 m/s plus flutter were built.
- Five different laser ultrasonic detectors were evaluated, including demonstrations on moving paper at production speeds with three (Fabry-Pérot, photoinduced-EMF, self-mixing).

2. *Development of image analysis and light scattering methods for fiber orientation distribution (FOD) measurements.*

- Design and building of a direct fiber orientation measurement instrument using dyed fibers in paper.
- Investigation of a light scattering/transmission method to measure fiber orientation, including comparison of different analysis methods.

In addition to these goals, other tasks (some from Phases II & III) were begun as well:

- Characterization of a wide range of samples as reference samples.
- Investigation into using an optical scanner to reduce texture noise levels on moving paper.
- Investigation of different laser wavelengths for efficient generation of ultrasound, including a literature survey and experimental work.
- Beginning of evaluation of the effect of temperature and moisture on ultrasonic properties.

These technologies are the basis to better understand the papermaking process. During Phase II (years II and III), these technologies will be optimized and integrated together to make an attempt at monitoring the papermaking process in a laboratory environment. Phase II will involve extensive testing of the above technologies on moving paper, as well as beginning to understand how they interact with the various papermaking variables. Phase II will culminate in the demonstration of an on-line, integrated instrument demonstration in the laboratory.

This on-line laboratory instrument will be taken in Phase III to two mill demonstrations, where single-point on machine measurements will be made during the fourth year of the project. Phase III will focus on making the necessary modifications to the instrument to make it a robust performer in the mill. The tradeoffs between economics and technical capabilities will be evaluated, with the ideal of a capable yet cost effective instrument package as the final goal.

5 LITERATURE CITED

Baum, G.A. "Elastic properties, paper quality, and process control," Appita, 40(4), 288-294 (1987).

Baum, G.A., Pers, K., Shepard, D.R. and Ave'Lallemant, T.R., "Wet Straining of Paper", TAPPI J. 67(5): 100-104 (1984).

Biermann, C., "Handbook of Pulping and Papermaking", Academic Press, 492-495 (1996).

Brodeur, P.H., Johnson, M.A., Berthelot, Y.H., and Gerhardstein, J.P., "Noncontact Laser Generation and Detection of Lamb Waves in Paper", J. Pulp and Paper Sc. 23(5) J238-J243 (1997).

Castagnede, B., Berthelot, Y.H. "Photoacoustic interactions by modulation and laser impact: Applications in mechanics and physics of anisotropic solids", J. Acoustique, 5, 417-453 (1992).

Cheng, J.C. and Berthelot, Y.H., "Theory of Laser-generated Transient Lamb Waves in Orthotropic Plates", J. Phys. D: Appl. Phys., 29: 1857-1867 (1996).

Delaye, P., Blouin, A., Drolet, D., de Montmorillon, L.A., Roosen, G., Monchalin, J.P., "Detection of ultrasonic motion of a scattering surface by photorefractive InP:Fe under an applied DC field", J. Opt. Soc. Am. B, 14(7), 1723-1734 (1997).

Edwards, C., Taylor, G.S., Palmer, S.B., "Ultrasonic generation with a pulsed TEA-CO2 laser", J.Phys. D: Applied Physics, 22(9), 1266-1270 (1989).

Gould, J.M., "Characterization of Lignin *in Situ* by Photoacoustic Spectroscopy", Plant Physiology 70, 1521-1525 (1982).

Habeger C. C., Mann R. W., and Baum, G. A., "Ultrasonic Plate Waves in Paper", Ultrasonics **17** , 57 (1979).

Habeger, C.C. and Wink, W.A., "Ultrasonic Velocity Measurements in the Thickness Direction of Paper", Journal of Applied Polymer Science, 32, 4503-4540 (1986).

Habeger, C.C., Van Zummeren, M.L., Wink, W.A., Pankonin, B.M. and Goodlin, R.S., "Using a Robot-based Instrument to Measure the In-plane Ultrasonic Velocities of Paper", Tappi J. 72(7): 171-175 (1989).

Hale, T.C., Telschow, K. "Optical Lock-in Vibration Detection using Photorefractive Frequency Domain Processing," Appl. Phys. Lett. 69, 2632 (1996).

Hale, T.C., Telschow, K.L., Deason, V.A., "Photorefractive optical lock-in vibration spectral measurement," Applied Optics, 111, 8248 – 8258, (1997).

Hess, T.R. and Brodeur, P.H., "Effects of Wet Straining and Drying on Fibre Orientation and Elastic Stiffness Orientation", J. of Pulp & Paper Sc. 22(5) J160-J164 (1996).

Ing, R.K., Monchalin, J.P., "Broadband optical detection of ultrasound by two-wave mixing in a photorefractive crystal", Appl. Phys. Lett. 59(25), 3233-3235 (1991)

Ishisaki, M., "Comparative Study of Fiber and Stiffness Orientation Distribution", *A190 Independent Research Report*, Institute of Paper Science and Technology (1997).

Johnson, M., "Investigation of the Mechanical Properties of Copy Paper using Laser Generated and Detected Lamb Waves", *Ph.D. Thesis*, Georgia Institute of Technology (May 1996).

Jordan, B.D., O'Neill, M., "Round Robin Study of Paper Colorimetry", J Pulp and Paper Sc. 14(5) J113-J120 (September 1988).

Kohl, A. and Hartig, W., "Optical Determination of Fiber Orientation", Das Papier 39(10A): V172-V177 (1985).

O'Shea, D., *Elements of Modern Optical Design*, John Wiley and Sons, Inc. (1985).

Mann, R.W., "Elastic Wave Propagation in Paper", *Ph.D. Thesis*, Institute of Paper Chemistry (1978).

Mann, R.W., Baum, G.A., and Habeger, C.C., Determination of All Nine Orthotropic Elastic Constants for Machine-made Paper, Tappi, 63(2), 163-166 (1980).

Monchalin, J.-P., "Optical Detection of Ultrasound", IEEE Trans. UFFC 33, 485 (1986).

Monchalin, J.-P., and Héon, R., "Laser Ultrasonic generation and Optical detection with a Confocal Fabry-Perot Interferometer", Mater. Eval. 44, 1231 (1986).

Niskanen, K.J. and Sadowski, J.W., "Critical Evaluation of Some Methods used to Determine Fibre Orientation in Paper", Proc. Paper Phys. Conf., 107-111 (1987).

Pope, J.M., "Near-Infrared Spectroscopy of Wood Products", from *Surface Analysis of Paper*, ed. by Conners, T., Banerjee, S., CRC Press, 142-151 (1995).

Pourdeyhimi, B., "Assessing Fiber Orientation in Nonwoven Fabrics", INDA Journal of Nonwovens Research, 5(4), 29-36, (1993).

Sachse, W. and Pao, Y.H., "On the Determination of Phase and Group Velocities of Dispersive Waves", J. Appl. Phys., 49(8): 4320-4327 (1978).

Schulgasser, K, "Fiber Orientation in Machine-made Paper", J. Mater. Sci., 20: 859-866 (1985).

Schumacher, N.A., Burger, C.P. and Gien, P.H., "A Laser-based Investigation of High-order Modes in Transient Lamb Waves", J. Acoust. Soc. Am. 93(5): 2981-2984 (1993).

Scott, W.E., Dearth, L.R., "Optical Properties of Paper", from *Pulp and Paper Manufacture, Volume 9, Mill Control & Control Systems: Quality & Testing, Environmental, Corrosion, Electrical*, ed. by Kouris, M., Kocurek, M., Joint Textbook Committee, 152-191 (1992).

Scruby C. and Drain, L. *Laser Ultrasonics*, Adams Hilger, New York (1990).

Silvy, J. "Structural Study of Fiber Networks: The Cellulosic Fiber Case", *Doctoral Thesis*, L'Institut National Polytechnique, Grenoble, France (1982).

Syre, H.R. and Hagen, W., "Improving paper Quality through On-line Measurement and Control of Fiber Orientation", conference proceedings On Papermaking and Paper Machine Technology, Helsinki, Finland, 51-60 (1995).

Tappi Test Methods, TAPPI Press (1998).

Telschow, K.L., Walter, J.B. and Garcia, G.V., "Laser Ultrasonic Monitoring of Ceramic Sintering", J. Appl. Phys. 68 (12), 6077 (1990).

Telschow, K.L., Deason, V. A., Ricks, K.L. and Schley, R. S., "Photorefractive laser ultrasound spectroscopy for materials characterization," accepted for publication in the Proceedings of the Eighth International Symposium on Nondestructive Characterization of Materials, Boulder, CO, June 15-20, (1997).

Telschow, K.L., Deason, V. A., "Structural Vibration Mode Imaging Using Photorefractive Holography," Proceedings of the 16th International Congress on Acoustics / 135th Acoustical Society of America Meeting Seattle, WA, pp 1873-1874, June 20-26, 1998.

Telschow, K.L., Deason, V. A., Schley, R. S., and Watson, S. M., "Imaging of Lamb Waves in Plates for Quantitative Determination of Anisotropy using Photorefractive Dynamic Holography," submitted to the Reviews of Progress in Quantitative NDE, Vol. 19, edited by D. O. Thompson and D. E. Chimenti, Plenum Press, New York (1998).

Van Zummeren, M., Young, D., Habeger, C., Baum, G., and Treleven, R., "Automatic Determination of Ultrasound Velocities in Planar Materials", Ultrasonics, 25, 288-294 (1987).

Viktorov, I.A., "Rayleigh and Lamb Waves", *Plenum Press*, New York (1967).

Wagner, J. W., "Optical Detection of Ultrasound," *Physical Acoustics*, Vol.XIX, Eds. Thurston, R.N., and Pierce, A.D., Academic Press, New York, Ch. 5 (1990).

Webb, D.J, Kiebling, A., Sturman, B. I., Shamonina, E., and Ringhofer, K. H. "Verification of the standard model of the photorefractive nonlinearity in BSO crystals", Optics Comm. 108 31-36 (1994).

Yeh, P., "Introduction to Photorefractive Nonlinear Optics" John Wiley and sons, New York (1993).

6 APPENDIX A - Research Proposal

CONTACTLESS REAL-TIME MONITORING OF
PAPER MECHANICAL BEHAVIOR DURING PAPERMAKING

IPST Proposal No. 4628

June 13, 1997

Proposal submitted to the U.S. Department of Energy

NOTE: The original research program, as described in the proposal submitted to the AF&PA Sensors and Control Operating Task Group (November 23, 1996), specified a three-phase project spanned over four years. DOE has requested that the research program be revised to consider funding for Phase I (Year 1 - Laboratory Demonstration) and Phase II (Years 2 and 3 - Demonstration of On-machine Prototype System) at this time. Hence, details about Phase III (Year 4 - Field Evaluation of Sensor Technology) have been left out of this document. It is assumed that DOE will support Phase III conditional to full success during Phase II.

RESEARCH TEAM

Pierre H. Brodeur (Principal Investigator) Associate Professor of Physics Fiber and Paper Physics Division Institute of Paper Science and Technology (IPST) 500 10th St. N.W., Atlanta, GA 30318 Phone (404) 894-7702 / FAX (404) 894-4778 e-mail: pierre.brodeur@ipst.edu	Charles C. Habeger, Jr. Professor of Physics Fiber and Paper Physics Division Institute of Paper Science and Technology (IPST) 500 10th St. N.W., Atlanta, GA 30318 Phone (404) 894-7534 / FAX (404) 894-4778 e-mail: chuck.habeger@ipst.edu
Kenneth L. Telschow Senior Scientist Idaho National Engineering Laboratory (INEEL) Lockeed Martin Idaho Technologies P.O. Box 1625, Idaho Falls, ID 83415-2209 Phone (208) 526-1264 / FAX (208) 526-0690 e-mail: telsch@inel.gov	Vance A. Deason Senior Scientist Idaho National Engineering Laboratory (INEEL) Lockeed Martin Idaho Technologies P.O. Box 1625, Idaho Falls, ID 83415-2211 Phone (208) 526-2501 / FAX (208) 526-2814 e-mail: vac@inel.gov
Yves H. Berthelot Professor of Mechanical Engineering School of Mechanical Engineering Georgia Institute of Technology (GIT) Atlanta, GA 30332-0405 Phone (404) 894-7482 / FAX (404) 894-7790 e-mail: yves.berthelot@me.gatech.edu	John D. Goss Engineering Director - Sensor Development Honeywell Measurex One Results Way, Cupertino, CA 95014 Phone (408) 255-1500 / FAX (408) 864-7551 e-mail: goss_john@measurex.com

Abstract (November 23, 1996)

A four-year R&D program is proposed to demonstrate, from laboratory- to on-machine prototype level, a contactless method to monitor paper mechanical behavior on the dry end of a paper machine. The measurement technique is based on laser ultrasonics principles. It involves laser systems to excite and detect Lamb waves propagating in the plane of paper. Assuming that appropriate Lamb wave velocity measurements are obtained, paper stiffness properties are determined and used to predict mechanical properties of interest to the papermaker. The proposed work goes beyond sensor development and addresses the simultaneous monitoring of stiffness and fiber orientation distributions as a unique means to evaluate built-in stresses in paper and provide information on basic processes such as wet pressing, wet straining, and restrained drying. The project has three phases. Phase I investigates the capabilities of two laser ultrasonics methods to determine paper stiffness on moving paper in a laboratory environment. Phase II considers the development of a rugged prototype sensor for on-machine simultaneous detection of stiffness and fiber orientation distributions. Also, decoupling of these distributions and relationships to built-in stresses and papermaking processes are studied. Field evaluations of the sensor technology in fine paper and linerboard mills are proposed during Phase III.

Background

The development of on-machine paper stiffness or "strength" sensors has been an on-going process for over 25 years because mechanical properties are critical to the papermaking process, converting operations, and end-use performance [1]. While the development of sturdy but contact methods is at the center stage [2-16], contactless concepts did not receive full attention even though they are far more desirable to the papermaker [17-21]. Merits of the latter methods include elimination of potential damage to the moving web and monitoring of fine papers, coated grades, and paperboards. Also, it is hypothesized that the availability of a contactless method would simplify the development of full sheet inspection systems for paper stiffness. Assuming that Lamb waves can be excited and detected in a noncontact manner using ultrasonic principles, one distinguishes two different test approaches: air-coupled transduction and laser ultrasonics.

Air-coupled Transduction. Considerable progress has been made in recent years toward the development of efficient air-coupled capacitive transducers, which are more sensitive and have a larger bandwidth than air-coupled piezoelectric transducers [22]. These transducers are relatively inexpensive. However, their utilization remains limited by the air medium itself: sound absorption in air increases with frequency, sound velocity in air is temperature dependent, and path lengths are sensitive to turbulence [23]. A resonance technique to induce and detect Lamb waves using air-coupled transducers was successfully tested on stationary paper [17-18]; an on-line implementation is hardly possible because the transmitter-receiver assembly must be rotated to get the maximum transfer of energy into the paper. Also, the sheet must be fairly thick to excite Lamb waves (> 400 μm) [18]. A proposal considering the applicability to paper of air-coupled capacitive transducers has been submitted to Agenda 2020 [24].

Laser Ultrasonics. The second approach, laser ultrasonics, considers the laser generation and detection of Lamb waves. The discipline is now well-established [25] and applications exist in the metal and plastic industries. Merits include point source excitation (ideal configuration for detection of stiffness orientation distribution), absence of measurement artifacts due to the coupling medium (insensitivity to air temperature and moisture, turbulence), uniqueness of information, large bandwidth, and the availability of extensive R&D support. Also, it offers

unique conditions for the simultaneous optical detection of the fiber orientation distribution. Difficulties, which can be overcome as discussed below, relate to surface roughness dependency (speckle averaging), sheet fluttering (also true for air-coupled transduction), and complexity of equipment. Three patents involving the use of lasers to generate Lamb waves in paper exist [19-21]. However, contact transducers [19-20] and unproved optical deflectometry [21] are used for detection. None of these patents considers optical heterodyne interferometry for detection as is proposed here to enhance measurement sensitivity [26]. A formal demonstration of laser ultrasonics on stationary paper was recently performed as part of a joint exploratory project IPST-GIT [27-28]. Also, a fundamental study of Lamb wave propagation in copy paper using laser generation and detection principles was recently completed [29-30].

It is the opinion of this research team that the laser ultrasonics approach offers an unmatched compromise to the successful and meaningful development of a sensor technology for continuous monitoring of paper mechanical behavior during papermaking. Its deployment is challenging, but it should provide the necessary information to fulfill the needs of elaborate papermaking control strategies.

Objectives

Phase I: Laboratory Demonstration

- To demonstrate a time domain laser ultrasonics method to determine paper stiffness on simulated moving paper in a laboratory environment (IPST-GIT);
- To demonstrate a frequency domain laser ultrasonics method to determine paper stiffness on simulated moving paper in a laboratory environment (INEEL);
- To redevelop an image analysis method to perform direct fiber orientation measurements using dyed fibers (IPST);
- To investigate a light scattering method to infer fiber orientation distribution (IPST);
- To perform a preliminary assessment of the sensor technology (IPST-GIT-INEEL-Honeywell Measurex).

Phase II: Demonstration of On-machine Prototype System

- To design and build a rugged prototype instrument for on-machine simultaneous detection of stiffness and fiber orientation distributions (IPST-GIT-INEEL-Honeywell Measurex);
- To develop a method to decouple stiffness and fiber orientation distributions and evaluate built-in stresses in paper as a function of basic papermaking processes (IPST);
- To demonstrate the on-machine sensor technology using IPST's Web Handling System (IPST).

General Experimental Approach

Referring to Fig. 1, when a normally incident pulse of light from a focused laser beam is absorbed by the paper, localized heating and accompanying thermal expansion occur in the network of cellulosic fibers. This leads to the formation of plate waves (Lamb waves) propagating in the plane of paper from the point of illumination. Excessive laser pulse power density can be detrimental to the paper (burning effect) and wave excitation (poor coupling).

However, these problems can be prevented by optimizing beam diameter, pulse energy, pulse width, and wavelength. Fig. 2 depicts a microscopic view of a single laser shot on a linerboard sample, as obtained using a pulsed Nd:YAG laser in the IPST-GIT work. There is a slight "bleaching" effect not visible to the naked eye. One would expect source optimization to reduce or eliminate this effect.

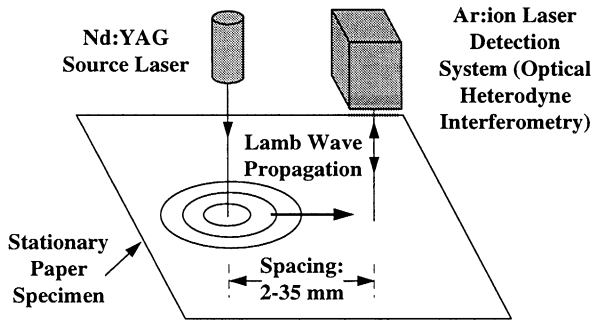

Fig. 1 Laser ultrasonics measuring principles.

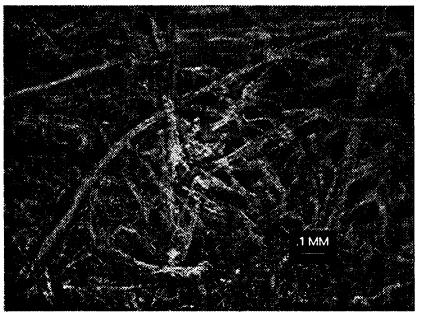

Fig. 2 Microscopic view of a single laser shot on brown paper.

Propagating Lamb waves in the paper are detected at some other point along the paper surface as shown in Fig. 1. Both the fundamental dilatational (S_0) and bending (A_0) modes for Lamb waves exist. They can be measured directly by recording the surface displacement in the time domain using optical heterodyne interferometry. Out-of-plane and in-plane surface displacement detection systems were used in the IPST-GIT project. Fig. 3 shows a typical normalized out-of-plane surface displacement recording for copy paper. The first pulse is a noise signal attributed to the firing of the YAG laser; it can be eliminated. The second and third signals correspond to the S_0 and A_0 modes, respectively. Similar recordings were obtained using the in-plane surface displacement detection system. As expected, the S_0 mode is nondispersive [29].

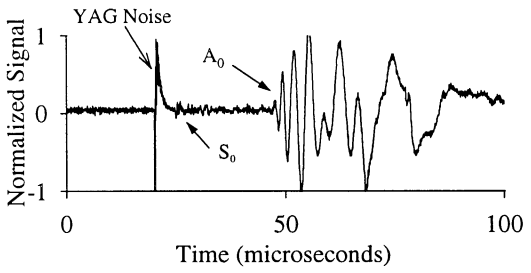

Fig. 3. Lamb waves in copy paper using out-of-plane motion detection system.

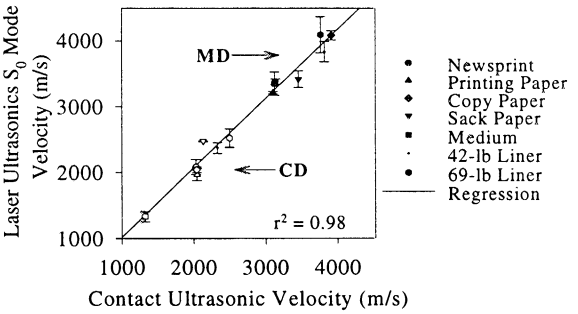

Fig. 4 S_0 mode contactless velocity vs. contact velocity for different grades.

Using a pair of polarized contact bimorph transducers operated at 80 kHz (low frequency limit of S_0 mode) [31], MD and CD longitudinal velocities were obtained for different paper grades. Similarly, MD and CD velocities were evaluated for the laser ultrasonics S_0 mode. Results are displayed in Fig. 4. Considering that the test equipment was far from being optimized, it is remarkable that both data sets correlate so well. Specific planar longitudinal stiffnesses Q_{11}/ρ

and Q_{22}/ρ can be evaluated by squaring MD and CD velocities, respectively (ρ is the apparent density of paper). From the dispersion analysis of the A_0 mode, specific out-of-plane shear stiffnesses C_{55}/ρ (MD-ZD) and C_{44}/ρ (CD-ZD) can be determined. The recent measurement of C_{55}/ρ and C_{44}/ρ for copy paper was a premiere [29] because out-of-plane shear testing (using contact method) is not recommended for paper grades less than 100 μm thick [32].
Since laser ultrasonics enables the simultaneous detection of Q_{22}/ρ and C_{44}/ρ (along CD), it provides a unique means to predict CD compressive strength for linerboard [1]. Moreover, it eliminates the need for different in-plane and out-of-plane technologies, thus optimizing data accuracy and contributing to cost reduction. One should mention that the rationale for performing in-plane and out-of-plane measurements steams from the fact that in-plane measurements do not provide sufficient information to discriminate between effects of fiber orientation and papermaking processes such as wet straining, restrained drying, and calendering; out-of-plane measurements are insensitive to fiber orientation, but sensitive to papermaking processes [1].

Assuming that laser detection is performed at different angles with respect to MD, the stiffness orientation distribution (either S_0 or A_0 mode) can be obtained. Since it is known that the ellipticity of a laser beam passing through paper best correlates to direct fiber orientation testing using dyed fibers [33], an integrated sensor aimed at detecting scattered light from the source laser can be used to infer fiber orientation distribution, and hence, provide information on the degree of geometric anisotropy (insensitive to moisture and built-in stresses). It is hypothesized that the simultaneous detection of the stiffness and scattered light-inferred fiber orientation distributions can be used to determine built-in stresses in paper, and hence, gather genuine information on wet pressing, wet straining, and restrained drying; dimensional stability monitoring is also possible. A comparative analysis of fiber and stiffness orientation angles was recently performed for different wet straining and restrained drying conditions [34]. Also, a preliminary theoretical analysis of decoupling of stiffness and fiber orientation distributions was recently accomplished [35]. A rugged and compact commercial fiber-optic interferometer has been demonstrated [36].

Frequency domain analysis, an alternative approach to the time domain detection method, excites Lamb waves continuously with a modulated laser beam. The resulting surface displacement is recorded synchronously by a photodetector. This frequency domain method, developed by INEEL, utilizes the photorefractive effect in select materials [37-38]. This effect utilizes the optical interference pattern obtained when scattered light and a reference beam mix in the photorefractive crystal causing a redistribution of electronic charge. The charge distribution "mirrors" in real-time the amplitude and spatial pattern of the surface displacement. This method is capable of imaging directly the anisotropic propagation of the A_0 mode; and perhaps the S_0 mode as well depending on ultimate sensitivity. The frequency domain technique discriminates between the S_0 and A_0 modes by spatial pattern rather than by time delay as in the time domain method. Most importantly, the photorefractive effect (particularly the INEEL technique) has been proven to accommodate speckle from surface roughness [39]. It has not yet been tested on paper.

Statement of Work

Tasks for Phases I and II are as follows:

Phase I: Laboratory Demonstration

I.1 Experimental Design (All Partners)

A meeting will be held at IPST very early in the project to brainstorm the proposed work. A work plan for Phases I and II will be developed and expectations for all partners will be clearly defined.

I.2 Laboratory Demonstration of Time Domain Laser Ultrasonics Method (IPST-GIT-H.M.)

A fully-dedicated time domain laser ultrasonics setup will be developed by IPST in collaboration with GIT and Honeywell Measurex. This setup will be installed at IPST in a TAPPI conditioned laboratory. It will be used to optimize laser generation and detection of Lamb waves on selected non-moving and moving paper samples. A variable-speed, rotating/translating drum will be developed by Honeywell Measurex to simulate moving paper and sheet fluttering [Note: a duplicate system will be built for use by INEEL - Task I.3].

The source laser will be a 200 mJ pulsed Nd:YAG operating at 1064 nm. Built-in frequency doublers will be used to perform additional observations at 532 and 455 nm, and hence, investigate Lamb wave excitation as a function of wavelength. An all solid-state, rugged 5 W CW Nd:YVO4 (Nd:Vandanate) laser operating at 532 nm will be used for detection [Note: since the delivery time for this laser may be as much as 6 months, a CW Ar:ion laser will be supplied on a temporary basis at no additional cost to the project]. It is expected that the solid-state laser (long-life expectancy, small foot-print, no cooling system) will be used for the full duration of the project. Out-of-plane and in-plane detection systems will be implemented. Two high-speed A-to-D boards will be used for simultaneous detection of a minimum of two signals (e.g. MD and CD velocities). LabVIEW-based software will be developed for data acquisition and control. Non-Gaussian optics and active optical tracking will be examined to compensate for low frequency vibrations and sheet fluttering. While the emphasis will be on dry paper, wet paper testing will be explored.

A full-time postdoc will be hired by IPST to perform the laser ultrasonics work; he will be assisted by a part-time IPST research engineer (Joe Gerhardstein). Both individuals have laser ultrasonics background. Consulting services on the fundamentals of wave propagation in paper will be provided by Prof. Charles Habeger from IPST. Consulting services on laser ultrasonics principles will be provided by Prof. Yves Berthelot from GIT. In order to facilitate technology transfer (2), Honeywell Measurex will delegate personnel to IPST at regular intervals.

I.3 Laboratory Demonstration of Frequency Domain Laser Ultrasonics Method (INEEL)

INEEL will modify its existing frequency domain laser ultrasonics setup to perform noncontact measurements on non-moving and moving paper samples supplied by IPST. It will investigate the use of different source lasers available at INEEL to optimize Lamb wave generation. Also, photorefraction will be explored as a means to compensate for paper surface roughness. INEEL research work will be under the supervision of Drs. Ken Telschow and Vance Deason.

I.4 Development of Image Analysis System for Direct Fiber Orientation Testing (IPST)

IPST will redevelop its automated image analysis system for direct fiber orientation to eliminate technical limitations, improve measurement accuracy, and improve processing time. The new system will be built around a 1024 x 1024 digital camera with square pixels. It will enable rapid testing of precision-made oriented sheets with a small percentage of dyed fibers (visible and/or fluorescent). Visible and ultraviolet light sources will be installed. The imaging system will used throughout the project to perform reference fiber orientation measurements. A part-time research engineer with an image analysis background will be hired by IPST to develop the system.

I.5 Development of a Light Scattering Method to Infer Fiber Orientation (IPST)

A light scattering method to infer fiber orientation distribution will be developed. Forward scattering and wire/felt backscattering modes will be investigated. An existing 150 mW Ar:ion laser available at IPST will be used for experimentation. The method will be developed in the context of the simultaneous detection of stiffness and fiber orientation distributions (Task II.1). A full-time postdoc will be hired by IPST to perform the work. It is expected that this individual will gain expertise on paper physics fundamentals and initiate preliminary work toward the development of a model to decouple stiffness and fiber orientation distributions (Task II.3).

I.6 Identification of Paper Company for Field Trials (IPST)

IPST will seek the participation of a paper company (may be two) for the field evaluation study to be performed during Phase III.

I.7 Preliminary Assessment of Sensor Technology (All Partners)

A preliminary assessment of the sensor technology will be made by all partners. Pluses and minuses of the time and frequency domain detection methods will be reviewed. The most likely successful technology for an on-machine implementation will be determined (it could be a combination of both methods). A report detailing results of Phase I will be prepared and submitted to the Department of Energy and AF&PA Sensors and Controls Operating Task Group.

Phase II: Demonstration of On-machine Prototype System

II.1 Development of an On-machine Prototype Instrument (All Partners)

An on-machine prototype instrument aimed at monitoring stiffness and fiber orientation distributions in a simultaneous manner will be developed according to the research findings obtained during Phase I. All partners will contribute and Honeywell Measurex will provide expertise on on-line instrumentation. Sub-systems will be developed at IPST (in collaboration with GIT), INEEL, and Honeywell Measurex. The sensor technology will be designed as a stand-alone, portable system capable of surviving harsh paper mill conditions.

II.2 Fundamentals of Lamb Wave Propagation in Paper (IPST)

The experimental setup developed at IPST during Phase I will be used to further understand the propagation of Lamb waves in paper. Also, laser generation and detection of out-of-plane bulk waves will be explored as a further means to discriminate in-plane stiffness dependency on fiber orientation from processes such as wet straining and restrained drying. Prof. Charles Habeger will focus his attention to this aspect of the project.

II.3 Development of Stiffness/Fiber Orientation Decoupling Method (IPST)

IPST will engage in a paper physics research program to develop a method to decouple stiffness and scattered light-inferred fiber orientation distributions and determine built-in stresses in paper. The method will consider on-machine parameters such as grammage and moisture. Effects of processes such as refining, wet pressing, wet straining, and restrained drying will be addressed. A series of laboratory oriented handsheets will be prepared using a dynamic sheet former available at IPST. A computer-controlled biaxial straining/drying apparatus will be used to simulate different wet straining and restrained drying conditions. The method will be implemented and tested on the prototype instrument. The postdoc hired during Phase I to conduct light scattering experiments will perform the above work. He will be partially assisted by the research engineer hired to develop the imaging system.

II.4 System Integration (All Partners)

The on-machine system will be integrated at IPST. A series of preliminary tests will be performed on IPST's web handling system using different paper grades.

II.5 Assessment of On-machine Sensor Technology (All Partners)

An assessment of the technology will be made by all partners. Technical issues for field trials to be conducted during Phase III will be considered. A report detailed results obtained during Phase II will be prepared and submitted to the Department of Energy and AF&PA Sensors and Controls Operating Task Group.

Deliverable:

Laboratory-demonstrated, contactless real-time sensor technology to monitor paper mechanical behavior during papermaking.

Benefits to the Industry

Benefits are pulp usage optimization (less fiber usage and/or better use of virgin/reclaimed fibers), reduction of energy consumption (less refining and/or less repulping/remanufacturing), monitoring of papermaking processes, product quality optimization, and basis for manufacturing strategies prioritizing mechanical properties and de-emphasizing grammage and thickness (may imply fiber usage reduction while meeting targeted strength properties).

Schedule

Tasks (Months)	3	6	9	12	15	18	21	24	27	30	33	36
I.1 Exp. Design / All Partners	->											
I.2 Time Domain Method / IPST-GIT-HM	--	--	--	->								
I.3 Frequency Domain Method / INEEL	--	--	--	->								
I.4 Image Analysis Method / IPST	--	->										
I.5 Light Scattering Method / IPST	--	--	--	->								
I.6 Mill Identification / IPST		--	--	->								
I.7 Preliminary Assessment / All Partners				->								
II.1 On-Machine Instrument / All Partners					--	--	--	--	--	--	->	
II.2 Lamb Wave Study / IPST					--	--	--	->				
II.3 Decoupling Method / IPST					--	--	--	--	--	--	--	->
II.4 System Integration / All Partners										--	--	->
II.5 Assessment / All Partners											--	->

Detailed Budget (see attached forms)

Bibliography of Literature

[1] G.A. Baum, "Elastic Properties, Paper Quality, and Process Control," *Appita*, vol. 40(4), pp. 288-293, 1987.

[2] E.P. Papadakis. "Ultrasonic Methods for Modulus Measurement in Paper," *Tappi J.*, vol. 56(2), pp. 74-77, 1973.

[3] M.T. Lu, "On-line Measurement of Strength Characteristics of a Moving Sheet," *Tappi J.*, vol. 58(6), pp. 80-81, 1975.

[4] G.A. Baum and C.C. Habeger, "On-line Measurements of Paper Mechanical Properties," *Tappi J.*, vol. 63(7), pp. 63-66, 1980.

[5] G.A. Baum and C.C. Habeger, "On-line Ultrasonic Velocity Gauge," U.S. Patent No. 4,291,577, 1981.

[6] K.R. Kazys, "Ultrasonic Methods for Non-destructive Testing of Paper," in *Proc. XXth Inter. Conf. on Acoustics and Ultrasound*, Prahq, 1981, pp. 192-193.

[7] E. Senko and J. Thorpe, "On-line Ultrasonic Measurement of Sheet Modulus," *Tappi J.*, vol. 68(2), pp. 95-99, 1985.

[8] C.C. Habeger and G.A. Baum, "On-line Measurement of Paper Mechanical Properties," *Tappi J.*, vol. 69(6), pp. 106-11, 1986.

[9] D.W. Vahey, "An Ultrasonic-based Strength Sensor for On-line Measurements," *Tappi J.*, vol. 70(3), pp. 79-82, 1987.

[10] J.J. Orkosalo, "System and Process for Measuring Ultrasonic Velocity," U.S. Patent No. 4,688,423, 1987.

[11] D.W. Vahey, "Correlating the On-line Measurement of Ultrasonic Velocity with Strength Properties," *Tappi J.*, vol. 71(4), pp. 149-152, 1988.

[12] L. Chase, J. Goss, and L. Anderson, "On-line Sensor for Measuring Strength Properties," *Tappi J.*, vol. 72(12), pp. 89-97. 1989.
[13] P.H. Brodeur, M.S. Hall, and C. Esworthy, "Sound Dispersion and Attenuation in the Thickness Direction of Paper Materials," *J. Acoust. Soc. Am.*, vol. 94(4), pp. 2215-2225, 1993.
[14] P.H. Brodeur, "Out-of-plane Ultrasonic Testing of Paper Materials Using Fluid-filled Rubber Wheels," *Tappi J.*, vol. 77(3). pp. 213-218, 1994.
[15] T.M. Cresson, J.D. Goss, and B.W. Wallace, "Sensor, System and Method for Determining Z-directional Properties of a Sheet," U.S. Patent No. 5,297,062, 1994.
[16] P. Williams and B.M. Pankonin, "On-line Measurement of Ultrasonic Velocities in Wet Manufacturing Processes," U.S. Patent No. 5,398,538, 1995.
[17] M. Luukkala, P. Heikila, and J. Surakka, "Plate Wave Resonance, A contactless Test Method," *Ultrasonics*, vol. 9, pp. 201-208, 1971.
[18] C.C. Habeger, R.W. Mann, and G.A. Baum, "Ultrasonic Plate Wave in Paper," *Ultrasonics*, vol. 17, pp. 57-62 (1979).
[19] M.A. Leugers, "Laser Induced Acoustic Generation for Sonic Modulus," U.S. Patent No. 4,622,853, 1986.
[20] S.A. Pace and S.S. Salama, "Laser Induced Acoustic Generation for Sonic Modulus," U.S. Patent No. 4,674,332, 1987.
[21] M.A. Keyes and W.L. Thompson, "Non-contacting On-line Paper Strength Measuring System," U.S. Patent No. 5,025,665, 1991.
[22] D.W. Schindel, D.A. Hutchins, L. Zou, and M. Sayer, "The Design and Characterization of Micromachined Air-coupled Capacitance Transducers," *IEEE Trans. Ultrason. Ferroelec. Freq. Cont.*, vol. 42, no. 1, pp. 42-50, 1995.
[23] D. W. Schindel and D.A. Hutchins, "Applications of Micromachined Capacitance Transducers in Air-coupld Ultrasonics and Nondestructive Evaluation", *IEEE Trans. Ultrason. Ferroelec. Freq. Cont.*, vol. 42, no. 1, pp. 51-58, 1995.
[24] J.C. Koo, J.E. Hernandez, and P.H. Brodeur, "Capacitive Sensor Array for 100% Paper Web On-Line Measurements," proposal submitted to Agenda 2020, 1996.
[25] C.B. Scruby and L. Drain, *Laser Ultrasonics - Techniques and Applications*, Adam Hilger-IOP Publishing, Bristol, 1990.
[26] J.P. Monchalin, J.-D. Aussel, R. Heon, C.K. Ken, A. Boudreault, and R. Bernier, "Measurement of In-plane and out-of-plane Ultrasonic Displacements by Optical Heterodyne Interferometry," J. Nondestr. Eval., vol. 8, no. 2, 121-133, 1989.
[27] P.H. Brodeur, Y.H. Berthelot, M.A. Johnson, and J.P. Gerhardstein, "Paper Stiffness Monitoring Using Laser Ultrasonics," *Proc. 1996 IEEE Int. Ultrasonics Symp.*, San Antonio, Nov. 3-6, 1996.
[28] P.H. Brodeur, M.A. Johnson, Y.H. Berthelot, and J.P. Gerhardstein, "Noncontact Laser Generation and Detection of Lamb Waves in Paper," *J. Pulp & Paper Sc.* 23(5) J238-J243, 1997.
[29] M. A. Johnson, "Investigation of the Mechanical Properties of Copy Paper using Laser Generated and Detected Lamb Waves," Ph.D. Thesis, Georgia Inst. of Tech., 1996.
[30] M.A. Johnson, Y.H. Berthelot, P.H. Brodeur, and L.A. Jacobs, "Investigation of Laser Generation of Lamb Waves in Copy Paper," *Ultrasonics*, vol. 34, no. 7, pp. 703-710, 1996.
[31] C.C. Habeger, M.L. Van Zummeren, W.A. Wink, B.M. Pankonin, and R.S. Goodlin, "Using a Robot-based Instrument to Measure the In-plane Ultrasonic Velocities of Paper," *Tappi J.*, vol. 72(7), pp. 171-175, 1989.
[32] C.C. Habeger and W.A. Wink, "Ultrasonic Velocity Measurements in the Thickness Direction of Paper, *J. Appl. Pol. Sc.*, vol. 32, pp. 4503-4540, 1986.
[33] D. Drouin, R. Gagnon, J. Silvy, A. Schroder, and M. Butel, "L'orientation des fibres et les proprietes mecaniques du papier: methode de controle de l'anisotropie de la feuille," *Proc. 47th ATIP Meeting*, Oct 11-13, 1994.
[34] T. R. Hess and P.H. Brodeur, "Effects of Wet Straining and Drying on Fiber Orientation and Elastic Stiffness Orientation," *J. Pulp & Paper Sci.*, vol. 22, no. 5, pp. J160-J164, 1996.
[35] K. Haynes, "Decoupling of Fiber and Stiffness Orientation Distributions," A390 Research Proposal, IPST, unpublished, 1996.
[36] J.J. Alcoz, C.E. Duffer, and S. Nair, "Noncontact Detection of Ultrasound with Rugged Fiber-Optic Interferometer," *Proc. 1996 IEEE Int. Ultrasonics Symp.*, San Antonio, Nov. 3-6, 1996.
[37] T.C. Hale and K. Telschow, "Optical lock-in vibration detection using photorefractive frequency domain processing," *Appl. Phys. Lett.*, vol. 69, p. 2632, 1996.
[38] T.C. Hale and K.L. Telschow, "Vibration Modal Measurement using All-optical Photorefractive Processing," *SPIE 1996 Intern. Symp. on Optical Sc., Eng., and Instrum.*, Denver, CO., August 4-9, in press, 1996.

[39] R.K. Ing, and D. Roy, "Ultrasound Detection on Rough Surfaces Using Heterodyne Photorefractive Interferometer: Applications to NDE," *Proc. 1996 IEEE Int. Ultrasonics Symp.*, San Antonio, Nov. 3-6, 1996.

Qualifications of Key Personnel

See attached resumes

1) Dr. Pierre H. Brodeur, IPST
2) Dr. Charles C. Habeger, Jr., IPST
3) Dr. Yves H. Berthelot, GIT
4) Dr. Kenneth L. Telschow, INEEL
5) Mr. Vance A. Deason, INEEL
6) Dr. John D. Goss, Honeywell Measurex

PIERRE H. BRODEUR

Education

Ph.D. Physics, University of Montreal, Montreal, 1984
M.Eng. Electrical engineering, McGill University, Montreal, 1980
M.Sc. Physics, McGill University, Montreal, 1978
B.Sc. Honors Physics, McGill University, Montreal, 1978

Work Experience

1996-present	Associate Professor of Physics, Institute of Paper Science and Technology
1989-1996	Assistant Professor of Physics, Institute of Paper Science and Technology
1986-1989	Research Associate, University of Quebec, Trois-Rivieres, QC Canada
1985-1986	Research Associate, INRS- Division of Energy, Varennes, QC Canada
1984-1985	Research Scientist, CAE Electronics Ltd., St.Laurent, QC Canada

Selected Refeered Papers (16 papers)

Brodeur, P.H., Johnson, M.A., Berthelot, Y.H., and Gerhardstein, J.P., Noncontact Laser Generation and Detection of Lamb Waves in Paper J. Pulp & Paper Sci. 23(5) J238-J243 (1997).
Johnson, M.A., Berthelot, Y.H., and Brodeur, P.H., Investigation of Laser Generation of Lamb Waves in Copy Paper. *Ultrasonics* 34(7) 703-710 (1996).
Brodeur, P.H. and Runge, T.M., Compactibility of a Wet Fiber Mat Using Acoustic Radiation Pressure. *J. Pulp & Paper Sci.* 22(8) J278-J282 (1996).
Hess, T.R. and Brodeur, P.H., Effects of Wet Straining and Drying on Fiber Orientation and Elastic Stiffness Orientation. *J. Pulp & Paper Sci.* 22 (5) J160-J164 (1996).
Brodeur, P.H., Out-of-plane Ultrasonic Testing of Paper Materials Using Fluid-filled Rubber Wheels. *Tappi J.* 77(3) 213-218 (1994)
Brodeur, P.H., Hall, M.S., and Esworthy, C., Sound Dispersion and Attenuation in the Thickness Direction of Paper Materials. *J. Acoust. Soc. Am.* 94 2215-2225 (1993).
Brodeur, P.H., Motion of Fluid Suspended Fibers in a Standing Wave Field. *Ultasonics* 29 302-307 (1991).
Brodeur, P., Dion, J.L., Garceau, J.J., Pelletier, G., and Massicotte, D., Fiber Characterization in a Stationary Ultrasonic Field. *IEEE Trans. Ultrason. Ferroelec. Freq. Control.* 36 549-553 (1989).
Garceau, J.J., Dion, J.L., Brodeur, P., and Luo, H., Acousto-optical Fiber Characterization. *Tappi J.* 72 171-173 (1989).

Patent

Hall, M.S., Brodeur, P.H., and Jackson, T.G., System for Measuring the Ultrasonic Velocity in the Thickness Direction of Moving Webs without Errors Due to Delays in the Onset of Digitization, U.S. Patent No. 5,493,911 (February 27, 1996).

CHARLES C. HABEGER, JR.

Education

Ph.D. Physics, University of Oklahoma, 1971
B.S. Engineering Physics, University of Oklahoma, 1966

Work Experience

1997-present	Professor of Physics, Institute of Paper Science and Technology
1988-1996	Senior Research Fellow, James River Corporation
1978-1988	Associate Professor of Physics, Institute of Paper Chemistry
1974-1978	Electronic Design Engineer, Applied Automation Inc.
1972-1974	Electronic Components Engineer, Radiation Inc.

Selected Refereed Papers (28 papers)

Habeger, C. C., *An Ultrasonic Technique for Testing the Orthotropic Symmetry of Polymeric Sheets by Measuring their Elastic Shear Coupling Coefficients,* Trans. ASME J. Engr. Mater. and Tech. 112: 366-371 (1990)
Habeger, C. C., Wink, W. A., *Development of a Double-Element Pulse Echo, PVDF Transducer,* Ultrasonics 28(1): 52-54 (1990)
Habeger, C. C., Van Zummeren, M. L., Wink, W. A., Pankonin. B. M., Goodlin, R. S., *Using a Robot-Based Instrument to Measure the In-Plane Ultrasonic Velocities of Paper,* Tappi 72(7) 171-175 (1989)
Habeger, C. C., Wink, W. A., Van Zummeren, M. L., *Using Neoprene-Faced PVDF Transducers to Couple Ultrasound into Solids,* J. Acoust. Soc. Am. 84(4): 1388-1396 (1988)
Pankonin B. M., Habeger, C. C., *A Strip Resonance Technique for Measuring the Ultrasonic Viscoelastic Parameters of Polymeric Sheets with Application to Cellulose,* J. Poly. Sci. B Poly. Physics 26: 339-352 (1988)
Habeger, C. C., Wink, W. A. *Ultrasonic Velocity Measurements in the Thickness Direction of Paper,* J. Appl. Poly. Sci. 32: 4503-40 (1986)
Habeger, C. C., *The Attenuation of Ultrasound in Dilute Polymer Fiber Suspensions*, J. Acoust. Soc. Am. 72(3): 870-878 (1982)
Habeger, C. C., Mann, R. W., Baum, G. A., *Ultrasonic Plates Waves in Paper*, Ultrasonics 17: 57-62 (1979)

Patents (8 patents)

Baum, G. A. Habeger, C. C., *On-line Ultrasonic Velocity Gauge,* U.S. Patent No. 4,291,577 (Sep. 29, 1981)
Habeger, C. C., Wink, W. A. W. A., *Ultrasonic Transducer,* U. S. Patent No. 4,769,571, (Sep 6, 1988)

Dr. Yves H. Berthelot
Woodruff School of Mechanical Engineering
Georgia Institute of Technology
Atlanta, GA 30332-0405 USA

Tel: (404) 894-7482
FAX: (404) 894-7790
e-mail: yves.berthelot@me.gatech.e du

VITA

Yves H. Berthelot is currently Professor and Woodruff Fellow in the School of Mechanical Engineering at the Georgia Institute of Technology. He received a Diplôme d'ingénieur in 1981 from the Université de Technologie de Compiègne (France), a M.S. in 1982 from the Institute of Sound and Vibration Research (ISVR) at the University of Southampton (England) and a Ph.D. in 1985 from the University of Texas at Austin. His main research interests are in the area of laser instrumentation for structural acoustics, nondestructive testing and material characterization by noncontact methods (laser ultrasonics). He is also interested in scale modeling problems in acoustics, especially those related to diffraction and scattering of sound in outdoor long range propagation. Since 1985, he has received over $3 million in research contracts from ONR, NSF, NASA, among others. Dr. Berthelot received in 1988 a Presidential Young Investigator award from the National Science Foundation. He is also the 1991 recipient of the Gold medal of the American Society of Mechanical Engineers (Pi Tau Sigma) and the 1991 co-winner of the Lindsay award of the Acoustical Society of America. He was elected Fellow of that Society in 1995.

Allan D. Pierce and Yves H. Berthelot, ``Acoustics", in Eshbach's *Handbook of Engineering Fundamentals*, 4th Edition, Ed. F. Tapley, Wiley, New York, 1990.

J. Vignola, Y. H. Berthelot, and J. Jarzynski, ``Laser detection of sound", J. Acoust. Soc. Am., 90(3), 1275-1286 (1991).

Costley, R. D., Berthelot, Y. H., and Jacobs, L. J., ``Laser–based techniques to resolve mode propagation of Lamb waves in plates," J. Acoustic Emission, Vol. 12, No. 1, 27-38 (1994).

U.S. Patent No 5,477,324 ``Method and Apparatus for detecting surface wave vector dynamics using three beams of coherent light" (Y. Berthelot, J. Jarzynski, and M. Yang)

Y. H. berthelot and J. Jarzynski, ``Directional laser generation and detection of ultrasound with arrays of optical fibers," J. Nondestructive Eval., Vol 9 No 4, 271-277 (1990)

R. D. Costley, Y. H. Berthelot and L. Jacobs, `` Fresnel arrays for the study of Lamb waves in laser ultrasonics," J. Nondestructive Eval., Vol. 13 No 1, 33-42 (1994)

M. Johnson, Y. H. Berthelot, P. Brodeur, and L. Jacobs ``Investigation of laser generation of Lamb waves in copy paper," Ultrasonics, 34, 703-710 (1996)

KENNETH LOUIS TELSCHOW

Department of Materials Physics
Idaho National Engineering Lab. (DOE)
Lockheed Martin Idaho Technologies Co.
P.O. Box 1625
Idaho Falls, ID 83415-2209
(208)526-1264 FAX (208)526-0690 email: telsch@inel.gov

K. L. Telschow's background and interests are in the fields of acoustic, ultrasonic and magnetic properties of materials at high and low temperatures. Currently, he is conducting research concerning noncontacting laser ultrasonics for materials characterization during processing and the electromagnetic behavior of superconductors. He came to the Idaho National Engineering Laboratory in 1984 and has been instrumental in developing laser ultrasonics for in-process materials characterization including ceramic sintering and molten metal solidification using conventional and nonlinear optical interferometry. As a consulting scientist at the INEEL, he leads research programs investigating new methods of optical acoustic/ultrasonic generation and detection in materials using nonlinear optics and the photorefractive effect. He is also actively engaged in developing electromagnetic approaches to superconductor NDE and the use of high temperature superconducting quantum interference devices (SQUIDs) for nondestructive characterization of material properties, such as, fatigue in stainless steel. His work has resulted in over 50 refereed publications and conference proceedings and 4 patents.

PROFESSIONAL DATA
Ph.D., Physics, UCLA, Los Angeles, California, 1973, B.S., Physics, 1969
CURRENT EXPERIENCE
Idaho National Engineering Laboratory, Lockheed Martin Idaho Technologies, Inc., Consulting Scientist
PREVIOUS EXPERIENCE
Southern Illinois University-Carbondale, 1976-81, Assist. Prof., 1981-84, Assoc. Prof., Depart. of Physics
University of Massachusetts-Amherst, 1974-76, Postdoctoral Research Associate, Department of Physics
MEMBER: American Physical Society, Acoustical Society of America
RECENT PUBLICATIONS

L. S. Koo and K. L. Telschow, "Method for Determining the Critical State Response of Superconductors in Tape Geometry", Phys. Rev. B 53, 1996, 8743.

T. C. Chatters and K. L. Telschow, "Optical Lock-in Vibration Detection using Photorefractive Four-wave Mixing", Reviews of Progress in Quantitative NDE, Vol. 15 edited by D. O. Thompson and D.E.Chimenti (Plenum Press, New York, 1996) 2165-2171.

J. B. Walter and K. L. Telschow, "Laser Ultrasonic Detection of the Solidification Front During Casting", Reviews of Progress in Quantitative NDE, Vol. 15A edited by D. O. Thompson and D.E.Chimenti (Plenum Press, New York, 1996) 607-613.

T.C. Hale and K. Telschow, "Optical lock-in vibration detection using photorefractive frequency domain processing," Appl. Phys. Lett. 69, 2632 (1996).

K.L. Telschow, J.B. Walter, R.J. Conant and S.E. Garwick, "Laser Ultrasonic Monitoring of Molten Metal Processes", 9th International Conference on Photoacoustic and Photothermal Phenomena, Nanjing, China, June 27-30, 1996, (INVITED) in press

T.C. Hale and K.L. Telschow, "Vibration Modal Measurement using All-optical Photorefractive Processing", SPIE 1996 International Symposium on Optical Science, Engineering, and Instrumentation, Denver, CO., August 4-9, 1996 in press

K.L. Telschow, F.W. Bruneel, J.B. Walter, and L.S. Koo, "Noncontacting Ultrasonic and Electromagnetic HTS Tape NDE", 1996 Applied Superconductivity Conference, Pitts. PA, August 25-30, 1996 in press.

VANCE ALBERT DEASON

Advisory Scientist: Electro-Optical Systems
Department of Optical and Plasma Physics

Idaho National Engineering Lab. (DOE)
LMITCO
P.O. Box 1625,
Idaho Falls, ID 83415-2211

Tel. (208) 526-2501
Fax (208) 526-2814
Email: vac@inel.gov

PROFESSIONAL CAPABILITIES

Advanced Instrumentation Design and Development	Instrumentation for Adverse Environments
Corrosive, High Temperature and High Pressure Steam	Cryogenic Systems
Holography and Holographic Interferometry	Moiré and diffraction moiré techniques
Dynamic moiré Interferometry	Pulsed Ruby Laser Techniques
CW Laser Techniques	Interferometric Techniques
Diffractive Optics	Laser Doppler Velocimetry
Non Linear and Photorefractive Effects	Fiber Optic Applications
Dynamic and Static Diffraction Moiré Interferometry	Coarse and Shadow Moiré
Modeling and Analysis	Aerosol Measurements
High Frame Rate and Streak Cameras	Photographic and Video Techniques
Transducer Design and Application	Strobe

WORK HISTORY

1977-Present: Idaho National Engineering Lab., Idaho Falls ID

Title: Advisory Scientist

Responsibilities: Develop projects, prepare and present reports, conceive, design, develop and prove novel measurement techniques, especially those involving precision optical techniques. Presently involved in adapting and developing such optical techniques as non-linear processes, interferometry, diffraction, high speed photography and video image analysis to solve problem relating to materials behavior and three dimensional measurement methods. Develop novel diffractive optics elements and optical data storage methods. Provide interface between various government agencies and between such agencies and industry in cooperative research projects.

VANCE A. DEASON CURRENT PATENT ACTIVITY
(ALL PATENT RIGHTS ASSIGNED TO THE U.S. DOE OR LITCO)

Total Patent Disclosures: 50; Patents Granted: 8, Pending: 1, In Preparation: 2

AWARDS

1990 R&D-100 Award for development of one of the 100 best new devices or processes of 1989 (Portable Moiré Interferometer).

1991 Federal Laboratory Consortium award for excellence in technology transfer

John D. Goss

Education

1989 Stanford University Engineering Executive Program
1984 University of Santa Clara - General Managers Seminars
1970 Ph. D. in Physics from The Ohio State University
1967 M.S. in Physics from The Ohio State University
1965 B.S. in (Eng.) Physics (Summa Cum Laude) from The Ohio State University

Work Experience

09/75 - Present Measurex Corporation, Cupertino California
05/70 - 09/75 University of Notre Dame, Notre Dame, Indiana
09/74 - 09/75 Assistant Faculty Fellow
09/73 - 09/74 Staff Faculty Fellow
05/70 - 09/73 Post Doctoral Fellow

Selected Referred Papers

"On-line strength measurement for predicting end-use performance," L. Chase, J.Goss, T. Cresson, L. Anderson (Measurex), and J. Challas (American Paper Institute), World Pulp & Paper Technology, 190 (1991).
"On-line sensor for measuring strength properties," L. Chase, J. Goss, and L. Anderson, Tappi Journal, Vol. 72, No. 12, December 1989.
"Application of on-line measurement techniques for strength control," L.M. Chase, T.M. Cresson, J.D. Goss (Measurex), J. Challas (American Paper Institute), M. Hutten, and R.L. Ellis (Institute of Paper Science and Technology), Tappi Journal, Vol. 76, No. 10, October 1993.

Presentations

"Advanced Techniques for Surface Smoothness Measurement and Control," L. Chase, E. Belotserkovsky, and J. Goss, SPCI Sweden, June 4, 1996.
"Advanced Techniques for Surface Smoothness Measurement and Control," L. Chase, E. Belotserkovsky, and J. Goss," TAPPI 1996 Finishing & Converting Conference," October 6, 1996

Patents

John Goss, et al

#4678915 7/7/87 System and Process for Measuring and Correcting the Values of a Parameter of a Sheet Material.
#4920265 4/24/90 System for Deterring the Basis Weight of Cord Reinforced Tire Fabric
#4936140 6/36/90 Device and Method for Calibrating a Non-destructive Sheet Strength Measuring Device
#4970895 11/20/90 System and Method for the Determination of Certain Physical Characteristic of Sheet Materials
#4991432 2/12/91 Sensor and System for Continuous Determination of Sheet Characteristics
#5014288 5/7/91 X-Ray Coating Weight Controller and Sensor
#5029469 7/9/91 Sheet Tension Sensor
#5101661 4/7/92 Fiber Orientation Sensor
#5111688 5/12/92 Device and Method for Calibrating a Non-Destructive Sheet Strength Measuring System
#5138878 8/18/92 Fiber Orientation Sensor
#5171403 12/15/92Method for Determining the Bending Stiffness of a Moving Sheet
#5297062 3/22/94 Sensor System and Method for Determining Z-Directional Properties of a Sheet
#5315124 5/24/94 Nuclear Gauge

7 APPENDIX B – STATEMENT OF WORK - TIME SCHEDULE

STATEMENT OF WORK

(Revised April 13, 1998)

Phase I: Laboratory Demonstration (Sept 15, 1997 - Sept 14, 1998)

Experimental Design (IPST, INEEL, HMX)

A meeting will be held at IPST very early in the project to brainstorm the proposed work. A work plan for Phases I and II will be developed and expectations for all partners will be clearly defined.

Evaluation of Single-point Photorefractive Method (IPST)

Development of Laser Ultrasonics Setup

A fully-dedicated time domain laser ultrasonics setup will be developed by IPST in collaboration with INEEL for demonstration experiments. This setup will be installed at IPST in a TAPPI conditioned laboratory. It will be used to investigate laser generation and detection of Lamb waves on selected non-moving and moving paper samples. While the emphasis will be on dry paper, wet paper testing will be explored if time permits.

The source laser will be a 200 mJ pulsed Nd:YAG operating at 1064 nm (repetition rate: 20 Hz). Frequency doublers will be used to perform additional observations at 532 and 355 nm, and hence, investigate Lamb wave excitation as different wavelengths.

Two lasers will be used for detection. First a temporary 2 W CW Ar:Ion laser will be used to perform preliminary experiments at 514 nm. Then, a 600 mW diode-pumped solid-state single-frequency infrared laser system (1064 nm) will be used on a more permanent basis.

Single-point detection using a photorefractive interferometric system will be the preferred method for Lamb wave detection (*Test Method #1*).

Development of Web Simulators (2)

Two identical web simulators to be used by IPST and INEEL (see Tasks 1.4 and 1.5) will be developed to simulate moving paper at different machine speeds and sheet fluttering condtions. The systems will be computer-controlled and capable of machine speeds up to 3000 ft/min (to be upgraded to 7000 ft/min during Phase II). Also sheet fluttering simulation at frequencies up to 70 Hz will be possible.
Development of Test Station for Non-moving Paper Measurements

A dedicated system using an X-Y table will be built to support samples for non-moving paper experiments to be conducted at IPST.
Sample Collection, Preparation, and Characterization

IPST will collect, prepare, and characterize different paper samples for testing using IPST and INEEL equipment.

Evaluation of Commercial Laser Ultrasonics Systems (IPST)

IPST will evaluate two commercial systems using different laser ultrasonics detection principles (*Test Methods #2 and #3*).

Evaluation of Fabry-Pérot Interferometer (INEEL)

INEEL will use an existing Fabry-Pérot interferometer for experiments on non-moving and moving paper samples (*Test Method #4*).

Evaluation of Photorefractive Imaging Method (INEEL)

INEEL will modify its photorefractive imaging system (frequency domain) laser ultrasonics setup to perform non-contact measurements on non-moving and moving paper samples supplied by IPST (*Test Method #5*).

Image Analysis System for Direct Fiber Orientation Testing (IPST)

IPST will redevelop its automated image analysis system for direct fiber orientation to eliminate technical limitations, improve measurement accuracy, and improve processing time. The new reference system will utilize a digital camera with square pixels. It will enable rapid testing of laboratory oriented sheets with a small percentage of dyed fibers.

Development of Light Scattering Method (IPST)

A light scattering method to infer fiber orientation distribution will be developed. Forward scattering and wire/felt backscattering modes will be investigated. An existing 150 mW Ar:ion laser available at IPST will be used for experimentation.

Laser Ultrasonics Investigation of Moisture & Temperature Effects - Part 1 (GIT)

GIT will begin during Phase I the development of a laser ultrasonics test method to investigate the effects of moisture and temperature on different non-moving paper samples supplied by IPST. A special temperature/relative humidity controlled chamber will be built. A Mach-Zehnder interferometric setup will be used for detection. This investigation will continue during Phase II. Results will be used to correct for moisture/temperature variations.

Mechanical Behavior of Paper Vs. Papermaking Variables - Part 1 (IPST)

In parallel to technology development, IPST will engage in a substantial paper physics research effort to investigate relationships between paper stiffness properties and papermaking variables. Several paper parameters will be considered in addition to stiffness (e.g., grammage, fiber orientation, moisture/temperature). Also several papermaking variables will be considered (e.g., refining, jet-to-wire ratio, wet pressing, wet straining, restrained drying). This effort will continue during Phase II and the ultimate objective is to devise a preliminary semi-empirical model to be tested during Phase III. Two variants of the model will be developed for copy paper and linerboard.

Preliminary Assessment of Sensor Technology (IPST, INEEL, HMX)

A preliminary assessment of the five laser ultrasonics test methods investigated during Phase I (Tasks 1.2.1, 1.3, 1.4, 1.5) will be made to determine the most likely successful technique for on-machine implementation.

Phase I Report (IPST, INEEL, GIT, HMX)

A report detailing the research work performed during Phase I will be prepared and submitted to Honeywell-Measurex and the Department of Energy.

Phase II: Demonstration of On-machine Prototype System (Sept. 15, 1998 - Sept. 14, 2000)

Identification of Paper Machines for Mill Trials (IPST and HMX)

Very early during Phase II, contacts will be established with paper companies to identify two industry partners for mill trials to be conducted during Phase III. It is envisioned to perform mill trials using copy paper and linerboard machines (see Phase III).

Development of On-machine Prototype System (IPST, INEEL, HMX)

An on-machine prototype instrument aimed at simultaneous monitoring of stiffness and fiber orientation information will be developed according to the research findings obtained during Phase I. All partners will contribute and HMX will provide expertise on on-machine instrumentation. Sub-systems will be developed at IPST, INEEL, and HMX. The sensor technology will be designed as a stand-alone, portable system capable of surviving harsh paper mill conditions.

Fundamentals of Lamb Wave Propagation in Paper (IPST)

The experimental setup developed at IPST during Phase I (Task 1.2.1) will be used to further understand the propagation of Lamb waves in paper. Also, laser generation and detection of out-of-plane bulk waves will be explored as an attempt to get additional information for the modeling effort initiated during Phase I (Task 1.9).

Laser Ultrasonics Investigation of Moisture & Temperature Effects - Part 2 (GIT)

The investigation of moisture/temperature effects on paper stiffness properties will continue during Phase II (see Task 1.8).

Mechanical Behavior of Paper Vs. Papermaking Variables - Part 2 (IPST)

The investigation of relationships between paper stiffness properties and papermaking variables initiated during Phase I will continue during Phase II (see Task 1.9).

System Integration (IPST)

The on-machine prototype system will be integrated at IPST. The system will include a preliminary version of the software to relate paper stiffness properties to papermaking variables. Preliminary trials will be performed at IPST using the web simulator built during Phase I.

Assessment of On-machine Prototype System (IPST, INEEL, HMX)

An assessment of the prototype system will be made. Technical issues for mill trials will be considered.

Phase II Report (IPST, INEEL, GIT, HMX)

A report detailed results obtained during Phase II will be prepared and submitted to HMX and the Department of Energy.

Phase III: Mill Trials (Sept. 15, 2000 - Sept. 14, 2001)

Mechanical Behavior of Paper Vs. Papermaking Variables - Part 3 (IPST)

The investigation of the relationships between paper stiffness properties and papermaking variables will be continued during Phase III.

Mill Trials (IPST, INEEL, HMX)

The prototype system built during Phase II will be used for mill trials. It is proposed to perform two successive four-month mill trials using copy paper and linerboard machines.

Exploratory Analysis of Process Control Strategies (IPST and HMX)

In preparation for future work, IPST and HMX will perform an exploratory analysis of process control strategies relying on the use of laser ultrasonics monitoring technology.

Final Technology Assessment (IPST, INEEL, HMX)

A final technical/economical assessment of the technology will be performed.

Technology Transfer (IPST and HMX)

IPST will transfer the technology to Honeywell-Measurex.

Phase III Report (IPST, INEEL, HMX)

A final report will be prepared and submitted to Honeywell-Measurex and the Department of Energy.

TIME SCHEDULE

TASKS	PHASE I				PHASE II								PHASE III			
	Year 1				Year 2				Year 3				Year 4			
	Q 1	Q 2	Q 3	Q 4	Q 1	Q 2	Q 3	Q 4	Q 1	Q 2	Q 3	Q 4	Q 1	Q 2	Q 3	Q 4
1.1 Experimental Design	-															
1.2 Eval. of Single-Point Photorefractive Method		-	-	-												
1.2.1 Development of Laser Ultrasonics Setup	-	-	-													
1.2.2 Development of Web Simulators (2)	-	-	-													
1.2.3 Development of Test Station	-	-														
1.2.4 Sample Collection, Preparation, and Charac.	-	-														
1.3 Evaluation of Commercial L.U. Systems			-	-												
1.4 Evaluation of Fabry-Perot Interferometer		-	-	-												
1.5 Evaluation of Photorefractive Imaging Method			-	-												
1.6 Image Analysis Syst. for Direct Fiber Orient.		-	-													
1.7 Development of Light Scattering Method		-	-	-												
1.8 L.U. Invest. of Mois. & Temp. Effects - Part 1			-	-												
1.9 Mech. Beh. of Paper Vs. Paperm. Var. - Part 1			-	-												
1.10 Preliminary Technology Assessment				-												
1.11 Phase I Report				-												
2.1 Identific.of Paper Machines for Mill Trials					-											
2.2 Devel. of On-machine Prototype System					-	-	-	-	-	-						
2.3 Fundamentals of Lamb Wave Propagation					-	-	-	-	-	-						
2.4 L.U. Invest. of Moist. & Temp. Effects - Part 2					-	-	-	-	-	-	-	-				
2.5 Mech. Beh. of Paper Vs. Paperm. Var. - Part 2					-	-	-	-	-	-	-	-				
2.6 System Integration										-	-	-				
2.7 Assessment of On-machine Prototype System												-				
2.8 Phase II Report												-				
3.1 Mech. Beh. of Paper Vs. Paperm. Var. - Part 3													-	-		
3.2 Mill Trials (Fine Paper and Linerboard Mills)													-	-	-	
3.3 Explor. Analysis of Process Control Strategies															-	-
3.4 Final Technology and Economic Assessment																-
3.5 Technology Transfer																-
3.6 Final Report																-